Biomechanical Simulations of Human Pregnancy: Patient-Specific Finite Element Modeling

Andrea R. Westervelt

Submitted in partial fulfillment of the
requirements for the degree
of Doctor of Philosophy
in the Graduate School of Arts and Sciences

COLUMBIA UNIVERSITY

2019

Abstract

Biomechanical Simulations of Human Pregnancy: Patient-Specific Finite Element Modeling

Andrea Westervelt

Preterm birth (PTB) is the leading cause of childhood death and effects 10% of babies worldwide. First-time diagnosis is difficult, and as many as 95% of all PTBs are intractable to current therapies. The processes of both preterm labor and normal parturition are poorly understood, in part because pregnancy is a protected environment where experimentation contains the risk of causing harm to the gestation and fetus. This proposes the need for non-invasive investigations to understand both normal and high-risk pregnancies. Furthermore, each pregnancy can vary significantly which adds the complex need for patient-specific investigations.

To address this need, we propose the development of parameterized ultrasound-based finite element analyses to study the mechanics of the womb. As a first step, this dissertation work conducts sensitivity analyses on cervical, uterine, and fetal membrane parameters as well as model boundary conditions to determine which factors have the greatest impact on cervical tissue stretch. The effects of the range of patient geometries and material properties are reported. Findings show that a soft and short cervix result in greatest stretch at the internal os, and fetal membrane detachment increases cervical stretch.

Additionally, patient-specific finite element analyses are performed on low- and high-risk cohorts and results between the two are compared. Patient geometries are documented at various gestational timepoints, and the effect of a cervical pessary is determined based on changes in cervical geometry and stiffness. Findings showed that a soft cervix correlates with sooner delivery, and that high pessary placement is ideal to decrease stretch at the internal os.

Table of Contents

LIST OF FIGURES v

LIST OF TABLES xii

ACKNOWLEDGMENTS xiv

1 INTRODUCTION 1

1.1 The Pregnant Environment 1

1.1.1 Uterus 1

1.1.2 Cervix 4

1.1.3 Fetal membranes 6

1.1.4 Intrauterine forces 8

1.2 Clinical motivation: preterm birth 9

1.3 Biomechanical models 12

1.3.1 Solid models of pregnancy 15

1.3.2 Material models in pregnancy 17

1.3.3 Finite element analysis in pregnancy 18

1.3.3.1 Meshing, boundary conditions, and loading 21

1.3.3.2 Previous finite element analyses in pregnancy 23

1.4 Conclusion: A need for improved biomechanical models of pregnancy 25

2 ULTRASOUND-DERIVED FINITE ELEMENT ANALYSIS OF PREGNANCY: SENSITIVITY TO CERVICAL GEOMETRY AND MATERIAL 27

2.1 Methods 28

2.1.1 Ultrasound measurement of maternal anatomy 28

2.1.2 Computer (CAD) models of pregnancy 29

2.1.3 Finite element mesh generation 32

2.1.4 Material properties 33

2.1.5 Boundary conditions and loading 37

2.1.6 Finite element (FE) analysis and evaluation 38

2.1.7 Sensitivity to cervical structural parameters 38

2.2 Results 40

2.2.1 Baseline model 40

2.2.2 Cervical structural parameters 43

2.2.2.1 Sensitivity to anterior uterocervical angle (AUCA) 44
2.2.2.2 Sensitivity to cervical length (CL) 45
2.2.2.3 Sensitivity to posterior cervical offset (PCO) 47
2.2.2.4 Sensitivity to cervical stiffness 49

2.3 Discussion 50
2.3.1 Clinical considerations 52
2.3.2 Comparison to MRI-based model 54
2.3.3 Limitations 56

2.4 Conclusions 56

3 ULTRASOUND-DERIVED FINITE ELEMENT ANALYSIS OF PREGNANCY: SENSITIVITY TO UTERINE SHAPE AND MATERIAL FIBER ORIENTATION 58

3.1 Methods 61
3.1.1 Maternal anatomy data 62
3.1.2 CAD models of pregnancy 65
3.1.3 Finite element mesh generation 66
3.1.4 Material properties 67
3.1.5 Boundary conditions and loading 70
3.1.6 Finite element analysis and evaluation 71
3.1.7 Sensitivity to uterine parameters 72

3.2 Results 72
3.2.1 Sensitivity to uterine size and shape 72
3.2.2 Sensitivity to uterine material models 74

3.3 Discussion 75
3.3.1 Limitations 75

3.4 Conclusions 77

4 ULTRASOUND-DERIVED FINITE ELEMENT ANALYSIS OF PREGNANCY: SENSITIVITY TO FETAL MEMBRANE CONTACT AND MATERIAL 79

4.1 Methods 81
4.1.1 Maternal anatomy data 81
4.1.2 CAD models of pregnancy 81
4.1.3 Finite element mesh generation 83
4.1.4 Material properties 84
4.1.5 Boundary conditions and loading 87
4.1.6 Finite element analysis and evaluation 88

4.1.7 Sensitivity to membrane parameters 89

4.2 Results 89

4.2.1 Sensitivity to membrane adhesion 89

4.2.2 Sensitivity to membrane stiffness 92

4.3 Discussion 94

4.3.1 Limitations 96

4.4 Conclusions 96

5 OPTIMIZATION OF FINITE ELEMENT ANALYSIS INPUTS 98

5.1 Physiological Boundary Conditions 98

5.1.1 Rationale and methods 98

5.1.2 Results 100

5.1.3 Conclusions 100

5.2 Fetal membranes material model 101

5.2.1 Rationale and methods 101

5.2.2 Results 104

5.2.3 Conclusions 105

5.3 Order of finite element mesh shape functions 106

5.3.1 Rationale and methods 106

5.3.2 Results 107

5.3.3 Conclusions 108

6 LONGITUDINAL CLINICAL STUDIES OF PREGNANCY: SUBJECT-SPECIFIC GEOMETRY, MATERIAL, AND FINITE ELEMENT ANALYSIS 110

6.1 Low-risk cohort 113

6.1.1 Methods 114

6.1.1.1 Patient recruitment 114

6.1.1.2 Data acquisition 115

6.1.1.3 3D CAD models of the maternal anatomy and uterine cavity 116

6.1.1.4 Finite element mesh generation 119

6.1.1.5 Material properties 120

6.1.1.6 Boundary conditions and loading 121

6.1.1.7 Finite element analysis 122

6.1.2 Results 122

6.1.3 Discussion 125

6.1.4 Conclusions 126

6.2 High-risk cohort 127

6.2.1 Methods 131

6.2.1.1 Patient recruitment 131

6.2.1.2 Data acquisition 132

6.2.1.3 3D CAD models of the lower uterine segment 136

6.2.1.4 Finite element mesh generation 139

6.2.1.5 Material properties 140

6.2.1.6 Boundary conditions and loading 144

6.2.1.7 Finite element analysis 146

6.2.2 Results 146

6.2.2.1 Maternal anatomy and material stiffness 146

6.2.2.2 Finite element analysis 156

6.2.3 Discussion 165

6.2.3.1 Limitations 172

6.2.4 Conclusions 174

7 CONCLUSIONS AND FUTURE WORK 175

7.1 Recommendations for future work 176

REFERENCES 178

List of Figures

FIGURE 1-1: FEMALE PELVIC ANATOMY. THIS FIGURE SHOWS THE UPPER UTERINE BODY AND THE CERVIX, AS WELL AS THE PROXIMITY OF THE UTERUS TO THE BLADDER AND RECTUM[2]. 2

FIGURE 1-2: UTERINE GROWTH FROM 20 TO 36 WEEKS GESTATION TAKEN FROM X-RAY DATA[10] 3

FIGURE 1-3: PROGRESSION OF THE CERVIX FROM CLOSED (LEFT) TO EFFACEMENT AND DILATION[22]. 5

FIGURE 1-4: FETAL FIBRONECTIN INTERFACE IN THE CHORIODECIDUAL REGION[40]. 7

FIGURE 1-5: MRI-DERIVED (LEFT) AND ULTRASOUND-DERIVED PARAMETRIC (RIGHT) CAD MODELS OF PREGNANCY. 16

FIGURE 1-6: FORMULATION PROCESS FOR ULTRASOUND-BASED FINITE ELEMENT ANALYSIS OF PREGNANCY. MODELS ARE INFORMED WITH ULTRASOUND DIMENSIONAL DATA, EXPERIMENTAL TISSUE MECHANICAL PROPERTIES, LOADING, AND BOUNDARY CONDITIONS. MESH GENERATION IS AUTOMATED IN THE LINEAR SOLVER FOR MECHANICAL EVALUATION OF OUTPUT PARAMETERS. 21

FIGURE 2-1: UTERINE AND CERVICAL DIMENSIONS TAKEN VIA TRANSABDOMINAL AND TRANSPERINEAL ULTRASOUND AT 25 WEEKS OF GESTATION. UD=UTERINE DIAMETER, UT=UTERINE THICKNESS, CD=CERVICAL DIMENSION, CA=CERVICAL ANGLE. 28

FIGURE 2-2: 3D REPRESENTATION OF THE ENVIRONMENT OF PREGNANCY. THE CERVIX WAS SEPARATED INTO THREE SECTIONS FOR ANALYSIS: THE UPPER CERVIX, LOWER CERVIX, AND INTERNAL OS REGION. 31

FIGURE 2-3: SAMPLE MESH FOR BASELINE GEOMETRY. THE FETAL MEMBRANE WAS MESHED WITH HEXAHEDRAL ELEMENTS, WHILE ALL OTHER VOLUMES WERE MESHED WITH TETRAHEDRAL ELEMENTS. 33

FIGURE 2-4: BOUNDARY AND LOADING CONDITIONS. OUTSIDE OF THE ABDOMEN WAS FIXED IN X, Y, AND Z DIRECTIONS (DASHED LINES IN FIGURE). UNIFORM INTRAUTERINE PRESSURE (IUP) WAS APPLIED ON THE INNER SURFACE OF FM. TIED CONTACT WAS APPLIED BETWEEN FM (CYAN) AND UTERINE WALL (PURPLE) AND BETWEEN FM AND UPPER CERVIX (GREEN). SLIDING CONTACT WAS APPLIED BETWEEN FM AND CERVIX INTERNAL OS REGION (YELLOW). 37

FIGURE 2-5: THE COLOR MAP REPORTS THE 1ST PRINCIPAL RIGHT STRETCH FOR THE BASELINE GEOMETRY EVALUATED WITH IUPS OF (A&D) 25 WEEKS = 0.817 KPA, (B&E) 40 WEEKS = 2.33 KPA, AND (C&F) CONTRACTION = 8.67 KPA. THE PERCENTAGE REPORTS THE VOLUME FRACTION OF THE CERVICAL INTERNAL OS REGION ABOVE A 1.05 STRETCH. THE MEMBRANE IS REMOVED FOR CLARITY. 41

FIGURE 2-6: BASELINE RESULTS WITH VECTOR PLOTS TO SHOW STRETCH DIRECTIONS FOR (A) 1ST PRINCIPAL RIGHT STRETCH, (B) 2ND PRINCIPAL RIGHT STRETCH, (C) 3RD PRINCIPAL RIGHT STRETCH, AND (D) MAXIMUM SHEAR STRAIN. FOR 1ST PRINCIPAL RIGHT STRETCH, CIRCUMFERENTIAL STRETCH IS EXHIBITED AT THE INTERNAL OS WHILE RADIAL STRETCH IS OBSERVED AT THE ANTERIOR AND POSTERIOR SECTIONS OF THE UTEROCERVICAL INTERFACE. 43

FIGURE 2-7: UTERINE AND CERVICAL STRETCH PATTERNS AS AUCA (SHOWN TOP LEFT) IS VARIED. THE COLOR MAP REPORTS THE 1ST PRINCIPAL RIGHT STRETCH FOR REMODELED CERVIX WITH AUCA OF (A) 90◦, (B) 100◦, AND (C) 110◦, AND REMODELED CERVIX WITH AUCA OF (D) 90◦, (E) 100◦, AND (F) 110◦. THE PERCENTAGE REPORTS THE VOLUME FRACTION OF THE CERVICAL INTERNAL OS REGION ABOVE A 1.05 STRETCH. THE MEMBRANE IS REMOVED FOR CLARITY 45

FIGURE 2-8: UTERINE AND CERVICAL STRETCH PATTERNS AS CL (SHOWN TOP LEFT) IS VARIED. THE COLOR MAP REPORTS THE 1ST PRINCIPAL RIGHT STRETCH FOR NOT REMODELED CERVIX WITH CL OF (A) 25 MM, (B) 30 MM, (C) 35 MM, AND (D) 40 MM, AND REMODELED CERVIX WITH CL OF (E) 25 MM, (F) 30 MM, (G) 35 MM, AND (H) 40 MM. THE PERCENTAGE REPORTS THE VOLUME FRACTION OF THE CERVICAL INTERNAL OS REGION ABOVE A 1.05 STRETCH. THE MEMBRANE IS REMOVED FOR CLARITY. 46

FIGURE 2-9: UTERINE AND CERVICAL STRETCH PATTERNS AS PCO (SHOWN TOP LEFT) IS VARIED. THE COLOR MAP REPORTS THE 1ST PRINCIPAL RIGHT STRETCH FOR NOT REMODELED CERVIX WITH PCO OF (A) 0 MM, (B) 5 MM, (C) 10 MM, (D) 15 MM, (E) 20 MM, AND (F) 25 MM, AND REMODELED CERVIX WITH PCO OF (G) 0 MM, (H) 5 MM, (I) 10 MM, (J) 15 MM, (K) 20 MM, AND (L) 25 MM. THE PERCENTAGE REPORTS THE VOLUME FRACTION OF THE CERVICAL INTERNAL OS REGION ABOVE A 1.05 STRETCH. THE MEMBRANE IS REMOVED FOR CLARITY. 48

FIGURE 2-10: UTERINE AND CERVICAL STRETCH PATTERNS AS CERVICAL FIBER STIFFNESS IS VARIED. THE COLOR MAP REPORTS THE 1ST PRINCIPAL RIGHT STRETCH FOR THE BASELINE GEOMETRY EVALUATED WITH A CERVICAL FIBER STIFFNESS (Ξ) VALUE OF (A) 1.71, (B) 7.89, (C) 36.3, (D) 167, AND (E) 867 KPA. THE PERCENTAGE REPORTS THE VOLUME FRACTION OF THE CERVICAL INTERNAL OS ABOVE A 1.05 STRETCH. THE MEMBRANE IS REMOVED FOR CLARITY. 49

FIGURE 2-11: PRINCIPAL RIGHT STRETCH PLOTS OF THE MRI GEOMETRY MODEL (A1) AND THE PARAMETERIZED GEOMETRY MODEL (A2) UNDER AN IUP OF 0.817 KPA APPLIED TO THE FETAL MEMBRANE. FIRST PRINCIPAL STRETCHES (A1, A2) REFLECT THE AREAS OF HIGHEST TENSION AND ARE CONCENTRATED AROUND THE INTERNAL OS AND THE PROXIMAL PORTION OF THE CERVIX. THIRD PRINCIPAL STRAINS (C1, C2) REPRESENT AREAS OF COMPRESSION, WHICH ARE MOST PROMINENT IN THE MRI MODEL (C1). SHEAR STRAINS ARE SHOWN IN FIGURES D, AND ARE ALSO CONCENTRATED OVER THE INTERNAL OS, BUT ARE APPROXIMATELY TWICE AS LARGE IN THE MRI-DERIVED MODEL DUE TO THE IRREGULAR SURFACE OF THE GEOMETRY. 54

FIGURE 3-1: BIOLOGICAL LENGTH SCALES OF THE CERVIX AND UTERUS. THE CERVIX IS COMPOSED OF A HIERARCHAL CROSS-LINKED COLLAGEN NETWORK WITH EMBEDDED SMOOTH MUSCLE CELLS (SMC) AT THE INTERNAL OS[18], AND THE LOAD-BEARING MYOMETRIUM IS COMPOSED OF LAYERS OF PREFERENTIALLY-ALIGNED SMC BUNDLES[139,140]...59

FIGURE 3-2: FINITE ELEMENT MODEL CREATED IN FEBIO 2.6.2, MATERIAL PARAMETERS REPORTED IN [75,106] AND IUP REPORTED IN [52]. 62

FIGURE 3-3: TRANSVERSE DIAMETER OF THE UTERUS TAKEN FROM A SAGITTAL VIEW X-RAY[10]. VALUES ARE PLOTTED IN CENTIMETERS AND MAY BE GREATER THAN REAL LIFE DUE TO X-RAY DISTORTION, THOUGH THE DISTORTION REMAINS CONSTANT ACROSS PATIENTS SO THE RELATIVE VALUES ARE ACCURATE. NOTE THAT ELONGATION DIMINISHES AFTER THE 32^{ND} WEEK OF GESTATION. 63

FIGURE 3-4: ELONGATION OF THE HUMAN UTERUS[10]. LENGTH IS THE GREATEST LENGTH OF THE UTERUS; WIDTH IS THE ANTERIOR-POSTERIOR DIAMETER. AS L/W INCREASES IN VALUE, THE CURVE RISES AND THE UTERUS ELONGATES. NOTE THE RAPID ELONGATION UNTIL THE 32^{ND} WEEK OF GESTATION. 63

FIGURE 3-5: WEIGHT OF UTERUS, FETUS, AND UTERINE WALL THICKNESS THROUGHOUT GESTATION[10]. AFTER THE 20^{TH} WEEK, UTERINE GROWTH DIMINISHES, AND THE MYOMETRIUM, THEREFORE, BEGINS TO THIN. 64

FIGURE 3-6: SAMPLE MESH FOR 35-WEEK GEOMETRY. THE FETAL MEMBRANE WAS MESHED WITH HEXAHEDRAL ELEMENTS, WHILE ALL OTHER VOLUMES WERE MESHED WITH TETRAHEDRAL ELEMENTS. 67

FIGURE 3-7: BOUNDARY AND LOADING CONDITIONS. THE ABDOMEN WAS FIXED ALONG ITS OUTSIDE IN X, Y, AND Z DIRECTIONS (DASHED LINES IN FIGURE). UNIFORM INTRAUTERINE PRESSURE (IUP) WAS APPLIED ON THE INNER SURFACE OF FM. TIED CONTACT WAS APPLIED BETWEEN FM (CYAN) AND THE UTERINE WALL (PURPLE) AND BETWEEN FM AND UPPER CERVIX (GREEN). SLIDING CONTACT WAS APPLIED BETWEEN FM AND CERVIX INTERNAL OS REGION (YELLOW). 71

FIGURE 3-8: UTERINE AND CERVICAL STRETCH AT IUP = 8.6KPA USING REFERENCE GEOMETRIES BASED ON A) 20 WEEKS, B) 25 WEEKS, C) 30 WEEKS, AND D) 35 WEEKS X-RAY DATA[10]. CERVICAL LOADING CALCULATED ABOVE 1.05 STRETCH. TRANS=TRANSVERSE UTERINE DIAMETER, A-P=ANTERIOR-POSTERIOR UTERINE DIAMETER, LONG=LONGITUDINAL UTERINE DIAMETER, T=UTERINE WALL THICKNESS. DIMENSIONS ARE IN MM. ABDOMEN AND MEMBRANES ARE REMOVED FOR CLARITY. 73

FIGURE 3-9: UTERINE AND CERVICAL STRETCH AT IUP = 8.6KPA FOR A A) 20 WEEK AND B) 35-WEEK UTERINE GEOMETRY EXPOSED TO CONTRACTION-MAGNITUDE INTRAUTERINE PRESSURE. THE INSET ZOOMS ON THE LOWER UTERINE SEGMENT TO SHOW A STRETCH GRADIENT IN THE UTERINE WALL. PRINCIPAL STRETCH IS GREATEST AT THE INNER UTERINE WALL AND DECREASES MOVING TOWARD THE OUTER WALL. 73

FIGURE 3-10: UTERINE STRETCH AT IUP = 8.67KPA FOR A A) RANDOMLY ORIENTED UTERINE FIBER MATERIAL B) PREFERENTIALLY-ALIGNED FIBERS IN THE CIRCUMFERENTIAL AND C) LONGITUDINAL DIRECTION. THE INSET ZOOMS ON THE LOWER UTERINE SEGMENT TO SHOW A STRETCH GRADIENT IN THE UTERINE WALL. 74

FIGURE 4-1: DIAGRAM OF THE FETAL MEMBRANE LAYERS AND THEIR RESPECTIVE SUBLAYERS. THE AMNION IS THE LOAD-BEARING LAYER CLOSEST TO THE FETUS, AND THE CHORION ADHERES TO THE MATERNAL DECIDUA[152]. 79

FIGURE 4-2: SAMPLE MESH FOR BASELINE GEOMETRY. THE FETAL MEMBRANE WAS MESHED WITH HEXAHEDRAL ELEMENTS, WHILE ALL OTHER VOLUMES WERE MESHED WITH TETRAHEDRAL ELEMENTS. 84

FIGURE 4-3: BOUNDARY AND LOADING CONDITIONS. THE POSTERIOR SIDE OF THE ABDOMEN WAS FIXED IN X, Y, AND Z DIRECTIONS (DASHED LINES IN FIGURE). UNIFORM INTRAUTERINE PRESSURE (IUP) WAS APPLIED ON THE INNER SURFACE OF FM. TIED CONTACT WAS APPLIED BETWEEN FM (CYAN) AND THE UTERINE WALL (PURPLE) AND BETWEEN FM AND UPPER CERVIX (GREEN). SLIDING CONTACT WAS APPLIED BETWEEN FM AND CERVIX INTERNAL OS REGION (YELLOW). 88

FIGURE 4-4: FETAL MEMBRANES LOSING ADHERENCE RESULTS IN INCREASED CERVICAL STRESS, AND MOVES UTERINE STRESS ANTERIORLY. MODELS SHOW 1^{ST} PRINCIPAL STRESS IN THE UTERUS AND CERVIX. THE MEMBRANE IS REMOVED FOR CLARITY. 90

FIGURE 4-5: FETAL MEMBRANES LOSING ADHERENCE RESULTS IN AN INCREASED CERVICAL STRETCH, AND MOVES UTERINE STRETCH ANTERIORLY. MODELS SHOW 1^{ST} PRINCIPAL STRETCH IN THE UTERUS AND CERVIX. THE MEMBRANE IS REMOVED FOR CLARITY. PERCENTAGES SHOW THE VOLUME FRACTION OF THE CERVICAL INTERNAL OS REGION ABOVE A 1.2 STRETCH THRESHOLD. 90

FIGURE 4-6: 2^{ND} (LEFT) AND 3^{RD} (RIGHT) PRINCIPAL STRETCHES IN UTERINE AND CERVICAL TISSUE IN THE CASE OF A FULLY-ADHERED MEMBRANE (TOP) AND FULL-DETACHED MEMBRANE (BOTTOM). 91

FIGURE 4-7: FETAL MEMBRANE ADHESION DOES NOT AFFECT MEMBRANE STRESS. MODELS SHOW 1ST PRINCIPAL STRESS IN THE FETAL MEMBRANES. UTERUS AND CERVIX ARE REMOVED FOR CLARITY. 92

FIGURE 4-8: STIFFER FETAL MEMBRANES RESULT IN REDUCED CERVICAL AND UTERINE STRESS. MODELS SHOW 1ST PRINCIPAL STRESS IN THE UTERUS AND CERVIX. THE MEMBRANE IS REMOVED FOR CLARITY. 92

FIGURE 4-9: STIFFER FETAL MEMBRANES RESULT IN REDUCED CERVICAL AND UTERINE STRETCH. MODELS SHOW 1ST PRINCIPAL STRETCH IN THE UTERUS AND CERVIX. THE MEMBRANE IS REMOVED FOR CLARITY. PERCENTAGES SHOW THE VOLUME FRACTION OF THE CERVICAL INTERNAL OS REGION ABOVE A 1.1 STRETCH THRESHOLD. 93

FIGURE 4-10: 2ND (LEFT) AND 3RD (RIGHT) PRINCIPAL RIGHT STRETCHES IN THE UTERUS AND CERVIX AS THE MEMBRANE IS ADJUSTED FROM BASELINE STIFFNESS (TOP) TO 5X (MIDDLE) AND 10X (BOTTOM) STIFFNESS....93

FIGURE 4-11: STIFFER FETAL MEMBRANES RESULT IN REDUCED MEMBRANE STRESS. MODELS SHOW 1ST PRINCIPAL STRESS IN THE FETAL MEMBRANES. THE UTERUS AND CERVIX ARE REMOVED FOR CLARITY. 94

FIGURE 5-1: ORIENTATION OF A PREGNANT UTERUS WITHIN THE ABDOMEN, AND ITS REFERENCE TO BONES SUCH AS THE SPINE AND PUBIC BONES. [159] 99

FIGURE 5-2: UTERUS DEFORMATION FROM A SPHERICAL REFERENCE CONFIGURATION AT 16 WEEKS TO AN ELLIPTICAL DEFORMED CONFIGURATION AT 24 WEEKS. 100

FIGURE 5-3: STRESS-STRAIN MATERIAL FIT RESULTS OF FIBER-BASED MATERIAL FOR FETAL MEMBRANES COMPARED TO EXPERIMENTAL DATA[36]. 103

FIGURE 5-4: EXTENSION-COMPRESSION MATERIAL FIT RESULTS OF FIBER-BASED MATERIAL MODEL OF FETAL MEMBRANES FIT TO EXPERIMENTAL DATA[36]....103

FIGURE 5-5: COMPARISON IN THE DEFORMATION BETWEEN OGDEN AND FIBER-BASED MEMBRANE MATERIAL MODELS....104

FIGURE 5-6: COMPARISON OF UTERINE AND CERVICAL STRETCH BETWEEN OGDEN AND FIBER-BASED MEMBRANE MATERIAL MODELS....105

FIGURE 5-7: LINEAR (LEFT) AND QUADRATIC (RIGHT) SHAPE FUNCTION ELEMENTS. THE TOP ROW IS HEXAHEDRAL ELEMENTS AND THE BOTTOM ROW IS TETRAHEDRAL ELEMENTS[162]. 106

FIGURE 5-8: MEAN, MEDIAN, AND 95TH PERCENTILE 1ST PRINCIPAL CERVICAL STRAIN IN FINITE ELEMENT ANALYSES WITH LINEAR (LEFT) AND QUADRATIC (RIGHT) ELEMENT SHAPE FUNCTIONS. 108

FIGURE 6-1: FOURTEEN SOLID MODELS. EACH ROW SHOWS TWO, MATCHED MODELS—ONE MODEL FROM THE SECOND TRIMESTER AND ONE FROM THE THIRD TRIMESTER. THE MODELS ARE MATCHED BY THE DISTANCE OF THE CONJUGATE DIAMETER OF THE PELVIC BONE. THE FIRST TWO COLUMNS DEMONSTRATE CERVICAL LENGTH. THE MIDDLE TWO COLUMNS SHOW AN ANTERIOR VIEW AND THE CERVIX IS TRANSPARENT. THE LAST TWO COLUMNS SHOW A POSTERIOR VIEW. IN ALL MODELS, THE VOLUME OF THE AMNIOTIC CAVITY BELOW THE DIAGONAL CONJUGATE IS LARGER IN THE THIRD TRIMESTER COMPARED TO THE SECOND TRIMESTER. IN ADDITION, THE TRANSITION FROM THE CERVIX TO THE UTERUS IS WIDER IN THE THIRD TRIMESTER COMPARED TO THE SECOND TRIMESTER (COMPARE (C) VS. (D), (G) VS. (H), (I) VS. (J), (K) VS. (M)). MODEL (N) SHOWS A CERVIX THAT IS COMPLETELY EFFACED AT 31 WEEKS. THIS PATIENT DELIVERED AT 33 WEEKS. DIMENSIONS ARE IN MILLIMETERS[77]. 110

FIGURE 6-2: WHAT KINEMATICS DOES THE UTERUS EXPERIENCE FROM 16 TO 24 WEEKS? GEOMETRIC DRAWINGS OF THE UTERUS FROM ONE LOW-RISK PATIENT AT 16W2D AND 24W2D GESTATION....113

FIGURE 6-3: MATERNAL ANATOMY DIMENSIONS TAKEN VIA SAGITTAL TRANSABDOMINAL (A-C), TRANSVERSE TRANSABDOMINAL (D-E), AND SAGITTAL TRANSVAGINAL ULTRASOUND(F). 116

FIGURE 6-4: GEOMETRIES OF THE UTERUS, CERVIX, VAGINAL CANAL, ABDOMEN, AND ABDOMINAL CAVITY OF DEFORMED CONFIGURATION OF THE UTERUS....117

FIGURE 6-5: FINITE ELEMENT MESH OF THE UTERUS, CERVIX, AND ABDOMEN WITH CAVITY AS THE DEFORMED CONFIGURATION OF THE UTERUS. ALL VOLUMES ARE MESHED USING TETRAHEDRAL ELEMENTS....119

FIGURE 6-6: FINITE ELEMENT BOUNDARY AND LOADING CONDITIONS. THE CERVIX WAS TIED TO THE ABDOMINAL CAVITY, AND THE REFERENCE UTERUS WAS ALLOWED TO SLIDE FREELY ALONG THE INSIDE OF THE DEFORMED UTERINE SIZED ABDOMINAL CAVITY. INTRAUTERINE PRESSURE WAS APPLIED TO THE INNER SURFACE OF THE UTERUS UNTIL THE REFERENCE CONFIGURATION TOUCHED ALL WALLS OF THE ABDOMINAL CAVITY. 121

FIGURE 6-7: MAGNITUDE OF STRAIN IN THE UTERUS AND CERVIX OF A REPRESENTATIVE PATIENT. THE 1^{ST} PRINCIPAL STRAIN IS PLOTTED THROUGHOUT THE UTERUS AND CERVICAL TISSUE (LEFT). THE MEDIAN AND 95^{TH} PERCENTILE MAGNITUDE OF 1^{ST}, 2^{ND}, AND 3^{RD} PRINCIPAL STRAINS ARE ALSO SHOWN (RIGHT). 123

FIGURE 6-8: MAGNITUDE OF STRAIN IN THE UTERUS AND CERVIX AT ALL 5 PATIENTS, IN ORDER FROM LARGEST TO SMALLEST MAGNITUDE. THE 1^{ST} PRINCIPAL STRAIN IS VISUALIZED THROUGHOUT THE UTERUS AND CERVIX (TOP). THE MEDIAN AND 95^{TH} PERCENTILE MAGNITUDE OF 1^{ST}, 2^{ND}, AND 3^{RD} PRINCIPAL STRAINS ARE SHOWN (BOTTOM)....124

FIGURE 6-9: SILICONE ARABIN PESSARY[169]....127

FIGURE 6-10: ARABIN PESSARY INSERTED INTO THE VAGINA AND AROUND A PATIENT'S CERVIX IN ORDER TO MECHANICALLY SUPPORT AND KEEP IT CLOSED[170]. 128

FIGURE 6-11: MATERNAL ANATOMY DIMENSIONS TAKEN FROM SAGITTAL TRANSABDOMINAL (A-C), TRANSVERSE TRANSABDOMINAL (D-E), AND SAGITTAL TRANSVAGINAL (F) ULTRASOUND....134

FIGURE 6-12: CLINICAL USE OF THE CERVICAL ASPIRATION DEVICE. THE PROBE IS INSERTED INTO THE VAGINAL CANAL DURING A SPECULUM EXAM AND CERVICAL STIFFNESS IS MEASURED ON THE ANTERIOR CERVICAL LIP. 135

FIGURE 6-13: COLLECTIVE RESULTS OF CLOSURE PRESSURE P_{CL} OF THE REFERENCE GROUP AND DURING GESTATION: CLOSURE PRESSURE P_{CL} OF NONPREGNANT (NP, LEFT) AND PREGNANT WOMEN DURING PREGNANCY (MONTHS 2–9) AND POSTPARTUM (PP, RIGHT) ARE SHOWN AS VERTICAL BARS – CROSSES INDICATE CERVICAL LENGTH (CL), AND THE VALUES REFER TO THE SECOND VERTICAL AXIS ON THE RIGHT. FOR ALL VALUES, MEANS, AND STANDARD DEVIATIONS ARE REPORTED[146]. 136

FIGURE 6-14: 3D REPRESENTATION OF THE ENVIRONMENT OF PREGNANCY. THE MODEL INCLUDES THE UTERUS (MAGENTA), CERVIX (YELLOW), FETAL MEMBRANES (GREEN), AND A SURROUNDING ABDOMEN WITH A VAGINAL CANAL CUTOUT (CYAN)....137

FIGURE 6-15: FINITE ELEMENT MESH OF THE UTERUS (MAGENTA), CERVIX (YELLOW), ABDOMEN (CYAN), AND FETAL MEMBRANES (GREEN). THE UTERUS, CERVIX, AND ABDOMEN ARE MESHED WITH QUADRATIC TETRAHEDRAL ELEMENTS AND THE MEMBRANES ARE MESHED USING QUADRATIC HEXAHEDRAL ELEMENTS. 140

FIGURE 6-16: MODEL BOUNDARY, CONTACT, AND LOADING CONDITIONS. 145

FIGURE 6-17: UTERINE DIAMETERS THROUGHOUT GESTATION COMPARING LOW-RISK (UTAH) AND HIGH-RISK (ATOPS) COHORTS. DIAMETERS WERE MEASURED IN THE LONGITUDINAL DIRECTION (UD1), ANTERIOR-POSTERIOR DIRECTION (UD23), AND LEFT-RIGHT DIRECTION (UD4). 147

FIGURE 6-18: UTERINE DIAMETERS AT RECRUITMENT AND FOLLOW-UP VISITS COMPARING PROGESTERONE ONLY AND PROGESTERONE+PESSARY TREATMENT GROUPS IN A HIGH-RISK (ATOPS) COHORT. DIAMETERS WERE MEASURED IN THE LONGITUDINAL DIRECTION (UD1), ANTERIOR-POSTERIOR DIRECTION (UD23), AND LEFT-RIGHT DIRECTION (UD4). THE PESSARY SUBGROUP WAS MEASURED BOTH IMMEDIATELY PRIOR TO (VISIT 1(PRE)) AND IMMEDIATELY AFTER (VISIT 1(POST)) PESSARY INSERTION, WHILE THE PROGESTERONE ONLY GROUP WAS ONLY MEASURED ONCE DURING THE FIRST VISIT. BOTH GROUPS WERE SCANNED ONCE AT THE FOLLOW-UP VISIT (VISIT 2). 148

FIGURE 6-19: UTERINE WALL THICKNESSES THROUGHOUT GESTATION COMPARING LOW-RISK (UTAH) AND HIGH-RISK (ATOPS) COHORTS. WALL THICKNESS WAS MEASURED AT THE FUNDUS (UT1), ANTERIOR WALL NEAR THE UMBILICAL LEVEL (UT2), AND LEFT OR RIGHT WALL AT THE UMBILICAL LEVEL (UT3), AND AT THE ANTERIOR LOWER UTERINE SEGMENT (UT4). 149

FIGURE 6-20: UTERINE WALL THICKNESSES AT RECRUITMENT AND FOLLOW-UP VISITS COMPARING PROGESTERONE ONLY AND PROGESTERONE+PESSARY TREATMENT GROUPS IN A HIGH-RISK (ATOPS) COHORT. WALL THICKNESS WAS MEASURED AT THE FUNDUS (UT1), ANTERIOR WALL NEAR THE UMBILICAL LEVEL (UT2), AND LEFT OR RIGHT WALL AT THE UMBILICAL LEVEL (UT3), AND AT THE ANTERIOR LOWER UTERINE SEGMENT (UT4). THE PESSARY SUBGROUP WAS MEASURED BOTH PRIOR TO (VISIT 1(PRE)) AND IMMEDIATELY AFTER (VISIT 1(POST)) PESSARY INSERTION, WHILE THE PROGESTERONE ONLY GROUP WAS ONLY MEASURED ONCE DURING THE FIRST VISIT. BOTH GROUPS WERE SCANNED ONCE AT THE FOLLOW-UP VISIT (VISIT 2). 150

FIGURE 6-21: CERVICAL LENGTH (CL) AND OUTER CERVICAL DIAMETER (CD1) THROUGHOUT GESTATION COMPARING LOW-RISK (UTAH) AND HIGH-RISK (ATOPS) COHORTS. 151

FIGURE 6-22: CERVICAL LENGTH (CL) AND OUTER CERVICAL DIAMETER (CD1) AT RECRUITMENT AND FOLLOW-UP VISITS COMPARING PROGESTERONE ONLY AND PROGESTERONE+PESSARY TREATMENT GROUPS IN A HIGH-RISK (ATOPS) COHORT. THE PESSARY SUBGROUP WAS MEASURED BOTH PRIOR TO (VISIT 1(PRE)) AND IMMEDIATELY AFTER (VISIT 1(POST)) PESSARY INSERTION, WHILE THE PROGESTERONE ONLY GROUP WAS ONLY MEASURED ONCE DURING THE FIRST VISIT. BOTH GROUPS WERE SCANNED ONCE AT THE FOLLOW-UP VISIT (VISIT 2). 152

FIGURE 6-23: ANTERIOR UTEROCERVICAL ANGLE (AUCA) AND POSTERIOR CERVICAL OFFSET (PCO) THROUGHOUT GESTATION COMPARING LOW-RISK (UTAH) AND HIGH-RISK (ATOPS) COHORTS. 153

FIGURE 6-24: ANTERIOR UTEROCERVICAL ANGLE (AUCA) AND POSTERIOR CERVICAL OFFSET (PCO) AT RECRUITMENT AND FOLLOW-UP VISITS COMPARING PROGESTERONE ONLY AND PROGESTERONE+PESSARY TREATMENT GROUPS IN A HIGH-RISK (ATOPS) COHORT. THE PESSARY SUBGROUP WAS MEASURED BOTH IMMEDIATELY PRIOR TO (VISIT 1(PRE)) AND IMMEDIATELY AFTER (VISIT 1(POST)) PESSARY INSERTION, WHILE THE PROGESTERONE ONLY GROUP WAS ONLY MEASURED ONCE DURING THE FIRST VISIT. BOTH GROUPS WERE SCANNED ONCE AT THE FOLLOW-UP VISIT (VISIT 2). 154

FIGURE 6-25: ASPIRATION CLOSE PRESSURE P_{CL} AT RECRUITMENT AND FOLLOW-UP VISITS COMPARING PROGESTERONE ONLY AND PROGESTERONE+PESSARY TREATMENT GROUPS IN A HIGH-RISK (ATOPS) COHORT. BOTH SUBGROUPS WERE GIVEN ASPIRATION ONCE PER VISIT. THE PESSARY GROUP WAS MEASURED BEFORE PESSARY INSERTION. THE BLUE LINE

IS A TRENDLINE FIT TO THE PATIENTS' FIRST VISIT DATA ONLY IN ORDER TO RULE OUT THE INFLUENCE OF PESSARY INTERVENTION.....155

FIGURE 6-26: ASPIRATION CLOSURE PRESSURE PCL VS. TIME TO DELIVERY COMPARING PROGESTERONE ONLY AND PROGESTERONE+PESSARY TREATMENT GROUPS IN A HIGH-RISK (ATOPS) COHORT. BOTH SUBGROUPS WERE GIVEN ASPIRATION ONCE PER VISIT. THE PESSARY GROUP WAS MEASURED BEFORE PESSARY INSERTION. THE BLUE LINE IS A TRENDLINE FIT TO THE PATIENTS' FIRST VISIT DATA ONLY IN ORDER TO RULE OUT THE INFLUENCE OF PESSARY INTERVENTION.....156

FIGURE 6-27: 1^{ST}, 2^{ND}, AND 3^{RD} PRINCIPAL RIGHT STRETCH IN P3 MODEL AT MEASURED (LEFT) AND ASSUMED NORMAL (RIGHT) CERVICAL FIBER STIFFNESS. 157

FIGURE 6-28: BASELINE RESULTS WITH VECTOR PLOTS TO SHOW STRETCH DIRECTIONS FOR $1^{ST,}$ 2^{ND}, AND 3^{RD} PRINCIPAL STRETCH IN THE UTERUS AND CERVIX. FOR 1ST PRINCIPAL RIGHT STRETCH, CIRCUMFERENTIAL STRETCH IS EXHIBITED AT THE INTERNAL OS WHILE RADIAL STRETCH IS OBSERVED AT THE ANTERIOR AND POSTERIOR SECTIONS OF THE UTEROCERVICAL INTERFACE.....158

FIGURE 6-29: EFFECTIVE STRESS IN THE UTERUS AND CERVIX FOR P3.....158

FIGURE 6-30: 1^{ST} PRINCIPAL RIGHT STRETCH VISUALIZATION OF EACH PATIENT WITH A MEASURED (LEFT) AND ASSUMED NORMAL (RIGHT) CERVICAL FIBER STIFFNESS. BAR GRAPH OF MEDIAN AND 95^{TH} PERCENTILE OF 1^{ST}, 2^{ND}, AND 3^{RD} PRINCIPAL STRETCH IN EACH PATIENT. 160

FIGURE 6-31: CERVICAL FUNNEL IN FINITE ELEMENT ANALYSIS (LEFT) VS. ULTRASOUND IMAGES (RIGHT).....163

FIGURE 6-32: VISUALIZATION OF 1^{ST} PRINCIPAL RIGHT STRETCH IN TWO PATIENTS WITH NO PESSARY, A LOW PESSARY INSERTED NEAR THE EXTERNAL OS, AND A HIGH PESSARY INSERTED CLOSER TO THE INTERNAL OS. 164

List of Tables

TABLE 2-1: BASELINE ULTRASOUND MEASUREMENTS. UD=UTERINE DIAMETER, PCO=POSTERIOR CERVICAL OFFSET, UT=UTERINE THICKNESS, AUCA=ANTERIOR UTEROCERVICAL ANGLE, CA=CERVICAL ANGLE *ARBITRARY VALUE, NOT MEASURED VALUE), CL=CERVICAL LENGTH, CD=CERVICAL DIAMETER 30

TABLE 2-2: MESH PROPERTIES FOR THE BASELINE MODEL....32

TABLE 2-3: UTERINE AND CERVICAL TISSUE VARIABLES TAKEN FROM MATERIAL FITS TO EXPERIMENTAL DATA. THESE VALUES ARE IMPLEMENTED IN A CONTINUOUS FIBER DISTRIBUTION MATERIAL MODEL USED IN FEBIO 2.4.2. 36

TABLE 2-4: FETAL MEMBRANES (FM) MATERIAL PROPERTIES DESCRIBED BY AN OGDEN MATERIAL MODEL IN EQUATION 2-5. 37

TABLE 2-5: MODEL GEOMETRIES, WITH RANGES FOR EACH VARIED PARAMETER. AUCA = ANTERIOR UTEROCERVICAL ANGLE, CL = CERVICAL LENGTH, PCO = POSTERIOR CERVICAL OFFSET 39

TABLE 2-6: SUMMARY OF RESULTS FOR THE VOLUME FRACTION OF CERVICAL INTERNAL OS ABOVE A 1.05 STRETCH THRESHOLD. AUCA=ANTERIOR UTEROCERVICAL ANGLE, CL=CERVICAL LENGTH, PCO=POSTERIOR CERVICAL OFFSET. THE GEOMETRIC PARAMETER PCO HAD THE LARGEST INFLUENCE ON THE AMOUNT OF TISSUE STRETCH AT THE CERVICAL INTERNAL OS, FOR BOTH A SOFT PG CERVIX AND A STIFFER NP CERVIX. THE MOST DRASTIC REDUCTION IN CERVICAL TISSUE STRETCH OCCURS FOR A SOFT CERVIX THAT IS ALIGNED WITH THE UTERINE LONGITUDINAL AXIS COMPARED TO A 25 MM PCO....44

TABLE 3-1: UTERINE CONFIGURATIONS BUILT FROM LATERAL AND ANTEROPOSTERIOR SOFT TISSUE X-RAYS OF 15 NORMAL PATIENTS[10]. 65

TABLE 3-2: MESH PROPERTIES FOR 35-WEEK MODEL....66

TABLE 3-3: UTERINE AND CERVICAL TISSUE VARIABLES TAKEN FROM MATERIAL FITS TO EXPERIMENTAL DATA. THESE VALUES ARE IMPLEMENTED IN A CONTINUOUS FIBER DISTRIBUTION MATERIAL MODEL USED IN FEBIO 2.6.2. 70

TABLE 3-4: FETAL MEMBRANES (FM) MATERIAL PROPERTIES DESCRIBED BY AN OGDEN MATERIAL MODEL IN EQUATION 4-5. 70

TABLE 4-1: UTERINE CONFIGURATIONS BUILT FROM LATERAL AND ANTEROPOSTERIOR SOFT TISSUE X-RAYS OF 15 NORMAL PATIENTS[10]. 82

TABLE 4-2: MESH PROPERTIES FOR THE BASELINE MODEL....83

TABLE 4-3: UTERINE AND CERVICAL TISSUE VARIABLES TAKEN FROM MATERIAL FITS TO EXPERIMENTAL DATA. THESE VALUES ARE IMPLEMENTED IN A CONTINUOUS FIBER DISTRIBUTION MATERIAL MODEL USED IN FEBIO 2.6.2. 86

TABLE 4-4: FETAL MEMBRANES (FM) MATERIAL PROPERTIES DESCRIBED BY AN OGDEN MATERIAL MODEL IN EQUATION 4-5. 87

TABLE 5-1: MATERIAL PARAMETERS OF THE FETAL MEMBRANES FIT TO EXPERIMENTAL DATA. 104

TABLE 6-1: FIVE PATIENT DIMENSIONS OF THE UTERUS IN BOTH REFERENCE (VISIT 2) AND DEFORMED (VISIT 3) CONFIGURATIONS. 118

TABLE 6-2: MESH PROPERTIES FOR A REPRESENTATIVE MODEL....119

TABLE 6-3: UTERINE AND CERVICAL TISSUE VARIABLES TAKEN FROM MATERIAL FITS TO EXPERIMENTAL DATA. THESE VALUES ARE IMPLEMENTED IN A NEO-HOOKEAN MATERIAL MODEL USED IN FEBIO 2.7.0. 121

TABLE 6-4: MEDIAN PRINCIPAL STRAIN MAGNITUDES FOR EACH PATIENT. 124

TABLE 6-5: 138

TABLE 6-6: MESH PROPERTIES FOR P3 139

TABLE 6-7: UTERINE AND CERVICAL TISSUE VARIABLES TAKEN FROM MATERIAL FITS TO EXPERIMENTAL DATA AND PATIENT-SPECIFIC CERVICAL ASPIRATION VALUES. CERVICAL FIBER STIFFNESS WAS DETERMINED USING INVERSE FINITE ELEMENT ANALYSIS. THESE VALUES ARE IMPLEMENTED IN A CONTINUOUS FIBER DISTRIBUTION MATERIAL MODEL USED IN FEBIO 2.8.5. 141

TABLE 6-8: FETAL MEMBRANES (FM) MATERIAL PROPERTIES DESCRIBED BY A CONTINUOUSLY DISTRIBUTED FIBER MODEL. 144

TABLE 6-9: 1ST PRINCIPAL RIGHT CERVICAL STRETCH RESULTS FOR EACH PATIENT AT THEIR MEASURED VALUE AND THE ASSUMED NORMAL VALUE FOR THEIR GESTATION. 161

TABLE 6-10: 95TH PERCENTILE MAGNITUDE OF 1ST PRINCIPAL CERVICAL STRETCH CORRELATES TO GESTATIONAL OUTCOME. 162

TABLE 6-11: 1ST PRINCIPAL RIGHT CERVICAL STRETCH VALUES FOR PATIENTS WITH AND WITHOUT THE INSERTION OF A PESSARY. 165

Acknowledgments

First and foremost, I would like to express my deepest gratitude to my advisor, Dr. Kristin Myers. I am incredibly grateful for your unwavering support and insight throughout the years.

Thank you to each member of my thesis committee, Drs. Gerard Ateshian, Chia-Ling Nhan-Chang, Edoardo Mazza, and Karen Kasza. Gerard, thank you for our weekly meetings filled with such invaluable feedback. Chia-Ling, thank you for the time spent developing clinical protocols and evaluating the translation of my work. Edoardo, thank you for developing the aspirator and your hospitality on my visits to Switzerland. And Karen, thank you for your inspiration and words of encouragement.

Thank you to my co-authors, especially those at CUMC, Intermountain Health, University of Wisconsin – Madison, Tufts Medical Center, and ETH Zurich. I appreciate all of the help in collecting patient data and for contributing to our manuscripts. Also, thank you to the team at Pregnolia who hosted us in Switzerland and provided training and technical support for the aspiration device. I also thank my funding sources, including the NSF for the Graduate Research Fellowship Program and the NIH Ancillary to TOPS trial. And of course, I remain grateful to the many pregnant women in New York and Provo who so willingly allowed the research measurements to be done.

To my Columbia friends and labmates past and present: thank you for your help in research and for making my time at Columbia such a joyous experience. Special thanks to Brandon Zimmerman, Michael Fernandez, Martin Perez-Colon, Mia Saade, Veronica Over, Lei Shi, and Erin Louwagie for all of your help with my finite element analyses. Nicole and Shu, thank you for forcing me to socialize, exercise, and binge eat junk food with you. Charles, thank you for expanding my French vocabulary. Krista, thank you for all of our talks about life goals. I also could not fail to mention my furry “lab”mates, Hedwig and Luna, for bringing a smile to my face each day.

To my amazing friends – thank you for always being there when I needed you the most. Amy, thanks for riding along in this Ph.D. boat with me and for always taking my side in a vent sesh. Erin, Alana, Anne, Kelly, Sarah, Matt, Dylan, and Scott – your friendship and humor kept me sane through the most stressful of times. Rodger, thank you for always challenging me. I am the luckiest to have you by my side.

I owe the utmost appreciation to my family – Dad, Mom, Matthew, and Sydney. Thank you, Mom, for being so proud even though you’re *still* not sure what this thesis is about. Thank you, Dad, for always encouraging me to reach my full potential. I love you guys and am so thankful to have the most loving and supportive family.

Dedicated to my best friend, Kerri.

I love and miss you every day.

1 Introduction

1.1 The Pregnant Environment

Pregnancy and labor are interactions between the fetus and the passageway through which delivery occurs. To ensure healthy pregnancies, it is imperative that we understand the anatomy and mechanics of the pregnant environment. Despite recent efforts and extensive research, knowledge of pregnancy progression and parturition remains limited. There are many components which make up the female reproductive system; for the purpose of the following studies, we will focus on the cervix, uterus, fetal membranes, and intrauterine forces exhibited throughout gestation.

1.1.1 Uterus

The nonpregnant uterus is a pear-shaped organ and lies in the pelvic cavity between the bladder anteriorly and the rectum posteriorly[1]. It is responsible for various functions such as gestation, menstruation, and labor and delivery. The uterus consists of two parts: the upper, larger body or "corpus", and the lower cervix (Figure 1-1). The union between the corpus and cervix is the isthmus, and the top of the uterus is called the fundus. In its nonpregnant state, the fundus is a flattened convexity between the fallopian tubes.

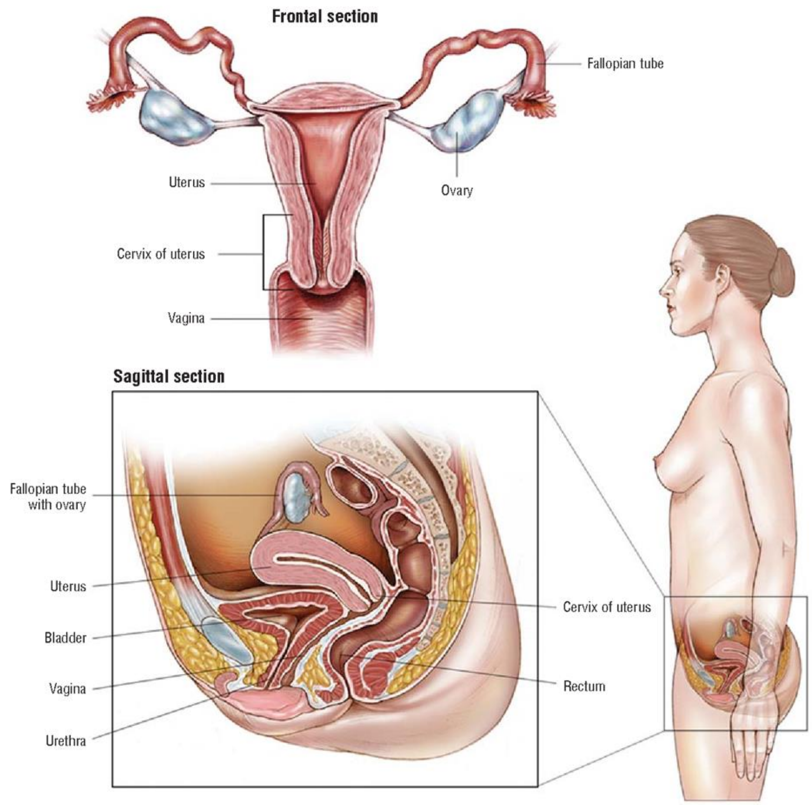

Figure 1-1: Female pelvic anatomy. This figure shows the upper uterine body and the cervix, as well as the proximity of the uterus to the bladder and rectum[2].

The nonpregnant uterus can be 6-8cm in length in nulligravid women and up to 10cm in multiparas[3,4]. The uterus averages 60 g in weight and weighs slightly more in parous women[5].

The majority of the uterine corpus is muscle. In nonpregnant women, the inner surfaces of the anterior and posterior walls lie almost in contact, and the uterine cavity is a small slit between the two. The uterine wall consists of three layers:

1) the outer perimetrium, a thin serous layer composed of epithelial cells,
2) the middle myometrium, primarily composed of smooth muscle cells and making up the bulk of the uterine wall, and

3) the innermost endometrium, which consists of the functional (superficial) and basal layers[6,7].

The myometrial fibers and orientation vary by location[1,8]. The anterior and posterior walls have greater muscle contact than the lateral walls. The inner endometrium varies greatly throughout the menstrual cycle. During pregnancy, the endometrium is called the decidua and undergoes dramatic hormonally driven alterations.

Throughout gestation, the uterus undergoes rapid growth and remodeling to accommodate the growing fetus (Figure 1-2). Its capacity can increase from 5 mL at its nonpregnant state to 4-5 L at term[9]. This substantial tissue growth is due to muscle fiber hypertrophy.

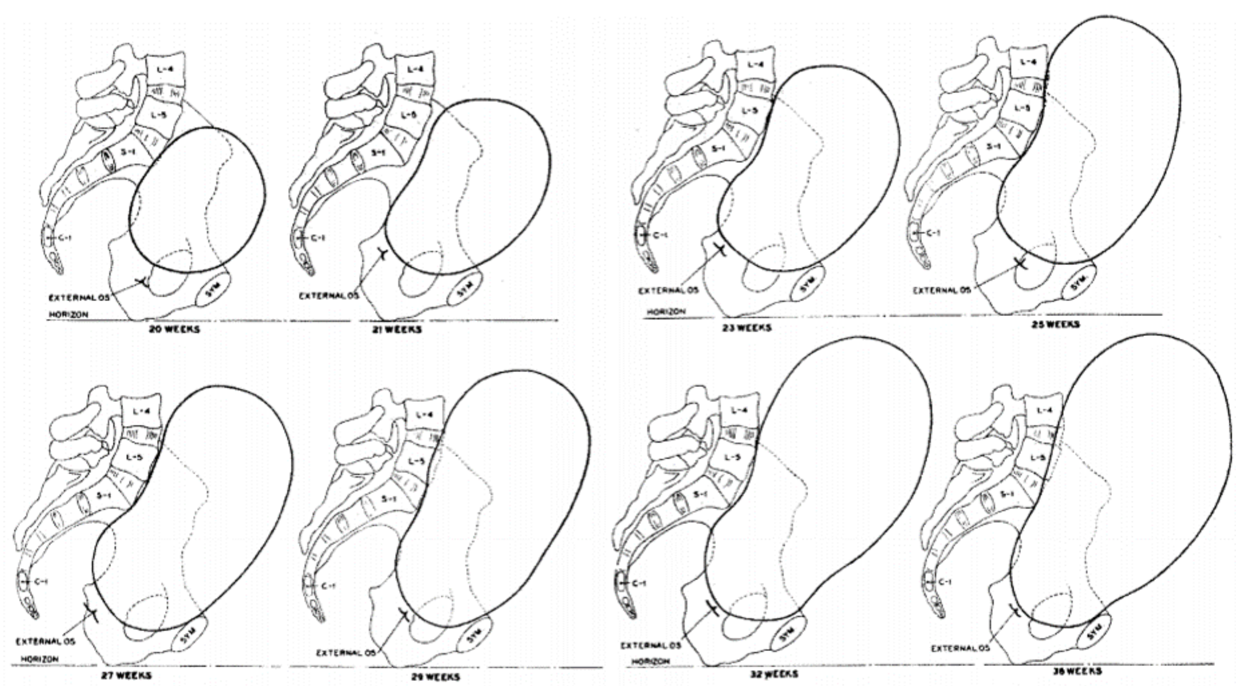

Figure 1-2: Uterine growth from 20 to 36 weeks gestation taken from x-ray data[10]

The original pear shape of the uterus remains during the first few weeks of pregnancy, but the organ becomes gradually softer. During the third month of pregnancy, the isthmus elongates to as much as three times its originally length[11]. It then unfolds to become the lower uterine segment. Both the corpus and the fundus open into a dome shape, and the uterus becomes spherical by week twelve[12]. It then maintains this spherical shape until around week 20, when it then elongates into an ellipsoid and continues to do so until week 32[10]. The timeline for if and when uterine hypotrophy stops and the myometrial wall thins has seen much debate[10,12–14]. Most agree that uterine growth curtails in the second half of gestation, as the myometrium thins after the first trimester, primarily in the lower uterine segment (LUS).

Immediately after delivery of the fetus and placenta, myometrial wall thickening occurs[15]. Shortly after, the fundus typically descends to the level of the umbilicus. Involution then occurs over the following weeks; the uterus returns to the pelvis by two weeks postpartum, and involution is complete by the fourth week. Sonographically, the uterus and endometrium return close to pregravid size by 8 weeks postpartum[16,17]. Yet, the uterus usually remains slightly larger than before the most recent pregnancy after each successive delivery.

1.1.2 Cervix

Although it is anatomically part of the uterus, the cervix is often viewed as a separate, complex organ. It is the lower, cylindrical portion of the uterus which holds the fetus inside the womb throughout gestation, and then dilates during labor to allow for the passage of the fetus through the vaginal canal. The cervix has two apertures at each end – the internal and external os – and an endocervical canal which runs through the cervix connecting the two. Unlike the uterine corpus, the cervix is comprised of 60% muscle near the internal os, and gradually declines to only 10% smooth muscle at the external os[1,18]. The remaining cervical tissue is made up of fibrous connective tissue, extracellular matrix (collagen, elastin, and proteoglycans), fibroblasts, and blood vessels[19]. Collagen comprises almost 80% of the cervix, with Types I and III as the major cervical collagen components[11,20].

The mechanical behavior of the cervix throughout gestation has a critical influence on the outcome of the pregnancy. The cervix has two functions: throughout the pregnancy, it must stay closed to protect the developing fetus; then at labor, ideally at full term, it must undergo effacement and dilation to allow for the fetal descent through the birth canal (Figure 1-3)[12,21].

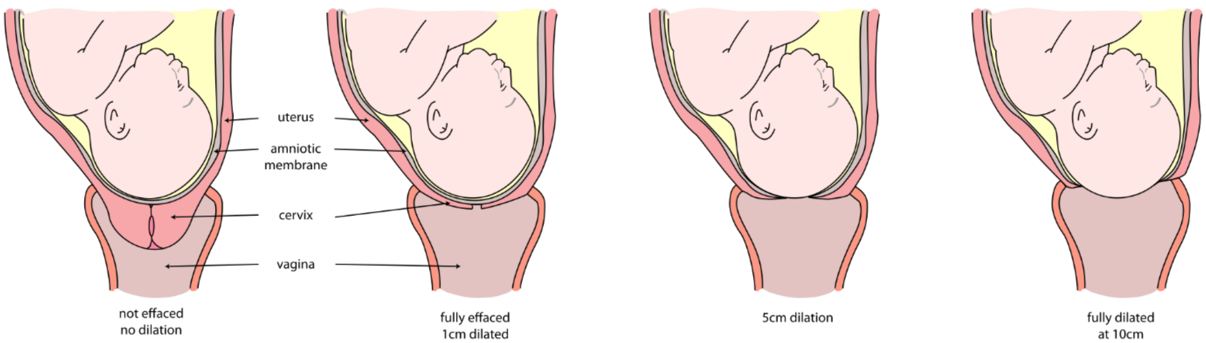

Figure 1-3: Progression of the cervix from closed (left) to effacement and dilation[22].

Because the cervix is the final passageway the fetus must pass through in delivery, cervical dimensions are among the most scrutinized aspects of pregnancy. Various risk-scoring methods based on cervical diameter, dilation, length, position, and consistency have been developed from consistently found a statistical correlation, though with low prognostic success[23]. Short cervical length has long been associated with preterm birth and the time since conception at which the measurement is taken impacts its predictive nature[24–26]. In healthy pregnancies, the median cervical length in the second trimester is 41mm[27]. There has been much clinical debate as to what length and at what gestation is considered a “short cervix”, but most clinicians agree a cervix shorter than 25mm at 18-22 weeks gestation puts a patient at risk for preterm delivery[26,28–31].

As soon as one month into the pregnancy, the cervix will soften and become bluish in tone, due to increased vascularity and edema, changes in the collagen network, and hypertrophy and hyperplasia of the cervical glands[32]. Collagen rearrangement is crucial for fetal retention until term, in dilation and delivery, and in postpartum repair[33]. After delivery, the cervical opening contracts slowly. By the end of the first week, the opening will narrow, the cervix will thicken, and the endocervical canal will reform. However, the external os does not completely resume its pregravid appearance; instead, it remains wider, softer, and contains permanent depressions at the site of cervical lacerations[1].

1.1.3 Fetal membranes

The fetal membranes (FM) contain two layers: the outer layer is the cellular chorion, whereas the inner layer facing the amniotic fluid is the load-bearing amnion, comprised of a dense layer of collagen fibrils[34,35]. The amnion is stiffer, stronger, and thinner than the chorion [36].

Fetal fibronectin (fFN) is a glycoprotein that is found in the extracellular substance of the decidua next to the intervillous space[37,38]. Its exact clinical function is poorly understood, but it seems to be a glue-like substance adhering the chorion to the uterine decidua (Figure 1-4)[39].

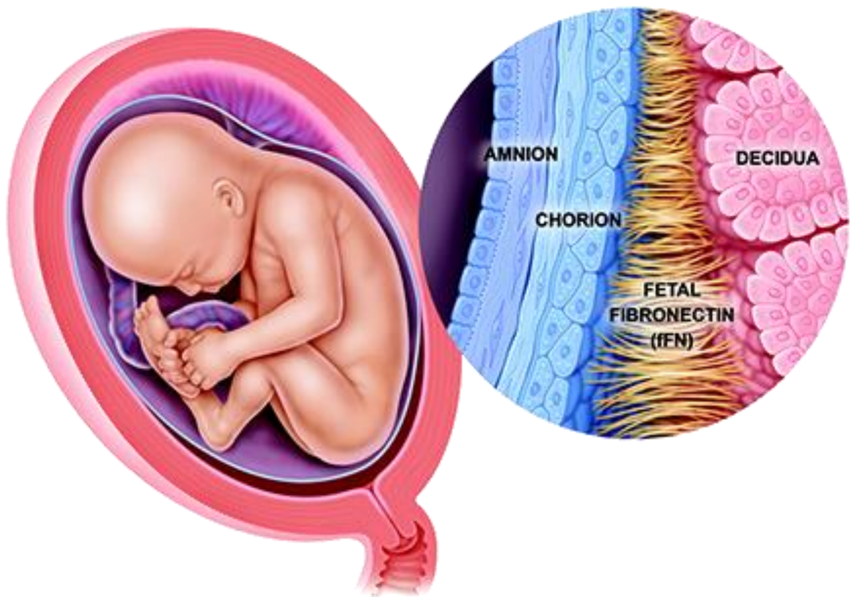

Figure 1-4: Fetal fibronectin interface in the choriodecidual region[40].

It is normally present in low concentrations in the vagina between 18 and 34 weeks of gestation, and its presence has been a useful marker of a pathologic disruption of the maternal-fetal interface. Studies have also been conducted on the chorion-amnion interface, and findings show that the interface is usually hydrophobic and therefore essentially frictionless, but it is significantly less hydrophobic in the instance of preterm premature membrane rupture[41,42].

Fetal membrane mechanical properties are often related to the collagen type and distribution in the tissue. Amnion contains collagen type I and III fibrils, in addition to filamentous collagen type V and VI, and type IV in the amniotic layer between the epithelium and the mesoderm [43,44]. Amnion electron microscopy shows collagen fibrils 50nm in diameter in loose bunches, randomly interwoven without preferential directionality [45]. Chorion contains fibrillar and collagen type IV [46]. Measured total collagen content of the fetal membranes ranges from 4-20% of dry weight [47,48]. Elastin also contributes to membrane mechanics but is poorly understood in fetal membranes. Studies report 0.08% dry weight or ranges of 2-36% wet weight of amnion [48–50].

In early pregnancy, the chorion will grow and expand until the chorionic villi come in contact with the decidua basalis, and they proliferate to form the leafy chorion. Until the end of the third month, the chorion is separated from the amnion by the exocoelomic cavity. The amnion and chorion usually fuse between 14-16 weeks gestation to form the avascular amniochorion[51]. The membranes surround the amniotic sac, which contains the amniotic fluid and the fetus. They play an important role in fetal-maternal communication[1]. The FM protect the fetus and help support its load throughout gestation. Rupture of the FM at term is a natural event that often signifies the onset of labor.

1.1.4 Intrauterine forces

Throughout gestation, the uterus is exposed to constant intrauterine pressure (IUP) from the weight of the fetus, the placenta, and the fluid pressure of the amniotic fluid. Between 8 and 34 weeks of pregnancy, amniotic pressure has been recorded between 1.1 and 13.1 mmHg via transamniotic invasive procedures[52]. In most cases, the average amniotic pressure is between 4 and 8 mmHg. These pressures can be higher in women with excessive amounts of amniotic fluid (i.e. polyhydramnios), or lower in those with low amniotic fluid (i.e. oligohydramnios).

In addition to amniotic pressure, the uterus also contracts throughout pregnancy, causing more forces to occur. Even in early gestation, there are low-amplitude high-frequency uterine contractions (i.e. Alvarez waves) with intensity less than 5 mmHg and frequency every 1 to 2 minutes[53]. These Alvarez waves are too small to be detected by the pregnant women themselves. Also, throughout gestation, though mainly appearing in the third trimester, the uterus undergoes Braxton-Hicks contractions. Braxton-Hicks contractions are low-frequency, irregular, and have a higher intensity of 10-15 mmHg[54]. Finally, at the onset of labor, the frequency and intensity of contractions increase and become more regular. During early labor, uterine contractions typically have a peak intensity between 25 and 30 mmHg, while 60 to 65 mmHg is ultimately reached in the second stage[12]. The sum of the intensity of all the contractions necessary for complete cervical dilation varies from 4000 to 8000 mmHg[55]. Therefore, approximately 80 to 160 uterine contractions are required to expel the fetus.

The fetus can also apply loads to the uterus through various movements. The first fetal movements of the head and neck occur at 10 weeks, and whole-body movements start at 15 weeks. The maternal sensation of fetal movements often occurs around 16-18 weeks. Peak fetal movement frequency occurs during the second trimester and decreases toward full term; this is likely due to the lack of extra room in the womb as the fetus grows. The largest fetal kick reaction force measured via cine-MRI is 46.64 N at 30 weeks gestation[56]. Taking into account the size of a fetal foot, the pressure applied by a kick can be up to ten times that of a uterine contraction in labor[57].

1.2 Clinical motivation: preterm birth

Preterm birth (PTB) is defined as a live birth that occurs before 37 weeks gestation[58]. It is the leading cause of death in children under the age of five, reaching 1.1 million annually[59]. Each year there are an estimated 500,000 cases of preterm birth in the US[58]. As many as 95% of cases are intractable to current therapies[60], suggesting the need for continued investigations and medical discoveries. The average cost of a preterm newborn's first year of life is over ten times that of a normal term baby's ($49,000 vs. $4,500)[61]. Furthermore, PTB often leads to lifelong health complications such as cerebral palsy, asthma, and numerous learning disabilities, and has an estimated societal cost of $26 billion in the United States each year[59].

Throughout gestation, the fetus is supported and protected by biologically active soft tissue structures. These structures send mechanical signals which can trigger tissue remodeling and contractility through mechano-sensitive cells (e.g. mechanotransduction). The mechanical integrity of the uterus, cervix, and fetal membranes are critical for a successful pregnancy, where the loss of structural integrity of these tissues is believed to contribute to spontaneous PTB. For example, in the case of cervical insufficiency (CI), the cervix dilates and shortens painlessly in the absence of uterine contractions[62]. CI is hypothesized to be caused by premature cervical remodeling and softening of the tissue. Preterm labor is believed to be caused, in part, by uterine overdistention, as evidenced by the higher rate of preterm labor for multiple gestations or excessive amniotic fluid[63,64]. A recent study investigated uterine overdistention in nonhuman primates by inflating intraamniotic balloons. Results showed uterine overdistention caused preterm labor triggering a cascade of cytokines and prostaglandins associated with inflammation[65]. Premature preterm rupture of membranes (PPROM) occurs due to damage of the collagen in the chorioamnion, causing a mechanical tear in the membrane. Clinical studies show excessive collagen degradation in chorioamnion and amniotic fluid samples that have experienced PPROM[66]. The hypothesized causes of PPROM include an insufficient cervix, hydramnios, trauma, and amniotic fluid infection[67].

Characterizing reproductive tissues in real time and accessing organs to measure anatomical and tissue properties throughout gestation is challenging. Hence, a driving engineering motivation is to use biomechanical models of pregnancy to understand the mechanical functions and dysfunctions of the tissues during pregnancy. Here we introduce and discuss engineering analysis tools to evaluate and predict the mechanical loads on the uterus, cervix, and fetal membranes. Medical imaging such as magnetic resonance imaging (MRI) and ultrasound are minimally invasive, yet provide thorough anatomies of a patient's anatomy. These anatomies can be implemented in biomechanical models to simulate gestational scenarios without providing any harm to pregnant patients. Here we will explore the potential of using computational biomechanics and finite element analysis to study the causes of preterm birth and to develop a diagnostic tool that can predict a gestational outcome.

A crucial challenge to lowering the rate of sPTB and its subsequent costs is to identify women who are at the highest risk, to identify these women early in their pregnancy, and to develop etiology- and patient-specific interventions. Equally important to reducing costs related to sPTB, is the ability to identify women at the lowest risk to avoid unnecessary and costly interventions. Without knowing the underlying mechanisms that result in sPTB, empirically introducing treatments can be ineffective, potentially detrimental, and costly[68,69]. Additionally, conducting a clinical trial to determine what single factor or group of factors cause mechanical dysfunction in pregnancy is extremely timely and expensive.

Biomechanical models of pregnancy can specifically address these clinical needs by providing a simulation framework to identify the structural factors that cause mechanical dysfunction and aid in minimally-invasive clinical diagnosis of preterm birth. Clinicians can use ultrasound to obtain anatomical dimensional data to inform patient-specific FEA. Computational results of tissue stress and stretch can then be reported within hours or even minutes. Furthermore, these models can guide mechanically-based patient-specific therapeutic interventions to prevent PTB. When implemented in clinical practice, biomechanical models of pregnancy can implement "what if" scenarios that clinicians cannot test in vivo. For example, we can build a patient-specific model and insert a cerclage or cervical pessary to predict how certain interventions will change tissue mechanics and deformation. These simulations can predict treatment safety and efficacy with significantly lower costs and possible harm to patients.

1.3 Biomechanical models

A biomechanical model quantitatively represents the geometry and mechanical properties for a single tissue, organ, or a system of load-bearing tissues and organs. The model aims to solve for the amount of tissue stress and stretch as the result of external mechanical loading. Mechanical models depend on strict definitions of force, deformation, stress, strain, and stretch. We briefly explain them here. The term stress represents the amount of force carried within the tissue normalized by its geometry. It is a three-dimensional term, where the amount of stress will vary depending on the direction. Simply put, stress (σ) is defined as a force (F) per unit area (A), $\sigma = \frac{F}{A}$, with units of pressure N/m^2 or Pa in metric and lb/in^2 or psi in the English unit system. Due to its direction-dependence, there are multiple types of stress: normal stress occurs when the force vector is perpendicular to the surface, and shear stress occurs when the force vector is parallel to the surface. If the force vector is somewhere in between perpendicular and parallel to the surface, both stress components are present. Strain (ε) is a measure of the deformation of the tissue due to stress, and it is also normalized by geometry. Because stress is direction-dependent, strain is also direction-dependent. Simply put, it can be expressed as the change in tissue length (Δl) over the original length (l_0), $\varepsilon = \frac{\Delta l}{l_0}$. Strain is often reported as a percentage. Stretch is similar to strain and is typically used for materials that undergo large deformations, such as soft biological tissues. Stretch (λ) is the ratio between the current length at a given applied force (l)

and the original length (l_0) of the material, $\lambda = \frac{l}{l_0}$. It is reported as a unitless ratio and not a percentage.

In addition to accurately describing the shape and size, a biomechanical model also requires the mechanical properties of the tissues in the system. Tissue mechanical properties are the quantitative values that relate the amount of tissue stress σ with the amount of strain ε (or stretch λ). This mathematical relationship is called a material model, and the equation parameters are the material properties of the tissue. Material properties are found by isolating the tissue and conducting a series of mechanical tests. The most basic, and often most informative, mechanical test is a uniaxial tensile test. In this test, a uniform piece of tissue is gripped within a material tester by each of its ends. The material tester displaces the grips by prescribed displacement values Δl, and the force F is measured as the tissue is pulled in tension. The material tester records force F as a function of grip displacement Δl, and stress σ and strain ε are then derived from these values and are normalized by the cross-sectional area A of the tissue.

The shape and magnitude of the experimental stress σ versus strain ε curve for a given material is the material behavior of the tissue. The mathematical equation describing the material behavior is the material model, where model parameters are tissue material properties (or tissue mechanical properties). Material properties must be strictly defined within each modeling context because the terms such as stiffness and strength have specific meanings in the field of mechanics. The simplest of material behavior is linear elastic, where there is a linear relationship between stress σ versus strain ε. This type of material is described by two material parameters: The Young's modulus E and the Poisson's ratio ν. The Young's modulus E of a material is often referred to as the stiffness of a material and is the slope of the stress σ versus strain ε curve.

Material compliance is the inverse of material stiffness $\frac{1}{E}$, often thought of as the material's flexibility. A material that deforms easily is said to be compliant, while a material that resists deformation is said to be stiff. Also identifiable on a stress-strain curve is the strength of a material. Yield strength is the point at which the stress-strain curve begins to deviate from a straight line, and represents the lowest stress that produces permanent deformation of a material. Poisson's ratio of a material (ν) is the ratio of lateral strain to axial strain when a material is in tension: $\nu = -\frac{\varepsilon_{yy}}{\varepsilon_{xx}}$. In other words, it is the amount of transverse extension divided by the amount of axial compression. For example, when you stretch a rubber band, the band will become longer, but the width of the band will become narrower. Materials that are truly incompressible have a Poisson's ratio ν of 0.5, since the sum of all their strains results in zero volume change.

Soft biological tissues have a complex material behavior because the material is made of an intricate network of long-chain proteins, cells, soft groundmatrix, and interstitial water[70]. Therefore, it is often not sufficient to use a linear material model because the shape of the stress σ - strain ε curve of a soft tissue is governed by the non-linear, time-dependent, and direction-dependent material behavior of the individual biological components. For example, hydrated collagenous tissues have a soft compliant region when they are first stretched (referred to as the small-strain regime). Then as deformation continues, collagen fibers are recruited and begin to contribute to the tensile stiffness as they become straightened. The resulting stress σ - strain ε curve is non-linear and resembles a J-curve[71]. Additionally, collagen fibers of organs often have a preferred-directionality and architecture depending on the direction of load they carry in the body. Therefore, the tissue will exhibit different stiffness properties in different directions.

This type of material is called anisotropic. Lastly, a time-dependent tissue will experience different levels of stress depending on the rate of mechanical loading or will continuously deform under a constant level of load in a behavior called creep. These examples provide an insight into the complexity of the mechanical behavior of soft biological tissues, and the material characterization of soft biological tissues represents an active field of study, with research groups aiming to develop micro-structurally-derived material models that accurately describe tissue material behavior. The most advanced material models aim to describe tissue material property evolution with age, disease, growth, and remodeling.

1.3.1 Solid models of pregnancy

Computer-aided design (CAD) is the use of software tools by engineers to design a countless number of products, such as buildings, bridges, robots, heavy machinery, etc. Solid CAD models are built from numerically-defined primitives (cubes, cylinders, spheres, etc.), sweeps (extrusions, revolutions, etc.), and the Boolean operations of such objects[72]. 3D parametric modeling uses geometries that are easy to modify. For the case of the pregnant anatomy, both magnetic resonance imaging (MRI) and ultrasound have been used to build organ and tissue solid models (Figure 1-5)[73–75].

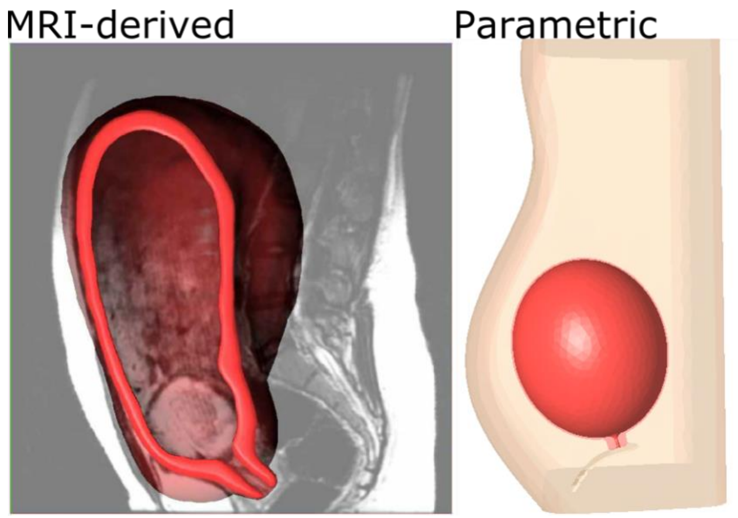

Figure 1-5: MRI-derived (left) and ultrasound-derived parametric (right) CAD models of pregnancy.

Solid models aid the visualization of the 3D anatomy and can be converted into numerical models suitable for biomechanical modeling[73]. Converting medical images to numerical models can be time-consuming and tedious[76,77]. To mediate this issue, it is sometimes beneficial to create simplified geometries which can capture the most sensitive aspects of the physiological anatomy[75]. Both more detailed and simplified models have their advantages. Complex geometries most accurately portray anatomical scenarios, consisting of layers of different tissues and boundary conditions like ligaments and fascia[76,78]. Simplified models have the potential to reduce pre-processing and computational time, while still capturing the most sensitive parameters of the desired physiology. Attempts are often made to determine exactly how much complexity a biomechanical simulation requires. Sensitivity studies determine the most crucial properties to accurately describe in a model. Model verification and validation are imperative to build credibility for models of intricate biological systems[79].

1.3.2 Material models in pregnancy

Compared to musculoskeletal and cardiovascular tissues, the mechanical properties of the female reproductive system are understudied and are often limited to animal models. A recent review article details the available mechanical testing data and corresponding material properties for uterus, cervix, vaginal wall, and pelvic ligaments[80]. As discussed above, the material properties of soft collagenous tissues are non-linear, time-dependent, and direction-dependent. Additionally, the female reproductive system undergoes dramatic material property changes during pregnancy. The growth and remodeling of the reproductive tissue depend on the mechanical environment of the tissues in addition to their genetic makeup[81]. Histological and biochemical studies demonstrate evidence of both cervical growth and remodeling in pregnancy. Studies of human tissues show that compared to nonpregnant cervical tissue, pregnant tissue experiences a significant decrease in collagen alignment and organization[82].

A logical starting point for a large-scale FEA model is to model the tissues as linear elastic materials, using material stiffness properties measured within a reasonable physiologic range of stretches. For unknown gestation-timed material parameters, an estimation can be made by comparing the relative change between material properties measured in the nonpregnant state compared to tissue samples collected at term or rates of remodeling can be extrapolated from available mouse models of normal and abnormal pregnancy. Linear elastic models are convenient and useful to use in an FEA when attempting to isolate the contribution of anatomical shape changes in pregnancy.

A logical progression for improving the material models of the FEA is to explore the consequence of material nonlinearity and tissue anisotropy. Tissue nonlinearity can be captured by using phenomenological mathematical expressions, such as a polynomial with more than one variable, fit to experimental data. These types of nonlinear models account for the fact that hydrated biologic tissues tend to be more compliant when they are first stretched. Researchers in biomechanics are moving towards more descriptive models that account for the tissue's biological composition. For example, the cervix can be treated as a fiber composite material with a preferentially-aligned collagen fiber network embedded in a soft compressible ground substance made of glycosaminoglycans[33]. Modeling the cervix in this manner accounts for the fact that the collagen fibers cannot give compressive resistance and can only hold a tensile force. Therefore, the resulting overall tissue behavior is very soft in compression and very strong in tension. An FEA model explored the difference between modeling the cervix as a linear elastic material and a fiber composite material[74]. The linear elastic model fit to compression mechanical data drastically underestimates the effective stiffness of the tissue because it neglects the tensile contribution of the fibers. Therefore, the FEA results show an overestimation of tissue stretching at the internal os. Including the three-dimensional (3D) dispersion of the cervical collagen network aids in supporting the loads in directions that are not aligned with the preferred fiber direction. The fibers of the 3D network are able to align and rotate in the directions of tissue stretch hence giving the cervix overall mechanical integrity. Active research is continuing to update material models to include time-dependent and growth and remodeling properties.

1.3.3 Finite element analysis in pregnancy

For simpler organs that carry a load in a single direction, the biomechanical model to determine tissue stress and stretch can be analytically solved with the standard force balance equations. For a complex system of organs, solving for physiologic tissue stress and stretch requires numerical simplification techniques to solve for the force balance equations. This type of biomechanical model is commonly referred to as a structural finite element analysis (FEA), a numerical technique that discretizes a complex domain to solve the equations of static equilibrium (Figure 1-6). FEA has been used in numerous biomechanical fields such as cardiovascular, orthopedics, ocular, brain, and many more[83–88]. FEA was first brought into the field of biomechanics in 1972 to evaluate stresses in human bones.

Finite element analysis requires the input of various parameters to obtain accurate results (Figure 1-6). The finite element method consists of five steps. Pre-processing involves importing a solid model CAD geometry and creating a mesh to approximate the geometry. In the case of biomechanical models, these geometries are often obtained with medical imaging techniques. A mesh is created by separating the input geometry into multiple smaller geometries, called elements. Meshing is a crucial step of finite element analysis as the quality of the mesh reflects directly on the results generated. Next, element formation occurs when governing equations are developed for each element. These equations take into account user definitions of material properties, boundary and loading conditions, and model constraints. The equations either solve for tissue displacement given a prescribed stress, or they solve for tissue stress given a prescribed displacement. The material characteristics are determined from experimental mechanical testing of tissues under loading conditions similar to those experienced physiologically. Boundary conditions are sometimes made through assumptions, like organ surrounding ligamenture. After they are formed, these equations for the individual elements are solved. During final post-processing, output parameters are determined and result visualizations are created.

Since many input parameters in biomechanical models are still based on assumptions, developing new technologies for accurate data collection is still needed. In cardiovascular biomechanics, many technologies exist to characterize the heart’s electromechanics: electrophysiology measurements, stem-cell derived cell and tissue models, and rapidly improving imaging technologies for in vivo and clinical evaluations[89–91]. The field of cardiology has recently turned to patient-specific modeling approaches, obtaining individual geometries and structures of the heart from clinical images. Image modalities in cardiac mechanics include MRI, CT, positron emission tomography (PET) and ultrasound at the organ level, micro-CT, intravascular ultrasound (IVUS) and optical coherence tomography (OCT) at the tissue level, confocal, multi-photon microscopy, coherent anti-stokes Raman scattering (CARS) and electron tomography at the cellular level, and x-ray crystallography at the molecular level[83]. Combining these with tissue-specific cellular models, electrophysiological, and mechanical information allows for dynamic patient-specific models[83]. These models can be used in clinical scenarios to aid medical professionals in diagnosis and treatment decisions. If engineers and clinicians can come to a point where models accurately portray clinical scenarios, these models can act as non-invasive diagnostics which will allow for disease monitoring. But first, it is necessary to determine the most crucial model parameters and to validate all material and mechanical assumptions.

Pregnancy is a protected environment and difficult to study in vivo. Biomechanical models of the growing and stretching uterus, cervix, and fetal membranes give the ability to assess and pinpoint biophysical factors causing tissue over-loading. These models can be used in discovery- and hypothesis-driven studies. For scientific exploration, models can assess the sensitivity of tissue loading to anatomical and tissue material properties. In a clinical setting, forward-predicting models can evaluate the risk of sPTB using mechanical threshold biomarkers assessed early in the pregnancy. Currently, biomechanical models of pregnancy are limited by the lack of time course data of the pregnant abdomen during gestation. Yet, it is possible to obtain pregnancy data from non-invasive medical imaging to create solid models of the pregnant abdomen.

1.3.3.1 Meshing, boundary conditions, and loading

FEA works by partitioning the object into a finite number of elements, in a process called meshing, and then the analysis predicts full model behavior by summing the behavior of each individual element[72]. Finite elements come in various dimensional shapes. For purposes of biomechanical modeling, we will only discuss 3D shapes in this section. 3D solid elements can either be hexahedral (bricks) or tetrahedral (triangles), and they are connected at individual nodes. Hexahedral elements are more accurate than tetrahedral, but will often not work on complex geometries. In FEA of pregnancy, tetrahedral elements are often used to maximize meshing accuracy while preserving geometries (Figure 1-6).

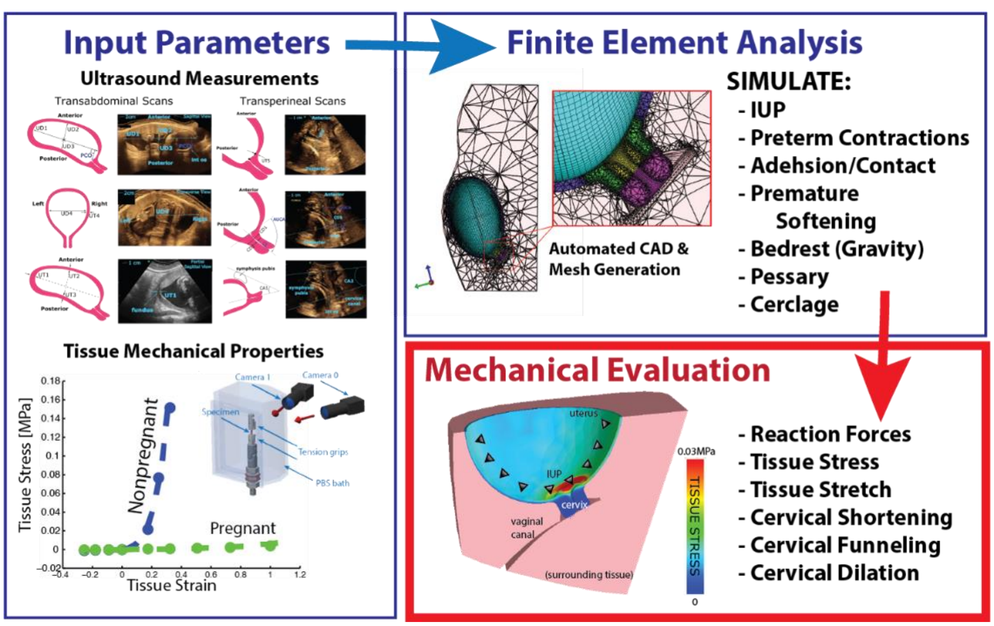

Figure 1-6: Formulation process for ultrasound-based finite element analysis of pregnancy. Models are informed with ultrasound dimensional data, experimental tissue mechanical properties, loading, and boundary conditions. Mesh generation is automated in the linear solver for mechanical evaluation of output parameters.

Finite element mesh quality is essential to model mathematical accuracy[72]. Ideal elements have uniform shapes like equilateral triangles and have smooth transitions in mesh density. Density refers to the size and number of elements. A higher density is often required near areas of geometric curvature or high strains. Increased mesh density has more, smaller elements, and is typically more mathematically accurate. However, it is also more computationally demanding; increasing mesh density can increase model solving time by hours, days, or even weeks in highly complex models. Mesh convergence tests are often performed to optimize mesh density. This is the process of refining a mesh until results converge to asymptotic behavior.

Boundary conditions are constraints placed on the model which remove spatial degrees of freedom. These may be fixed, cylindrical, pinned, and frictionless. In parametric finite element models of pregnancy, we fix only the outer abdomen of the model in all degrees of freedom. The fetal membranes are tied to the inner uterine wall to mimic membrane adhesion, and they are allowed to slide along the internal os of the cervix[92].

To predict model deformations, loads must be prescribed to the system. These can include forces, moments, pressures, temperatures, and accelerations. In pregnancy FEA, the intrauterine pressure (IUP) is usually the load applied to the inner amnion. It is necessary to define the load magnitude and orientation. One limitation to FEA in pregnancy is that in vivo geometries taken by medical images represent loaded model configurations. It is impossible to obtain unloaded reference configurations of the uterus and cervix throughout gestation. Experiments have been performed to try and estimate unloaded configurations of the fetal membranes[93], which is an important step in determining model input geometries.

1.3.3.2 Previous finite element analyses in pregnancy

Finite element (FE) modeling of the pregnant anatomy has been used previously to investigate cervical tissue stretch. The cervix is the final passageway to allow for delivery of the fetus during labor. Therefore, we hypothesize that the tissue stretch at the internal os is the most important output parameter. Since in vivo experiments are impossible to perform guaranteeing the safety of the fetus, finite element modeling in pregnancy is imperative to simulate clinical scenarios without harming humans or animals[78]. Previous studies have investigated 2D FE models of the uterus and cervix[78], 3D ultrasound-derived CAD-based FE models[76], and 3D magnetic resonance imaging (MRI)-derived models[31,74,94].

Mahmoud et al. point out that little has been done to investigate the uterine-cervix interaction through finite element modeling of pregnancy. They state the importance of capturing the complex material behavior of the uterine and cervical tissue, as well as the detailed anatomy and accurate boundary conditions[78]. Though the authors present a valid approach to building a predictive model, their FE models are only two-dimensional and exclude the necessary implementation of fetal membranes modeling.

House et al. used transabdominal 3D sonography images and segmented them to capture CAD geometries of the pregnant anatomy for six healthy patients and one patient with acute cervical insufficiency[76]. These FE analyses thoroughly modeled the uterus, cervix, fetal membranes, amniotic sac, endopelvic fascia, cardinal and uterosacral ligaments, abdominal cavity and fascia, and pelvic floor. House notes that the largest limitation of this study was the lengthy process of converting the ultrasound images to numerical models.

Paskaleva used MRI image stacks obtained by House et al. to construct 3D FE models of the pregnant anatomy[94]. The goal of this study was to feature cervical material growth and remodeling to simulate cervical insufficiency. Results demonstrated cervical loads were concentrated at the internal os, especially in the case where the fetal membranes were allowed to slide freely along the inner uterine wall. This result is consistent with the clinical procedure of fetal membranes stripping in order to induce labor. In addition, Paskaleva modeled various cerclage placement positions to investigate ideal scenarios. Models showed cerclage placement closer to the internal os as opposed to the external os resulted in decreased cervical funneling, predicting a minimized potential of cervical insufficiency. These results also coincide with clinical findings of cerclage placement to structurally support the cervix[95].

House et al. have also used MRI techniques to investigate cervical funneling in the TYVU deformation patterns[31]. Models demonstrated the deformation by varying cervical material properties and applying representative pelvic loads. The authors were unable to determine if TYVU deformation is caused by weak cervical structure or if it is caused by another physiological process.

Verbruggen et al. developed a series of simplified two-dimensional finite element models of the uterus and fetal membranes to investigate the mechanical behavior and rupture [96]. They found that modeling the chorion and amnion as a single-layer monolithic structure behaves much differently than a more anatomically correct composite bilayer, as it under-predicts membrane rupture and stress. This emphasizes the need to investigate the mechanics of the chorion as a separate structure in a physiologically accurate loading configuration.

Fernandez et al. used 3D MRI images of two pregnant patients to investigate the influence of anatomical geometry, cervical material properties, fetal membrane material properties and adhesion on the mechanical deformation and loading patterns of the cervix at the internal os[74]. The study showed that the uterus, cervix, and fetal membranes all share load-bearing of the fetus and amniotic sac. Key mechanical and structural factors affecting cervical stretch were lower uterine segment and cervical geometries, material properties of the cervical tissue, and fetal membrane material properties and adhesion scenarios.

Previous studies sought to simplify pregnant anatomy geometries in order to expedite the finite element process[75]. Ultrasound images were used to create a parameterized model of the uterus, cervix, fetal membranes, vaginal canal, and abdomen. It lacked intricate anatomical details such as bumps and grooves as it modeled the uterus as an ellipsoid with uniform thickness, and the cervix as a hollow cylinder. Findings showed a correlation to clinical practice, such as in the case of cervical length and angle. Intuitive results were also shown, where a softer cervix experienced more stretch than a stiffer cervix. New findings showed that the location of the cervix on the lower uterine segment may also affect tissue stretch at the internal os. Though the geometries in this study were not as anatomically detailed as MRI-derived studies, the entire process from image collection to result visualization could be completed in a matter of hours, rather than days or weeks taken with previous methods.

1.4 Conclusion: A need for improved biomechanical models of pregnancy

While a short cervical length and a raised cervical-vaginal fetal fibronectin concentration are the strongest predictors of spontaneous preterm birth, the process of parturition and the phenomena of preterm birth is still hard to detect, especially in cases of no previous obstetric history[97]. Furthermore, there is various conflicting evidence on clinical interventions for preterm birth such as the Arabin pessary[98–101]. With the goal to further understand the dynamic pregnant environment, we propose various methods to simulate the pregnant womb using finite element analysis. These methods will allow for both subject-specific investigations as well as sensitivity studies that can provide a quantitative assessment of the contributing factors necessary for improving preterm birth diagnosis. The eventual goal of these analyses is to provide a predictive tool with the capability to identify human subjects at risk for preterm birth, as well as forecast the likelihood of success for potential medical interventions to prolong gestation. As a starting point for the development of this tool, an understanding of the factors which influence tissue mechanics and pregnancy outcomes are presented here.

The main objective of this dissertation work is to characterize the geometric and kinematic changes of the womb throughout gestation and across multiple pregnancies using biomechanical models of the uterus, cervix, and fetal membranes, as well as calculate the tissue stretch and stress. The dissertation work is divided into the sensitivity analyses of various geometric and material parameters (Chapters 2-5) in addition to subject-specific analyses (Chapter 6). Sensitivity analyses include cervical material and geometric parameters (Chapter 2), uterine materials and shape (Chapter 3), fetal membrane stiffness and adhesion (Chapter 4), and model boundary conditions (Chapter 5). In the conclusion (Chapter 7), we discuss the parameters with the greatest impact on tissue mechanics and gestational outcomes, as well as suggested improvements for future iterations of pregnancy simulations.

2 Ultrasound-derived finite element analysis of pregnancy: sensitivity to cervical geometry and material

Characterizing reproductive tissues in real-time to understand these mechanical functions throughout gestation is challenging. Pregnancy is a protected environment and accessing organs to measure anatomical and tissue properties during this time is difficult. Hence, our driving engineering motivation is to create a finite element model of the mechanical environment of pregnancy based on the fewest and most minimally-invasive clinical measurements possible. In a preliminary finite element study using maternal anatomy segmented from MRI, we underscore the importance of capturing the interaction of the fetal membranes, uterus, and cervix and modeling the collagen architecture of these tissues[74]. Such a fully-segmented computational model requires expert knowledge in anatomy and computer-aided design (CAD), is not practical in a clinical setting, and the resulting finite element analysis is computationally expensive.

To address the need for a fast, flexible, and affordable computational assessment of the soft tissue mechanics in pregnancy we built a parametric finite element model that utilized ultrasound images of a pregnant abdomen at 25 weeks gestation. We scripted a user-friendly routine to convert these ultrasound parameters into a CAD model of the pregnant anatomy. This CAD model was used in finite element simulations to calculate the distribution of tissue stress and stretch at 25 weeks of gestation, where material parameters and loading and boundary conditions were informed or inferred by previously reported studies.

Motivated by the clinical significance of cervical length and recent clinical trials of a biomedical device that angles the cervix away from a mechanical load in patients at high-risk for sPTB[101–105], we investigate the effect of cervical structural parameters on the magnitude of tissue stretch at the cervical opening to the uterus (i.e. cervical internal os), which is the anatomical site of clinically-observed cervical failure.

2.1 Methods

2.1.1 Ultrasound measurement of maternal anatomy

Geometric dimensions of the uterus, cervix, and their position in reference to the symphysis pubis as a bony reference landmark were taken via ultrasound (GE Voluson E8) (Figure 2-1). All measurements were taken transabdominally or transperineally using the transabdominal probe (GE RAB4-8D, real-time 4D volume, curved array transducer, 4- 8.5MHZ). For the baseline model, dimensions were measured from a 35-year-old patient with no prior pregnancies at 25 weeks gestation with an empty bladder. The patient subsequently delivered the neonate at 40 weeks.

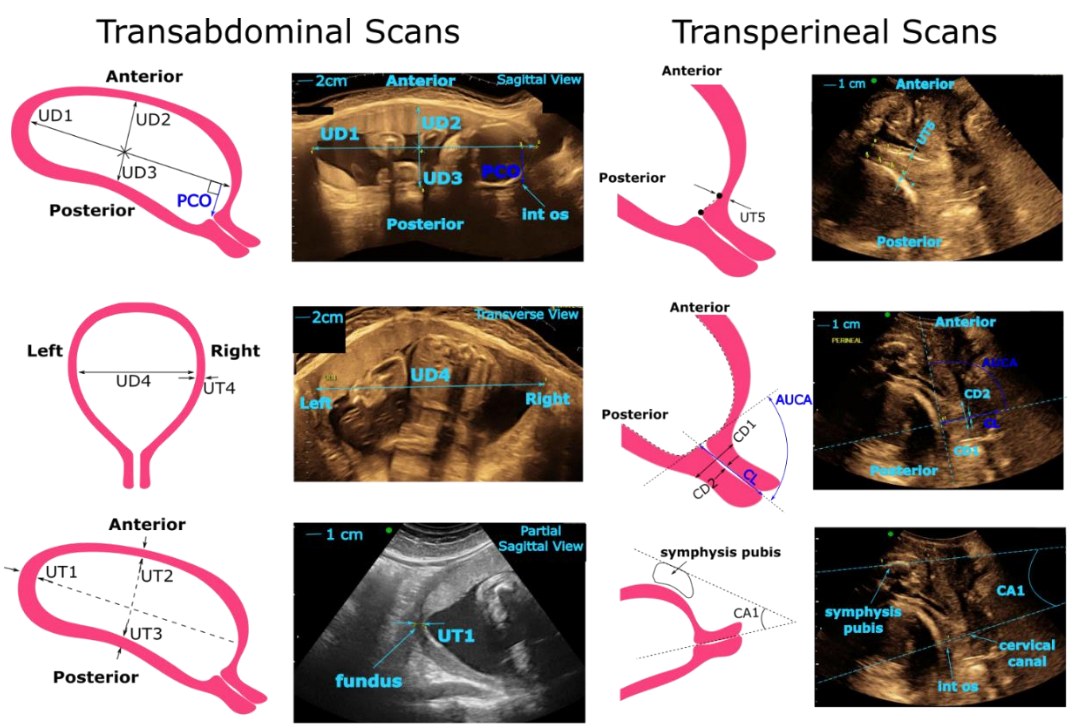

Figure 2-1: Uterine and cervical dimensions taken via transabdominal and transperineal ultrasound at 25 weeks of gestation. UD=uterine diameter, UT=uterine thickness, CD=cervical dimension, CA=cervical angle.

Uterine diameters (UDs) were measured with the extended view imaging feature of the Voluson E8, which automatically registered adjacent ultrasound images as the probe was swept across the abdomen from the fundus to the pubic bone at a steady rate of 2 cm/s. With this sagittal view, we obtained measurements of uterus longitudinal diameter (UD1), anterior-posterior diameter (UD2+UD3), and the offset of the cervical internal os from the uterus longitudinal diameter (PCO) (Figure 2-1A). To measure the transverse uterine diameter (UD4) in an extended axial view, the transabdominal probe was swept from left to right across the mid-abdomen and the uterus measured at its widest point (Figure 2-1B). Uterine wall thicknesses (UT1-5) were measured at multiple locations from the fundus to the lower uterine segment (LUS) with the transabdominal probe in a standard clinical resolution (Figure 2-1C & D) and were considered the echogenic signal from the serosa to the decidua. Cervical length (CL), diameter (CD1), canal width (CD2), angle with the anterior LUS (AUCA), and angle with the periosteum of the symphysis pubis (CA1) were assessed via transperineal scans (Figure 2-1E & F).

2.1.2 Computer (CAD) models of pregnancy

The maternal ultrasonic parameters were converted into CAD geometries with a custom computer script (Trelis Pro 15.1.3, csimsoft LLC). Geometries of the uterus, cervix, fetal membranes, vaginal canal, and abdomen were created with Boolean addition and subtraction of geometric primitives (Figure 2-2). Dimensions for the baseline model are given in Table 2-1. For this initial model, the uterus was built by transforming two spherical shells into ellipsoids. The interior uterus was scaled to the diameters obtained during ultrasound (UD1-4) and rotated in relation to the reference angle of the symphysis pubis (CA1). The current iteration of this model does not have CA1 as a measured value from the patient. Instead, it uses an arbitrary value of

15◦. The outer shell was then scaled, translated, and rotated to accommodate differences in uterine wall thickness (UT1-5) in the anterior-posterior, superior-inferior, and left-right directions.

Dimension	Measured Value
UD1	192 mm
UD2	68 mm
UD3	55 mm
PCO	25 mm
UD4	215 mm
UT1	5 mm
UT2	6 mm
UT3	6 mm
UT4	6 mm
UT5	5 mm
AUCA	90°
CA1	15°*
CL	30 mm
CD1	30 mm
CD2	4 mm

*Table 2-1: Baseline ultrasound measurements. UD=uterine diameter, PCO=posterior cervical offset, UT=uterine thickness, AUCA=anterior uterocervical angle, CA=cervical angle *Arbitrary value, not measured value), CL=cervical length, CD=cervical diameter*

The cervix was built by creating a cylinder representing the diameter of the inner canal (CD2) and subtracting that volume from a larger cylinder representing the outer cervical diameter (CD1) and cervical length (CL). The resultant hollow cylinder was then moved and rotated according to posterior cervical offset (PCO) and anterior cervical angle (AUCA). The cylinder was rounded at its corners to match the anatomical rounding of the uterocervical junction and to replicate the roundness of the most exterior end of the cervix (i.e. external os).

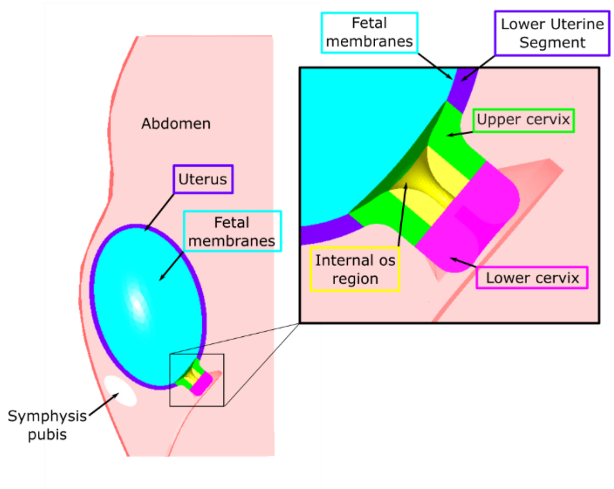

Figure 2-2: 3D representation of the environment of pregnancy. The cervix was separated into three sections for analysis: the upper cervix, lower cervix, and internal os region.

For the purpose of tissue loading analysis, the cervix was then separated into three different regions: an upper portion, a lower portion, and the internal os region (Figure 2-2). First, the cylindrical representation of the cervix was cut by a plane normal to the external os at a fixed distance of 15 mm from the internal os. Second, the top portion of the cervix was then separated by a surface extended from a smaller cylinder with a diameter that was twice of the cervical inner canal. Lastly, the vaginal canal was built by fitting a spline to three vertices located at the outside edges of the external os and one vertex at the approximate location of the vaginal introitus and the fetal membrane was generated with uniform thickness based on the contours of the inner uterine wall.

2.1.3 Finite element mesh generation

All meshes were generated using the automatic and manual meshing tools in Trelis Pro (v15.1.3, csimsoft LLC). The fetal membranes were meshed with hexahedral elements, while all other volumes were meshed with tetrahedral elements. Mesh properties varied from model to model. The baseline model mesh is given in Table 2-2, and is shown in Figure 2-3. All volumes except the fetal membranes were meshed with linear tetrahedral elements. The fetal membranes were meshed as a single continuous layer of linear hexahedral elements with a thickness of 0.1mm and no edges longer than 3 mm.

	Total	Uterus	Membrane	Abdomen	Upper Cervix	Lower Cervix	Internal Os
Element Type	-	Tet	Hex	Tet	Tet	Tet	Tet
Element Count	180,735	35,246	9,600	39,933	51,239	27,422	17,295
Average Element Volume	-	16.33 mm^3	0.994 mm^3	61.3 mm^3	0.236 mm^3	0.344 mm^3	0.131 mm^3

Table 2-2: Mesh properties for the baseline model

The uterus and cervix were connected at the node level to one another, so their boundaries were shared and moved congruently. Where the uterus and cervix shared a boundary with the abdomen volume, those boundaries were also node-tied. The lower cervix was not tied to the interior vaginal canal but floated freely inside the vaginal fornix. The mesh density of the cervix was set to the finest setting by the inherent Trelis element density function, in order to yield the most accurate deformation results for our analysis.

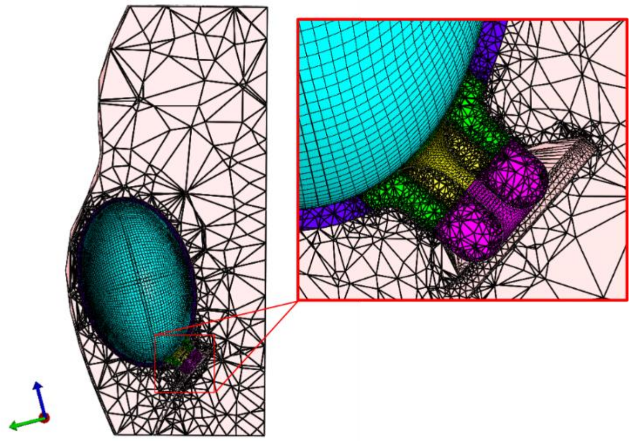

Figure 2-3: Sample mesh for baseline geometry. The fetal membrane was meshed with hexahedral elements, while all other volumes were meshed with tetrahedral elements.

Mesh convergence studies were performed by increasing the number of elements through the cervix. Mesh density was decreased from a factor of 7 (coarse mesh) to a factor of 1 (fine mesh). Our results use the finest mesh available in Trelis, with a refinement factor of 1. The mesh was considered converged if there was less than 5% change in the percentage of internal os region above the stretch threshold.

2.1.4 Material properties

The cervix and uterus materials were treated as continuously distributed fiber composites with a compressible neo-Hookean groundsubstance. This hyperelastic solid model was developed to describe the tension-compression nonlinearity in human[106] and mouse[107] cervical tissue. Considering not much is known about the multi-axial material behavior of these tissues during pregnancy, we investigated the full range of possible properties, where term pregnant (PG) tissue was considered the remodeled tissue and nonpregnant (NP) tissue represented the not remodeled tissue.

The total Helmholtz free energy density Ψ^{TOT} for the uterine and cervical materials were given by

$$\Psi^{TOT}(\boldsymbol{F}) = \Psi^{GS}(\boldsymbol{F}) + \Psi^{COL}(\boldsymbol{F})$$

Equation 2-1

Where $\boldsymbol{F}$ is the deformation gradient. The free energy density of the ground substance Ψ^{GS} is given by a standard isotropic, compressible neo-Hookean relation

$$\Psi^{GS} = \frac{\mu}{2}(\boldsymbol{I_1} - 3) - \mu \ln J + \frac{\lambda}{2}(\ln J)^2$$

Equation 2-2

where $I_1 = tr\boldsymbol{C}$ is the first invariant of the right Cauchy-Green tensor $\boldsymbol{C} = (\boldsymbol{F})^T\boldsymbol{F}$ and $J = \det \boldsymbol{F}$ is the Jacobian. μ and l are the standard lamé constants. These lamé constants combine to form the Young's modulus and Poisson's ratio of the ground substance $E^{GS} = \frac{\mu\left(3+\frac{2\mu}{\lambda}\right)}{1+\frac{\mu}{\lambda}}$ and $\nu^{GS} = \frac{1}{2\left(1+\frac{\mu}{\lambda}\right)}$, respectively. The strain energy density for the continuously distributed collagen fiber network is given by

$$\Psi^{COL} = \frac{1}{4\pi}\int_0^{2\pi}\int_0^{pi} H(I_n - 1)\Psi_r^{fiber}(\boldsymbol{I_n}) \sin\phi \, d\phi d\theta$$

Equation 2-3

where the Heaviside step function H ensures fibers hold only tension, $[\theta, \phi]$ are the polar and azimuthal angles in a spherical coordinate system. $I_n = \boldsymbol{n_o} \cdot \boldsymbol{C} \cdot \boldsymbol{n_o}$ is the square of the fiber stretch, where $\boldsymbol{n_o} = \cos\theta \sin\phi\, \boldsymbol{e_1} + \sin\theta \sin\phi\, \boldsymbol{e_2} + \cos\phi\, \boldsymbol{e_3}$ in a local Cartesian basis $\{\boldsymbol{e_1}, \boldsymbol{e_2}, \boldsymbol{e_3}\}$. Ψ^{fiber} is the strain energy density of a collagen fiber bundle given by

$$\Psi^{fiber} = \frac{\xi}{\beta}(\boldsymbol{I_n} - 1)^{\beta}$$

Equation 2-4

where ξ represents the collagen fiber stiffness with units of stress and $\beta > 2$ is the dimensionless parameter that controls the shape of the fiber bundle stiffness curve (here, the fiber strain energy density is cast in a different form than the model presented for the human cervical tissue[82], hence direct comparison can be made by considering the $\frac{1}{\beta}$ prefactor here).

To focus this study on the model sensitivity to maternal anatomy and collagen fiber stiffness parameters and not on the collagen ultrastructure, groundsubstance, or time-dependent properties, we made simplifying adjustments. Both material model fits were conducted on the material behavior after the transient force relaxation response died away. In this present study, we used a randomly distributed collagen fiber network as opposed to a preferentially-aligned collagen fiber network as presented in [106]. Cervical material properties used in this study (Table 2-3) represent collagen fiber parameters fit to the nonpregnant and term pregnant human uniaxial tension-compression data reported in [106,108,109], with the ground substance material properties kept constant. Considering we do not know material properties for the cervix at 25 weeks, we chose to approximate interim cervical fiber stiffness at constant increments between the known values. Uterine material properties represent a material model fit to passive, nonpregnant and term pregnant human uniaxial tension data reported in [110]. Fibers in both the uterus and cervix are randomly distributed. They rotate and stretch in the direction of principal stress. Previous work compared the difference between preferential and randomly distributed fiber directionality in an initial finite element model of pregnancy and found a negligible difference between the two scenarios[74]. As we continue to characterize the directionality and dispersion of the collagen fiber architecture for both the uterus and the cervix[111,112], we will examine the effects of tissue architecture on tissue loading.

Tissue Description	E^{GS} [kPa]	ν^{GS}	β	ξ [kPa]
Uterus – remodeled	2	0.3	2.71	190
Uterus – not remodeled	2	0.3	3	199
Cervix – remodeled	2	0.3	3.12	1.71
Cervix – interim 1	2	0.3	3.12	7.89
Cervix – interim 2	2	0.3	3.12	36.3
Cervix – interim 3	2	0.3	3.12	167
Cervix – not remodeled	2	0.3	3.12	769

Table 2-3: Uterine and cervical tissue variables taken from material fits to experimental data. These values are implemented in a continuous fiber distribution material model used in FEBio 2.4.2.

The outer abdomen was treated as a soft nearly incompressible neo-Hookean material with a modulus of 5 kPa. An incompressible Ogden material model based on equibiaxial tensile loading of human amnion[113] was employed for the fetal membrane layer material properties (Table 2-4), where the particular form of the Ogden strain energy density, as defined in FEBio, was given by,

$$\Psi^{FM} = \sum_{i=1}^{3} \frac{c_i}{m_i^2} \left(\lambda_1^{m_i} + \lambda_2^{m_i} + \lambda_3^{m_i} - 3 \right).$$

Equation 2-5

Tissue Description	c1 [MPa]	c2 [MPa]	c3 [MPa]	m1	m2	m3
FM	0.859	0.004	0.756	27.21	27.21	-16.64

Table 2-4: Fetal membranes (FM) material properties described by an Ogden material model in Equation 2-5.

2.1.5 Boundary conditions and loading

Boundary conditions were applied as described in Figure 2-4. The abdomen was fixed in the x, y, and z directions on its outside surface. The fetal membranes were prescribed a no-slip, tied contact along its outer surface (cyan in Figure 2-4) to the inner surface of the uterus (purple) and to the inner surface of the upper cervix region (green). A frictionless sliding contact condition was assigned between the outer surface of the fetal membranes (cyan) and the internal os region (yellow). Anatomically, in normal pregnancy, the outer layer of the fetal membranes is adhered fully to the uterine wall and the upper cervix throughout gestation and detaches at the onset of labor.

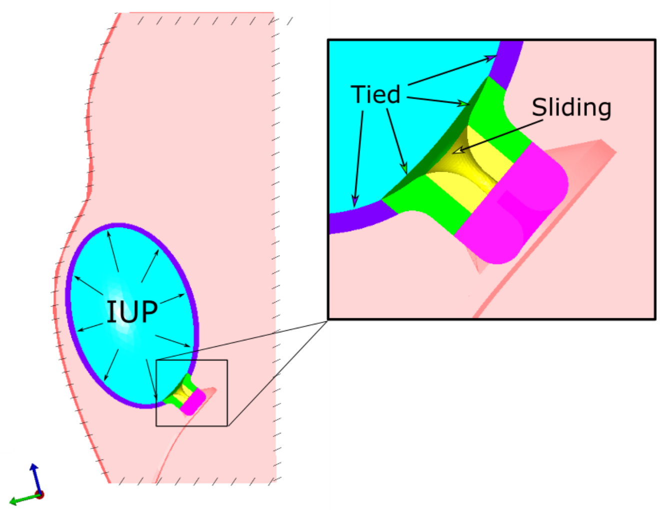

Figure 2-4: Boundary and loading conditions. Outside of the abdomen was fixed in x, y, and z directions (dashed lines in figure). Uniform intrauterine pressure (IUP) was applied on the inner surface of FM. Tied contact was applied between FM (cyan) and uterine wall (purple) and between FM and upper cervix (green). Sliding contact was applied between FM and cervix internal os region (yellow).

Pressure was applied to the inner surface of the fetal membranes to represent the intrauterine pressure (IUP). IUP magnitude was informed by previous studies that measured the amniotic sac cavity pressure via catheter puncture of the fetal membranes, where the values were reported after subtracting the gravitational pressure head from the reading[52]. IUP at 25 weeks (0.817 kPa) was calculated with the following equation from the Fisk et al. study:

$$\ln(y+1) = 0.12 + 0.23x - 0.010x^2 + 0.00015x^3,$$

Equation 2-6

where y is the amniotic pressure in mmHg and x is the gestation in weeks [52]. To compare stretch patterns between models, we ramped the pressure to the value of 40 weeks (2.33 kPa) and to the value of a labor contraction (8.67 kPa)[114].

2.1.6 Finite element (FE) analysis and evaluation

FE analyses were performed in FEBio 2.4.2 (http://www.febio.org.). Stress and stretch data were plotted as a function of IUP in PostView (PostView 1.9.1), FEBio's post-processor for visualization and analysis. These data were then imported into MATLAB (MATLAB R2014a) for further post analysis. To describe the deformation of the cervix, the extent of cervical 1st principal right stretch was evaluated as a percentage of the cervical internal os volume (Figure 2-2) above a 1.05 stretch threshold. The right stretch in this context is the symmetric tensor $\boldsymbol{U}$ in the polar decomposition of the deformation gradient $\boldsymbol{F} = \boldsymbol{RU}$.

2.1.7 Sensitivity to cervical structural parameters

After the evaluation of the baseline model, cervical structural parameters were scaled individually in order to assess each variable's impact on cervical internal os stretch. The range of values was based on literature values and represented clinical significance[115,116]. These parameters were: anterior uterocervical angle (AUCA), cervical length (CL), posterior cervical offset (PCO), and cervical stiffness (Table 2-5). Stretch magnitude and distribution were compared at a contraction-level IUP of 8.67 kPa to illuminate patterns.

Model	Cervical Angle [°]	Cervical Length [mm]	Cervical Offset [mm]	Cervical Fiber Stiffness ξ [kPa]
Baseline	90	30	25	1.71 & 769
AUCA	90 → 110	30	25	1.71 & 769
CL	90	25 → 40	25	1.71 & 769
PCO	90	30	0 → 25	1.71 & 769
Cervical Stiffness	90	30	25	1.71 → 769

Table 2-5: Model geometries, with ranges for each varied parameter. AUCA = anterior uterocervical angle, CL = cervical length, PCO = posterior cervical offset

AUCA in this analysis was defined as the angle between the cervical inner canal and the anterior LUS (Figure 2-1E). AUCA was varied in ten-degree increments from 90° in the baseline model to the most extreme value of 110° with respect to the anterior LUS. CL was varied in 5mm increments from 25mm (a clinical short cervix) to 40 mm. CL in this analysis was defined as the length of the inner canal from the internal os to the external os (Figure 2-1E). PCO was varied in 5mm increments from 0mm to the baseline value of 25 mm. PCO in this analysis was defined as the distance from the longest uterine diameter to the cervical internal os (Figure 2-1A). Cervical stiffness was varied by decreasing fiber stiffness ξ from the NP value of ξ = 769 kPa in even increments to reach the PG value of ξ = 1.71 kPa. All other parameters in the material model were kept constant.

2.2 Results

2.2.1 Baseline model

The baseline pregnancy model at 25 weeks of gestation shows minimal deformation under amniotic sac cavity pressure estimated for that week (Equation 2-6, IUP=0.817 kPa). At this level of pressure, the maximum level of tensile stretch for the cervix, uterus, and fetal membranes reached 1.04, 1.05, and 1.06 respectively, and the maximum level of compressive stretch for the cervix is 0.86. Minimal tissue stretch at this stage of pregnancy is supported by previous x-ray and histologic studies, where evidence shows that the uterus undergoes dramatic growth with limited stretching in the first half of pregnancy to accommodate the fetus and amniotic fluid[10]. Analysis was done for both remodeled (PG) and not remodeled (NP) uterine and cervical tissue properties for baseline IUP at 25 weeks (Figure 2-5A, D), baseline IUP at 40 weeks (Figure 2-5B, E), and contraction-magnitude IUP (Figure 2-5C, F).

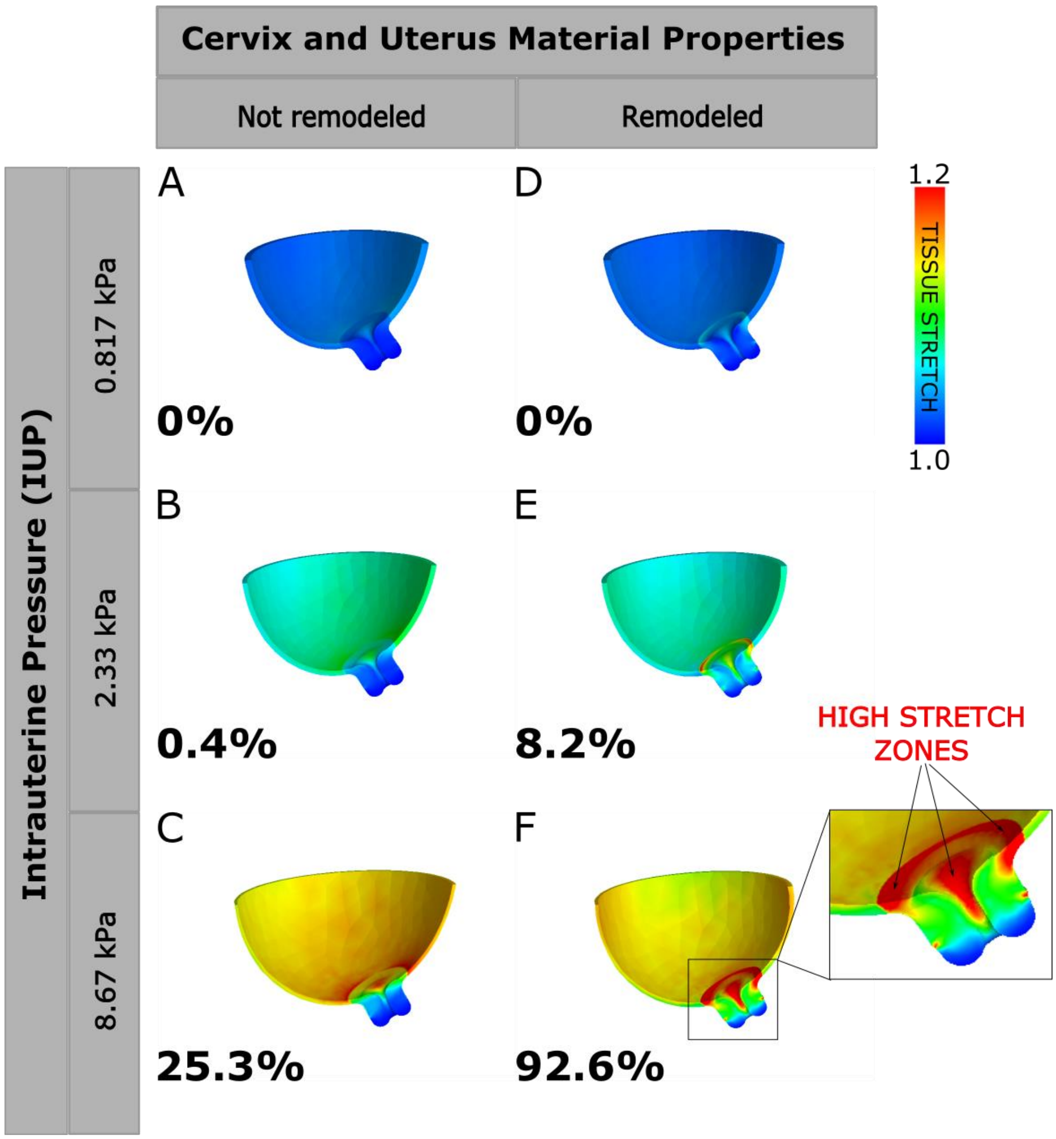

Figure 2-5: The color map reports the 1st principal right stretch for the baseline geometry evaluated with IUPs of (A&D) 25 weeks = 0.817 kPa, (B&E) 40 weeks = 2.33 kPa, and (C&F) contraction = 8.67 kPa. The percentage reports the volume fraction of the cervical internal os region above a 1.05 stretch. The membrane is removed for clarity.

To illuminate the pattern of tissue stretch, the model is investigated under a contraction-level intrauterine pressure of 8.67 kPa. There is a jump in tissue stretch distribution at the boundary of the uterus and cervix because of material property definition. Overall, the highest amounts of stretch are located near this uterocervical boundary for the uterus and at the internal os of the cervix. Because of the ellipsoidal shape of the uterus and the placement of the cervix in relation to the uterine axis, tissue stretch patterns follow anatomic quadrants. Zones of high stretch are apparent in the anterior-posterior sections of the uterus and the left-right sections of the cervix (red zones in Figure 2-5F). For the uterus, the maximum stretch is directed along the meridian in the anterior and posterior quadrants and along the circumference in the left-right quadrants. Throughout the uterine thickness, the stretch is at a maximum on its inner surface and decreases towards the outer surface. These stretch concentration patterns may vary for differing uterine shapes and sizes.

For the upper part of the cervix, its outer edges are dictated by the direction of the uterine wall tension, where the anterior-posterior cervix is pulled in a radial direction and the left-right quadrants are pulled in circumferential tension. The stretch pattern of the inner core of the cervix does not show quadrant patterns. Instead, the first principal stretch is directed circumferentially in all anatomic quadrants (Figure 2-6A). For compressive stretch, the distribution is off-centered and the maximum magnitude is located in the posterior section (Figure 2-6C). Second principal stretch is largest in the left and right quadrants of the uterus (Figure 2-6B), and maximum shear strain occurs at the posterior uterus and uterocervical interface (Figure 2-6D). These stretch patterns are most likely dominated by the geometric features of the uterus and fetal membranes adhesion at both the inner uterine surface and the inner surface of the upper cervix region. The stretch plotted here is for uniform intrauterine pressure and does not include the fluid pressure head due to gravity. Gravitational forces will most likely shift this distribution towards the anterior direction.

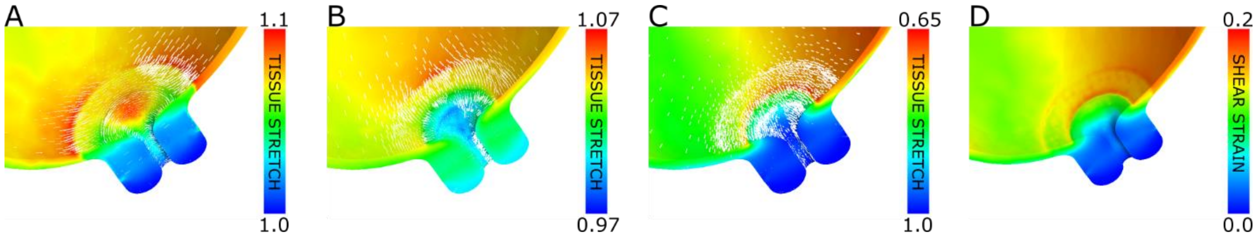

Figure 2-6: Baseline results with vector plots to show stretch directions for (A) 1st principal right stretch, (B) 2nd principal right stretch, (C) 3rd principal right stretch, and (D) maximum shear strain. For 1st principal right stretch, circumferential stretch is exhibited at the internal os while radial stretch is observed at the anterior and posterior sections of the uterocervical interface.

2.2.2 Cervical structural parameters

Both the geometric and material properties of the cervix influence the distribution and magnitude of tissue stretch. Results indicate that geometric variations in anterior uterocervical angle (AUCA), cervical length (CL), and posterior cervical offset (PCO) are all more influential in a softer cervix (Table 2-6). The geometric parameter PCO has the largest effect on the loading at the internal os for both the soft pregnant (PG) cervix and the stiff nonpregnant (NP) cervix. Aligning the cervical canal with the uterine longitudinal axis reduces the amount of tissue stretch at the internal os. For the PG cervix, when PCO = 0 mm the volume fraction of cervical tissue above the 1.05 stretch threshold reduces by 50% compared to the most extreme case investigated, which is the baseline value of PCO = 25 mm. Even for the NP cervix, aligning the cervical canal with the uterine axis reduces the tissue stretch volume fraction by 16%. For the NP cervix, CL and AUCA have a negligible influence on the outcome tissue stretch measurement. For the PG cervix, lengthening the cervix from 25 mm to 40 mm results in a 22% reduction in the volume fraction of the cervical internal os above the 1.05 stretch threshold, while varying cervical angle still has little effect on the volume fraction. There are no scenarios in which an NP cervix had the same amount of loading as the PG cervix.

	Baseline	AUCA [°]			CL [mm]				PCO [mm]					
		90	**100**	**110**	**25**	**30**	**35**	**40**	**0**	**5**	**10**	**15**	**20**	**25**
NP Cervix (stiff) Volume fraction above 1.05 stretch	25.3	25.3	26.0	26.1	26.2	25.3	26.0	26.8	21.2	21.2	22.0	23.3	24.1	25.3
PG Cervix (soft) Volume fraction above 1.05 stretch	92.6	92.6	94.2	94.8	93.2	92.6	80.2	72.5	46.0	48.5	50.1	58.1	82.2	92.6

Table 2-6: Summary of results for the volume fraction of cervical internal os above a 1.05 stretch threshold. AUCA=anterior uterocervical angle, CL=cervical length, PCO=posterior cervical offset. The geometric parameter PCO had the largest influence on the amount of tissue stretch at the cervical internal os, for both a soft PG cervix and a stiffer NP cervix. The most drastic reduction in cervical tissue stretch occurs for a soft cervix that is aligned with the uterine longitudinal axis compared to a 25 mm PCO.

2.2.2.1 Sensitivity to anterior uterocervical angle (AUCA)

As anterior uterocervical angle (AUCA) increases and the external os of the cervix is tilted towards the posterior, cervical stretch of the internal os region increases and the distribution of stretch moves posteriorly (Figure 2-7). In the not remodeled cervix material model, the 110° AUCA experiences a 3.2% increase in the volume fraction of cervical tissue above the 1.05 stretch threshold from the 90° AUCA. In the remodeled cervix material model, the 110° AUCA experiences a 2.4% increase in the volume fraction from the 90°AUCA. In both models, cervical tissue stretch is minimized when the cervix is aligned with the longitudinal uterine axis (AUCA = 90°).

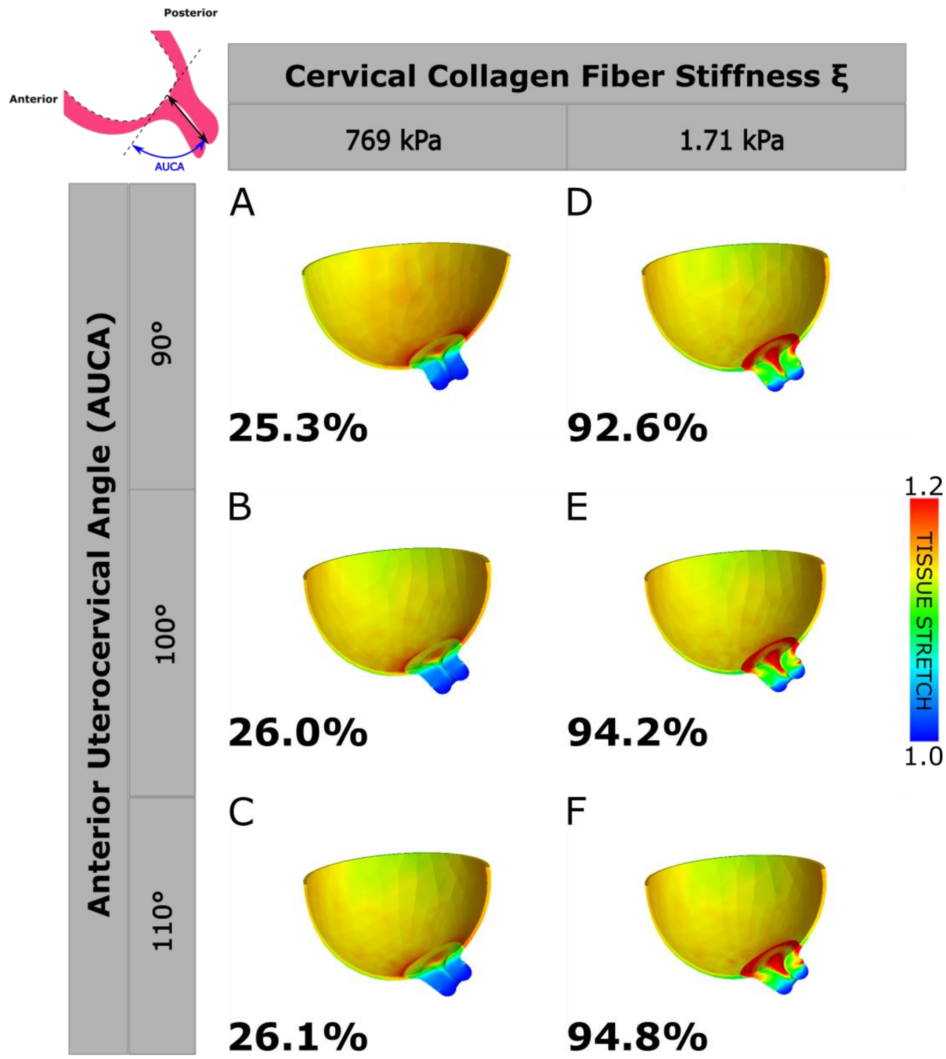

Figure 2-7: Uterine and cervical stretch patterns as AUCA (shown top left) is varied. The color map reports the 1st principal right stretch for remodeled cervix with AUCA of (A) 90°, (B) 100°, and (C) 110°, and remodeled cervix with AUCA of (D) 90°, (E) 100°, and (F) 110°. The percentage reports the volume fraction of the cervical internal os region above a 1.05 stretch. The membrane is removed for clarity.

2.2.2.2 Sensitivity to cervical length (CL)

Cervical length (CL) has an influence on cervical loading patterns only when the cervix has remodeled material properties (Figure 2-8). When the cervix has not remodeled and is as stiff as the nonpregnant state, increasing the cervical length does not alter the loading pattern at the internal os. For a cervix that has remodeled and is as soft as the term tissue, as cervical length is decreased the stretch at the internal os increases. The 25 mm CL experiences a 28.6% increase in the volume fraction of tissue over 1.05 stretch from the 40 mm CL.

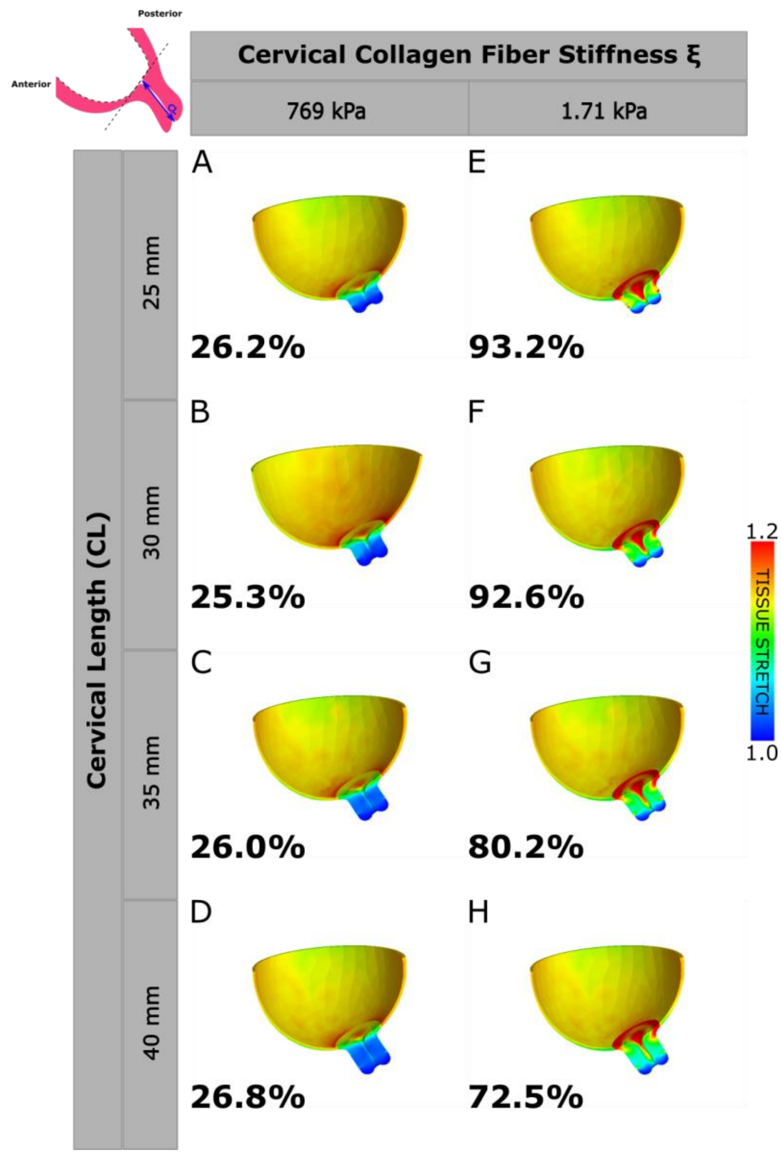

Figure 2-8: Uterine and cervical stretch patterns as CL (shown top left) is varied. The color map reports the 1st principal right stretch for not remodeled cervix with CL of (A) 25 mm, (B) 30 mm, (C) 35 mm, and (D) 40 mm, and remodeled cervix with CL of (E) 25 mm, (F) 30 mm, (G) 35 mm, and (H) 40 mm. The percentage reports the volume fraction of the cervical internal os region above a 1.05 stretch. The membrane is removed for clarity.

2.2.2.3 Sensitivity to posterior cervical offset (PCO)

As posterior cervical offset (PCO) increases, cervical stretch of the internal os region increases (Figure 2-9). In the not remodeled cervix material model, the 25 mm PCO experiences a 19.3% increase in the volume fraction of tissue over 1.05 stretch from the 0 mm offset, with intermediary values corresponding to this increasing trend. In the PG cervix material model, the 25 mm PCO experiences a 101.3% increase in the volume fraction of tissue over 1.05 stretch from the 0 mm offset, with intermediary values corresponding to this increasing trend. As seen with the CL parameters, the softer cervix is more sensitive to changes in geometric variables.

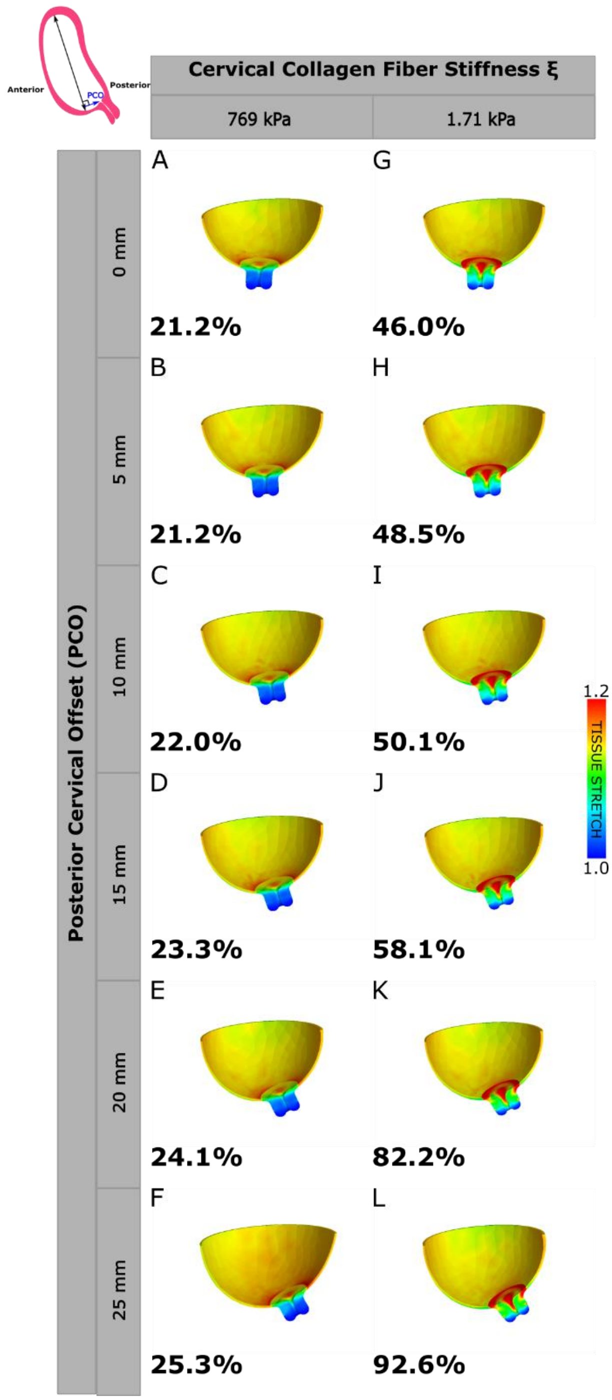

Figure 2-9: Uterine and cervical stretch patterns as PCO (shown top left) is varied. The color map reports the 1st principal right stretch for not remodeled cervix with PCO of (A) 0 mm, (B) 5 mm, (C) 10 mm, (D) 15 mm, (E) 20 mm, and (F) 25 mm, and remodeled cervix with PCO of (G) 0 mm, (H) 5 mm, (I) 10 mm, (J) 15 mm, (K) 20 mm, and (L) 25 mm. The percentage reports the volume fraction of the cervical internal os region above a 1.05 stretch. The membrane is removed for clarity.

2.2.2.4 Sensitivity to cervical stiffness

As the cervix is made softer by decreasing the value of the collagen fiber stiffness parameters ξ, cervical stretch of the internal os region increases (Figure 2-10). Keeping all other material parameters the same, the collagen fiber stiffness associated with a remodeled cervix experiences a 266% increase in cervical stretch from collagen fiber stiffness value associated with the not remodeled cervix.

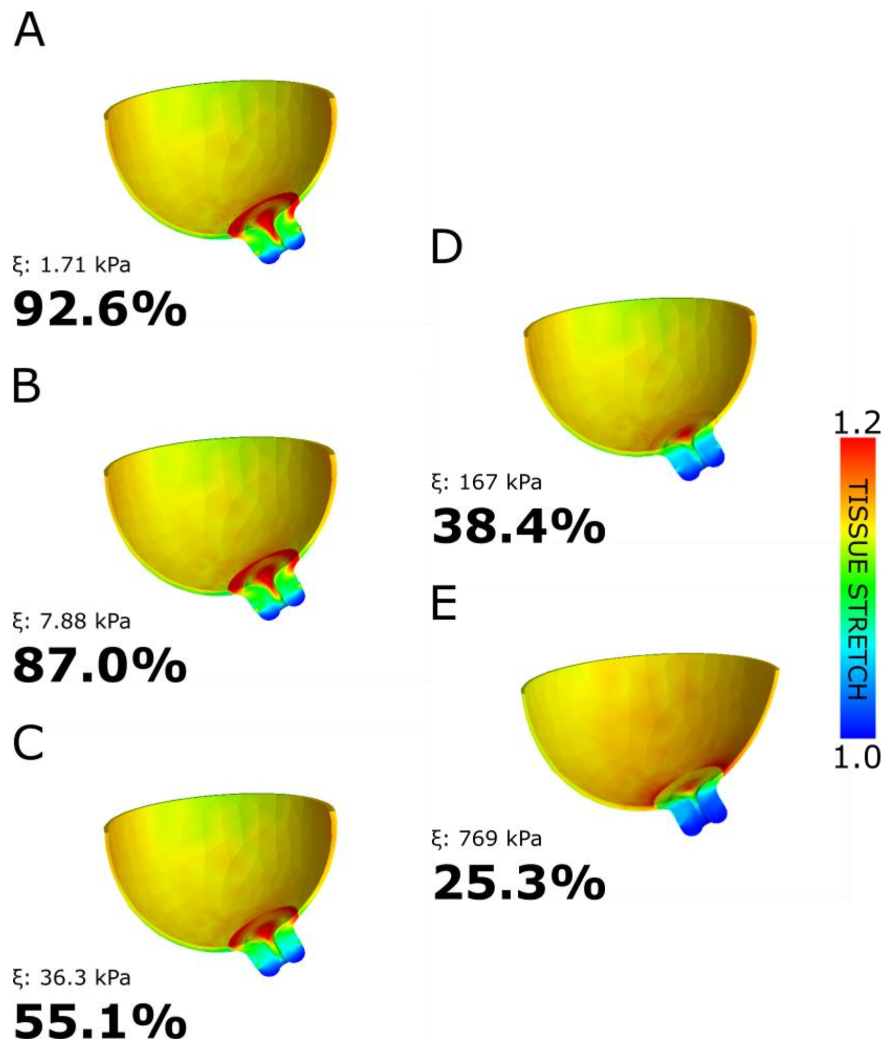

Figure 2-10: Uterine and cervical stretch patterns as cervical fiber stiffness is varied. The color map reports the 1st principal right stretch for the baseline geometry evaluated with a cervical fiber stiffness (ξ) value of (A) 1.71, (B) 7.89, (C) 36.3, (D) 167, and (E) 867 kPa. The percentage reports the volume fraction of the cervical internal os above a 1.05 stretch. The membrane is removed for clarity.

2.3 Discussion

This work develops a method to generate a patient-specific finite element model of the uterus, cervix, fetal membrane, and surrounding anatomy derived from maternal ultrasound scans. For a baseline investigation, we model a pregnant patient at 25 weeks of gestation and convert ultrasound measurements into a parametric computer model. With this computer model, and basing engineering assumptions on previously published data, we assess tissue stretch at various levels of intrauterine pressure (IUP). Results indicate that the distribution and magnitude of stretch of the cervix are affected by uterine wall mechanics, where direction and magnitude of cervical stretch are pulled towards uterine wall tension. Our results show a stretch concentration at the internal os of the cervix, matching findings from previous finite element models[31,73,74].

We also demonstrate the flexibility of this model by investigating the effects of cervical angle, length, offset, and material properties on the stretch generated at the internal os due to contraction-magnitude IUP. The sensitivity study of cervical structural parameters indicates that the effect of geometric parameters is magnified for a soft cervix and that cervical tissue stretching was most sensitive to posterior cervical offset (PCO) (Table 2-6). In this preliminary model, we show that cervical stretch is reduced if the cervical canal is aligned with the uterine axis, where there the cervical axis is collinear with the uterine axis.

The level of tissue stretch at the IUP for 25 weeks of gestation was minimal. Tissue tensile stretch levels remain below 1.044 for the entire model at this gestational age. In comparing our results to previous studies[74], we see larger tensile stretches due to different fetal membranes adhesion scenarios. In the previous study, the fetal membranes were only tied to the lower uterine segment, whereas in this study, they are tied to both the lower uterine segment and upper cervix. Minimal tissue loading is expected at the 25 weeks gestation timepoint considering the uterus grows and stretches to ac accommodate the enlarging amniotic sac. Uterine mass grows from 70 g to 1100 g and its volume capacity goes from 10 mL to 5 L[117]. Early histologic[11], x-ray[10], and amniotic cavity pressure catheter[52,118,119] studies offer the most complete view of pregnant uterine anatomy. We learn from these data that in the first 12 weeks of pregnancy, hormonal signals initiate a considerable uterine growth process under negligible mechanical loading[1,11,52,120]. From 12 to 16 weeks, the lower section of the uterine corpus unfolds into the lower uterine segment to allow for expansion of the amniotic sac without stretching the uterine wall[11]. X-ray data of pregnant anatomy confirms the uterine wall thickness stays constant until 16 weeks and then begins to thin and elongate along its diameters as the fetus begins its rapid growth between 16 and 24 weeks[10]. During this time the uterus both grows and stretches. After 24 weeks, x-ray and ultrasonic evidence support that the uterus stops growing and continues to stretch and thin considerably until term[10,13–15,117,121].

Evidence from ex vivo cervical fibroblast studies suggests that cervical tissue stretch controls cervical material modeling processes[122–124]. Hence, it is postulated that excessive cervical tissue stretch triggers premature cervical remodeling and possibly preterm birth. To evaluate the effect of cervical geometric parameters on cervical tissue stretch, we evaluated model outcome variables at a contraction-level IUP. Cervical tissue stretch is most sensitive to posterior cervical offset (PCO, Figure 2-9) and is least sensitive to anterior uterocervical angle (AUCA, Figure 2-7). Cervical tissue stretch is only sensitive to cervical length (CL, Figure 2-8) if the cervix has already remodeled and is soft.

2.3.1 Clinical considerations

These results of this initial sensitivity study help explain the conflicting results seen in the clinical literature. The mechanical role of the cervix is recognized clinically, where both risk assessment and management of spontaneous preterm birth (sPTB) rely heavily on the serial ultrasound assessment of cervical length[125,126]. The positive predictive value of a sonographic short cervix is low as many women with a short cervix go on to deliver near term[127–134]. Our results show that assessing cervical length alone will not indicate the likelihood of the cervix to continue to deform. Instead, both cervical length and cervical material property must be evaluated to better predict cervical deformation under load.

Cervical angle has recently been the topic of clinical studies focusing on diagnosis and prevention of preterm birth. Two retrospective cohort studies investigating cervical angle as an indicator of sPTB showed conflicting results. One study found that an extreme posterior angle is associated with preterm birth[115] and the other did not[135]. The efficacy of clinical interventions that are thought to restore the mechanical function of the cervix to prevent preterm birth also remains unclear. The cervical pessary, a silicone ring-shaped diaphragm meant to angle the cervix away from the mechanical load[102] is currently the subject of multiple large-scale randomized clinical trials in the US and in Europe. Results have been conflicting. A Spanish clinical trial of pessary use showed a benefit to pessary use in singleton[103] and twin[101] pregnancies at risk for sPTB. However, this success has not been replicated in the largest clinical trials to date for twin[99,104] and singleton[105,136] pregnancies. It was concluded that the use of the pessary did not result in the reduction of sPTB nor adverse neonatal outcomes. Our simulation results suggest cervical angle has a minimal effect on cervical tissue stretch.

In contrast, our results show the novel notion that posterior cervical offset (PCO) could be measured sonographically to contribute to risk assessment of preterm birth. Yet this contradicts the Bishop Score method used traditionally in the clinic to predict readiness for birth. A posterior cervix results in a low Bishop Score, which correlates to a low chance of labor induction. A mid-line cervix has a moderate Bishop Score, and an anterior cervix has a high Bishop Score. Most often in pregnancy, the cervix lies posterior throughout gestation and moves anteriorly nearing labor. One counterpoint to this result is that if there is strong adhesion between the cervix, decidua, and fetal membranes, the cervix will be pushed posteriorly as the head descends with increased fetal growth. This scenario would result in a posterior cervix, but with reduced cervical stretch due to strong adhesion. Therefore, it is important to note that a posterior cervix results in increased stretch over a centered cervix only in the event that the membrane adhesion scenario is the same in both.

Since our baseline model is symmetric, the increased stretch in a large posterior cervical offset may also be observed in the case of a large anterior cervical offset instead. Future iterations of this model will investigate an anterior cervical offset, in addition to each scenario for a retroverted uterus (uterus tilted posteriorly). We believe that the posterior and anterior cervical offset parameters will yield similar results, and having the cervical canal axis aligned with the longitudinal uterine axis is ideal to minimize cervical stretch at the internal os.

It should be noted that hydrostatic pressure on the internal os is neglected in this model. The only scenario in this sensitivity study that would be affected by including hydrostatic pressure would be the posterior cervical offset since changing this parameter moves the internal os to a different height within the uterus. However, moving the cervix posteriorly by a maximum of

25mm would change the hydrostatic pressure by no more than 0.2 kPa, which can be considered negligible in comparison to the 8.67 kPa intrauterine pressure applied in the analysis.

2.3.2 Comparison to MRI-based model

To facilitate the creation of a more clinically applicable simulation and to reduce computational needs, we pursued the analytical method as shown here to create a pregnant anatomy. To understand how these simplifications affect cervical tissue stretch patterns, we compared a parameterized model with a model generated from our previously published MRI-segmentation methods[74]. Briefly, dimensions of the uterus and cervix were measured from MRI data of the normal subject presented in[74], and these measurements were implemented in our parameterized procedure detailed here. Since this modeling method includes simplifications, the parameterized model does not contain bumps, divots, and variations in thickness that the segmented geometry includes. In Figure 2-11 we compare tissue stretch patterns between the MRI-segmented and analytical geometries. Here, we use the same material models, mesh density, membrane thickness, contact definitions, and boundary conditions between the two models.

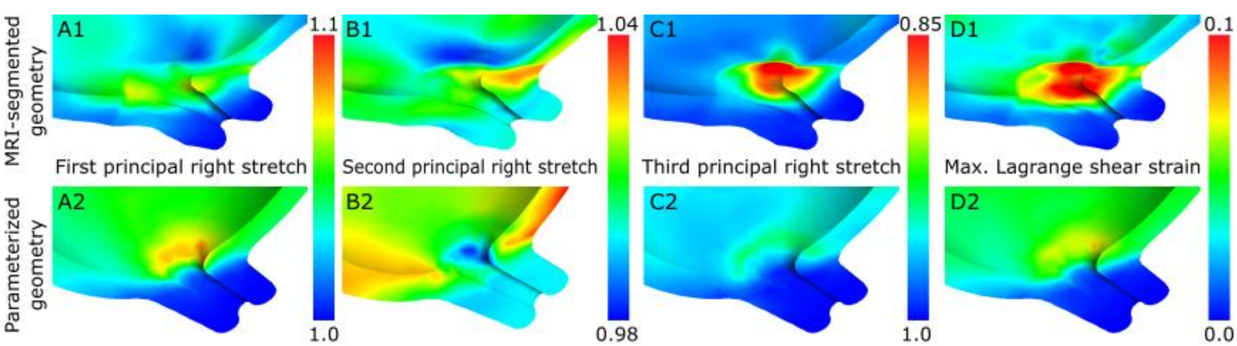

Figure 2-11: Principal right stretch plots of the MRI geometry model (A1) and the parameterized geometry model (A2) under an IUP of 0.817 kPa applied to the fetal membrane. First principal stretches (A1, A2) reflect the areas of highest tension and are concentrated around the internal os and the proximal portion of the cervix. Third principal strains (C1, C2) represent areas of compression, which are most prominent in the MRI model (C1). Shear strains are shown in figures D, and are also concentrated over the internal os, but are approximately twice as large in the MRI-derived model due to the irregular surface of the geometry.

Overall, after application of intrauterine pressure of 0.817 kPa, the parameterized model predicts similar locations for strain concentration patterns as the MRI-segmented model does. Figure 2-11A1-D2 demonstrate that the largest differences occur at the site of a geometric feature in the MRI-based model at the location of the posterior internal os. At this location, the top of the cervix protrudes slightly into the volume of the uterus. This geometric irregularity cannot

be captured in the current set of geometric measurements we have defined. Clinically, any measurements need to be well-defined, repeatable, and easily teachable to ensure correct procedures are followed. Characterization of these kinds of geometric features is doubly challenging as the internal pelvic anatomy is not static, and can change substantially even during the same ultrasound session (for example, with contractions or from the bladder filling or being emptied).

Because both models use exactly the same material models and membrane contact definitions, this disagreement must arise from differences between the geometries. In particular, the MRI model geometry is inherently less geometrically stiff in the mode of internal pressurization because it has hills and valleys on the surface, making it equivalent to a rope with slack being pulled under tension. On the other hand, the geometric primitive-based ellipsoidal geometry in the parameterized model has less play under increasing internal pressurization, because its basic geometry is more stable.

These effects will be important to characterize in future iterations of the model, and a mechanism to capture this behavior will be developed. The mechanism may take the form of better replicating the in-vivo geometry or of modifying the constitutive model to reduce the low-strain stiffness to an amount equivalent to the geometric slack we see in the

MRI-models.

Despite the differences between the results of each method, the parameterized model is an important tool in bridging the gap between future numerical clinical tools and the current clinical state of the art due to its unlimited flexibility and much-reduced patient measurement to simulation timeline.

2.3.3 Limitations

As we work towards a more accurate finite element model of pregnancy, we use simplified simulations to explore the effect of model parameters on outcome variables. Simplifying assumptions in this model include the difference between actual anatomic geometry and the simplified geometry, the assumption of material property homogeneity, the lack of dynamic analysis and tissue growth, and the fact that measurements were taken in vivo in a loaded configuration. Additionally, for a more accurate model we would need to directly measure intrauterine and abdominal cavity pressures and in vivo fetal membranes, uterus, and cervix material properties. We would also need to measure the properties of abdominal boundary conditions, such as the placenta, to accurately represent the displacement of the top half of the uterus and fetal membrane. While we work towards obtaining these data from minimally-invasive methods, we relied on literature values of the intrauterine pressure (IUP) [30,31] and mechanical measurements of ex vivo tissue samples.

2.4 Conclusions

We present here a method for incorporating simplified anatomical geometries, fetal membrane contact conditions, IUP interaction, and cervical material properties into a mechanical simulation of pregnancy. In this study, we calculate the 1st principal right stretch under contraction-magnitude IUP levels in sonographically estimated FE models of pregnancy. Various cervical structural parameters are varied over a physiological range to analyze the sensitivity of each dimension on cervical stretch. We chose to analyze AUCA, CL, PCO, and cervical stiffness, and our results show that a combination of AUCA, PCO, and cervical stiffness is the most significant LUS dimension measurement affecting the mechanical stretch state within the cervix, particularly near the internal os. Our simulation result supports the need for additional maternal anatomy parameters and the evaluation of cervical material properties to better predict the occurrence of preterm birth. In future studies, we will conduct sensitivity studies on uterine, fetal membranes, and boundary condition geometries and material properties as well. Our goal is that our model will serve as a preliminary platform for the development of sPTB diagnostic tools and procedures. In addition, it serves as a first step in modeling the uterine and cervical growth and remodeling in pregnancy.

3 Ultrasound-derived finite element analysis of pregnancy: sensitivity to uterine shape and material fiber orientation

Clinically, uterine over-distention has been associated with spontaneous preterm birth because twin pregnancies[23,63] and patients with excess amniotic fluid tend to deliver early[137]. Additionally, the mechanical failure of the uterine cervix caused by the premature remodeling, shortening, and dilation of the cervix is thought to be the final common pathway for many etiologies of spontaneous preterm birth[24,138]. Yet, the mechanical stretch of these tissues during pregnancy has not been determined, preventing an understanding of normal labor processes and an evaluation of the risk of preterm birth. The goals of this work are to take advantage of existing temporal x-ray data of the pregnant human anatomy[10] to construct finite element (FE) models of the pregnant abdomen and to calculate the magnitude of tissue stretch at various gestation timepoints. X-ray data show that the gravid uterus goes from a spherical shape before 20 weeks to an elliptical shape after 20 weeks when the fetal growth rate begins to accelerate. During this elliptical growth, its walls thin and its longitudinal diameter grows more quickly than the anterior-posterior and left-right diameters, with maximum elongation rate occurring between 20 and 32 weeks (Figure 1-2)[10,13].

Furthermore, the muscular myometrium of the uterine wall has multiple layers with various fiber directions (Figure 3-1). There is an external layer containing two sub-layers, one composed of circular, and the second made up of longitudinal fibers. The intermediate layer has interlaced muscle fibers running diagonally. Finally, the innermost myometrial layer has circular fibers[12,139,140].

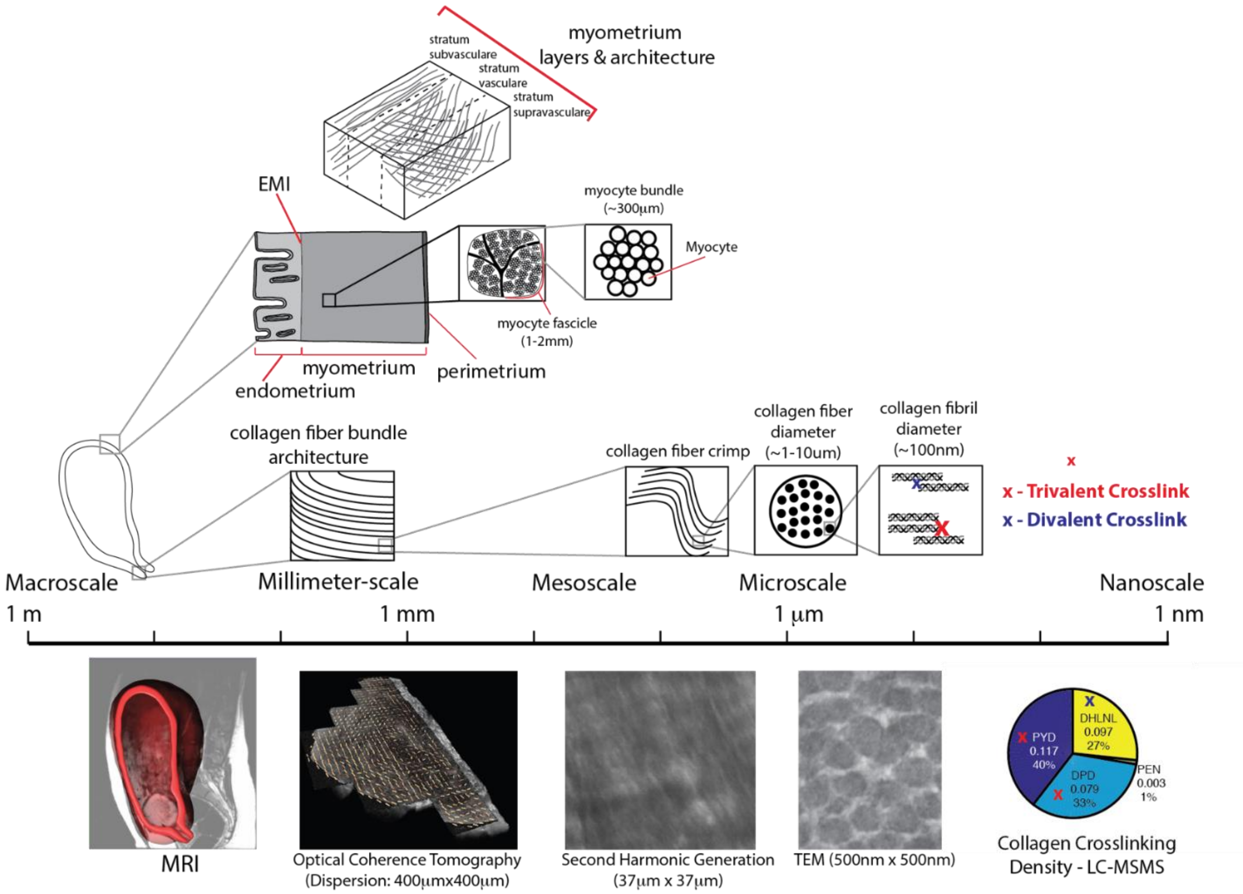

Figure 3-1: Biological length scales of the cervix and uterus. The cervix is composed of a hierarchal cross-linked collagen network with embedded smooth muscle cells (SMC) at the internal os[18]*, and the load-bearing myometrium is composed of layers of preferentially-aligned SMC bundles*[139,140].

This particular study focuses on the effect of uterine shape throughout gestation and uterine fiber directionality on tissue stretch in the uterus and in the cervix, particularly at the internal cervical os, which is the hypothesized site of premature cervical remodeling[141]. This is an initial study of overall shape and materials based on preexisting datasets. The rationale behind this study is to create simple models to tease out on specific contributions of anatomy and material properties and analyze their effect on tissue stretch. Cervical tissue stretch is chosen as an output parameter because cervical smooth muscle cells are known to produce enzymes and inflammatory chemokines/cytokines that are involved in extracellular matrix (ECM) remodeling, and also may play a role in activating or propagating uterine contractility[18]. When the cervical smooth muscle cells sense a mechanical stretch, they may trigger collagen remodeling and therefore result in cervical softening. Uterine tissue stretch is chosen as an output parameter because uterine overdistention is also believed to activate uterine activity[65].

We hypothesize that uterine shape and fiber architecture will both influence uterine and cervical mechanics. An elongated, elliptical uterus will likely experience greater stretch in the anterior and posterior areas as the intrauterine pressure aims to expand the uterus into a sphere, but boundary conditions (such as the spine and abdomen) will not allow it to do so. The later gestational timepoints also have thinner uterine walls, which will similarly increase uterine stretch. An elliptical uterus may also increase cervical stretch, as the pressure on the anterior, posterior, left, and right walls of the uterus push out the uterine wall and pull up on the cervical tissue near the internal os. We hypothesize that uterine fiber architecture may influence uterine stretch. Circumferentially oriented fibers may reduce stretch in the anterior, posterior, left, and right directions, and increase stretch at the fundus and near the cervix.

We acknowledge that we make various engineering assumptions in this study that may influence our results: the initial size and shape of the uterus are taken in a loaded configuration, model geometries are simplified to Boolean shapes, intrauterine pressure is applied at the largest magnitude of a labor contraction, and the effect gravity is ignored. We discuss the rationale behind these limitations in Section 3.3.1.

This work was presented at the 64th Annual Meeting of the Society for Reproductive Investigation on March 16, 2017, in Orlando, FL[142,143].

3.1 Methods

For FE analysis, the uterus and cervix were modeled as collagenous composite materials meshed using linear tetrahedral elements, based on material fits to passive length-tension curves of pregnant tissue[106,144], while the FM was modeled as Ogden nonlinear material meshed with hexahedral elements[145]. The fetal membrane was prescribed a tied contact to the inner uterine wall and a sliding contact to the cervical internal os. To compare how uterus shape and structure alone influence loading patterns, and to present the largest relative difference between different models, intrauterine pressure (IUP) was applied at contraction magnitude (8.67 kPa)[12] and the magnitude of the principal tissue stretch was calculated. The extent of cervical stretch was evaluated as a percentage of cervical internal os region (Figure 3-2) volume above a 1.05 stretch threshold.

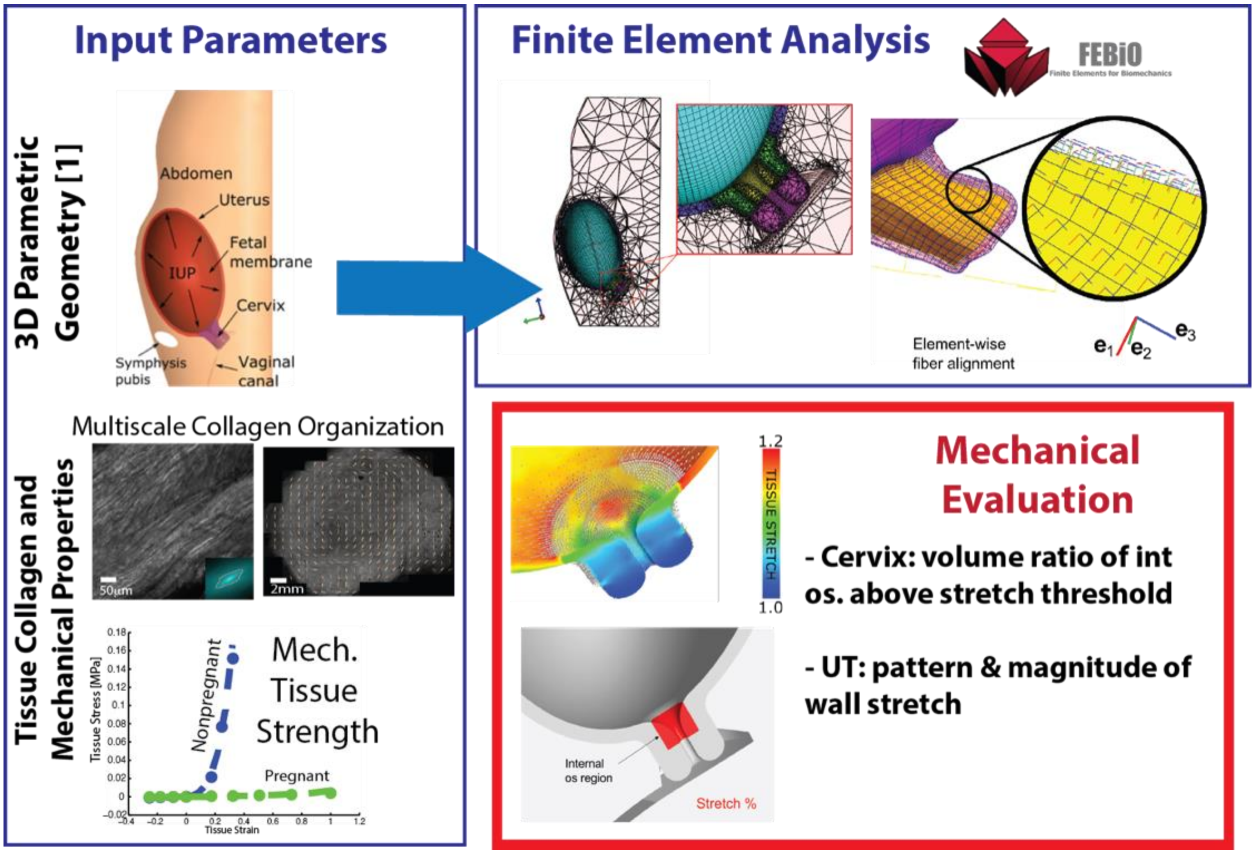

Figure 3-2: Finite element model created in FEBio 2.6.2, material parameters reported in [75,106] *and IUP reported in* [52].

3.1.1 Maternal anatomy data

Uterine diameters and wall thickness measurements were taken via x-ray time course data of 15 normal pregnant patients at four gestational timepoints: 20, 25, 30, and 35 weeks[10]. Longitudinal and transverse diameters of the uterus were assumed to be the same, and derived from Figure 3-3. For the uterine fiber orientation analysis, the 35-week patient geometry was used.

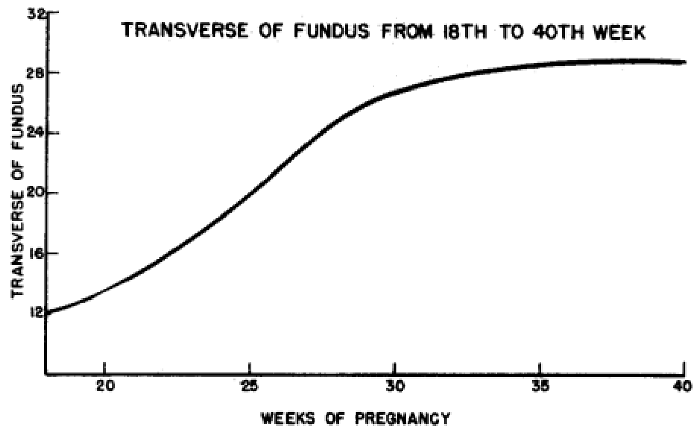

Figure 3-3: Transverse diameter of the uterus taken from a sagittal view x-ray[10]. *Values are plotted in centimeters and may be greater than real life due to x-ray distortion, though the distortion remains constant across patients so the relative values are accurate. Note that elongation diminishes after the 32nd week of gestation.*

The anterior-posterior diameter of the uterus was derived from the length/width ratio in Figure 3-4. The uterus rapidly elongates until the 32nd week of pregnancy, and then expands more in the anterior-posterior direction until term.

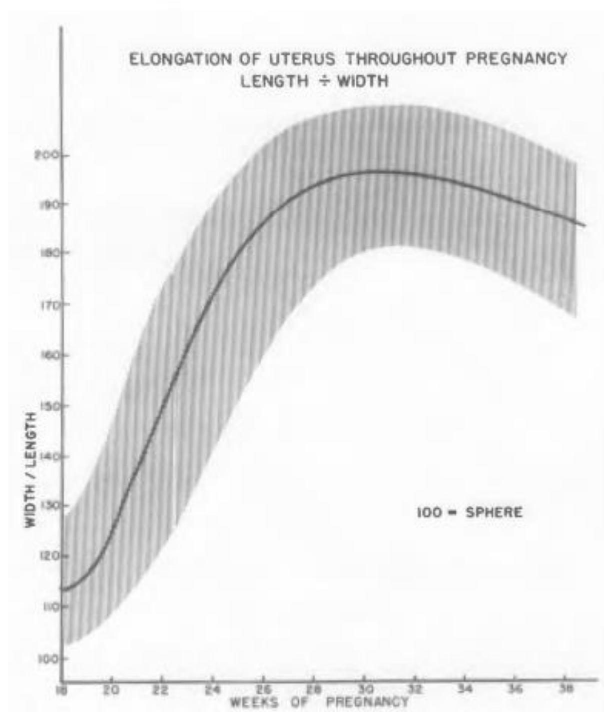

Figure 3-4: Elongation of the human uterus[10]. *Length is the greatest length of the uterus; width is the anterior-posterior diameter. As L/W increases in value, the curve rises and the uterus elongates. Note the rapid elongation until the 32nd week of gestation.*

Uterine wall thickness at each timepoint was measured from Figure 3-5. After the 20th week of gestation, the increase in uterine weight diminishes, and therefore the uterus begins to stretch and the myometrial thickness decreases.

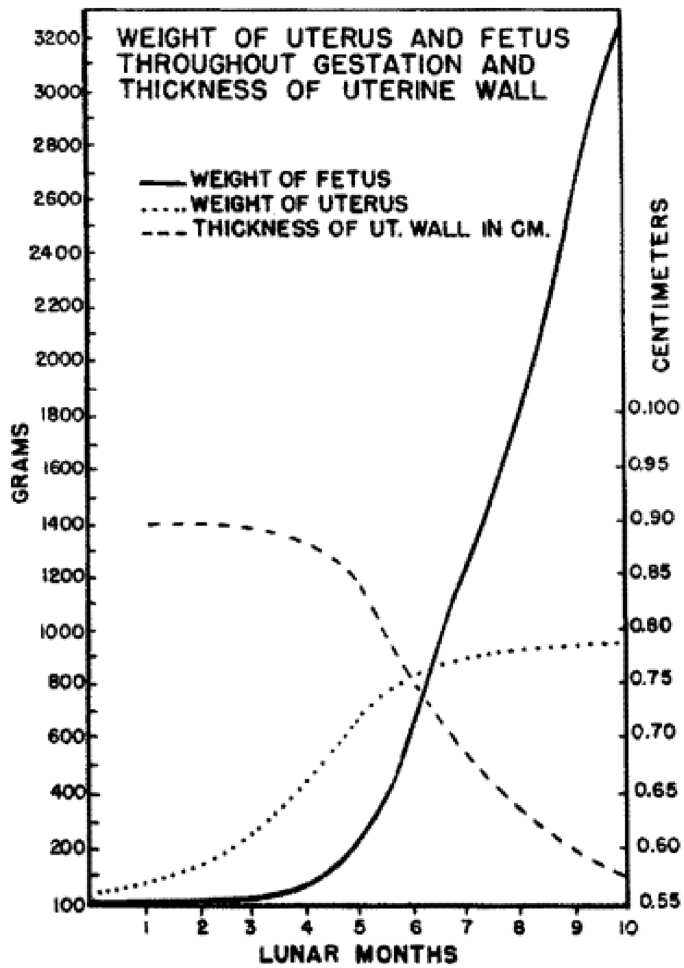

Figure 3-5: Weight of uterus, fetus, and uterine wall thickness throughout gestation[10]. *After the 20th week, uterine growth diminishes, and the myometrium, therefore, begins to thin.*

Cervical, fetal membrane, and abdominal parameters were kept constant to investigate the influence of uterine dimensions and fiber directionality only. Cervical dimensions used in each model were obtained from an ultrasound of one nulliparous 35-year-old patient at 25 weeks gestation[75].

3.1.2 CAD models of pregnancy

The maternal geometric parameters were converted into CAD geometries with a custom computer script (Trelis Pro 15.1.3, csimsoft LLC). Geometries of the uterus, cervix, fetal membranes, vaginal canal, and abdomen were created with Boolean addition and subtraction of geometric primitives (Figure 2-2). Dimensions for the model at each gestational timepoint are given in Table 3-1. For this initial model, the uterus was built by transforming two spherical shells into ellipsoids. The interior uterus was scaled to the diameters obtained from x-ray data. The outer shell was then scaled, translated, and rotated to accommodate uterine wall thickness in the anterior-posterior, superior-inferior, and left-right directions.

Gestational Age	Uterus Transverse Diameter [mm]	Uterus Anterior-Posterior Diameter [mm]	Uterus Longitudinal Diameter [mm]	Uterine Wall Thickness [mm]
20 weeks	135	123	135	8.4
25 weeks	190	124	190	7.3
30 weeks	260	143	260	6.6
35 weeks	280	155	280	6.1

Table 3-1: Uterine configurations built from lateral and anteroposterior soft tissue x-rays of 15 normal patients[10].

The cervix was built by creating a cylinder representing the diameter of the inner canal and subtracting that volume from a larger cylinder representing the outer cervical diameter and cervical length, detailed in Section 2.1.2. The resultant hollow cylinder was then moved and rotated according to posterior cervical offset and anterior cervical angle. The cylinder was rounded at its corners to match the anatomical rounding of the uterocervical junction and to replicate the roundness of the most exterior end of the cervix (i.e. external os). For the analyses represented here, the posterior cervical offset was kept at 0 and the anterior uterocervical angle at 90° in order to have the uterine fibers aligned evenly about the internal os.

For the purpose of tissue loading analysis, the cervix was then separated into three different regions: an upper portion, a lower portion, and the internal os region (Figure 2-2). First, the cylindrical representation of the cervix was cut by a plane normal to the external os at a fixed distance of 15 mm from the internal os. Second, the top portion of the cervix was then separated by a surface extended from a smaller cylinder with a diameter that was twice of the cervical inner canal. Lastly, the vaginal canal was built by fitting a spline to three vertices located at the outside edges of the external os and one vertex at the approximate location of the vaginal introitus and the fetal membrane was generated with uniform thickness based on the contours of the inner uterine wall.

3.1.3 Finite element mesh generation

All meshes were generated using the automatic and manual meshing tools in Trelis Pro (v15.1.3, csimsoft LLC). The fetal membranes were meshed with hexahedral elements, while all other volumes were meshed with tetrahedral elements. Mesh properties varied from model to model. The baseline model mesh is given in Table 3-2 and is shown in Figure 3-6. All volumes except the fetal membranes were meshed with linear tetrahedral elements. The fetal membranes were meshed as a single continuous layer of linear hexahedral elements with a thickness of 0.1mm.

	Total	Uterus	Membrane	Abdomen	Upper Cervix	Lower Cervix	Internal Os
Element Type	-	Tet	Hex	Tet	Tet	Tet	Tet
Element Count	347,295	137,239	9,600	104,258	51,848	27,487	16,863
Average Element Volume	-	8.04 mm^3	1.80 mm^3	266 mm^3	0.244 mm^3	0.343 mm^3	0.128 mm^3

Table 3-2: Mesh properties for 35-week model

The uterus and cervix were connected at the node level to one another, so their boundaries were shared and moved congruently. Where the uterus and cervix shared a boundary with the abdomen volume, those boundaries were also node-tied. The mesh density of the cervix was set to the finest setting by the inherent Trelis element density function, in order to yield the most accurate deformation results for our analysis.

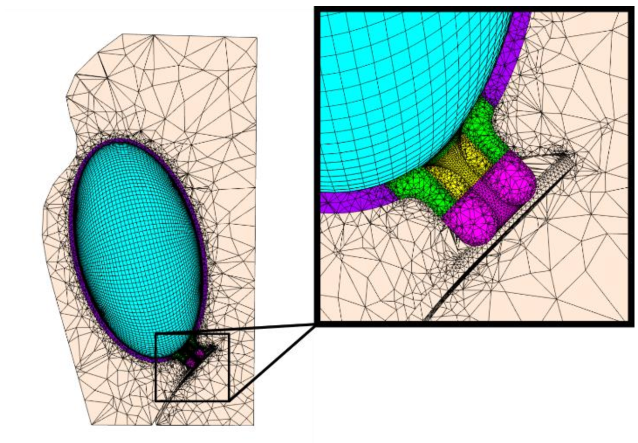

Figure 3-6: Sample mesh for 35-week geometry. The fetal membrane was meshed with hexahedral elements, while all other volumes were meshed with tetrahedral elements.

3.1.4 Material properties

The cervix and uterus materials were treated as continuously distributed fiber composites with a compressible neo-Hookean groundsubstance. This hyperelastic solid model was developed to describe the tension-compression nonlinearity in human[106] and mouse[107] cervical tissue. Considering not much is known about the multi-axial material behavior of these tissues during pregnancy, we chose to investigate the uterus and cervix at term pregnant (PG) tissue properties.

The total Helmholtz free energy density Ψ^{TOT} for the uterine and cervical materials were given by

$$\Psi^{TOT}(\boldsymbol{F}) = \Psi^{GS}(\boldsymbol{F}) + \Psi^{COL}(\boldsymbol{F})$$

Equation 3-1

Where $\boldsymbol{F}$ is the deformation gradient. The free energy density of the ground substance Ψ^{GS} is given by a standard isotropic, compressible neo-Hookean relation

$$\Psi^{GS} = \frac{\mu}{2}(\boldsymbol{I_1} - 3) - \mu \ln J + \frac{\lambda}{2}(\ln J)^2$$

Equation 3-2

where $I_1 = tr\boldsymbol{C}$ is the first invariant of the right Cauchy-Green tensor $\boldsymbol{C} = (\boldsymbol{F})^T\boldsymbol{F}$ and $J = \det \boldsymbol{F}$ is the Jacobian. μ and l are the standard lamé constants. These lamé constants combine to form the Young's modulus and Poisson's ratio of the ground substance $E^{GS} = \frac{\mu\left(3+\frac{2\mu}{\lambda}\right)}{1+\frac{\mu}{\lambda}}$ and $\nu^{GS} = \frac{1}{2\left(1+\frac{\mu}{\lambda}\right)}$, respectively. The strain energy density for the continuously distributed collagen fiber network is given by

$$\Psi^{COL} = \frac{1}{4\pi}\int_0^{2\pi}\int_0^{\pi} H(I_n - 1)\Psi_r^{fiber}(\boldsymbol{I_n}) \sin\phi \, d\phi d\theta$$

Equation 3-3

where the Heaviside step function H ensures fibers hold only tension, $[\theta, \phi]$ are the polar and azimuthal angles in a spherical coordinate system. $I_n = \boldsymbol{n_o} \cdot \boldsymbol{C} \cdot \boldsymbol{n_o}$ is the square of the fiber stretch, where $\boldsymbol{n_o} = \cos\theta \sin\phi \, \boldsymbol{e_1} + \sin\theta \sin\phi \, \boldsymbol{e_2} + \cos\phi \, \boldsymbol{e_3}$ in a local Cartesian basis $\{\boldsymbol{e_1}, \boldsymbol{e_2}, \boldsymbol{e_3}\}$. Ψ^{fiber} is the strain energy density of a collagen fiber bundle given by

$$\Psi^{fiber} = \frac{\xi}{\beta}(\boldsymbol{I_n} - 1)^{\beta}$$

Equation 3-4

where ξ represents the collagen fiber stiffness with units of stress and $\beta > 2$ is the dimensionless parameter that controls the shape of the fiber bundle stiffness curve (here, the fiber strain energy density is cast in a different form than the model presented for the human cervical tissue[82], hence direct comparison can be made by considering the $\frac{1}{\beta}$ prefactor here).

To focus this study on the model sensitivity to uterine parameters only and not on the cervical tissue ultrastructure, groundsubstance, or time-dependent properties, we made simplifying adjustments. Cervical material model fits were conducted on the material behavior after the transient force relaxation response died away. In this present study, we used a randomly distributed collagen fiber network as opposed to a preferentially-aligned collagen fiber network as presented in [106]. Cervical material properties used in this study (Table 3-3) represent collagen fiber parameters fit to term pregnant human uniaxial tension-compression data reported in [106,108,109]. Uterine material properties represent a material model fit to passive, term pregnant human uniaxial tension data reported in [110]. Fibers in both the uterus and cervix are randomly distributed. They rotate and stretch in the direction of principal stress.

To explore the effects of modeling different fiber distributions in the uterus, we chose three model configurations: random or spherical fiber distribution (SFD), preferentially aligned ellipsoidal fiber distribution (EFD) in the circumferential direction, and preferentially aligned EFD in the longitudinal direction. The preferentially aligned fiber models have fibers directed along the local $\boldsymbol{e_1}$ direction of each element of the uterus in its reference configuration, one in the circumferential direction around the internal os, and the other in the longitudinal direction from the fundus to the cervix. In the models investigating the effect of uterine size and shape, a randomly distributed fiber network is modeled similarly to the cervical material model.

Tissue Description	E^{GS} [kPa]	ν^{GS}	β	ξ [kPa]
Uterus	2	0.3	2.71	19
Cervix	0.65	0.3	2	1.71

Table 3-3: Uterine and cervical tissue variables taken from material fits to experimental data. These values are implemented in a continuous fiber distribution material model used in FEBio 2.6.2.

The outer abdomen was treated as a soft nearly incompressible neo-Hookean material with a modulus of 5 kPa. An incompressible Ogden material model based on equibiaxial tensile loading of human amnion[113] was employed for the fetal membrane layer material properties (Table 3-4), where the particular form of the Ogden strain energy density, as defined in FEBio, was given by,

$$\Psi^{FM} = \sum_{i=1}^{3} \frac{c_i}{m_i^2} \left(\lambda_1^{m_i} + \lambda_2^{m_i} + \lambda_3^{m_i} - 3\right).$$

Equation 3-5

Tissue Description	c1 [MPa]	c2 [MPa]	c3 [MPa]	m1	m2	m3
FM	0.859	0.004	0.756	27.21	27.21	-16.64

Table 3-4: Fetal membranes (FM) material properties described by an Ogden material model in Equation 4-5.

3.1.5 Boundary conditions and loading

Boundary conditions were applied as described in Figure 3-7. The abdomen was fixed in the x, y, and z directions along its entire outer surface. The fetal membranes were prescribed a no-slip, tied contact along its outer surface (cyan in Figure 3-7) to the inner surface of the uterus (purple) and to the inner surface of the upper cervix region (green). A frictionless sliding contact condition was assigned between the outer surface of the fetal membranes (cyan) and the internal os region (yellow).

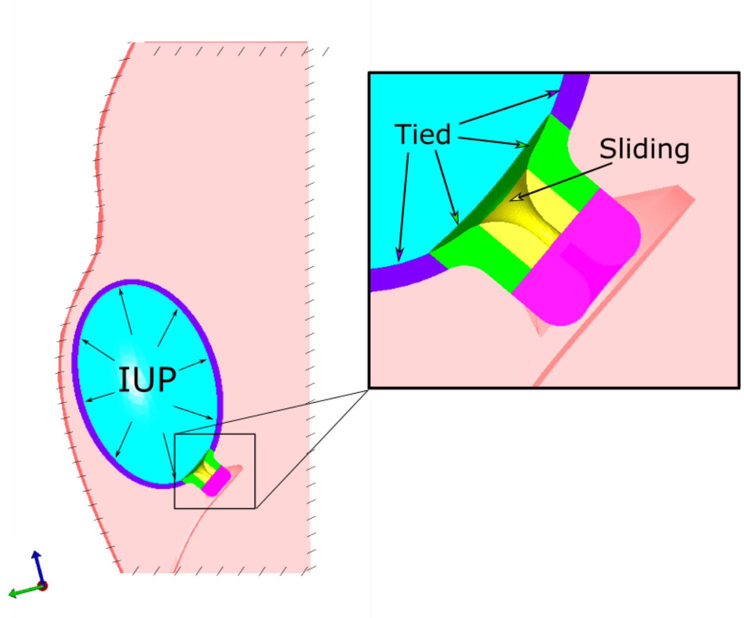

Figure 3-7: Boundary and loading conditions. The abdomen was fixed along its outside in x, y, and z directions (dashed lines in figure). Uniform intrauterine pressure (IUP) was applied on the inner surface of FM. Tied contact was applied between FM (cyan) and the uterine wall (purple) and between FM and upper cervix (green). Sliding contact was applied between FM and cervix internal os region (yellow).

Pressure was applied to the inner surface of the fetal membranes to represent the intrauterine pressure (IUP). Previous investigations by our group have shown that increasing IUP to contraction magnitude allows for easier evaluation of parameter sensitivity[75]. Therefore, the IUP in this study is applied at the value of a labor contraction (8.67 kPa)[114].

3.1.6 Finite element analysis and evaluation

FE analyses were performed in FEBio 2.6.2 (http://www.febio.org.). Stretch data was plotted as a function of IUP in PostView (PostView 1.10.3), FEBio's post-processor for visualization and analysis. These data were then imported into MATLAB (MATLAB R2014a) for further post analysis. To describe the deformation of the cervix, the extent of cervical 1st principal right stretch was evaluated as a percentage of the cervical internal os volume (Figure 3-7) above a

1.05 stretch threshold. The right stretch in this context is the symmetric tensor $\boldsymbol{U}$ in the polar decomposition of the deformation gradient $\boldsymbol{F} = \boldsymbol{RU}$.

3.1.7 Sensitivity to uterine parameters

Uterine fiber orientation was kept constant while each gestation timepoint was modeled in order to individually assess the impact of uterine size on tissue stretch. Similarly, in order to investigate the effect of tissue fiber orientation on stretch, uterine geometry was held constant and fibers were randomly, circumferentially, and longitudinally distributed. Stretch magnitude and distribution were compared at a contraction-level IUP of 8.67 kPa to illuminate patterns.

3.2 Results

3.2.1 Sensitivity to uterine size and shape

There are visible differences in the magnitude and pattern of tissue stretch at the various gestational timepoints (Figure 3-8). According to the x-ray data, uterine diameters increase and uterine wall thickness decrease as gestational age increases. As a result, uterine and cervical stretch increase overall with gestation. The most drastic change in the loading pattern and magnitude in the uterus and cervix is between 20 and 25 weeks. The volume ratio of the internal cervical os stretch above a 1.05 threshold jumped from 8.93% to 51.1% (Figure 3-8 A&B). After 25 weeks of gestation, as the uterus elongates the stretch pattern remains the same and the volume percent of the cervical os loaded above 1.05 stretch slightly increases from 51.1% to 61.3% (Figure 3-8 B&D).

As the uterus elongates, uterine stretch appears throughout the entire tissue but is the largest at the anterior and posterior lower uterine segment. This excessive stretch in the uterus also pulls the cervix open, seen by the increasing stretch at the cervical internal os.

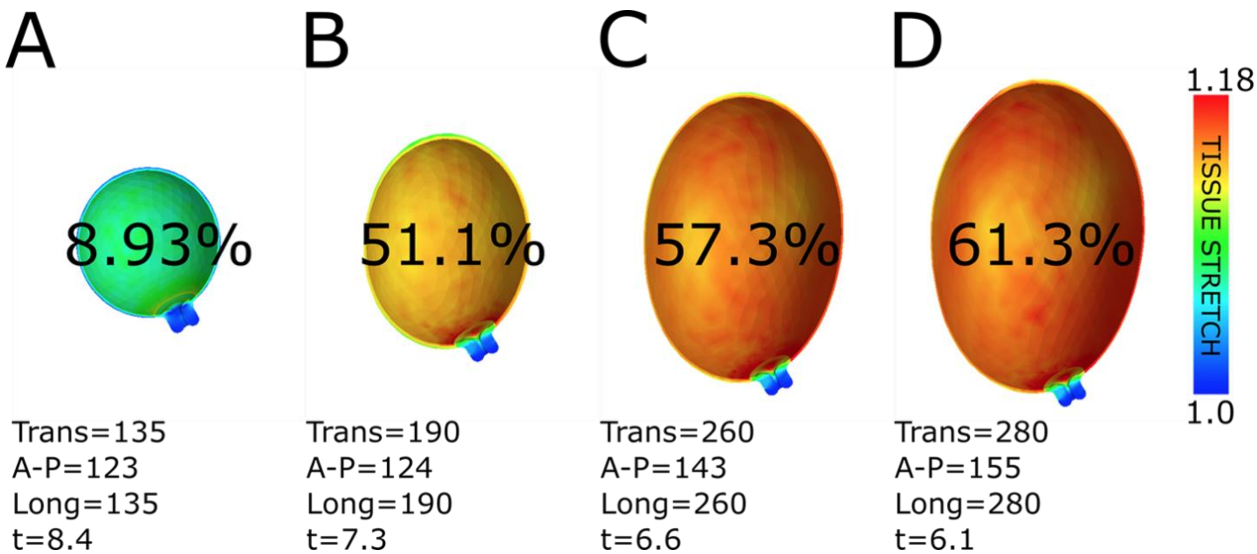

Figure 3-8: Uterine and cervical stretch at IUP = 8.6kPa using reference geometries based on A) 20 weeks, B) 25 weeks, C) 30 weeks, and D) 35 weeks x-ray data[10]*. Cervical loading calculated above 1.05 stretch. Trans=transverse uterine diameter, A-P=anterior-posterior uterine diameter, Long=longitudinal uterine diameter, t=uterine wall thickness. Dimensions are in mm. Abdomen and membranes are removed for clarity.*

As shown in Figure 3-9, uterine stretch is greater at the internal surface of the uterine wall, where the intrauterine pressure is applied in the model. The inset shows higher tissue stretch in the lower uterine segment on the inner surface of the uterus and gradually decreases toward the external uterine surface.

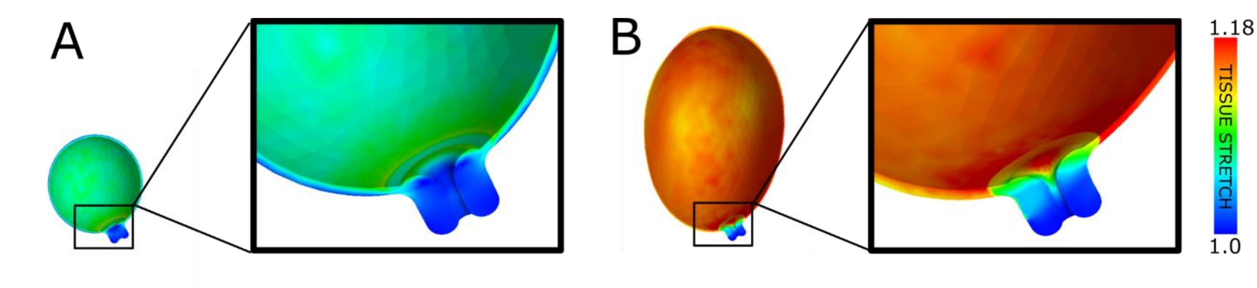

Figure 3-9: Uterine and cervical stretch at IUP = 8.6kPa for a A) 20 week and B) 35-week uterine geometry exposed to contraction-magnitude intrauterine pressure. The inset zooms on the lower uterine segment to show a stretch gradient in the uterine wall. Principal stretch is greatest at the inner uterine wall and decreases moving toward the outer wall.

3.2.2 Sensitivity to uterine material models

Comparisons between material models are given in Figure 3-10 for the 35-week uterine geometry. Moving from a random SFD model to a circumferentially-weighted EFD model does not significantly change the overall magnitude or direction of uterine stretch in the lower uterine segment. The SFD model has large stretch concentrations in the left and right sides of the uterus, whereas the circumferential EFD model has more stretch in the posterior uterus. Moving from the SFD model to a longitudinally-weighted EFD model does not significantly change the resulting stretch predictions. In each material model, the cervix is pulled up radially from the uterus at the anterior and posterior lower uterine segment, but much greater from the posterior side.

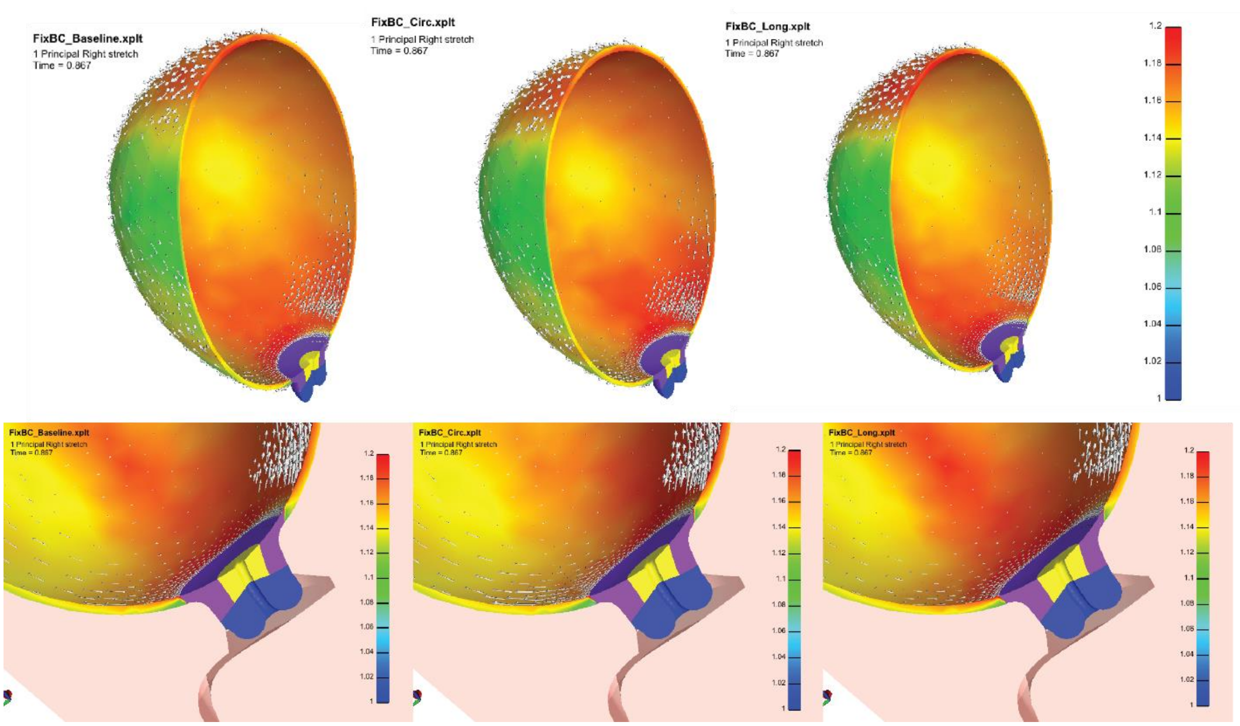

Figure 3-10: Uterine stretch at IUP = 8.67kPa for a A) randomly oriented uterine fiber material B) preferentially-aligned fibers in the circumferential and C) longitudinal direction. The inset zooms on the lower uterine segment to show a stretch gradient in the uterine wall.

3.3 Discussion

This work further develops a method to generate a patient-specific finite element model of the uterus, cervix, fetal membrane, and surrounding anatomy derived from maternal anatomy. We modeled a typical normal patient at four gestational timepoints: 20, 25, 30, and 35 weeks. We also investigated a baseline model of a 35-week pregnant patient with random, circumferential, and longitudinal fiber network distributions. With this computer model, and basing engineering assumptions on previously published data, we assess tissue stretch at contraction-magnitude intrauterine pressure (IUP).

Results indicated that overall uterine shape and ellipticity dominates the stress and stretch patterns generated in the uterus and cervix. As the uterus becomes more elliptical, the overall amount of cervical stretch increases at the internal os. This uterine shape change interestingly happens within the gestational timeframe that the cervix softens, according to longitudinal in vivo aspiration data[146].

Previous studies have shown the anisotropy of uterine tissue determined by collagen fiber orientation and muscle fiber orientation[147]. Our results indicate that the randomly orientated and preferentially-aligned ellipsoidal fiber models predict similar outcomes. The introduction of preferred directionality does not result in a significantly lower stretch in the uterus. This aligns with our group's previous work modeling cervical material fiber orientation[74].

3.3.1 Limitations

Mid-gestation uterine shape measurement and mechanical testing and architecture data on the pregnant human uterus are lacking. Hence, the methods and results here have a set of limitations. First, as gestation progresses, the IUP increases with the growth of the baby and the volume of the amniotic fluid. It is unknown how this increase in IUP is coupled with geometric changes, and how these changes may influence the mechanical environment. This applied force in any *in vivo* measurement of the uterus shows its loaded configuration, instead of its reference state. It is not possible to measure the uterine reference state at a given point in gestation because it continues to grow and stretch simultaneously. In this study, we begin with the loaded configuration and apply an additional load. This additional load, which is the magnitude of a contraction, is one order of magnitude higher than gestation-matched IUP and therefore would still cause large deformations similar to the model *in vivo*. Similarly, this contraction-magnitude IUP is much larger than gravity and therefore we ignore the effects of hydrostatic pressure. Even in the longest uterus measured in our clinical studies, the hydrostatic pressure due to gravity is less than 2.85 kPa, and therefore the magnitude of a contraction is more than three times that. In future studies, we will use 18 weeks as a reference state of the uterus because this is when the fetal membranes fuse together and are completely fused with the decidua[148]. Though tissue growth is not implemented in this model, we will use models like this to determine the areas that experience the greatest stress, and therefore may be subject to mechanosensitive growth.

As another limitation, the material properties of the tissues evolve during pregnancy, whereas this study assumed the tissues remained in their pregnant state. Doctor input expressed that pregnant tissue is softer to the touch than nonpregnant tissue, and therefore it would be more suitable to use term material properties rather than nonpregnant. Additionally, the maternal anatomy is idealized as simple geometric shapes, where the bends and folds in the uterine wall are neglected. These folds are difficult to capture via ultrasound, and comparisons to MRI models will be made in the future to determine their importance.

Our group is currently measuring uterine fiber architecture of pregnant tissue, but those results were not implemented in this model. The current uterine material model describes the fiber architecture as a distributed fiber network, as opposed to discrete fiber families. Implementation of discrete fiber orientation will have a larger anisotropic effect on material behavior. Future studies will directly inform FE models with experimental architecture data.

3.4 Conclusions

This study represents a first attempt to model the pregnant abdomen at various timepoints during the course of gestation. Understandably, obtaining longitudinal data on pregnant humans is difficult. Hence, we utilize an existing time-course dataset to inform our FE models of pregnancy at gestational ages of 20 to 35 weeks. As we discovered in our previous work, various material, anatomical, and contact factors influence the loading of the soft tissues that surround the fetus[149,150]. We chose to analyze uterine geometries and material models. As we initially hypothesized, increased ellipticity of the uterus and a decrease in uterine wall thickness increases the stretch in the uterus and the cervix. Our results show that uterine ellipticity has the largest impact on the mechanical stretch state within the uterus. In contrast to our initial hypothesis on tissue fiber architecture, uterine fiber orientation had little impact on tissue stretch.

The results from this model allow for simplification in future studies to assume randomly distributed collagen fibers in the uterus, as preferentially-aligned fibers do not influence tissue stretch. In future studies, we aim to capture a reference geometry of the uterus to better model the kinematics of the loaded configuration. Our goal is that our model will serve as a preliminary platform for the development of sPTB diagnostic tools and procedures. In addition, it serves as a first step in modeling the uterine tissue growth and remodeling in pregnancy.

One major finding in the optimization of our finite element analyses is the need for implementing local axes if we plan to include fiber directionality. In this study, we needed to use a PCO of 0 and an AUCA of 90 in order to have the uterine fibers revolve around the internal os. In future studies, it would be ideal to be able to rotate the uterine material axes.

4 Ultrasound-derived finite element analysis of pregnancy: sensitivity to fetal membrane contact and material

Previous computer modeling of the pregnant abdomen reveals that the mechanical load on the cervix is influenced by maternal anatomical features and the material properties of the uterus, FM, and cervix[74]. The extent to which each of these structural factors influences tissue loading remains to be determined. This study focuses specifically on the effects of fetal membrane mechanics on uterine and cervical tissue stretch. The fetal membranes consist of the collagen-rich, load-bearing amnion and the cellular chorion (Figure 4-1) [34,151].

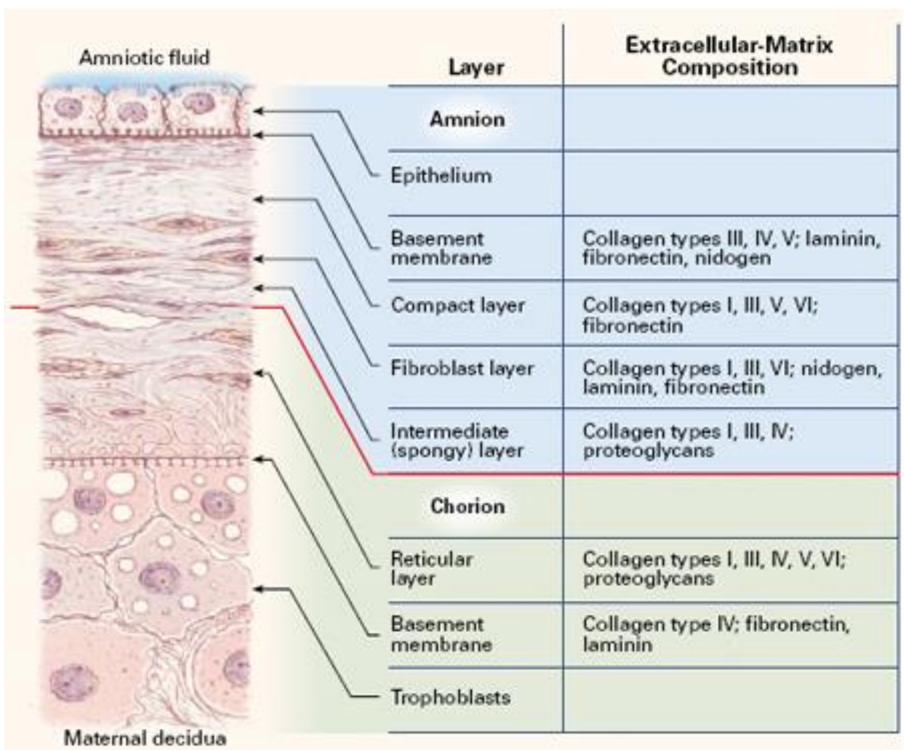

Figure 4-1: Diagram of the fetal membrane layers and their respective sublayers. The amnion is the load-bearing layer closest to the fetus, and the chorion adheres to the maternal decidua[152].

The integrity of both layers is essential for the maintenance of pregnancy, where its compliance is necessary to accommodate fetal growth. Yet, membrane rupture and fracture properties are required for normal term delivery[153]. Evidence suggests that the FM grows until the 2nd trimester[154], then stretches over the rest of pregnancy to accommodate the enlarging amniotic cavity. Evidence also suggests that the mechanical properties of the amnion, the load-bearing layer, at term is highly nonlinear[145]. The material properties of the membrane, the extent to which it is stretched at any given gestational age, and corresponding stresses, particularly over the internal os, are still unknown.

The objective of this study is to investigate the effects of fetal membrane stiffness and adhesion on tissue mechanics of the uterus, cervix, and fetal membranes. Anatomically, in normal pregnancy, the outer layer of the fetal membranes is adhered fully to the uterine wall and the upper cervix throughout gestation, and detaches at the onset of labor and begins to prolapse into the vaginal canal. In late pregnancy, if a doctor wants to accelerate the onset of labor, they may manually strip a patient's membranes from the cervix and lower uterine segment in order to release prostaglandins. We hypothesize this adhesion removal may also transfer some of the fetal load from the membrane and uterus to the internal os. Additionally, an important note related to adhesion that cannot be represented in our models is its impact on microbial invasion of the amniotic cavity (MIAC). The frequency of MIAC among women with cervical insufficiency is as high as 51%[155]. If the fetal membranes are not adhered to the inner uterine wall, this could allow for infection to travel along the decidual lining to the placenta, which increases the likelihood of preterm birth.

The output parameters are the volume fraction a designated internal os region above a 1.1 stretch threshold. Literature suggests that large tissue stretches can lead to tissue remodeling[156]. Another output parameter is membrane stress, as previous studies have investigated the stress at which membrane rupture occurs[93]. Here we quantify the amount of cervical stretch as a function of FM material properties using a parametric finite element model of pregnancy[75].

4.1 Methods

4.1.1 Maternal anatomy data

Uterine diameters and wall thickness measurements were taken via x-ray data from pregnant patients at 35 weeks gestation (Table 4-1)[10]. Longitudinal and transverse diameters of the uterus were assumed to be the same, and derived from Figure 3-3. Anterior-posterior diameter of the uterus was derived from the length/width ratio in Figure 3-4. The uterus rapidly elongates until the 32nd week of pregnancy, and then expands more in the anterior-posterior direction until term. Uterine wall thickness at each timepoint was measured from Figure 3-5. After the 20th week of gestation, the increase in uterine weight diminishes, and therefore the uterus begins to stretch and the myometrial thickness decreases.

Cervical, uterine, and abdominal parameters were kept constant to investigate the influence of membrane stiffness and adhesion only. Cervical dimensions used in each model were obtained from an ultrasound of one nulliparous 35-year-old patient at 25 weeks gestation[75].

4.1.2 CAD models of pregnancy

The maternal geometric parameters were converted into CAD geometries with a custom computer script (Trelis Pro 15.1.3, csimsoft LLC). Geometries of the uterus, cervix, fetal membranes, vaginal canal, and abdomen were created with Boolean addition and subtraction of geometric primitives (Figure 2-2). Dimensions for the model were taken from a 35-week pregnant patient given in Table 4-1. For this initial model, the uterus was built by transforming two spherical shells into ellipsoids. The interior uterus was scaled to the diameters obtained from x-ray time course data of 15 normal patients. The outer shell was then scaled, translated, and rotated to accommodate differences in uterine wall thickness in the anterior-posterior, superior-inferior, and left-right directions.

Gestational Age	Uterus Transverse Diameter [mm]	Uterus Anterior-Posterior Diameter [mm]	Uterus Longitudinal Diameter [mm]	Uterine Wall Thickness [mm]
35 weeks	280	155	280	6.1

Table 4-1: Uterine configurations built from lateral and anteroposterior soft tissue x-rays of 15 normal patients[10].

The cervix was built by creating a cylinder representing the diameter of the inner canal and subtracting that volume from a larger cylinder representing the outer cervical diameter and cervical length, detailed in Section 2.1.2. The resultant hollow cylinder was then moved and rotated according to posterior cervical offset and anterior cervical angle. The cylinder was rounded at its corners to match the anatomical rounding of the uterocervical junction and to replicate the roundness of the most exterior end of the cervix (i.e. external os).

For the purpose of tissue loading analysis, the cervix was then separated into three different regions: an upper portion, a lower portion, and the internal os region (Figure 2-2). First, the cylindrical representation of the cervix was cut by a plane normal to the external os at a fixed distance of 15 mm from the internal os. Second, the top portion of the cervix was then separated by a surface extended from a smaller cylinder with a diameter that was twice of the cervical inner canal. Lastly, the vaginal canal was built by fitting a spline to three vertices located at the outside edges of the external os and one vertex at the approximate location of the vaginal introitus and the fetal membrane was generated with uniform thickness based on the contours of the inner uterine wall.

4.1.3 Finite element mesh generation

All meshes were generated using the automatic and manual meshing tools in Trelis Pro (v15.1.3, csimsoft LLC). The fetal membranes were meshed with hexahedral elements, while all other volumes were meshed with tetrahedral elements. Mesh properties varied from model to model. The baseline model mesh is given in Table 4-2, and is shown in Figure 4-2. All volumes except the fetal membranes were meshed with linear tetrahedral elements. The fetal membranes were meshed as a single continuous layer of linear hexahedral elements with a thickness of 0.1mm.

	Total	Uterus	Membrane	Abdomen	Upper Cervix	Lower Cervix	Internal Os
Element Type	-	Tet	Hex	Tet	Tet	Tet	Tet
Element Count	206,456	44,515	9,600	52,686	54,983	27,212	17,460
Average Element Volume	-	22.6 mm^3	2.02 mm^3	1860 mm^3	0.211 mm^3	0.347 mm^3	0.135 mm^3

Table 4-2: Mesh properties for the baseline model

The uterus and cervix were connected at the node level to one another, so their boundaries were shared and moved congruently. Where the uterus and cervix shared a boundary with the abdomen volume, those boundaries were also node-tied. The mesh density of the cervix was set to the finest setting by the inherent Trelis element density function, in order to yield the most accurate deformation results for our analysis.

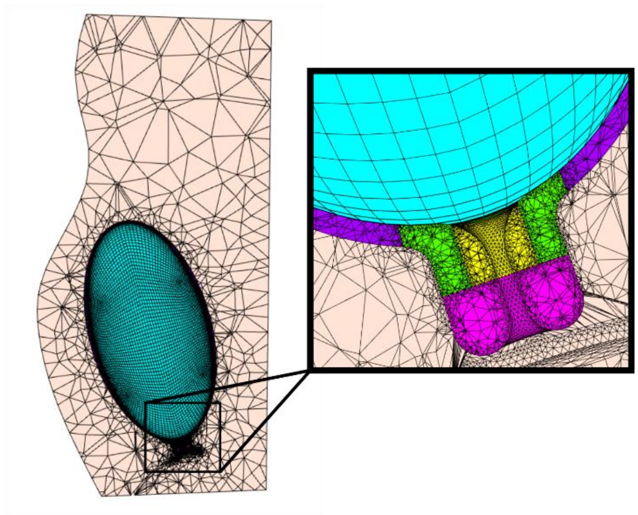

Figure 4-2: Sample mesh for baseline geometry. The fetal membrane was meshed with hexahedral elements, while all other volumes were meshed with tetrahedral elements.

4.1.4 Material properties

The cervix and uterus materials were treated as continuously distributed fiber composites with a compressible neo-Hookean groundsubstance. This hyperelastic solid model was developed to describe the tension-compression nonlinearity in human[106] and mouse[107] cervical tissue. Considering not much is known about the multi-axial material behavior of these tissues during pregnancy, we chose to investigate the uterus and cervix at term pregnant (PG) tissue properties.

The total Helmholtz free energy density Ψ^{TOT} for the uterine and cervical materials were given by

$$\Psi^{TOT}(\boldsymbol{F}) = \Psi^{GS}(\boldsymbol{F}) + \Psi^{COL}(\boldsymbol{F})$$

Equation 4-1

Where $\boldsymbol{F}$ is the deformation gradient. The free energy density of the ground substance Ψ^{GS} is given by a standard isotropic, compressible neo-Hookean relation

$$\Psi^{GS} = \frac{\mu}{2}(\boldsymbol{I_1} - 3) - \mu \ln J + \frac{\lambda}{2}(\ln J)^2$$

Equation 4-2

where $I_1 = tr\boldsymbol{C}$ is the first invariant of the right Cauchy-Green tensor $\boldsymbol{C} = (\boldsymbol{F})^T\boldsymbol{F}$ and $J = \det \boldsymbol{F}$ is the Jacobian. μ and l are the standard lamé constants. These lamé constants combine to form the Young's modulus and Poisson's ratio of the ground substance $E^{GS} = \frac{\mu\left(3+\frac{2\mu}{\lambda}\right)}{1+\frac{\mu}{\lambda}}$ and $\nu^{GS} = \frac{1}{2\left(1+\frac{\mu}{\lambda}\right)}$, respectively. The strain energy density for the continuously distributed collagen fiber network is given by

$$\Psi^{COL} = \frac{1}{4\pi}\int_0^{2\pi}\int_0^{pi} H(I_n - 1)\Psi_r^{fiber}(\boldsymbol{I_n}) \sin\phi \, d\phi d\theta$$

Equation 4-3

where the Heaviside step function H ensures fibers hold only tension, $[\theta, \phi]$ are the polar and azimuthal angles in a spherical coordinate system. $I_n = \boldsymbol{n_o} \cdot \boldsymbol{C} \cdot \boldsymbol{n_o}$ is the square of the fiber stretch, where $\boldsymbol{n_o} = \cos\theta \sin\phi \, \boldsymbol{e_1} + \sin\theta \sin\phi \, \boldsymbol{e_2} + \cos\phi \, \boldsymbol{e_3}$ in a local Cartesian basis $\{\boldsymbol{e_1}, \boldsymbol{e_2}, \boldsymbol{e_3}\}$. Ψ^{fiber} is the strain energy density of a collagen fiber bundle given by

$$\Psi^{fiber} = \frac{\xi}{\beta}(\boldsymbol{I_n} - 1)^{\beta}$$

Equation 4-4

where ξ represents the collagen fiber stiffness with units of stress and $\beta > 2$ is the dimensionless parameter that controls the shape of the fiber bundle stiffness curve (here, the fiber strain energy density is cast in a different form than the model presented for the human cervical tissue[82], hence direct comparison can be made by considering the $\frac{1}{\beta}$ prefactor here).

To focus this study on the model sensitivity to membrane stiffness and adhesion parameters and not on the cervical or uterine collagen ultrastructure, groundsubstance, or time-dependent properties, we made simplifying adjustments. Both material model fits were conducted on the material behavior after the transient force relaxation response died away. In this present study, we used a randomly distributed collagen fiber network as opposed to a preferentially-aligned collagen fiber network as presented in [106]. Cervical material properties used in this study (Table 4-3) represent collagen fiber parameters fit to the nonpregnant and term pregnant human uniaxial tension-compression data reported in [106,108,109], with the ground substance material properties kept constant. Uterine material properties represent a material model fit to passive, nonpregnant and term pregnant human uniaxial tension data reported in [110]. Fibers in both the uterus and cervix are randomly distributed. They rotate and stretch in the direction of principal stress. Previous work compared the difference between preferential and randomly distributed fiber directionality in an initial finite element model of pregnancy and found a negligible difference between the two scenarios[74]. The outer abdomen was treated as a soft nearly incompressible neo-Hookean material with a modulus of 5 kPa.

Tissue Description	E^{GS} [kPa]	ν^{GS}	β	ξ [kPa]
Uterus	2	0.3	2.71	19
Cervix	0.65	0.3	2	1.71

Table 4-3: Uterine and cervical tissue variables taken from material fits to experimental data. These values are implemented in a continuous fiber distribution material model used in FEBio 2.6.2.

An incompressible Ogden material model based on equibiaxial tensile loading of human amnion[113] was employed for the fetal membrane layer material properties. Considering we do not know material properties for the amnion at 25 weeks, we chose to investigate the influence of increased membrane stiffness at 5- and 10-times measured term properties (Table 4-4). The particular form of the Ogden strain energy density, as defined in FEBio, was given by

$$\Psi^{FM} = \sum_{i=1}^{3} \frac{c_i}{m_i^2}\left(\lambda_1^{m_i} + \lambda_2^{m_i} + \lambda_3^{m_i} - 3\right).$$

Equation 4-5

Tissue Description	c1 [MPa]	c2 [MPa]	c3 [MPa]	m1	m2	m3
FM - baseline	0.859	0.004	0.756	27.21	27.21	-16.64
FM – 5x stiffness	4.294	0.018	3.782	27.21	27.21	-16.64
FM – 10x stiffness	8.587	0.0368	7.564	27.21	27.21	-16.64

Table 4-4: Fetal membranes (FM) material properties described by an Ogden material model in Equation 4-5.

4.1.5 Boundary conditions and loading

Boundary conditions were applied as described in Figure 4-3. The abdomen was fixed in the x, y, and z directions on only the side that represents the patient's posterior, to allow the anterior "stomach" to grow along with the expanding uterus, as expected *in vivo*. In the baseline model, the fetal membranes were prescribed a no-slip, tied contact along its outer surface (cyan in Figure 4-3) to the inner surface of the uterus (purple) and to the inner surface of the upper cervix region (green). A frictionless sliding contact condition was assigned between the outer surface of the fetal membranes (cyan) and the internal os region (yellow).

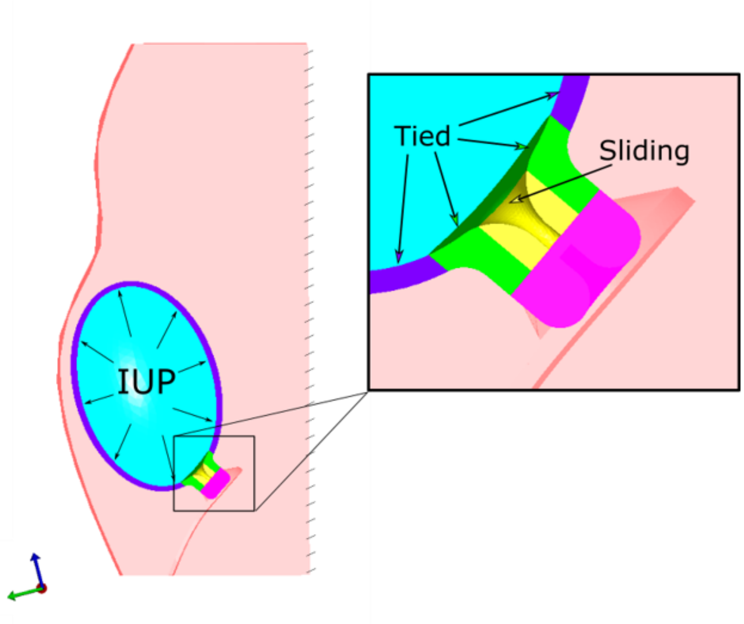

Figure 4-3: Boundary and loading conditions. The posterior side of the abdomen was fixed in x, y, and z directions (dashed lines in figure). Uniform intrauterine pressure (IUP) was applied on the inner surface of FM. Tied contact was applied between FM (cyan) and the uterine wall (purple) and between FM and upper cervix (green). Sliding contact was applied between FM and cervix internal os region (yellow).

Pressure was applied to the inner surface of the fetal membranes to represent the intrauterine pressure (IUP). Previous investigations by our group have shown that increasing IUP to contraction magnitude allows for easier evaluation of parameter sensitivity[75]. Therefore, the IUP in this study is applied to the value of a labor contraction (8.67 kPa)[114].

4.1.6 Finite element analysis and evaluation

FE analyses were performed in FEBio 2.6.2 (http://www.febio.org.). Stress and stretch data were plotted as a function of IUP in PostView (PostView 1.10.3), FEBio's post-processor for visualization and analysis. These data were then imported into MATLAB (MATLAB R2014a) for further post analysis. To describe the deformation of the cervix, the extent of cervical 1st principal right stretch was evaluated as a percentage of the cervical internal os volume (Figure 4-3) above a 1.1 stretch threshold. The right stretch in this context is the symmetric tensor $\boldsymbol{U}$ in the polar decomposition of the deformation gradient $\boldsymbol{F} = \boldsymbol{RU}$.

4.1.7 Sensitivity to membrane parameters

After the evaluation of the baseline model, membrane stiffness and adhesion to the uterine wall were scaled individually in order to assess each variable's impact on cervical internal os stretch. As the experimental values for fetal membrane stiffness were measured at term, we increased the stiffness by 5 and 10 times under the assumption that the membranes are stiffer at earlier timepoints in gestation, or may be stiffened by an inflammatory response in high-risk patients[157]. The membrane adhesion was varied from fully adhered to the uterine wall and top of the cervix, to fully detached and allowed to slide freely along the inner uterine wall. Stretch magnitude and distribution were compared at a contraction-level IUP of 8.67 kPa to illuminate patterns.

4.2 Results

4.2.1 Sensitivity to membrane adhesion

Removing adhesion of the fetal membranes to the uterine wall results in greater cervical stress at the internal os, and the uterine stress is moved anteriorly and inferiorly toward the lower uterine segment and cervix (Figure 4-4). When the membrane fully adheres to the uterine wall, the majority of uterine stress is at the middle level of the uterus and the lower uterine segment is loaded much less. In each scenario, there is greater stress at the inner uterine wall where the membrane is in contact with the uterus.

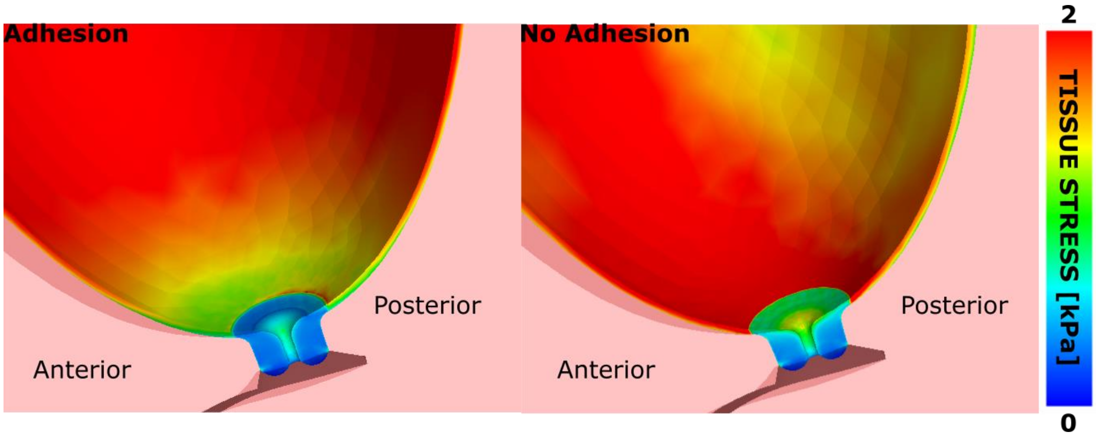

Figure 4-4: Fetal membranes losing adherence results in increased cervical stress, and moves uterine stress anteriorly. Models show 1st principal stress in the uterus and cervix. The membrane is removed for clarity.

Lack of fetal membrane adhesion also results in greater cervical stretch at the internal os. A fully detached membrane results in a 134% increase in the volume fraction of tissue over 1.20 stretch from the fully adhered scenario (Figure 4-5). Uterine stretch undergoes the same pattern as uterine stress as seen previously. When the membrane fully adheres, the uterine stretch occurs mostly at the mid-uterus in all directions. Once the membrane adhesion is removed, the stretch in the uterus moves anteriorly and toward the lower uterine segment.

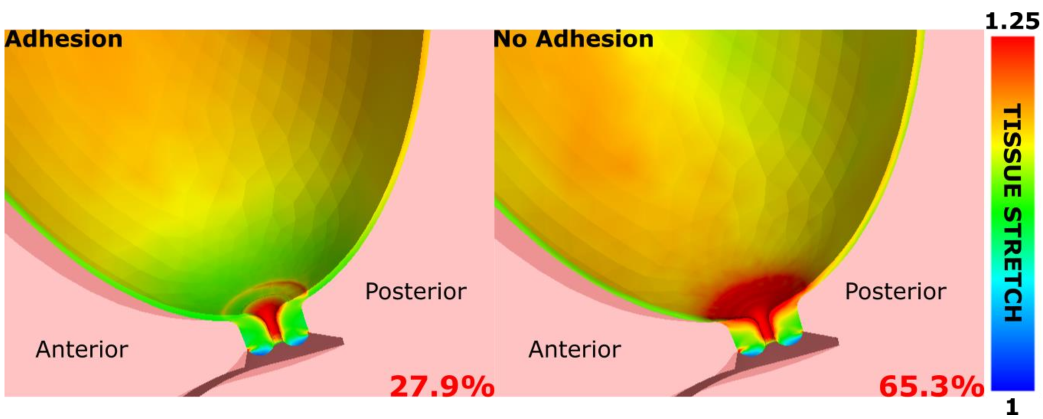

Figure 4-5: Fetal membranes losing adherence results in an increased cervical stretch, and moves uterine stretch anteriorly. Models show 1st principal stretch in the uterus and cervix. The membrane is removed for clarity. Percentages show the volume fraction of the cervical internal os region above a 1.2 stretch threshold.

Similarly, both 2nd and 3rd principal stretches increase at the internal os as the membrane loses adhesion (Figure 4-6).

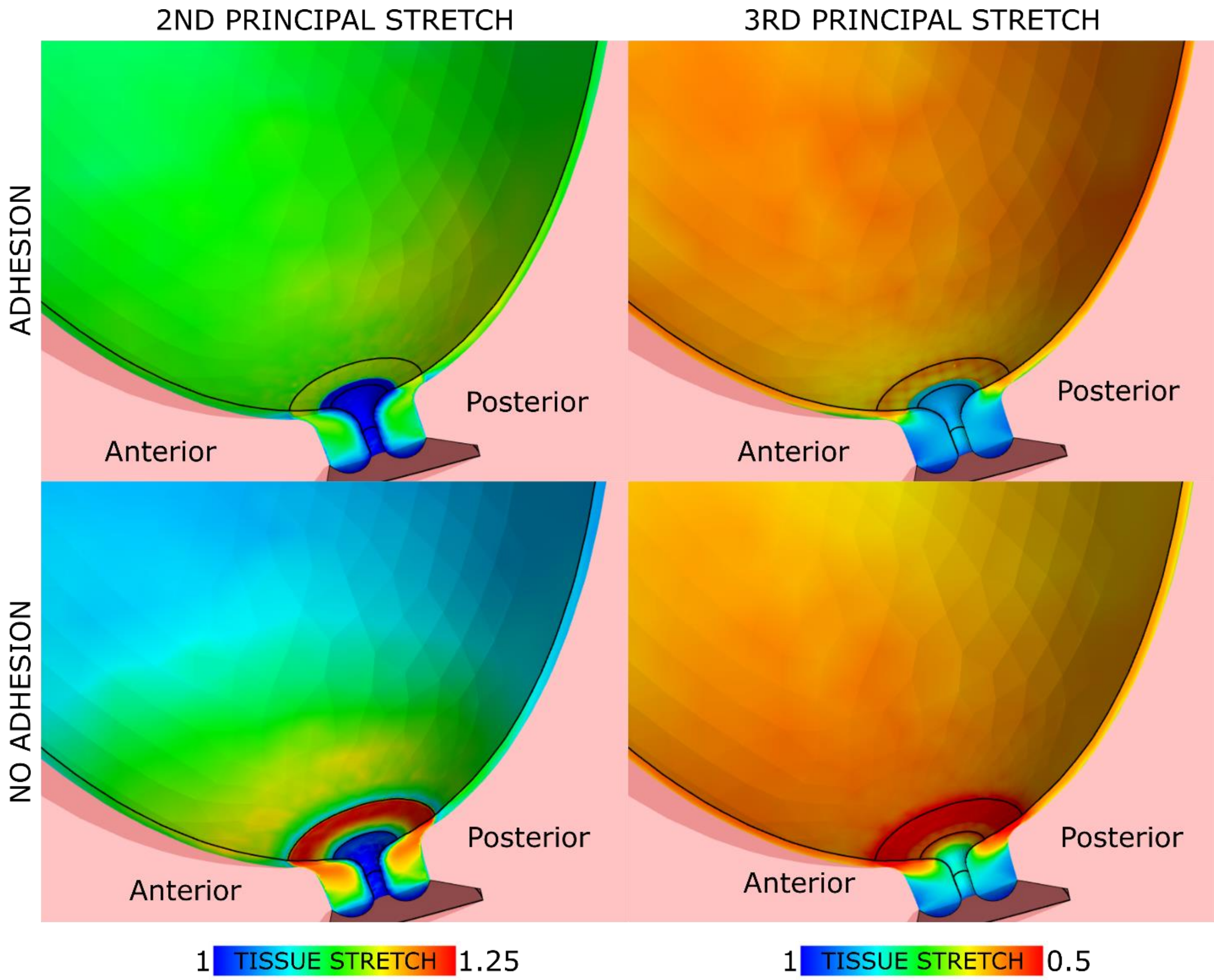

Figure 4-6: 2nd (left) and 3rd (right) principal stretches in uterine and cervical tissue in the case of a fully-adhered membrane (top) and full-detached membrane (bottom).

Unlike tissue stretch, fetal membrane adhesion does not affect membrane stress, which is largest at the umbilical level of the membrane and decreases at the superior and inferior ends of the membrane.

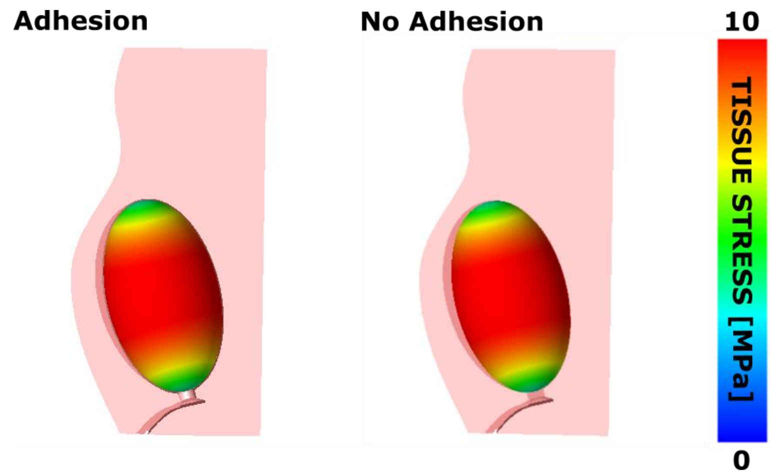

Figure 4-7: Fetal membrane adhesion does not affect membrane stress. Models show 1st principal stress in the fetal membranes. Uterus and cervix are removed for clarity.

4.2.2 Sensitivity to membrane stiffness

An increase in fetal membrane stiffness results in a decrease in tissue stress in both the uterus and the cervix. The uterus sees larger stress than the cervix because it is stiffer than the cervix (Figure 4-8). In all scenarios, there is a band of stress in the uterus around the edge of the cervix that occurs due to a jump in material properties. The pattern of uterine and cervical stretch is the same under all membrane stiffness scenarios, but the magnitude decreases as membrane stiffness increases.

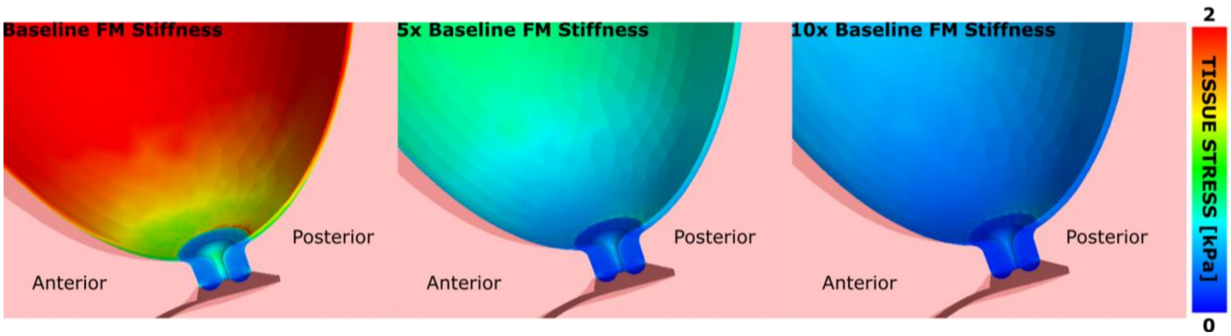

Figure 4-8: Stiffer fetal membranes result in reduced cervical and uterine stress. Models show 1st principal stress in the uterus and cervix. The membrane is removed for clarity.

An increase in membrane stiffness also results in reduced uterine and cervical tensile stretch (Figure 4-9). The baseline membrane material model with term pregnant material properties results in 27.9% of the internal os region above a 1.1 stretch threshold. Increasing the stiffness of the membrane fibers by 5 times reduces the volume fraction to 0.2%, and increases the stiffness by 10 times reduces the volume fraction to zero. Yet again, the pattern of stretch in the uterus and cervix remain the same with varying fetal membrane stiffness, but the magnitude of stretch decreases with increased membrane stiffness.

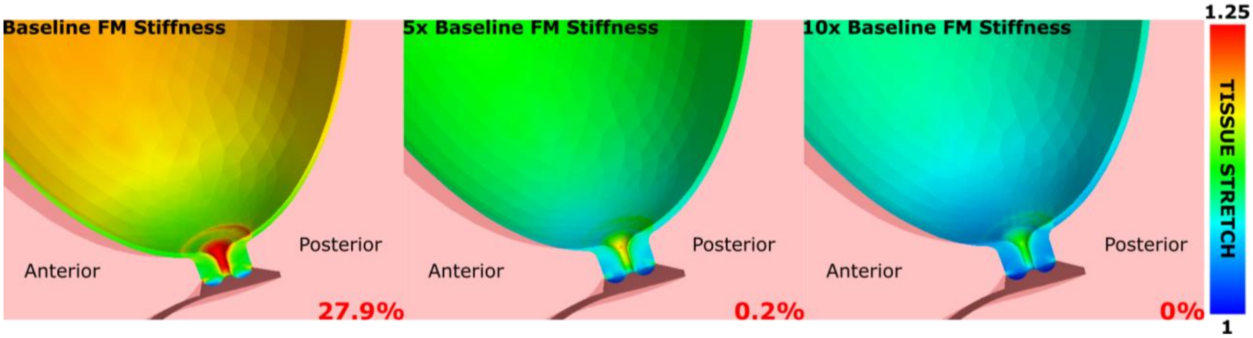

Figure 4-9: Stiffer fetal membranes result in reduced cervical and uterine stretch. Models show 1st principal stretch in the uterus and cervix. The membrane is removed for clarity. Percentages show the volume fraction of the cervical internal os region above a 1.1 stretch threshold.

Similarly, both 2nd and 3rd principal stretches decrease as membrane stiffness increases (Figure 4-10).

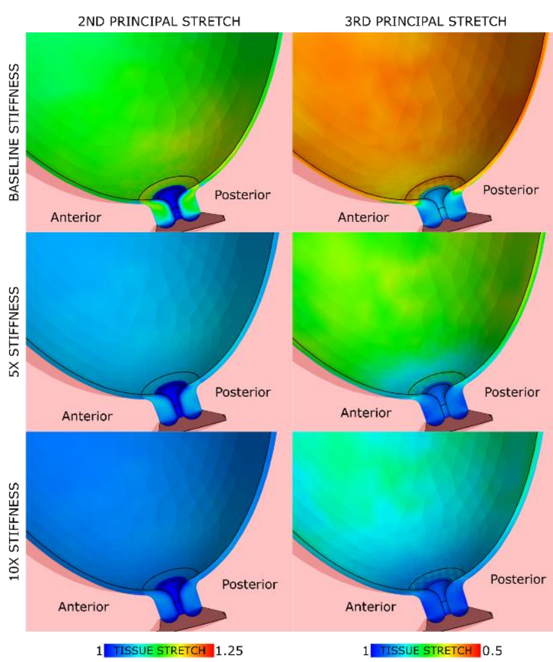

Figure 4-10: 2nd (left) and 3rd (right) principal right stretches in the uterus and cervix as the membrane is adjusted from baseline stiffness (top) to 5x (middle) and 10x (bottom) stiffness.

As membrane stiffness increases, we also see a reduction in membrane stress (Figure 4-11). The pattern, however, is consistent as the umbilical level membrane experiences the most stress, and the superior and inferior ends experience the lowest magnitude of stress.

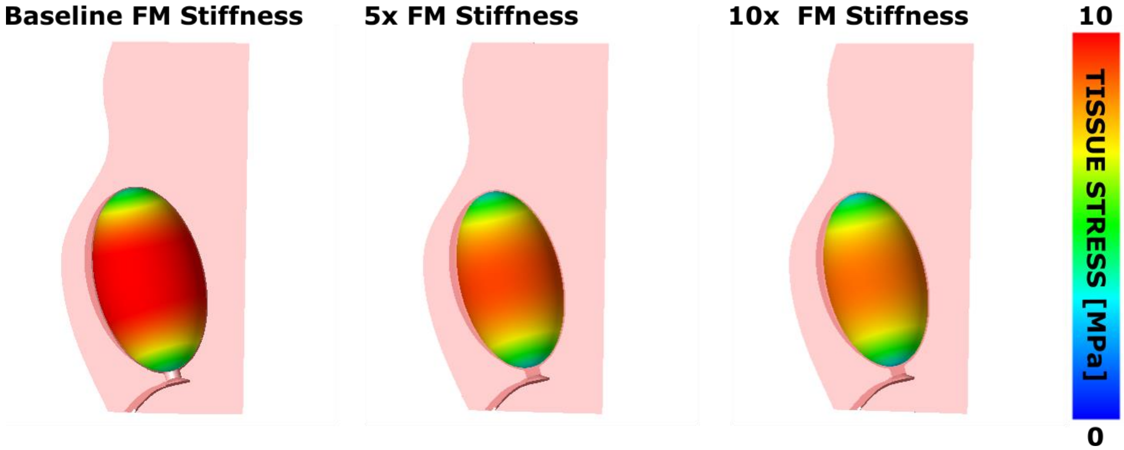

Figure 4-11: Stiffer fetal membranes result in reduced membrane stress. Models show 1st principal stress in the fetal membranes. The uterus and cervix are removed for clarity.

4.3 Discussion

This work furthers development in a method to generate a patient-specific finite element model of the uterus, cervix, fetal membrane, and surrounding anatomy derived from maternal anatomy, and evaluates the importance of fetal membrane stiffness and adhesion in pregnancy. We modeled a normal pregnant patient at 35 weeks gestation, keeping uterine and cervical parameters constant while we individually varied fetal membrane stiffness and adhesion to the uterine wall. With this computer model, and basing engineering assumptions on previously published data, we assess tissue stretch at contraction-magnitude intrauterine pressure (IUP).

Results indicated that increased fetal membrane adhesion results in reduced stretch to the cervix and uterus. Membrane stress is unaffected my membrane adhesion. Evidence from the literature suggests that increased loading and stretch in cervical tissue controls the cervical material modeling processes[122–124]. This implies that excessive stretch at the internal os may trigger tissue remodeling and possibly lead to preterm birth. Therefore, it is ideal that membranes remain adhered to the uterine wall for the duration of pregnancy until term. These results confirm the clinical practices of fetal fibronectin testing and membrane stripping. Fetal fibronectin is a glycoprotein whose purpose remains poorly understood, though it is hypothesized that it may be a glue-like substance that bonds the chorion to the decidua[97]. If a patient is believed to be at risk for preterm birth, clinicians may test for the presence of fetal fibronectin secretions in the patient's vaginal canal. If a patient has a positive result between weeks 22 and 34, they are at increased risk of preterm birth within seven days. In contrast, when a patient has reached term and a doctor wants to induce labor, they will insert their finger into the cervix and strip the membranes from the uterine wall, with the belief that it will speed up the labor process. This is supported by model results that show removing membrane adhesion increases cervical tissue stretch.

Additionally, evidence shows increased uterine stretch, or uterine overdistention, can also lead to premature uterine contractions and preterm labor[65]. Because the removal of membrane adhesion increases uterine stretch, membrane detachment may contribute to preterm contractions.

Increased membrane stiffness also reduced both cervical and uterine stretch, and therefore may be beneficial in pregnancy. The stiffer membrane models also reduced membrane stress, which may reduce the likelihood of premature preterm rupture of membranes (PPROM). Yet, in our models, all membranes surpass the experimentally measured rupture tension in fetal membranes of 295.08 kPa[93]. It may be possible that a stiffer membrane becomes brittle and therefore more likely to rupture, but this it also prevents large deformations from the same intrauterine pressure.

The results in this work confirm previous studies by our group that show load-sharing occurs between the fetal membrane, cervix, and uterus throughout pregnancy[74,92].

4.3.1 Limitations

It is extremely difficult to determine the mid-gestation mechanical properties of the fetal membranes. Hence, this study used experimentally-derived term pregnant amnion material properties and increased stiffness under the assumption that the membrane may remodel and soften near term[157].

While the membranes adhere to the uterine wall *in vivo*, there may be various modes of detachment that do not involve the entire membrane being either fully adhered or fully detached from the uterine wall. Our group is currently working on implementing a contact algorithm that will detach the membrane at individual elements as a threshold of shear force is reached[158]. In order to have this represent the physiological detachment of the membrane, our group is also experimentally measuring the force required to separate the fetal membranes from the uterine wall using shear testing. In vivo, there may also be a separation between the chorion and amnion layers, which we have not yet implemented in this model. Additionally, we are unable to model the impact that fetal membrane detachment will have on the ability to transmit infection throughout the amniotic cavity. This infection potential will likely strengthen our finding that fetal membrane adhesion is ideal for a healthy pregnancy.

4.4 Conclusions

This study represents a primary attempt to model the pregnant abdomen throughout the course of gestation, investigating the contribution of the fetal membrane sharing the load of the fetus with the uterus and cervix. Obtaining longitudinal data on pregnant humans is difficult.

Hence, we utilize previous x-ray and experimental data to inform our FE models of pregnancy at the gestational age of 35 weeks. As we discovered in our previous work[74,92], various material, anatomical, and contact factors influence the loading of the soft tissues that surround the fetus. The membrane taking on some of the intrauterine load may be protective for the uterus and the cervix. Hence, a stiff and fully-adhered membrane may be ideal to prolong gestation, though there are limitations to that. If the membrane is too stiff, it may reach its rupture point before term, resulting in premature preterm rupture of membranes. This indicates that there is a delicate balance between the fetal membrane and uterus load sharing that must be understood in subsequent studies.

5 Optimization of finite element analysis inputs

One purpose of creating simplified parametric models of anatomy is to continually improve towards more accurate representations of pregnancy and to verify any engineering assumptions that are made. This chapter describes some quick investigations on model boundary conditions, materials, and meshing in order to improve future iterations.

5.1 Physiological Boundary Conditions

5.1.1 Rationale and methods

The uterus is spherical until the 20th week of gestation and then elongates into an ellipsoidal shape for the remainder of the pregnancy[10]. However, as we apply uniform intrauterine pressure to the inner membrane in our finite element analyses, a globular uterus will continue to grow spherically. To discover potential reasons why the uterus does not continue to grow as a sphere throughout the entire pregnancy, we interviewed multiple clinicians at Columbia University Irving Medical Center, Tufts Medical Center, and at Intermountain Healthcare.

All of the clinicians we spoke to agreed that the uterus elongates due to abdominal boundary conditions. While the inner abdominal organs are soft and compressible, the uterus and growing fetus are the dominant force within the abdominal cavity. The conical shape of the pelvic bones is likely what influences the uterus to begin to grow upward and out of the pelvis in early pregnancy. While the uterus may start to grow spherically, the spine applies pressure on it posteriorly as it continues to grow, resulting in more elongation (Figure 5-1). The curvature of the spine is likely what leads to the uterus being kidney bean-shaped.

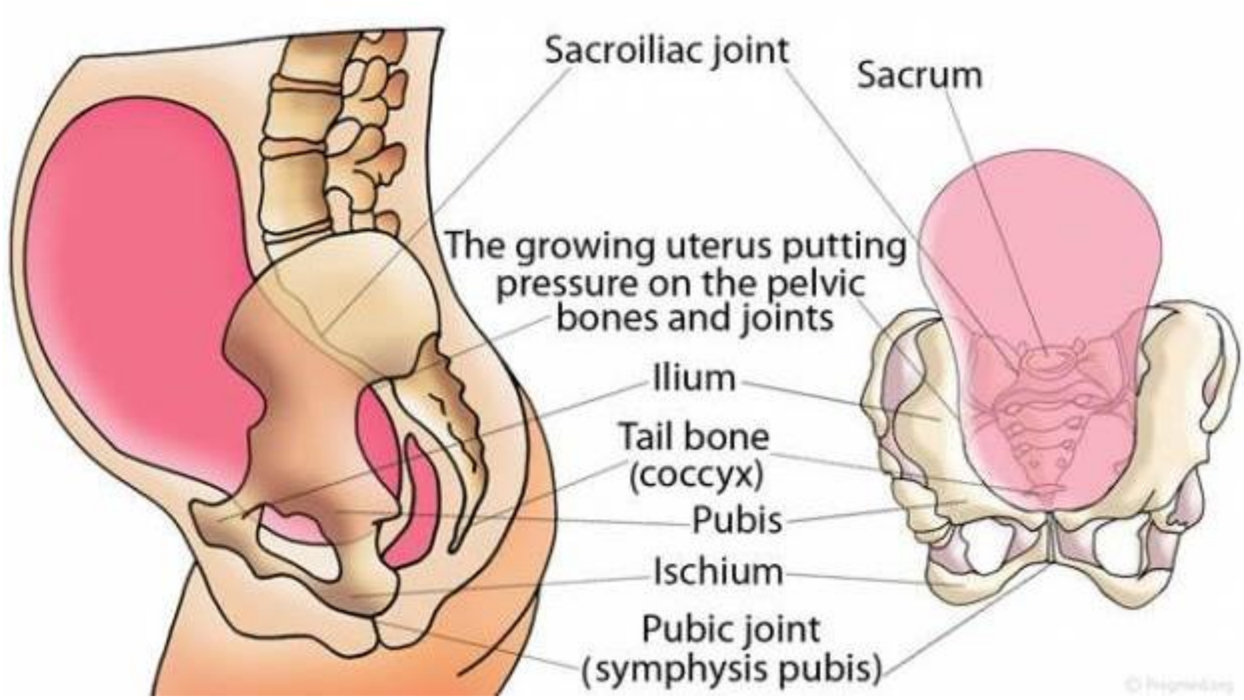

Figure 5-1: Orientation of a pregnant uterus within the abdomen, and its reference to bones such as the spine and pubic bones. [159]

While the spine applies pressure from the back, there must be another boundary at the anterior side of the uterus preventing it from extending the stomach outward. Many clinicians agree the abdominal muscles and stomach fascia are strong enough to resist the outward growth of the uterus. One clinician noted that patients who have received abdominoplasty show less outward growth in the uterus. For these reasons, we have chosen to add in the curvature of the spine into our full-anatomy models, and fix the abdomen on its external surface in every direction in all future models. We also developed a model with an abdominal cavity that is fixed to allow the uterus to stretch upward from its spherical reference configuration to its elliptical deformed figuration. This method is described in detail in Section 6.1.1.

5.1.2 Results

Our results show the use of a stationary abdominal cavity to influence uterine kinematics to deform from a spherical reference configuration at 16 weeks to an elliptical deformed configuration at 24 weeks (Figure 5-2).

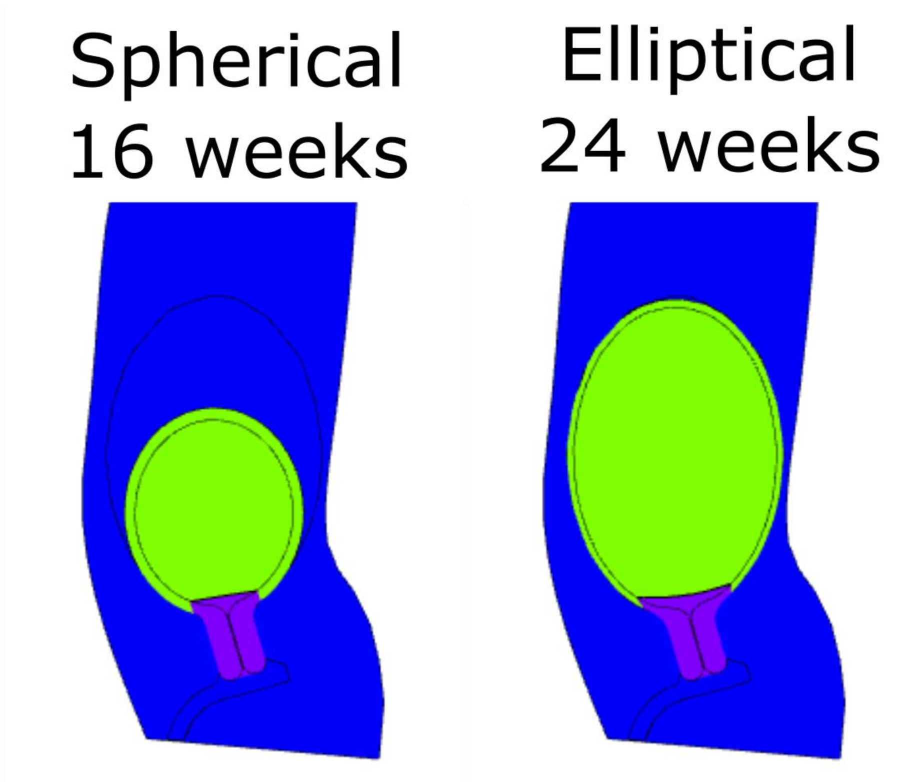

Figure 5-2: Uterus deformation from a spherical reference configuration at 16 weeks to an elliptical deformed configuration at 24 weeks.

More on the kinematics of this model is shown in Section 0.

5.1.3 Conclusions

Based on clinical input, we will include curvature of the spine and a fixed abdominal cavity in future iterations of the model where we intend to show uterine growth and stretch throughout gestation. These boundary conditions will allow for the uterus to elongate into an elliptical shape from a spherical reference configuration.

5.2 Fetal membranes material model

5.2.1 Rationale and methods

The fetal membranes are able to stretch and bend throughout pregnancy. In patients with a funneled cervix, the membranes often slip into the cervical funnel to completely touch the inner surface of the cervical canal. We observed that using an Ogden material in our finite element analysis did not allow for fetal membrane funneling into the internal os of the cervix. Therefore, our goal was to develop a material model for the amnion which captured the low bending stiffness of the membranes *in vivo* by utilizing a transversely isotropic fiber-based model.

Transversely isotropic materials are special orthotropic materials that have one axis of symmetry. They have a single material direction and whose response in the plane orthogonal to this direction is isotropic. Biological membranes often have bundles of fibers that present a preferred direction and the presence of these fibers generally results in a stiffer response in their preferred direction, also identified as transverse isotropic behavior[71,160,161]. Like most biological membranes, the fetal membrane is transversely isotropic as the properties in the plane of the membrane are different than those in the perpendicular direction. When the membrane is pulled or stretched in its plane of symmetry, the material is stiff. However, it is very soft in other directions as it can bend easily. The Ogden material will correctly account for this mismatch in directional stiffness in the event that the membrane is very thin. However, due to computational difficulties and FEBio not consisting of shell elements, we cannot model the membrane as extremely thin. Therefore, the Ogden material lacks the ability to capture the bending behavior of the fetal membrane and thus we chose to use a transversely isotropic material model instead.

The material model here has a Neo-Hookean ground substance and randomly distributed fibers. More detail is given on the material in Section 6.2.1.5.

We utilized the experimental dataset from uniaxial tension tests on amnion to inform the material parameter optimization[113]. We informed the model with a fiber-based material and the material parameter values [E_{GS}, ν_{GS}, α, β, and ξ] were fit to the experimental data. The optimization was used with fminsearchbnd routine in MATLAB (R2014b) available on the MathWorks File Exchange,

$$F_{obj} = \sum_{i=1}^{n} \left[\frac{\left(F_i - \hat{F}_i\right)^2}{F_i} \right]$$

Equation 5-1

where the primed variables are the FEA model prediction. The model was validated by comparing the FEA prediction to the experimental data of stress and strain in the length and width direction. The model fit to stress-strain data is shown in Figure 5-3 and fit to extension-compression data is shown in Figure 5-4.

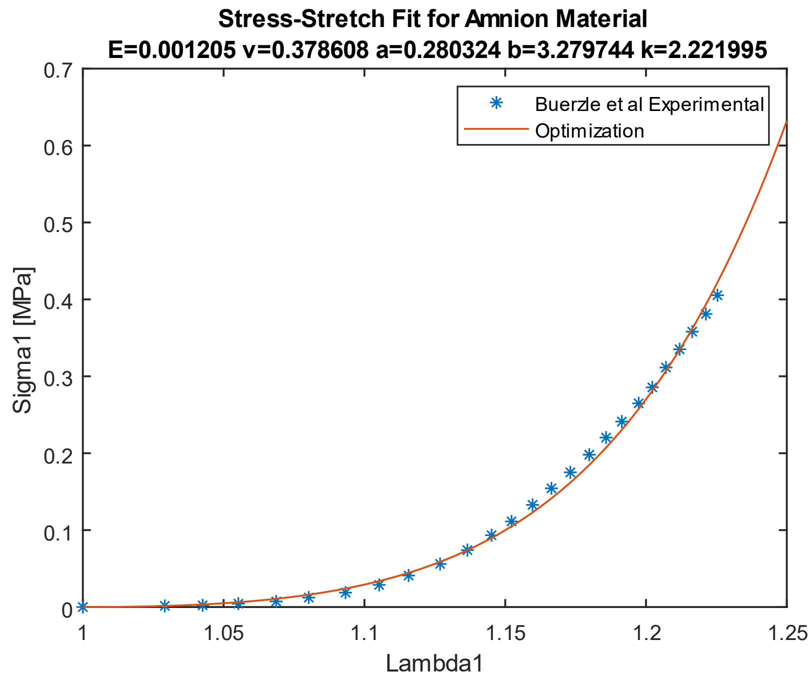

Figure 5-3: Stress-strain material fit results of fiber-based material for fetal membranes compared to experimental data[36].

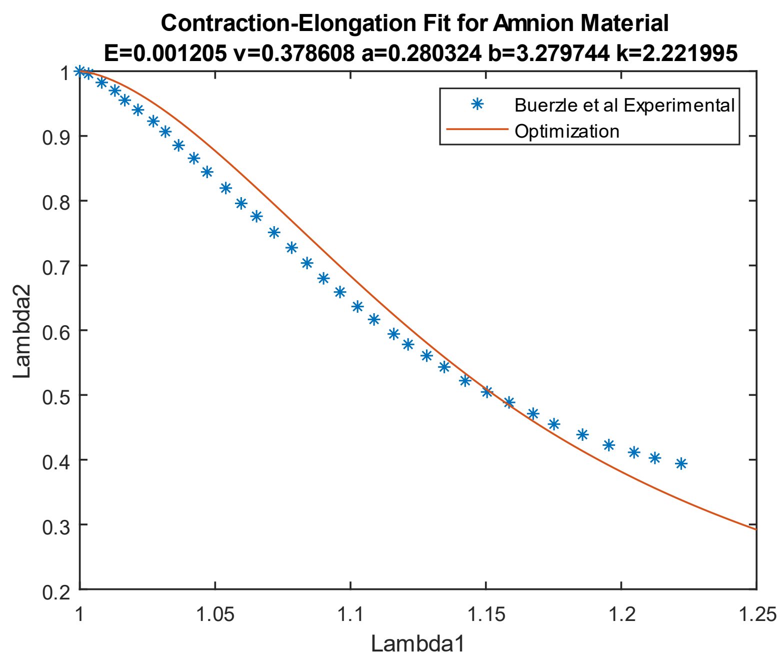

0

Figure 5-4: Extension-compression material fit results of fiber-based material model of fetal membranes fit to experimental data[36].

Optimized material parameters are shown in Table 5-1.

Tissue Description	E^{GS} [kPa]	ν^{GS}	α	β	ξ
Fetal membranes	1.21	0.38	0.28	3.33	2.22

Table 5-1: Material parameters of the fetal membranes fit to experimental data.

We conducted a sensitivity study on the new material by implementing it and the Ogden material in the same model configuration with the same boundary conditions and loading scenarios and then comparing results. In each model, an intrauterine pressure of 1 kPa was applied, and a rigid sphere was prescribed a displacement of 1mm into the cervix in order to attempt to create funneling.

5.2.2 Results

Results show that there is much larger deformation in the fiber-based model than in the Ogden model (Figure 5-5). At the beginning of the simulation, the Ogden membrane lifts up from the uterine surface when it is pushed into the cervical canal, and the fiber-based model remains in contact with the uterine wall through the entire simulation duration.

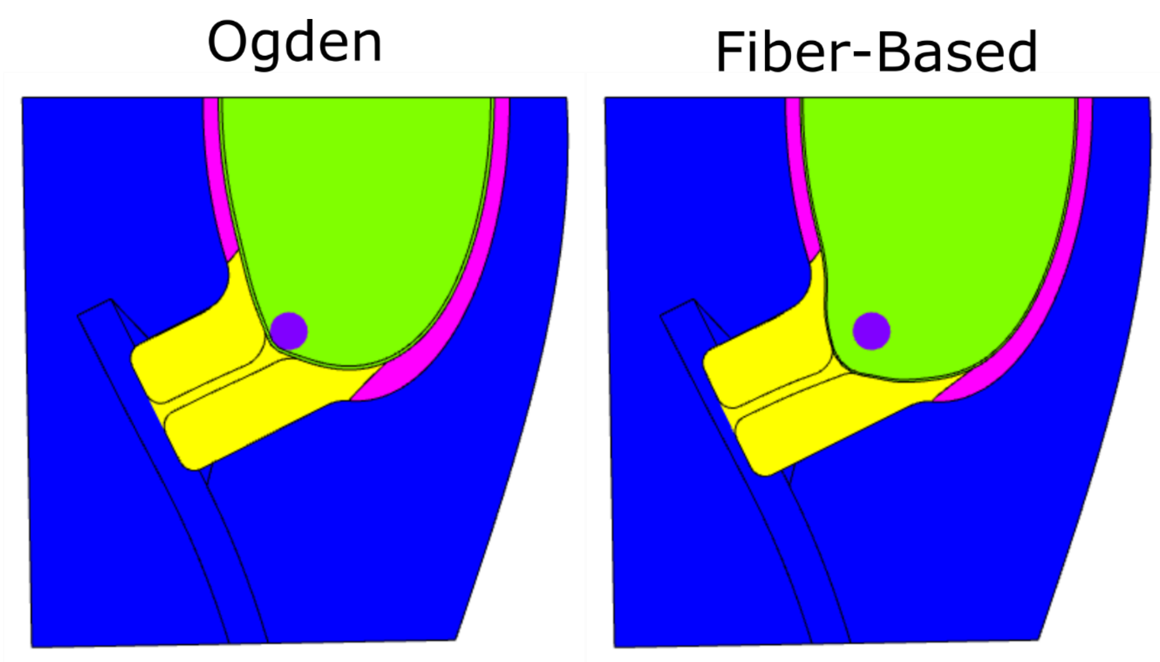

Figure 5-5: Comparison in the deformation between Ogden and fiber-based membrane material models

The fiber-based model is able to bend into the internal os, and cervical funneling occurs, whereas the Ogden model does not bend. There is an increased stretch at the internal os when the fiber-based membrane is implemented (Figure 5-6).

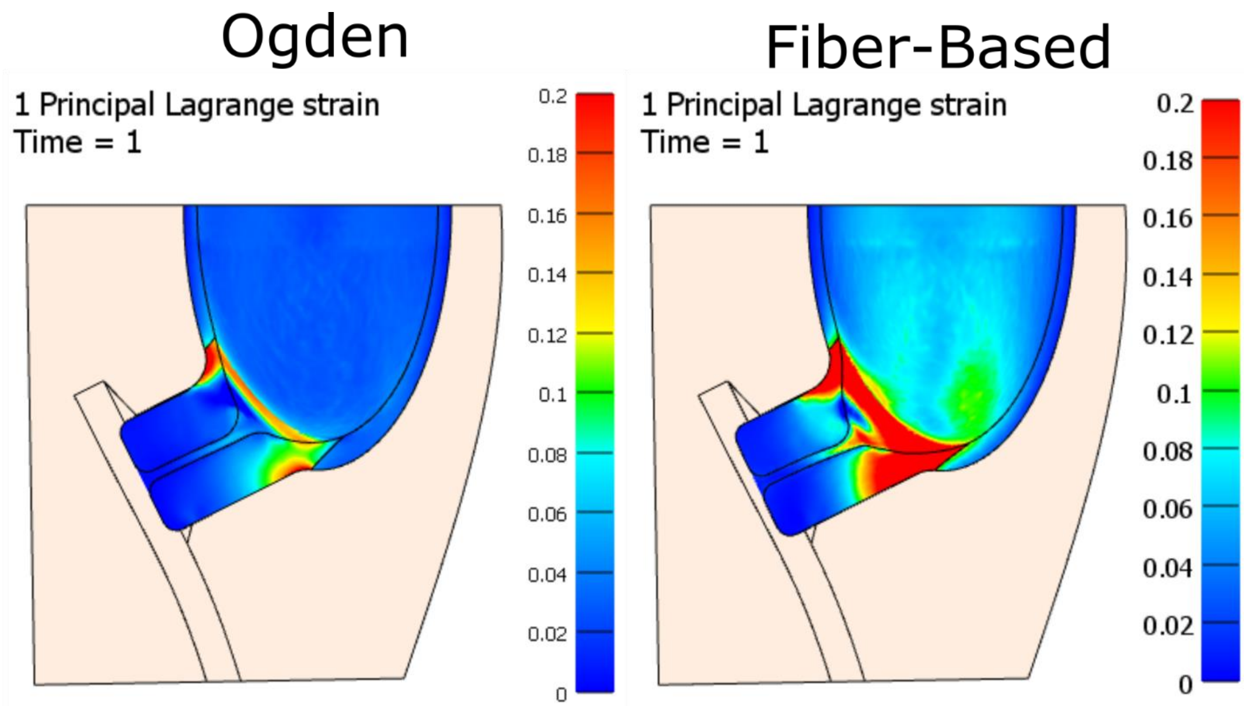

Figure 5-6: Comparison of uterine and cervical stretch between Ogden and fiber-based membrane material models

5.2.3 Conclusions

The fiber-based membrane shows greater deformation at the cervix internal os and allows for funneling in our analyses. Due to the computational necessity of modeling the membrane as thick as 1mm, an Ogden material was not able to accurately represent the bending behavior of the fetal membranes. As the membranes have a low bending stiffness *in vivo*, we will implement the fiber-based transversely isotropic model in future iterations of our analyses, which will allow for the membrane to remain stiff in-plane, and softly bend in its other directions.

5.3 Order of finite element mesh shape functions

5.3.1 Rationale and methods

Finite element meshes can be created with various element types and shape functions. In our models, we use both hexahedral (top row in Figure 5-7) and tetrahedral (bottom row in Figure 5-7) elements. Elements will have a number of nodes depending on their shape function. Higher order shape functions have more nodes. For example, quadratic shape function elements (right in Figure 5-7) will have nodes at the midpoint of each edge in addition to each vertex, while linear elements (left in Figure 5-7) only have nodes at the vertices. Linear hex elements have 8 nodes, while quadratic hex elements have 20. Linear tet elements have 4 nodes, while quadratic tet elements have 10.

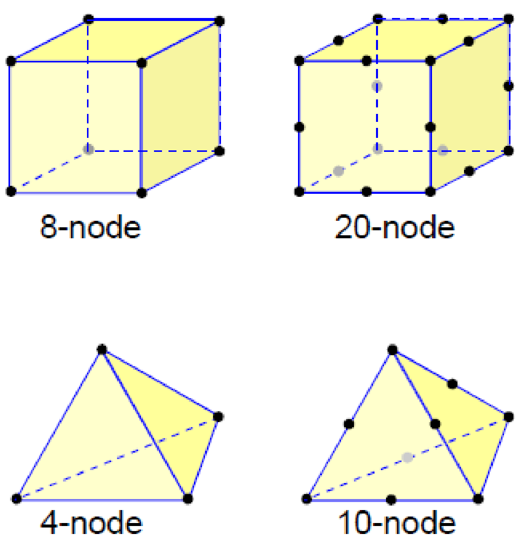

Figure 5-7: Linear (left) and quadratic (right) shape function elements. The top row is hexahedral elements and the bottom row is tetrahedral elements[162].

For many structural analyses, linear elements with no midside nodes will provide sufficient results in an acceptable amount of time. However, it is often recommended that quadratic elements are used instead in bending problems and in analyses of soft materials undergoing large deformations, in order to avoid shear locking.

Because the tissues in pregnancy are very soft and our goal in some simulations is to have the fetal membrane bend into the cervical canal, we chose to investigate the effect of quadratic vs. linear elements in our finite element models. A linear mesh was created in Trelis and imported into FEBio to convert into a quadratic mesh. All other model parameters were kept the same in order to investigate the effect of the order of shape functions on model outcome parameters. The outcome parameters in this study are the mean, median, and 95th percentile of 1st principal strain in the cervix.

5.3.2 Results

Results show that there is not a large difference between overall tissue stretch in the cervix between linear and quadratic mesh elements (Figure 5-8). Quadratic elements see slightly more deformation, with only a 1.1% increase in mean strain. This can lead to the conclusion that it is likely acceptable to use linear elements for our analysis.

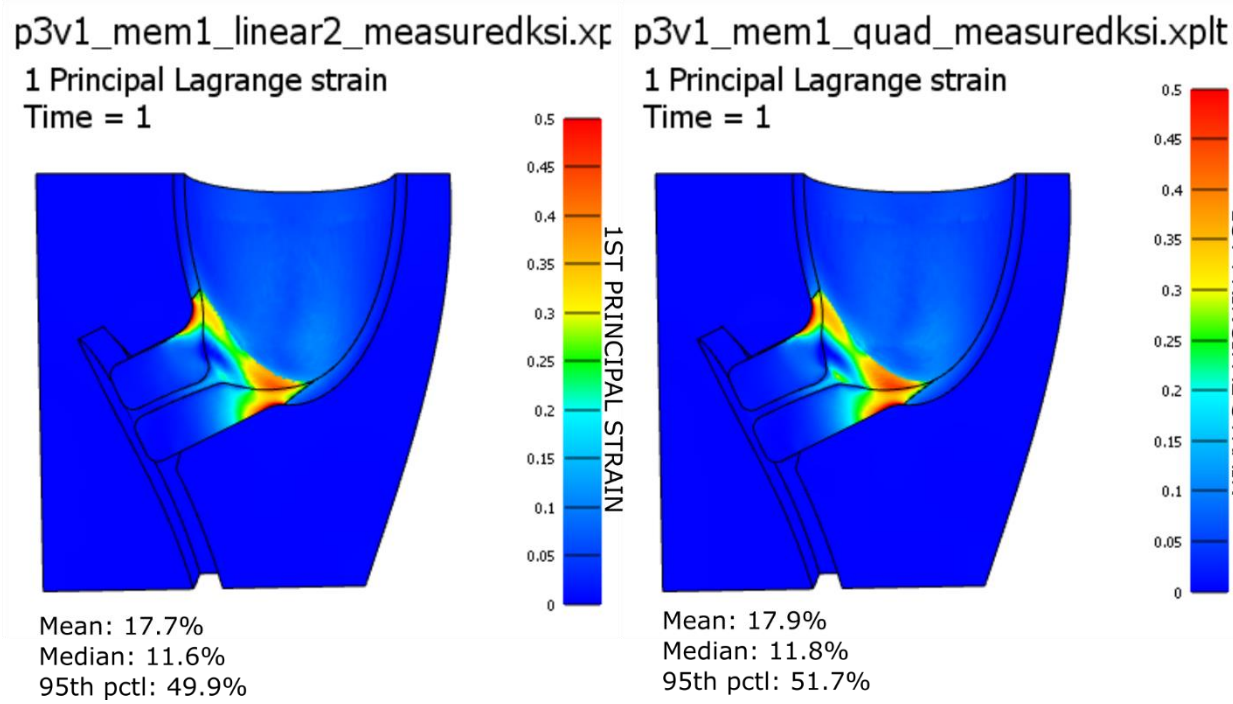

Figure 5-8: Mean, median, and 95th percentile 1st principal cervical strain in finite element analyses with linear (left) and quadratic (right) element shape functions.

However, when comparing the visualizations of tissue stretch in the linear and quadratic elements, it seems that the quadratic mesh may undergo slightly more stretch at the top of the cervix. Because this is our area of interest and we would like to guarantee the best accuracy in our models, we will choose to investigate future models using a quadratic mesh shape function instead of linear.

5.3.3 Conclusions

Beginning with studies of our high-risk patient cohort (Section 6.2), we will implement quadratic shape function mesh elements in our finite element analyses. We believe these are more accurate in capturing the large deformations at the top of the cervix, and therefore provide the best analyses for our outcome variable of interest. Linear elements should be sufficient for comparative sensitivity studies, especially when deformation is small and total tissue strain is less than 50%.

6 Longitudinal clinical studies of pregnancy: subject-specific geometry, material, and finite element analysis

Longitudinally measured biomarkers are useful to predict the risk of clinical outcomes such as preterm birth. Subject-specific timecourse markers are especially useful for determining critical windows and discovering etiology of outcomes. This is especially true in pregnancy, as patient anatomies vary greatly at a given gestational timepoint (Figure 6-1).

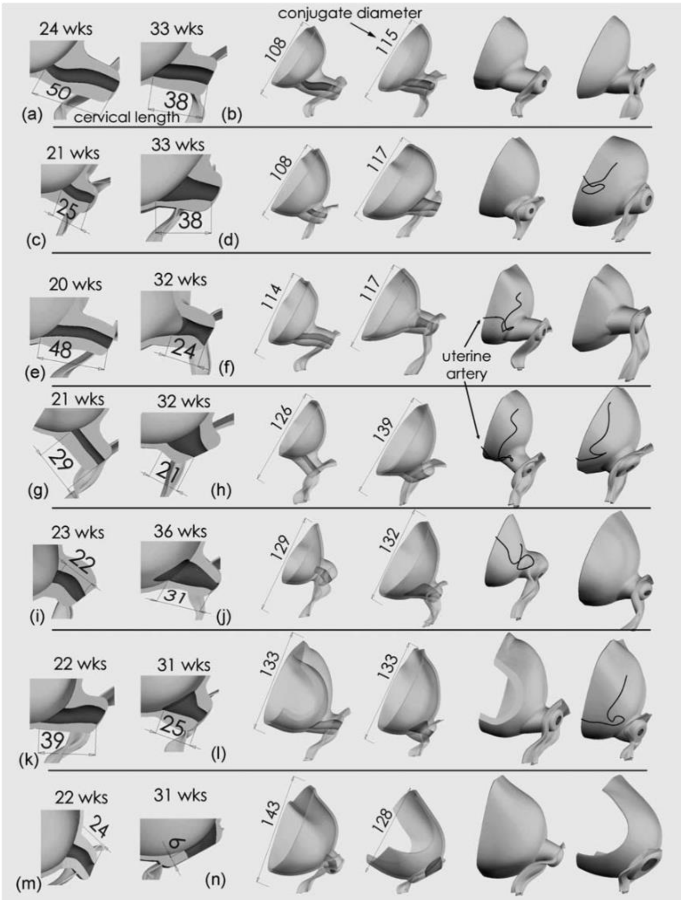

Figure 6-1: Fourteen Solid Models. Each row shows two, matched models—one model from the second trimester and one from the third trimester. The models are matched by the distance of the conjugate diameter of the pelvic bone. The first two columns demonstrate cervical length. The middle two columns show an anterior view and the cervix is transparent. The last two columns show a posterior view. In all models, the volume of the amniotic cavity below the diagonal conjugate is larger in the third trimester compared to the second trimester. In addition, the transition from the cervix to the uterus is wider in the third trimester compared to the second trimester (compare (c) vs. (d), (g) vs. (h), (i) vs. (j), (k) vs. (m)). Model (n) shows a cervix that is completely effaced at 31 weeks. This patient delivered at 33 weeks. Dimensions are in millimeters[77].

Currently, little is understood about the anatomical changes and mechanics of the maternal anatomy throughout pregnancy. In the following studies, we aim to close that gap by sonographically quantifying the growth and shape change of the uterus and cervix longitudinally throughout gestation in both low- and high-risk patient cohorts. Our objective is to compare the anatomies of the two cohorts to determine which dimensions and parameters should be investigated further as potential clinical biomarkers of preterm birth. The low-risk cohort consists of patients with a cervix longer than 20mm, with no prior history of preterm birth, and with no health complications related to preterm birth. The high-risk cohort includes patients with a short cervix shorter than 20mm but with no history of preterm birth. In the high-risk cohort, patients are randomized to receive progesterone only as a preventative treatment or to receive progesterone and a cervical pessary.

In both cohorts, we will report maternal anatomy throughout gestation and in the high-risk cohort, we will report cervical aspiration, an index of cervical stiffness, with gestation. We hypothesize that there is shared importance in maternal anatomy and patient-specific material properties that affect the mechanics of the soft tissues throughout pregnancy.

Results showed that the strain patterns in the uterus are very different amongst patients, even in a low-risk cohort. In a normal pregnancy, the uterus likely adds mass to grow at these points of high strain. In patients with a short cervix, cervical stiffness is an important factor in determining birthing outcome. Patients with a soft and short cervix are more likely to deliver sooner than those with a stiff cervix.

Findings also showed that cervical shortening may be preceded by thinning and compression of the lower uterine segment, as we saw patients with a short cervix had thinner lower uterine segments than those with a normal cervix. In these patients with short cervices, the pessary did not lengthen the cervix long-term or make permanent changes to cervical position. These findings lead to observations about the location of pessary placement and the importance of patient anatomy in the effectiveness of the device.

6.1 Low-risk cohort

There are many hypothesized risk factors that lead to the multiple etiologies of preterm birth. And because the final passageway of preterm birth is cervical dilation, a lot of research focuses on the dilemma of cervical insufficiency. While this is certainly important, our group also wants to look at the uterus, or the organ that surrounds the fetus throughout pregnancy. The uterine tissue needs to grow exponentially in order to accommodate the growing fetus and amniotic sac. Throughout gestation, uterine weight increases by 15 times while the capacity can increase more than 500 times. And yet the best longitudinal data we can find is from x-rays of pregnancy patients taken in 1950[10]. In order to better understand the geometric changes throughout pregnancy, we captured maternal ultrasound anatomy from 30 patients, each at 4 gestational timepoints. This anatomical data is a first step in understanding uterine kinematics and mechanics in pregnancy. We see from our own preliminary data that the uterus also does not grow uniformly in size. Instead, it grows at different rates in different directions and stretches out depending on maternal boundary conditions (Figure 6-2).

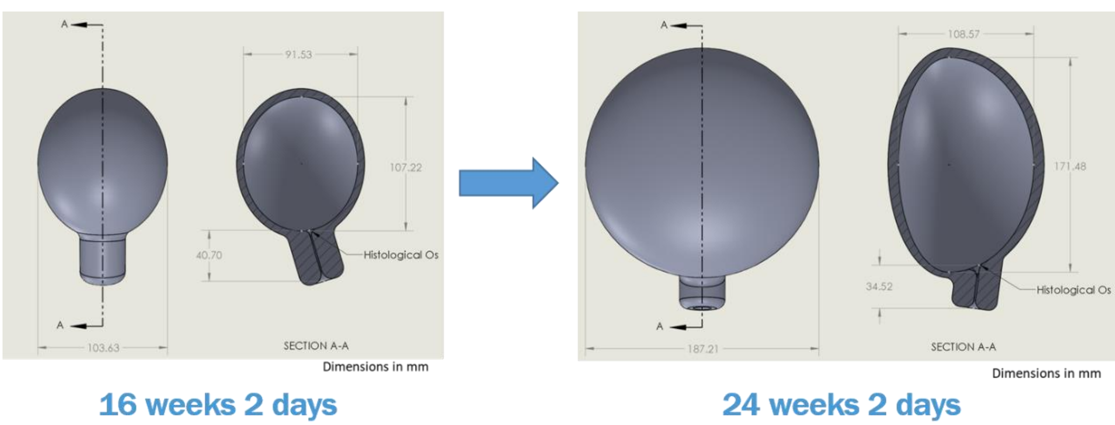

Figure 6-2: What kinematics does the uterus experience from 16 to 24 weeks? Geometric drawings of the uterus from one low-risk patient at 16w2d and 24w2d gestation.

Our goal is to characterize uterine tissue growth and stretch throughout gestation using patient-specific ultrasound data and finite element analysis. We want to understand the kinematics of the uterus as pregnancy progresses, and identify areas where we may need to incorporate growth in future iterations of our model. We hypothesize that the uterus will have patterns in strain and each patient will have similar kinematics of the uterine tissue as gestation progresses from 16 to 24 weeks.

6.1.1 Methods

6.1.1.1 Patient recruitment

Deidentified B-mode ultrasound images were obtained from 30 female patients 18-45 years old with a singleton pregnancy. All subjects were recruited from the low-risk Ob/Gyn and Certified Nurse Midwife clinics at Intermountain Medical center and provided written, informed consent as part of the Biomarkers Of Uterine aNd Cervical ChangeE (BOUNCE) study. This study was performed in collaboration with Helen Feltovich, Timothy Hall, and the rest of their team at Intermountain. These patients included 21 multiparous and 9 nulliparous. Exclusion criteria included a history of preterm delivery, cesarean delivery, cervical surgery (LEEP, trachelectomy, conization), collagen vascular disease, known uterine malformation, premature rupture of membranes, morbidly adherent placenta, placenta previa, placental abruption, chorioamnionitis, or preterm delivery. The following clinical data were obtained for each patient: age, height, weight, medical history, surgical history, gravidity, parity, previous obstetrical history, and birthing outcome. Patients in this study are identified by UTAHxXX, where XX is the patient ID number.

6.1.1.2 Data acquisition

Each subject underwent an ultrasound exam at four different gestational timepoints: 8-13 weeks, 15-17 weeks, 22-25 weeks, and 32-35 weeks. Six B-mode ultrasound images of the uterus and cervix were obtained to measure maternal anatomical dimensions during each visit – three with the patient in the supine orientation, and three with her standing. The three images included a transabdominal sagittal view of the uterus and cervix, a transabdominal axial view of the uterus, and a transvaginal view of the cervix and lower uterine segment. All designated research sonographers were certified for transvaginal exams through the Perinatal Quality Foundation's Cervical Length Education and Review (CLEAR) program[163]. Transabdominal measurements followed the protocol described by Saul et al. In the initial publication of transabdominal cervical length measurement, upon which subsequent studies and US cervical length screening recommendations have been based[164].

Transabdominal images were acquired using the SieScape panoramic imaging feature on the Siemens S3000 ultrasound system, which automatically registered adjacent images together as the probe was swept across the abdomen. In the sagittal view transabdominal scan, dimensions measured were uterus longitudinal diameter (UD1), uterus anterior radius (UD2), uterus posterior radius (UD3), the perpendicular offset of the cervical internal os from the uterus longitudinal diameter (PCO), uterine wall thickness at the fundus (UT1), and uterine wall thickness at the anterior uterine wall (UT2) (Figure 6-3:A-C). In the transverse view, dimensions measured were transverse uterine diameter (UD4) and uterine wall thickness at either the left or right wall (UT3) (Figure 6-3:D-E). Measurements were also taken via sagittal transvaginal imaging such as uterine wall thickness at the lower uterine segment (UT4), cervical length (CL), cervical outer diameter (CD1), cervical canal diameter (CD2), and the anterior uterocervical angle (AUCA) were measured (Figure 6-3:F). All measurements were made on deidentified images after each exam using Fiji[165].

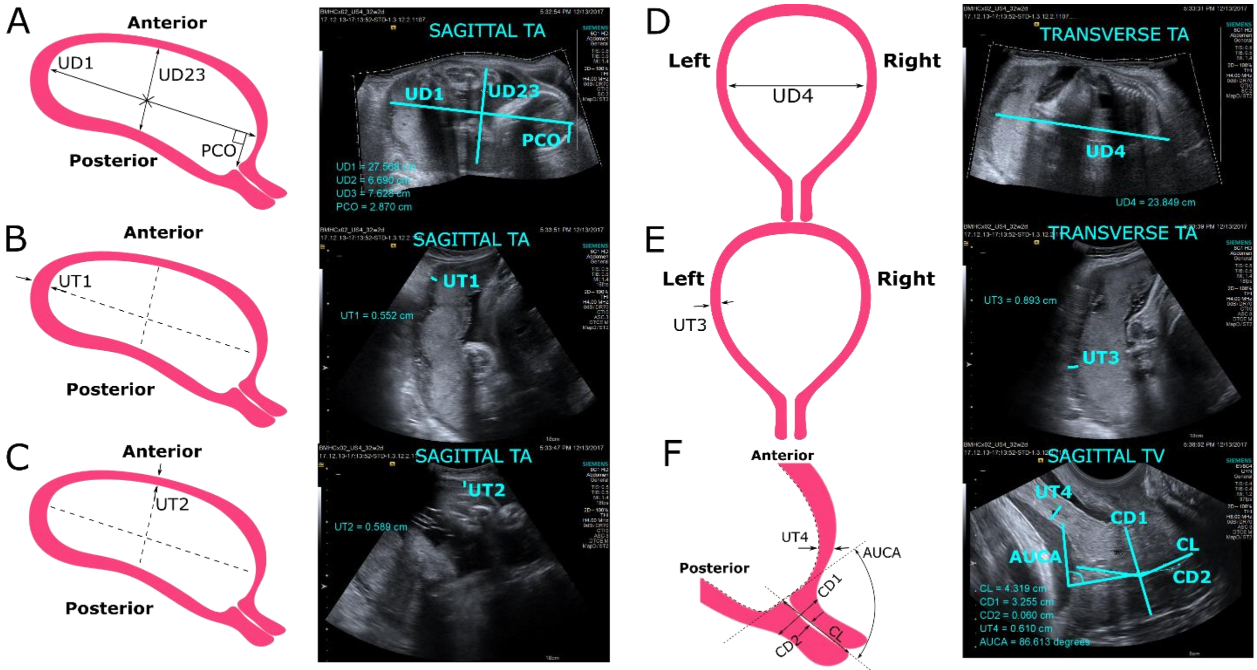

Figure 6-3: Maternal anatomy dimensions taken via sagittal transabdominal (A-C), transverse transabdominal (D-E), and sagittal transvaginal ultrasound(F).

6.1.1.3 3D CAD models of the maternal anatomy and uterine cavity

The maternal geometric parameters of 5 patients in their second and third clinical visits were converted into CAD geometries with a custom computer script (Trelis Pro 15.1.3, csimsoft LLC). The geometry of the second visit was used as the reference configuration for the uterus and cervix, as this is when the gestational tissue becomes fully adhered to the uterine wall and the tissue begins to stretch[51]. Geometries of the uterus, cervix, vaginal canal, abdomen, and abdominal cavity of the deformed configuration of the uterus were created with Boolean addition and subtraction of geometric primitives (Figure 6-4).

Figure 6-4: Geometries of the uterus, cervix, vaginal canal, abdomen, and abdominal cavity of deformed configuration of the uterus.

The uterus was built by transforming two spherical shells into ellipsoids. The interior uterus was scaled to the diameters obtained from the ultrasound data. The outer shell was then scaled, translated, and rotated to accommodate uterine wall thickness in the anterior-posterior, superior-inferior, and left-right directions. A third-visit deformed uterine geometry was built in the same manner but was then subtracted from the outer abdomen volume. This allowed for the creation of a cavity that the reference size of the uterus could grow into in order to determine the kinematics of the uterus as the shape and size change throughout gestation. Each patient's uterine dimensions are shown below in Table 6-1.

Patient	Config	Long. Diam. (UD1) [mm]	Ant-post diam (UD23) [mm]	L/R diam (UD4) [mm]	Fundus wall t (UT1) [mm]	Ant. wall t (UT2) [mm]	L/R wall t (UT3) [mm]	LUS wall t (UT4) [mm]
UTAHx01	Reference	107.22	91.53	90.01	6.56	5.52	6.81	5.86
UTAHx01	Deformed	171.48	108.57	168.01	7.56	8.39	9.6	4.44
UTAHx02	Reference	96.73	76.09	98.08	8.18	4.66	7.43	8.85
UTAHx02	Deformed	151.58	108.84	134.18	6.02	4.11	11.98	13.19
UTAHx03	Reference	136.57	62.86	110.76	12.30	9.91	14.45	7.66
UTAHx03	Deformed	200.12	107.28	163.23	8.14	6.47	11.27	7.66
UTAHx04	Reference	130.91	85.67	107.14	4.13	3.99	4.71	7.60
UTAHx04	Deformed	228.23	115.17	202.17	5.33	4.23	5.5	4.67
UTAHx05	Reference	124.72	92.93	99.14	6.37	5.34	8.27	6.17
UTAHx05	Deformed	188.60	114.53	163.23	6.49	7.34	9.25	5.09

Table 6-1: Five patient dimensions of the uterus in both reference (visit 2) and deformed (visit 3) configurations.

The cervix was built by creating a cylinder representing the diameter of the inner canal and subtracting that volume from a larger cylinder representing the outer cervical diameter and the reference cervical length. The resultant hollow cylinder was then moved and rotated according to posterior cervical offset and anterior cervical angle. The cylinder was rounded at its corners to match the anatomical rounding of the uterocervical junction and to replicate the roundness of the most exterior end of the cervix (i.e. external os). Cervical geometries were kept constant between both the reference and deformed configuration of the uterus.

Then, the vaginal canal was built by fitting a spline to three vertices located at the outside edges of the external os and one vertex at the approximate location of the vaginal introitus and the fetal membrane was generated with uniform thickness based on the contours of the inner uterine wall.

6.1.1.4 Finite element mesh generation

All meshes were generated using the automatic and manual meshing tools in Trelis Pro (v16.1.1, csimsoft LLC). All volumes were meshed with linear tetrahedral elements. Mesh properties varied from model to model. A representative mesh is described in Table 6-2 and is shown in Figure 6-5.

	Total	Uterus	Abdomen	Cervix
Element Type	-	Tet	Tet	Tet
Element Count	76,256	19,682	12,524	44,050
Average Element Volume	143 mm^3	9.91 mm^3	855 mm^3	0.673 mm^3

Table 6-2: Mesh properties for a representative model

The uterus and cervix were connected at the node level to one another, so their boundaries were shared and moved congruently. Each volume was meshed independently using Trellis's inherent meshing function, where a mesh refinement factor was chosen in order to optimize for model accuracy and solving time.

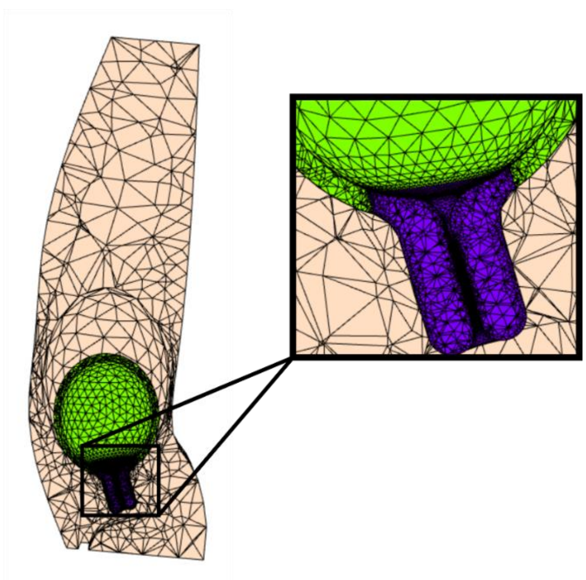

Figure 6-5: Finite element mesh of the uterus, cervix, and abdomen with cavity as the deformed configuration of the uterus. All volumes are meshed using tetrahedral elements.

6.1.1.5 Material properties

The cervix and uterus materials were treated as hyperelastic neo-Hookean materials hyperelastic NH model containing no fibers. It is an isotropic material, similarly stiff in tension and compression. The free energy density of the uterine and cervical materials Ψ^{NH} is given by a standard isotropic, compressible neo-Hookean relation

$$\Psi^{NH} = \frac{\mu}{2}(\boldsymbol{I_1} - 3) - \mu \ln J + \frac{\lambda}{2}(\ln J)^2$$

Equation 6-1

where $I_1 = tr\boldsymbol{C}$ is the first invariant of the right Cauchy-Green tensor $\boldsymbol{C} = (\boldsymbol{F})^T\boldsymbol{F}$ and $J = \det \boldsymbol{F}$ is the Jacobian. μ and l are the standard lamé constants. These lamé constants combine to form the Young's modulus and Poisson's ratio of the ground substance $E^{GS} = \frac{\mu\left(3+\frac{2\mu}{\lambda}\right)}{1+\frac{\mu}{\lambda}}$ and $\nu^{GS} = \frac{1}{2\left(1+\frac{\mu}{\lambda}\right)}$, respectively. We used these materials to get better model convergence because the reference configuration of the uterus in this analysis was undergoing such large deformations.

Considering not much is known about the multi-axial material behavior of these tissues during pregnancy, we investigated using properties of term pregnant (PG) tissue fit to term uniaxial tension data reported in [110] in the expectation that mid-gestation tissue would be remodeled more than that of non-pregnant tissue. Cervical material properties used in this study (Table 6-3) used the same parameters as the uterine material so that the uterus would undergo more strain than the cervix to solely investigate the kinematics of uterine expansion.

Tissue Description	E^{GS} [kPa]	ν^{GS}
Uterus	80	0.3
Cervix	80	0.3

Table 6-3: Uterine and cervical tissue variables taken from material fits to experimental data. These values are implemented in a Neo-Hookean material model used in FEBio 2.7.0.

The outer abdomen was treated as a neo-Hookean material with a modulus of 2 MPa so that it didn't deform and the uterus instead deformed into it.

6.1.1.6 Boundary conditions and loading

Boundary conditions were applied as described in Figure 6-6. The abdomen was fixed in the x, y, and z directions along its entire exterior so that the cavity would remain undeformed and the reference configuration uterus could expand into it. The cervix (purple in Figure 6-6) was tied to the abdominal cavity (magenta) so that it did not move throughout the analysis. The uterus (green) was prescribed a frictionless sliding contact along the inner wall of the abdominal cavity so that it could expand upwards towards the fundus.

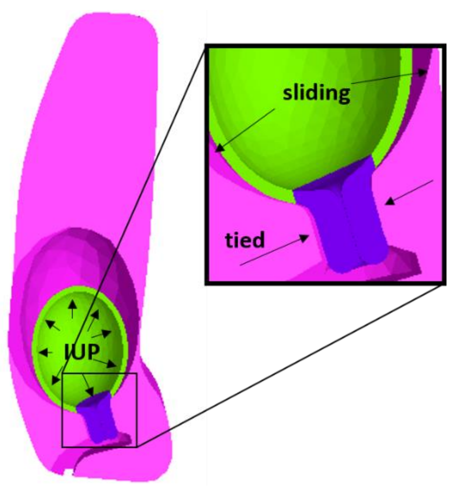

Figure 6-6: Finite element boundary and loading conditions. The cervix was tied to the abdominal cavity, and the reference uterus was allowed to slide freely along the inside of the deformed uterine sized abdominal cavity. Intrauterine pressure was applied to the inner surface of the uterus until the reference configuration touched all walls of the abdominal cavity.

Pressure was applied to the inner surface of the uterus to represent the intrauterine pressure (IUP). Pressure was applied until the reference configuration reached the inner wall of the abdominal cavity at all points, and therefore was not applied according to gestational pressure measurements. Depending on each patient, the pressure required to reach the deformed configuration was anywhere between 1.5 and 6.2 kPa.

6.1.1.7 Finite element analysis

FE analyses were performed in FEBio 2.7.0 (http://www.febio.org.). Stress and stretch data were plotted as a function of IUP in PostView (PostView 2.2.0), FEBio's post-processor for visualization and analysis. These data were then imported into MATLAB (MATLAB R2017a) for further post analysis. To describe the deformation of the cervix, the extent cervical 1st principal right strain is visualized for each patient, and 1st, 2nd, and 3rd principal are plotted at their median and 95th percentile values.

6.1.2 Results

Results show that strain in the uterus is not equibiaxial, as shown in Figure 6-7. In this particular patient (Patient UTAHx05), the uterus experiences the largest strains at the lower uterine segment, posterior wall, and fundus. The median 1st principal strain is 78.5%, while the median 2nd and 3rd principal strains are 43.2% and -31.1, respectively. The pressure required to meet the deformed configuration was 6.16 kPa.

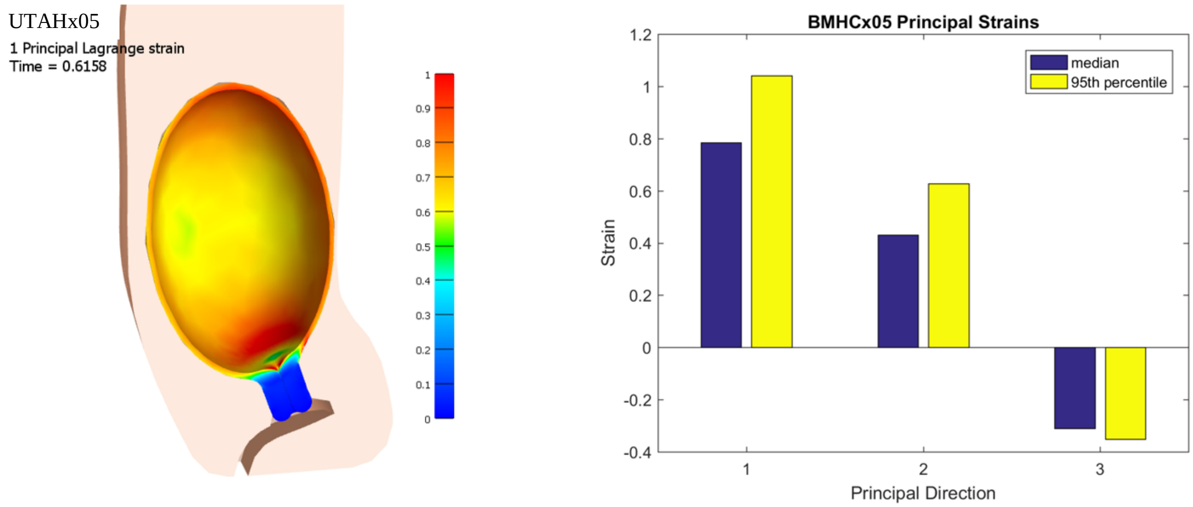

Figure 6-7: Magnitude of strain in the uterus and cervix of a representative patient. The 1st principal strain is plotted throughout the uterus and cervical tissue (left). The median and 95th percentile magnitude of 1st, 2nd, and 3rd principal strains are also shown (right).

Strain varies across patients at the same gestational timepoints (Figure 6-8). In each patient, strain patterns are largely dominated by boundary conditions. For example, Patient UTAHx03 experiences the greatest amount of strain in the lower uterine segment. Patient UTAHx04 has much smaller strain in the lower uterine segment, but undergoes large magnitude strain at the top of the uterus, increasing towards the fundus. Patient UTAHx01 has almost uniform strain throughout the uterus, with slightly larger magnitude in the left and right directions. Both patients UTAHx05 and UTAHx02 have greater strains at the lower uterine segment and posterior uterus, but patient UTAHx05 also has more strain at the fundus, while UTAHx02 has large amounts at the anterior uterus. Median and 95th percentile strain magnitudes for each patient in this study are shown in Figure 6-8.

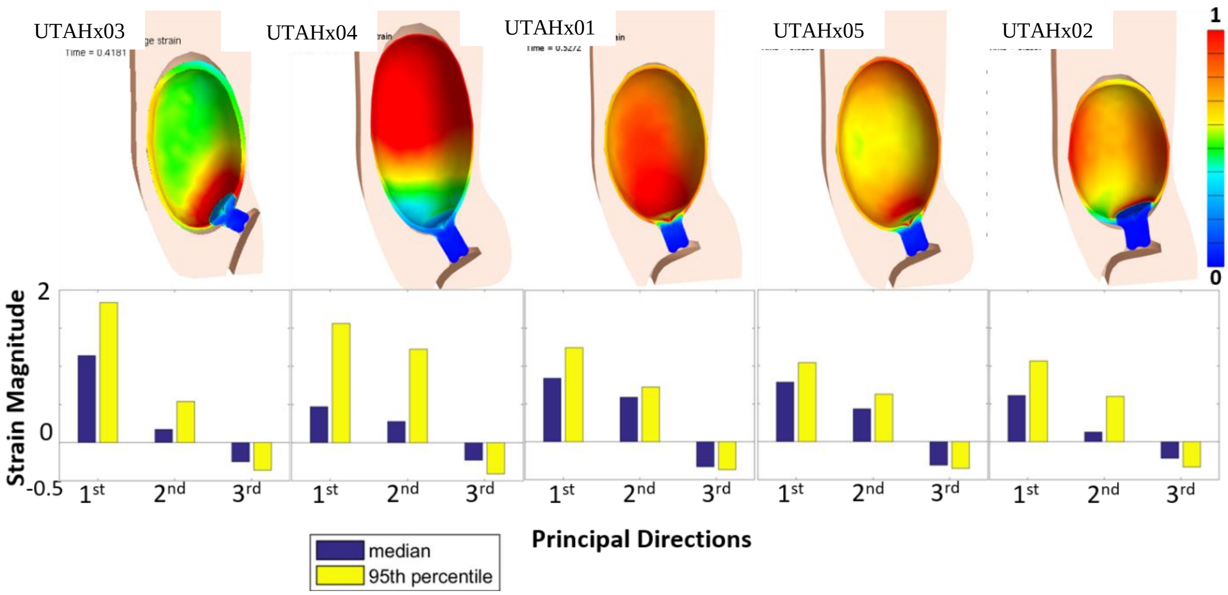

Figure 6-8: Magnitude of strain in the uterus and cervix at all 5 patients, in order from largest to smallest magnitude. The 1st principal strain is visualized throughout the uterus and cervix (top). The median and 95th percentile magnitude of 1st, 2nd, and 3rd principal strains are shown (bottom).

The range of magnitudes of strain in the patients studied is extremely large. For example, Patient UTAHx03 has a median 1st principal strain that is 243% of that in Patient UTAHx04. Median values for each patient are reported in Table 6-4.

Patient	**Median 1st principal strain [%]**	**Median 2nd principal strain [%]**	**Median 3rd principal strain [%]**
UTAHx01	83.9	58.9	-33.0
UTAHx02	61.2	12.7	-21.9
UTAHx03	114	17.4	-25.1
UTAHx04	47.0	27.9	-22.9
UTAHx05	78.5	43.2	-31.1

Table 6-4: Median principal strain magnitudes for each patient.

6.1.3 Discussion

There is no unifying pattern in uterine tissue strain, or even in patient anatomies. Because we created an empty abdominal cavity for the uterus to expand into, the strain pattern in each patient model is largely dominated by boundary conditions. For example, if a patient's uterus was measured to be mostly spherical at visit 2 and grew by visit 3 to be an ellipse with a major axis much larger than its minor axes, the uterus showed large strains at the fundus and lower uterine segment. On the other hand, if the reference configuration of the patient's uterus was already elliptical, there is more strain in the anterior and posterior or left and right sides of the uterine wall. The lack of a dominant strain pattern in patients emphasizes the need for patient-specific modeling, diagnosis, and treatment in pregnancy, specifically in the case of preterm birth. It is necessary to determine what restricts growth in certain dimensions and drives the shape in each patient.

The pressures required to reach the deformed configuration of patients UTAHx01, UTAHx02, UTAHx03, UTAHx04, and UTAHx05 are 5.27, 1.51, 4.18, 3.59, and 6.16 kPa, respectively. The estimated difference in intrauterine pressure (IUP) between the patients' visits 2 and 3 is only 0.09 kPa[52]. Similarly, the uterine walls in the stretched uterus are thinner than the measured wall thickness from each patient's visit 3 ultrasound scans. Therefore, there must be immense amounts of growth occurring between the two timepoints or interim gestational material properties must be different than those used in this model. Yet so far in the literature, the timeline for if and when uterine hypotrophy stops and the myometrial wall thins has seen much debate[10,12–14]. Future studies should be performed to determine the amount of increased mass of the uterus throughout gestation in order to properly incorporate growth into computational models. Similarly, it is necessary to determine where this growth should be added. It is widely believed that changes in external stimulus such as the relative level of physical stress cause a predictable adaptive response in all biological tissue, often in the form of hypertrophy[56,156,166–168]. Therefore, future iterations of this model may implement tissue growth at the sites of highest tissue stretch.

We acknowledge that the results in this study are limited solely to qualitative kinematics, as unrealistic tissue properties and boundary conditions are used here.

6.1.4 Conclusions

We present here a method for investigating the kinematics of the changing uterus throughout gestation in a low-risk patient cohort. In this study, we calculate the 1st, 2nd, and 3rd principal strains in the uterus as the tissue stretches from a reference configuration at 16 weeks to a deformed configuration at 24 weeks, as well as the intrauterine pressure required to do so.

Our simulation result supports the need for the inclusion of uterine tissue hypertrophy in patient-specific simulations of pregnancy. In future studies, we will also investigate uterine changes throughout pregnancy in a high-risk cohort and compare the changes to those presented here.

6.2 High-risk cohort

Patient-specific data was obtained from a high-risk cohort in Columbia University Irving Medical Center's Randomized Trial of Pessary in Singleton Pregnancies With a Short Cervix (TOPS) clinical trial. The objective of TOPS is to determine whether the Arabin pessary reduces the risk of preterm birth in women with a singleton pregnancy and a short cervix. The Arabin pessary (Figure 6-9) is a silicone donut-shaped device fit onto the outside of a woman's cervix (Figure 6-10) with the hope that it may mechanically support the cervix to prolong gestation.

Figure 6-9: Silicone Arabin pessary[169]

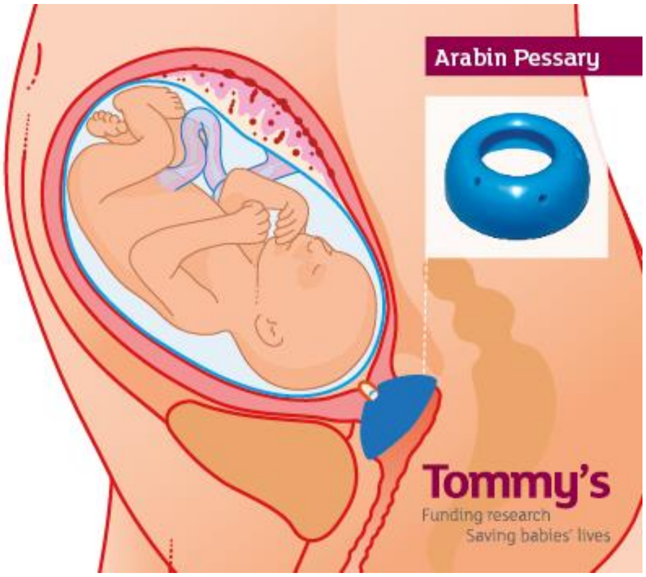

Figure 6-10: Arabin pessary inserted into the vagina and around a patient's cervix in order to mechanically support and keep it closed[170].

The success of the Arabin pessary at reducing preterm birth rates remains controversial. Though its mechanism of action is unknown, its proponents have several hypotheses how it might help to prevent spontaneous preterm birth and possibly preterm premature rupture of membranes (PPROM). It has been suggested the pessary encompasses the cervix and changes the uterocervical angle to become more acute, thereby preventing direct pressure on the membranes at the level of internal cervical os and on the cervix itself, and instead transferring the weight of the fetus onto the lower uterine segment[100,171,172]. It may also help keep the cervix closed, and preserve the cervical mucus plug which may keep out infection and therefore reduce inflammation in the fetal membranes[173]. In the past decade, there have been six major randomized controlled trials to determine the pessary's effectiveness with conflicting conclusions:

1. The 2012 PECEP study with 385 women placed pessaries in singleton pregnant women with a cervical length $\leq$ 25mm measured between 18-22 weeks gestation. The primary

outcome was spontaneous preterm labor before week 34. This rate was significantly lower in the pessary group (6%) vs. the control group (27%)[103].

2. In 2013, Hui et al. published a study for pessary placement in singleton pregnancies with a cervical length ≤ 25mm at 20-24 weeks gestation. The primary outcome of this study was the same as the PECEP study, but no significant differences were observed in the rate of preterm birth before 34 weeks (9.4% vs. 5.5%)[136].
3. Nicolaides et al published a trial in 2016 where 935 patients with cervix ≤ 25mm between 20 weeks 0 days and 24 weeks 6 days were recruited. The primary outcome was the same as the two previous studies, and there were no significant differences between the pessary and control groups (12% vs. 10.8%, respectively)[105].
4. The ProTWIN study in 2013 placed pessaries in 808 women with a multiple pregnancy regardless of cervical length at 16-22 weeks gestation. The primary outcome was deficient perinatal outcome and it did not differ significantly in both groups (13% in the pessary group vs. 14% in the control group)[99].
5. A second PECEP study was conducted in 2016 on 137 asymptomatic women with twin gestations, regardless of their obstetric history and with cervix ≤25mm between 18-22 weeks. The rate of spontaneous preterm birth in gestations shorter than 34 weeks was significantly lower in the pessary group (16.2% vs. 39.4% in the control group)[101].
6. A second Nicolaides study was conducted in 2016 on 1180 pregnant women with twin gestations. There were no significant differences in the rate of preterm delivery before 34 weeks (13.6% vs. 12.9%), perinatal death (3.4% vs. 30.7%), low weight < 2500g (77.2% vs. 0.1% 69), or adverse neonatal event (15.2% vs. 11.9%)[104].

With such inconclusive evidence, there is a need for further investigation into the mechanism and success of the Arabin pessary, which we aim to provide in this study. This study is an ancillary to the TOPS trial, called ATOPS. The objective of this study is to quantify the mechanical environment of pregnancies complicated by a short cervix and randomized in the TOPS study with ultrasound imaging and aspiration. ATOPS has three aims:

1. To determine the biomechanical properties of a prematurely remodeled cervix.
2. To determine the impact of pessary placement on the biomechanical properties of a prematurely remodeled cervix and establish if the pessary reduces the mechanical load on the cervix through computer modeling informed by ultrasonographic measurement and cervical stiffness measurements.
3. To determine if the differences in the cervical biomechanical properties after pessary placement lead to improved birth outcomes as compared to the progesterone only group.

A similar study was recently done by the PECEP trial investigators, where 33 women with a short cervix and 24 reference women with normal cervical length were enrolled and measurements were taken via 2D and 3D ultrasound[174]. The variables evaluated were: cervical length, uterocervical angles, cervical consistency indices (cervical consistency index and cervical length consistency index), cervical volume, and vascular indices. All variables were re-assessed immediately after pessary placement and four to six weeks later in all participants. Immediately after pessary placement, it was observed that cervical length increased, uterocervical angles were narrower and cervical consistency increased significantly. When the magnitude of change in cervical variables was compared over time between the reference group and the study group, median CL had increased in the study group (1.47 mm) while it had shortened in the reference group (-2.56 mm).

We hypothesize that while the pessary will increase cervical length and adjust uterocervical angle, but increased pressure on the outer cervical tissue may cause inflammation, or even prostaglandin release leading to premature cervical tissue remodeling[122–124]. We also hypothesize that the cervical pessary may not be necessary in the case of patients with a short but stiff cervix, and should only be required in those with both a short and soft cervix.

6.2.1 Methods

6.2.1.1 Patient recruitment

Deidentified B-mode ultrasound images and cervical aspiration pressure measurements were obtained from 24 female patients 18-45 years old with a singleton pregnancy. All subjects were recruited from the Columbia University Irving Medical Center's A Randomized Trial of Pessary in Singleton Pregnancies With a Short Cervix (TOPS) clinical trial cohort and provided written, informed consent. This study was therefore called the Ancillary to the TOPS trial (ATOPS). In order to qualify for ATOPS, patients must be enrolled in the TOPS trial. They must have a gestational age at randomization between 16 weeks 0 days and 23 weeks 6 days based on clinical information and evaluation of the earliest ultrasound. Cervical length on transvaginal examination must be less than or equal to 20mm within 10 days prior to randomization by a study-certified sonographer. There is no lower cervical length threshold.

Exclusion criteria include the following: cervical dilation of 3 cm or greater on digital examination, evidence of prolapsed membranes beyond the external cervical os, fetal anomaly or imminent fetal demise including lethal anomalies, or anomalies that may lead to early delivery or increased risk of neonatal death e.g., gastroschisis, spina bifida, serious karyotypic abnormalities, previous spontaneous preterm birth, planned treatment with intramuscular 17-α hydroxyprogesterone caproate, placenta previa, active vaginal bleeding greater than spotting at the time of randomization, symptomatic, untreated vaginal or cervical infection, active, unhealed herpetic lesion on labia minora, vagina, or cervix, rupture of membranes, more than six contractions per hour, known major Mullerian anomaly of the uterus (specifically bicornuate, unicornuate, or uterine septum not resected), any fetal/maternal condition which would require invasive in-utero assessment or treatment, for example significant red cell antigen sensitization or neonatal alloimmune thrombocytopenia, major maternal medical illness associated with increased risk for adverse pregnancy outcome or indicated preterm birth (treated hypertension requiring more than one agent, treatment for diabetes prior to pregnancy, chronic renal insufficiency defined by creatinine >1.4 mg/dL, carcinoma of the breast, conditions treated with chronic oral glucocorticoid therapy, lupus, uncontrolled thyroid disease, and New York Heart Association(NYHA) stage II or greater cardiac disease, planned cerclage or cerclage already in place, planned indicated delivery prior to 37 weeks, and allergy to silicone.

As participants in the TOPS trial, patients were randomized to receive usual care (vaginal progesterone), or usual care + an Arabin pessary. In this selected cohort, 15 patients received progesterone and a pessary and the remaining 9 were treated with progesterone only. Of the 24 patients recruited, 7 delivered preterm, 1 received an emergency cerclage, 1 received dilation and evacuation, 13 delivered at term, and 2 have not yet delivered. Obstetric and gynecologic history, age, race, body mass index, smoking history, and outcome of the current pregnancy were recorded for all patients.

6.2.1.2 Data acquisition

Each subject underwent an ultrasound exam at two different gestational timepoints: 16+0weeks to 23+6weeks and again at a follow-up visit 5-9 weeks later. If the patient was randomized to the pessary treatment group, a scan was taken again immediately post-insertion. Six B-mode ultrasound images of the uterus and cervix were obtained to measure maternal anatomical dimensions during each visit – five transabdominally and one transvaginally. The five transabdominal images included a transabdominal sagittal view of the uterus from the fundus to the lower uterine segment, a transabdominal axial view of the uterus from the left to right, and uterine wall thickness at the fundus, anterior, and left/right sides. The transvaginal image recorded a sagittal view of the cervix and lower uterine segment. All images were taken by any one of three designated study obstetricians. Transvaginal measurements followed the CLEAR protocol, and transabdominal measurements followed the protocol described by Saul et al. In the initial publication of transabdominal cervical length measurement, upon which subsequent studies and US cervical length screening recommendations have been based[28,164].

Transabdominal images were acquired using the Extended View panoramic imaging feature on the GE Voluson E8 and E10 ultrasound systems, which automatically registered adjacent images together as the probe was swept across the abdomen. In the extended sagittal view transabdominal scan, dimensions measured were uterus longitudinal diameter (UD1), uterus anterior-posterior diameter (UD23), the perpendicular offset of the cervical internal os from the uterus longitudinal diameter (PCO) (Figure 6-11:A). In the extended axial view, dimensions measured were transverse uterine diameter (UD4) (Figure 6-11:C). Uterine wall thickness measurements were taken from regular field-of-view ultrasound images and included the uterine wall thickness at the fundus (UT1), uterine wall thickness at the anterior uterine wall (UT2), and uterine wall thickness at the left or right wall (UT3) (Figure 6-11:B-C,E). From the transvaginal images, uterine wall thickness at the lower uterine segment (UT4), cervical length (CL), cervical outer diameter (CD1), cervical canal diameter (CD2), and the anterior uterocervical angle (AUCA) were measured (Figure 6-11:F). Because these high-risk patients often have a cervical funnel, a reference cervical length (CLref) was also taken in order to determine what may have been the initial length of the cervix. All measurements were made on deidentified images after each exam using image-processing software Fiji[165].

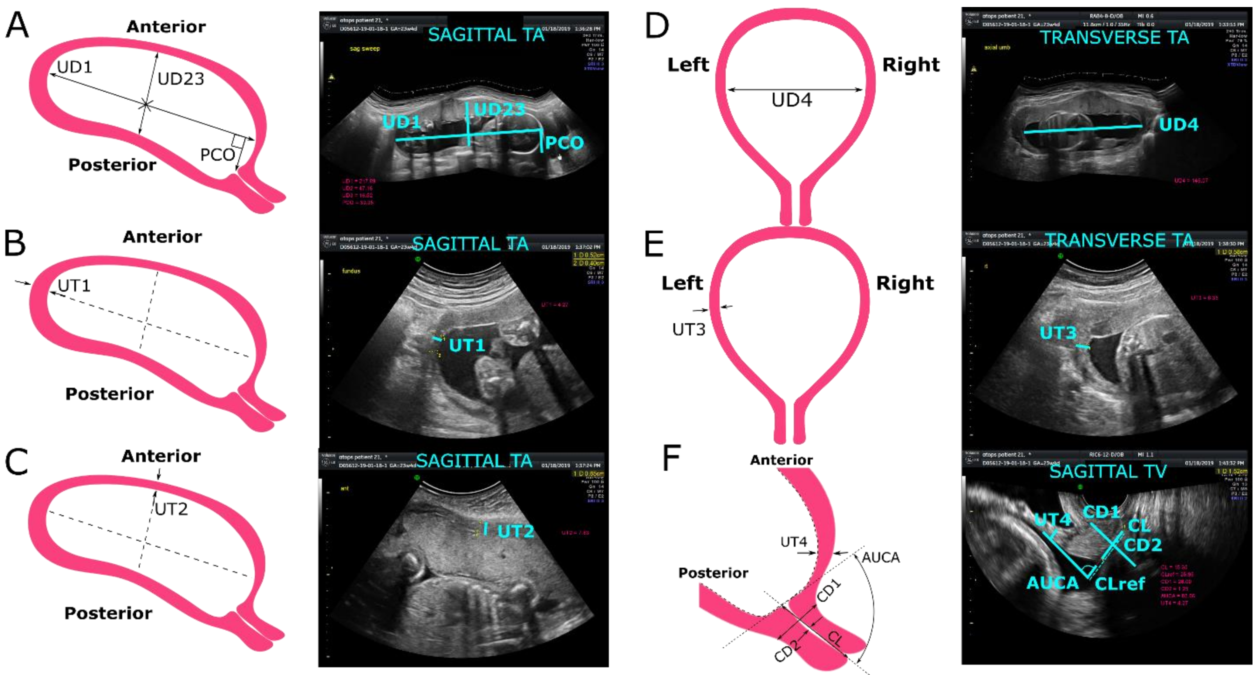

Figure 6-11: Maternal anatomy dimensions taken from sagittal transabdominal (A-C), transverse transabdominal (D-E), and sagittal transvaginal (F) ultrasound.

In addition to ultrasound dimensions, we also measured the mechanical strength of the uterine cervix with a non-invasive mechanical aspiration device that can be applied during a speculum exam[146,175,176]. The clinicians measured cervical stiffness by inserting the aspirator probe into the vaginal canal and placing the end of the probe lightly on the anterior lip of the cervix at 12 o’clock (Figure 6-12).

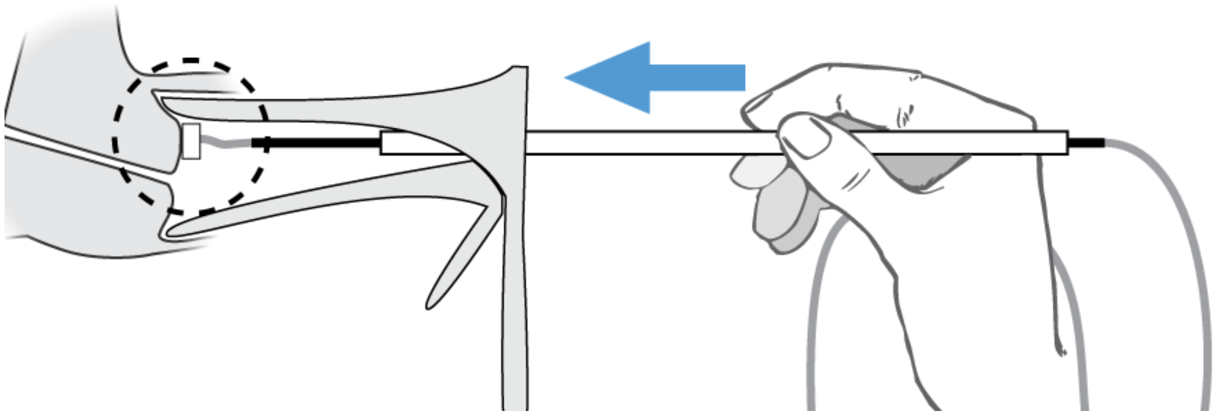

Figure 6-12: Clinical use of the cervical aspiration device. The probe is inserted into the vaginal canal during a speculum exam and cervical stiffness is measured on the anterior cervical lip.

Once the aspirator has been placed on the cervix, a foot pedal is pressed to apply a negative vacuum to the tissue. The vacuum pulls the external os tissue a distance of 4mm into the probe and records the corresponding pressure required to do so. Corresponding closure pressure will be shown on the aspiration control unit. A small closure pressure correlates with a soft cervix, while a large closure pressure signifies a stiffer cervical material. Normal aspiration pressure readings for various timepoints in gestation are shown in Figure 6-13, where patients at ATOPS randomization should have a pressure of approximately 90 mbar.

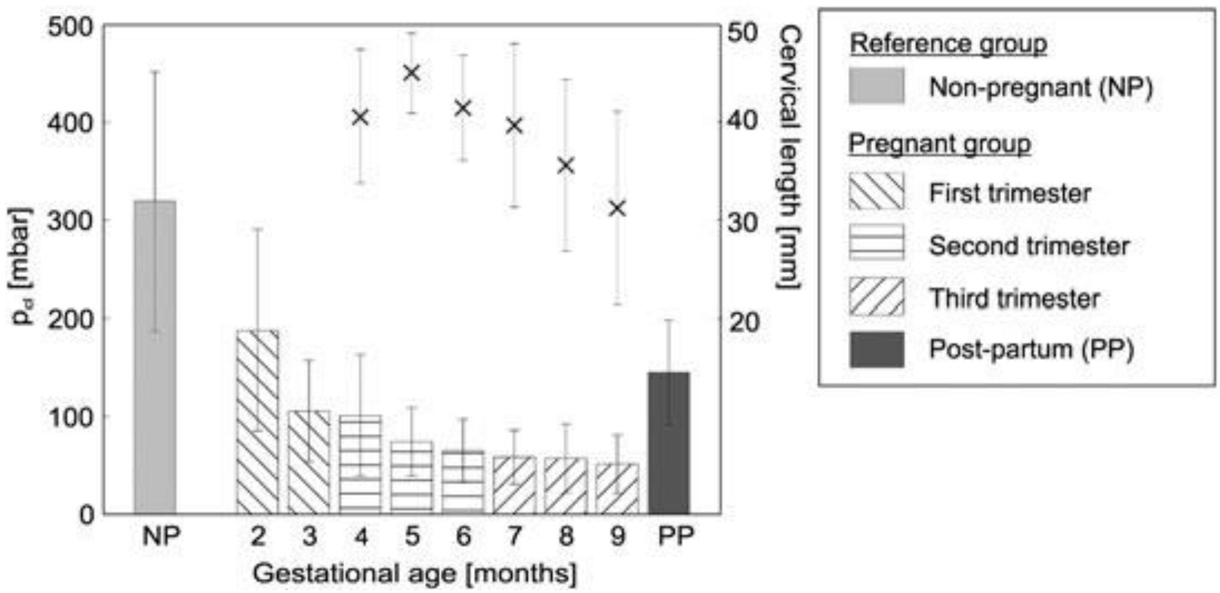

Figure 6-13: Collective results of closure pressure p_{cl} of the reference group and during gestation: Closure pressure p_{cl} of nonpregnant (NP, left) and pregnant women during pregnancy (months 2–9) and postpartum (PP, right) are shown as vertical bars – crosses indicate cervical length (CL), and the values refer to the second vertical axis on the right. For all values, means, and standard deviations are reported[146].

6.2.1.3 3D CAD models of the lower uterine segment

The maternal geometric parameters of 5 patients in their first clinical visit were converted into CAD geometries with a custom computer script (Trelis Pro 15.1.3, csimsoft LLC). Of these 5 patients, 3 were treated with a pessary and 2 were not. In the treatment subgroup without a pessary, one patient delivered preterm and one patient delivered at term. In the pessary arm, two patients delivered at term and one preterm. Geometries of the uterus, cervix, fetal membranes, vaginal canal, and abdomen were created with Boolean addition and subtraction of geometric primitives. In this study, we chose to analyze a quarter model of the maternal anatomy due to assumed symmetries in the left-right direction, and because we believe the upper half of the uterus can be simplified as it is farther away from the area of interest, the cervix (Figure 6-14).

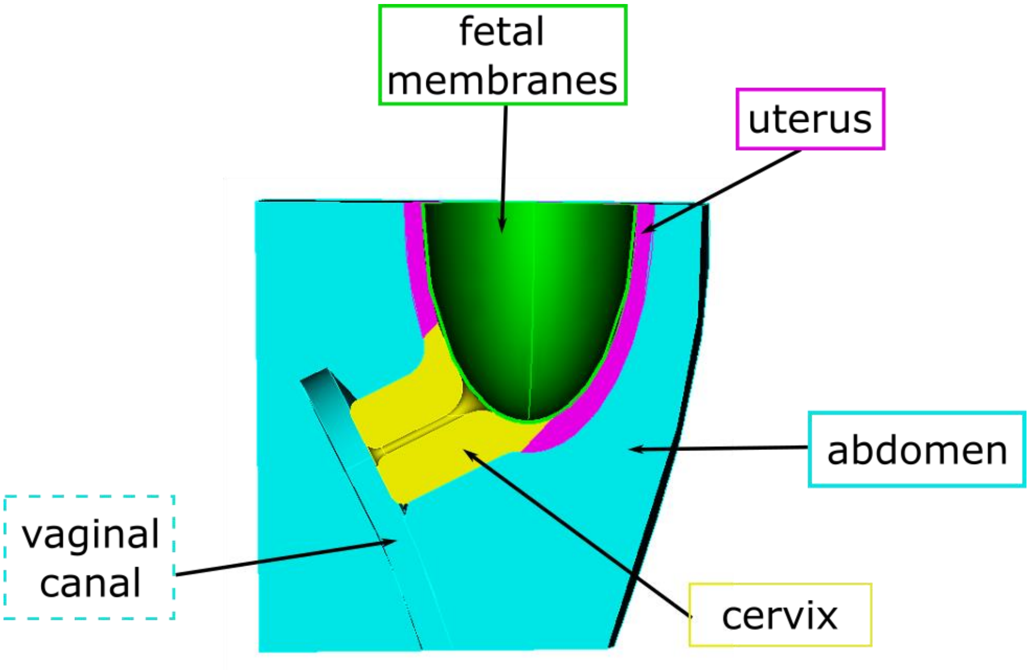

Figure 6-14: 3D representation of the environment of pregnancy. The model includes the uterus (magenta), cervix (yellow), fetal membranes (green), and a surrounding abdomen with a vaginal canal cutout (cyan).

Dimensions and tissue stiffness for each patient are given in Table 6-5. The uterus was built by transforming two spherical shells into ellipsoids. The interior uterus was scaled to the diameters obtained from the ultrasound data. The outer shell was then scaled, translated, and rotated to accommodate uterine wall thickness in the anterior-posterior, superior-inferior, and left-right directions.

Patient	P3	P4	P7	P11	P19
Treatment group	Progesterone only	Progesterone + Pessary	Progesterone + Pessary	Progesterone only	Progesterone + Pessary
Gestational age at randomization [weeks+days]	21+0	19+3	19+2	23+4	21+5
Gestational age at delivery [weeks+days]	23+3	39+2	28+0	39+2	38+1
Average aspiration closure pressure [mbar]	34.5	107.5	46.5	160.5	48.7
UD1 [mm]	141.91	144.68	158.04	225.29	199.26
UD23 [mm]	69.89	79.35	83.06	81.00	72.97
UD4 [mm]	154.22	147.81	155.22	160.36	149.07
UT1 [mm]	8.07	9.25	4.97	9.75	7.02
UT2 [mm]	5.44	9.58	4.66	9.01	7.28
UT3 [mm]	10.78	5.93	7.80	7.12	8.87
UT4 [mm]	9.19	6.01	4.07	5.70	3.71
PCO [mm]	14.99	21.12	8.22	12.58	28.9
AUCA [°]	109.14	72.92	88.35	87.74	89.33
CL [mm]	13.15	16.19	9.19	20.60	19.73
CLref [mm]	39.56	36.10	33.28	42.84	27.16
CD1 [mm]	37.06	18.07	29.21	29.13	33.21
CD2 [mm]	1.68	1.28	0.82	1.09	0.61

Table 6-5:

The cervix was built by creating a cylinder representing the diameter of the inner canal and subtracting that volume from a larger cylinder representing the outer cervical diameter and the reference cervical length. The resultant hollow cylinder was then moved and rotated according to posterior cervical offset and anterior cervical angle. The cylinder was rounded at its corners to match the anatomical rounding of the uterocervical junction and to replicate the roundness of the most exterior end of the cervix (i.e. external os). Then, the vaginal canal was built by fitting a spline to three vertices located at the outside edges of the external os and one vertex at the approximate location of the vaginal introitus and the fetal membrane was generated with uniform thickness based on the contours of the inner uterine wall. Finally, the model was reduced to a quarter model by cutting down the sagittal plane at the center of the abdomen and at the axial plane at the center of the uterine ellipsoid. The inferior left quarter of the model was used for analysis.

6.2.1.4 Finite element mesh generation

Linear meshes were generated using the automatic and manual meshing tools in Trelis Pro (v16.1.1, csimsoft LLC). The fetal membranes were meshed with hexahedral elements, while all other volumes were meshed with tetrahedral elements. Geometries were then imported into FEBio (v2.8.5) and the mesh was converted from linear to quadratic. Mesh properties varied from model to model, and an example of P3 is given in Table 6-6 and is shown in Figure 6-15. All volumes except the fetal membranes were meshed with linear tetrahedral elements. The fetal membranes were meshed as a single continuous layer of linear hexahedral elements with a thickness of 1mm and an interval of 40 hex elements along its edge.

	Total	Uterus	Membrane	Abdomen	Cervix
Element Type	-	Tet	Hex	Tet	Tet
Element Count	111,038	37,085	2,400	45,150	26,403
Average Element Volume	-	2.44 mm^3	4.56 mm^3	54.7 mm^3	0.982 mm^3

Table 6-6: Mesh properties for P3

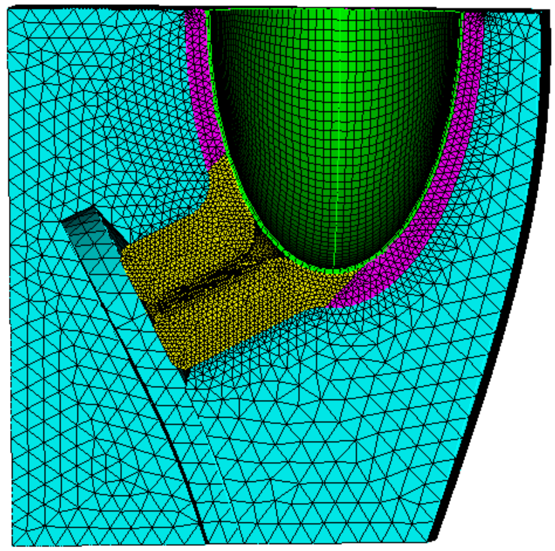

Figure 6-15: Finite element mesh of the uterus (magenta), cervix (yellow), abdomen (cyan), and fetal membranes (green). The uterus, cervix, and abdomen are meshed with quadratic tetrahedral elements and the membranes are meshed using quadratic hexahedral elements.

The mesh density of the cervix was set to a very fine setting by the inherent Trelis element density function, in order to yield the most accurate deformation results for our analysis. Trelis allows for mesh refinement from a factor of 1 (finest) to a factor of 7 (coarsest). The cervix, uterus, and abdomen were all meshed using a factor of 3. In order to allow for a quadratic mesh that allowed for model convergence, the abdomen could not be meshed with a factor larger than 3. This was due to large stresses on the outer cervix at top of the vaginal canal from triangular element faces along the abdomen curvature.

6.2.1.5 Material properties

The cervix and uterus materials were treated as continuously distributed fiber composites with a compressible neo-Hookean groundsubstance. This hyperelastic solid model was developed to describe the tension-compression nonlinearity in human[106] and mouse[107] cervical tissue. Considering not much is known about the multi-axial material behavior of these tissues during pregnancy, we chose to investigate the uterus at term pregnant (PG) tissue properties. The cervix material is informed with patient-specific material parameters based on aspiration closure pressure measurements and the normal measured value of 90mbar. Material parameters are shown in Table 6-7.

Tissue Description	E^{GS} [kPa]	ν^{GS}	β	ξ [kPa]
Uterus	2	0.3	2.71	19
Cervix – P3 (measured)	2	0.3	3	1.8
Cervix – P3 (90mbar)	2	0.3	3	15
Cervix – P4 (measured)	2	0.3	3	27
Cervix – P4 (90mbar)	2	0.3	3	20
Cervix – P7 (measured)	2	0.3	3	2.8
Cervix – P7 (90mbar)	2	0.3	3	9
Cervix – P11 (measured)	2	0.3	3	72
Cervix – P11 (90mbar)	2	0.3	3	24
Cervix – P19 (measured)	2	0.3	3	5
Cervix – P19 (90mbar)	2	0.3	3	22

Table 6-7: Uterine and cervical tissue variables taken from material fits to experimental data and patient-specific cervical aspiration values. Cervical fiber stiffness was determined using inverse finite element analysis. These values are implemented in a continuous fiber distribution material model used in FEBio 2.8.5.

The total Helmholtz free energy density Ψ^{TOT} for the uterine and cervical materials were given by

$$\Psi^{TOT}(\boldsymbol{F}) = \Psi^{GS}(\boldsymbol{F}) + \Psi^{COL}(\boldsymbol{F})$$

Equation 6-2

Where $\boldsymbol{F}$ is the deformation gradient. The free energy density of the ground substance Ψ^{GS}, is given by a standard isotropic, compressible neo-Hookean relation

$$\Psi^{GS} = \frac{\mu}{2}(\boldsymbol{I_1} - 3) - \mu \ln J + \frac{\lambda}{2}(\ln J)^2$$

Equation 6-3

where $I_1 = tr\boldsymbol{C}$ is the first invariant of the right Cauchy-Green tensor $\boldsymbol{C} = (\boldsymbol{F})^T\boldsymbol{F}$ and $J = \det \boldsymbol{F}$ is the Jacobian. μ and l are the standard lamé constants. These lamé constants combine to form the Young's modulus and Poisson's ratio of the ground substance $E^{GS} = \frac{\mu\left(3+\frac{2\mu}{\lambda}\right)}{1+\frac{\mu}{\lambda}}$ and $\nu^{GS} = \frac{1}{2\left(1+\frac{\mu}{\lambda}\right)}$, respectively. The strain energy density for the continuously distributed collagen fiber network is given by

$$\Psi^{COL} = \frac{1}{4\pi}\int_0^{2\pi}\int_0^{pi} H(I_n - 1)\Psi_r^{fiber}(\boldsymbol{I_n}) \sin\phi \, d\phi d\theta$$

Equation 6-4

where the Heaviside step function H ensures fibers hold only tension, $[\theta, \phi]$ are the polar and azimuthal angles in a spherical coordinate system. $I_n = \boldsymbol{n_o} \cdot \boldsymbol{C} \cdot \boldsymbol{n_o}$ is the square of the fiber stretch, where $\boldsymbol{n_o} = \cos\theta \sin\phi \, \boldsymbol{e_1} + \sin\theta \sin\phi \, \boldsymbol{e_2} + \cos\phi \, \boldsymbol{e_3}$ in a local Cartesian basis $\{\boldsymbol{e_1}, \boldsymbol{e_2}, \boldsymbol{e_3}\}$. Ψ^{fiber} is the strain energy density of a collagen fiber bundle given by

$$\Psi^{fiber} = \frac{\xi}{\beta}(\boldsymbol{I_n} - 1)^{\beta}$$

Equation 6-5

where ξ represents the collagen fiber stiffness with units of stress and $\beta > 2$ is the dimensionless parameter that controls the shape of the fiber bundle stiffness curve (here, the fiber strain energy density is cast in a different form than the model presented for the human cervical tissue [177], hence direct comparison can be made by considering the $\frac{1}{\beta}$ prefactor here).

To focus this study on the model sensitivity to patient-specific geometries and material stiffness and not on the cervical or uterine collagen architecture, groundsubstance, or time-dependent properties, we made simplifying adjustments. Both material model fits were conducted on the material behavior after the transient force relaxation response died away. In this present study, we used a randomly distributed collagen fiber network as opposed to a preferentially-aligned collagen fiber network as presented in [106].

Patient-specific cervix material properties (Table 6-7) were determined using inverse finite element analysis informed by cervical aspiration and ultrasound data. An infinitely long cylindrical cervix was created for each patient with measured cervical diameters and aspiration pressure[178]. Cervical collagen fiber stiffness ξ was varied until the tissue was displaced 4mm as it is clinically, while all other material parameters were kept consistent fit to term pregnant human uniaxial tension-compression data reported in [106,108,109]. Models were created for both the patient's measured value and the 5th month of pregnancy assumed normal value of 90mbar.

Uterine material properties represent a material model fit to passive, term pregnant human uniaxial tension data reported in [110]. Fibers in both the uterus and cervix are randomly distributed. They rotate and stretch in the direction of principal stress. Previous work compared the difference between preferential and randomly distributed fiber directionality in an initial finite element model of pregnancy and found a negligible difference between the two scenarios[74]. The outer abdomen was treated as a nearly incompressible neo-Hookean material with a modulus of 100 kPa.

A continuously distributed transversely isotropic fiber-based material model with a compressible Neo-Hookean groundsubstance was used for the membrane in this study based on equibiaxial tensile loading of human amnion[113] was employed for the fetal membrane layer material properties. We transitioned to this model from the previous implementation of an Ogden material in order to incorporate membrane bending as detailed in Section 5.2. The membrane was thickened to 1mm in order to improve model convergence and fit to experimental data of term delivered amnion using inverse finite element analysis in FEBio (Table 6-8Table 4-4). The membrane material has similar constitutive equations as the uterus and cervix, with a slight variation in fiber strain energy density as the coefficient of exponential argument α is not equal to zero,

$$\Psi^{fiber} = \frac{\xi}{\alpha\beta}\left(exp\left[\alpha(I_n - 1)^{\beta}\right] - 1\right)$$

Equation 6-6

Where $\xi > 0$, $\alpha \geq 0$, and $\beta \geq 2$. Fibers were in a circular distribution with a 2D trapezoidal scheme.

Tissue Description	E^{GS} [kPa]	ν^{GS}	α	β	ξ [kPa]
Fetal membranes	1.21	0.38	0.28	3.33	2.22

Table 6-8: Fetal membranes (FM) material properties described by a continuously distributed fiber model.

6.2.1.6 Boundary conditions and loading

Boundary conditions were applied as shown in Figure 6-16.

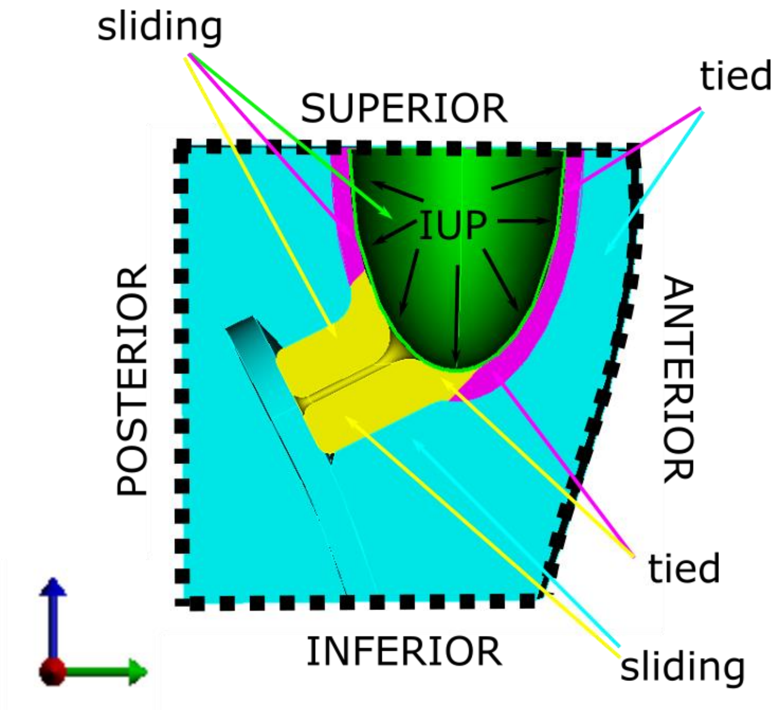

Figure 6-16: Model boundary, contact, and loading conditions.

The abdomen was fixed along its outer surface in the directions normal to its surface, i.e. fixed x on the axis of symmetry and the left side, fixed in y on the anterior and posterior surfaces, and fixed in z on the super and inferior surfaces.

Upon conversion in FEBio from linear to quadratic elements, geometries that were originally node-tied in Trelis were no longer so in the model. Therefore, a tied elastic condition was prescribed between the uterus and abdomen and between the uterus and cervix. The cervix was allowed to slide freely along the abdomen surface to model its interaction with the vaginal wall *in vivo*. The fetal membranes were prescribed a sliding elastic contact condition contact along its outer surface to the inner surface of the uterus to the top surface of the cervix as well as the cervical canal. It was necessary to tie the membranes top elements to the uterus in order to achieve model convergence.

Pressure was applied to the inner surface of the fetal membranes to represent the intrauterine pressure (IUP). A constant mid-gestational intrauterine pressure of 1 kPa was applied across all models in order to compare the effect of maternal geometries and material stiffness only. For comparison of patients with and without a pessary, an additional pressure of 1 kPa was applied to the outer cervix in patients who received the pessary treatment. We investigated the effect of pessary placement by applying this pressure at two locations: on the outer cervix near the internal os and on the outer cervix near the external os. Models with the pessary were compared to those without to determine if the device may reduce cervical loads.

6.2.1.7 Finite element analysis

FE analyses were performed in FEBio 2.8.5 (http://www.febio.org.). Stress and stretch data were plotted as a function of IUP in PostView (PostView 2.3.0), FEBio's post-processor for visualization and analysis. These data were then imported into MATLAB (MATLAB R2019a) for further post analysis. To describe the deformation of the cervix, the median and 95th percentile of right tissue stretch were determined. The right stretch in this context is the symmetric tensor $\boldsymbol{U}$ in the polar decomposition of the deformation gradient $\boldsymbol{F} = \boldsymbol{RU}$. Due to mesh refinement and the use of quadratic elements, each analysis took between 7-10 hours to fully converge.

6.2.2 Results

6.2.2.1 Maternal anatomy and material stiffness

We compared all dimensions of maternal anatomy in this high-risk ATOPS cohort to the low-risk UTAH cohort described in Section 6.1. While both supine and standing measurements were taken in the UTAH cohort, only supine dimensions are compared here as ATOPS patients were scanned in the supine orientation. Uterine diameters increased in all directions throughout gestation for both the low- and high-risk cohorts (Figure 6-17). High-risk patients have similar longitudinal diameters (UD1) to low-risk patients, but both the anterior-posterior diameter (UD23) and left-right diameter (UD4) were on average smaller in high-risk patients than those at low risk.

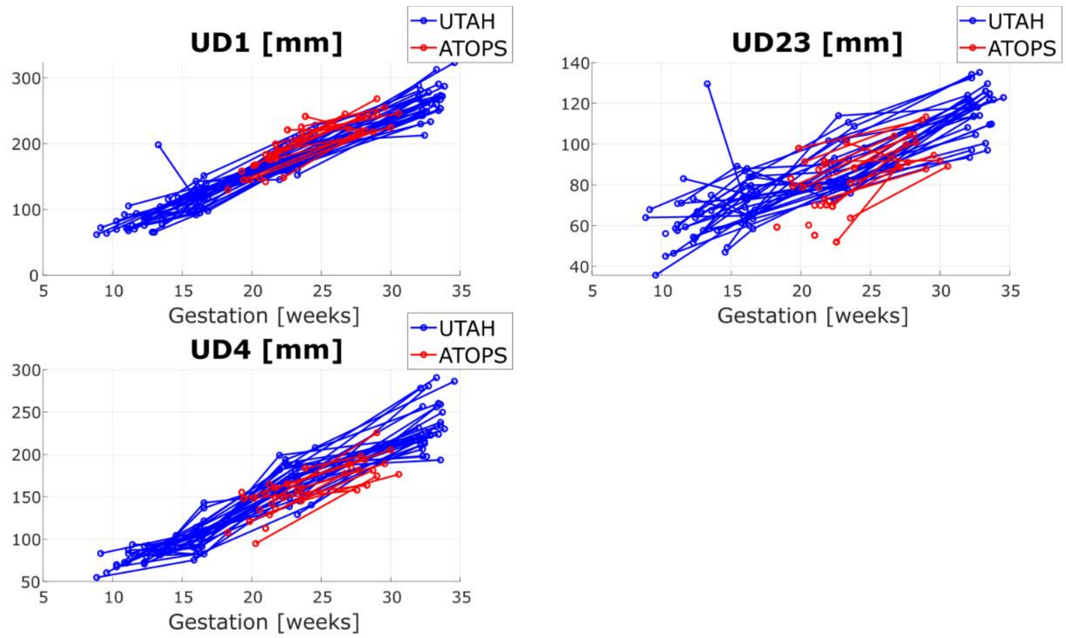

Figure 6-17: Uterine diameters throughout gestation comparing low-risk (UTAH) and high-risk (ATOPS) cohorts. Diameters were measured in the longitudinal direction (UD1), anterior-posterior direction (UD23), and left-right direction (UD4).

We also compared all dimensions of maternal anatomy between patients in the high-risk cohort who received progesterone only and those who received progesterone+pessary. In almost all patients, uterine diameter increased in all directions from visit 1 to visit 2 (Figure 6-18). In patients that received a pessary, most uterine diameters decreased in all directions immediately after pessary insertion but increased again by visit 2.

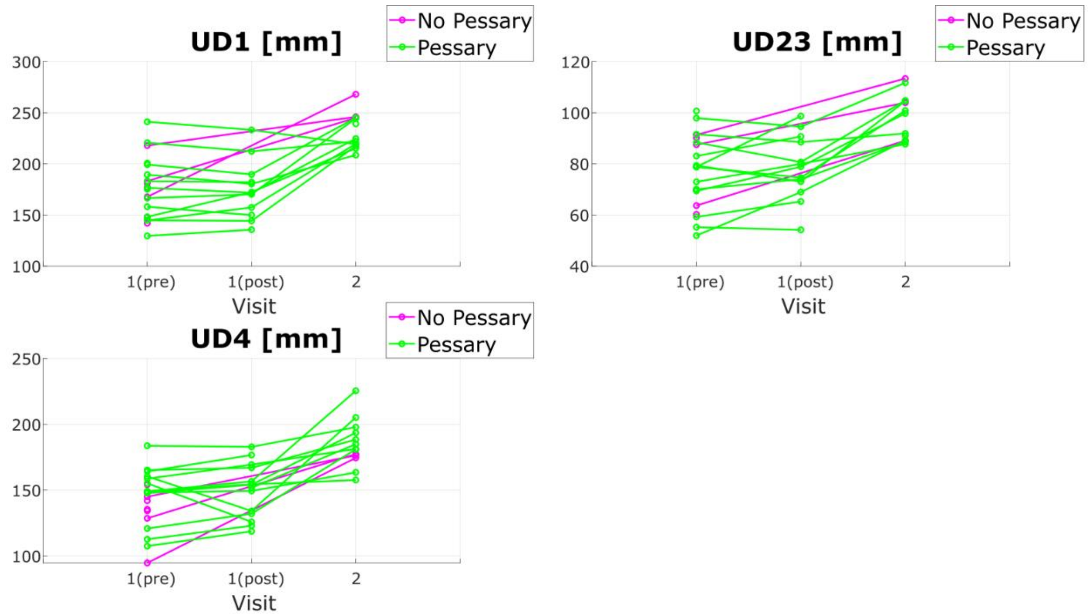

Figure 6-18: Uterine diameters at recruitment and follow-up visits comparing progesterone only and progesterone+pessary treatment groups in a high-risk (ATOPS) cohort. Diameters were measured in the longitudinal direction (UD1), anterior-posterior direction (UD23), and left-right direction (UD4). The pessary subgroup was measured both immediately prior to (Visit 1(pre)) and immediately after (Visit 1(post)) pessary insertion, while the progesterone only group was only measured once during the first visit. Both groups were scanned once at the follow-up visit (Visit 2).

Uterine wall thickness at the fundus (UT1), anterior uterus (UT2), and left/right uterus (UT3) showed no distinct pattern throughout gestation (Figure 6-19). In each patient, they remained relatively constant with some variability. There was no major difference in these wall thicknesses between high- and low-risk patient cohorts. Wall thickness of the lower uterine segment (UT4), however, decreased throughout gestation. Patients in the high-risk (ATOPS) cohort had thinner lower uterine segment walls than those in the low-risk (UTAH) cohort.

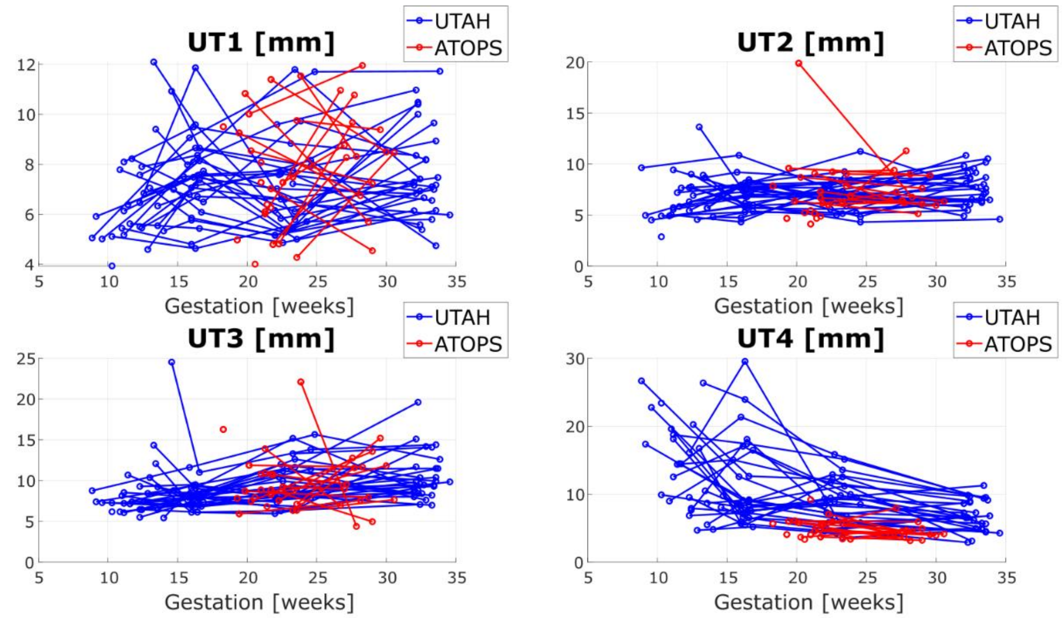

Figure 6-19: Uterine wall thicknesses throughout gestation comparing low-risk (UTAH) and high-risk (ATOPS) cohorts. Wall thickness was measured at the fundus (UT1), anterior wall near the umbilical level (UT2), and left or right wall at the umbilical level (UT3), and at the anterior lower uterine segment (UT4).

In the high-risk cohort, there was no noticeable trend between the progesterone only and progesterone+pessary treatment groups (Figure 6-20). In patients that received a pessary, there was both measured increases and decreases in uterine wall thickness immediately after pessary placement at all locations on the uterus.

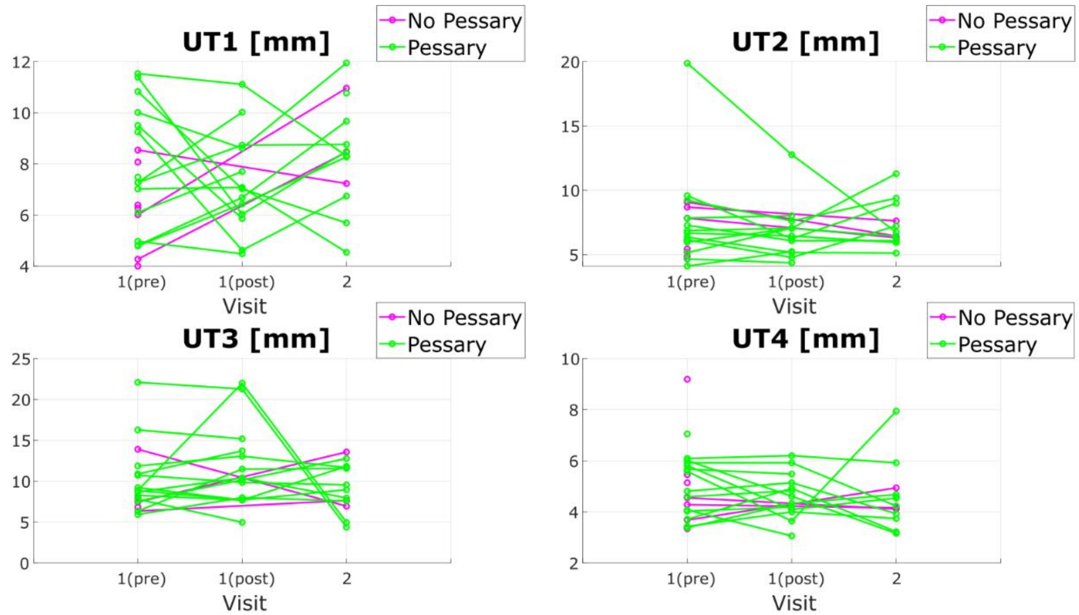

Figure 6-20: Uterine wall thicknesses at recruitment and follow-up visits comparing progesterone only and progesterone+pessary treatment groups in a high-risk (ATOPS) cohort. Wall thickness was measured at the fundus (UT1), anterior wall near the umbilical level (UT2), and left or right wall at the umbilical level (UT3), and at the anterior lower uterine segment (UT4). The pessary subgroup was measured both prior to (Visit 1(pre)) and immediately after (Visit 1(post)) pessary insertion, while the progesterone only group was only measured once during the first visit. Both groups were scanned once at the follow-up visit (Visit 2).

As a short cervical length (CL) was a recruitment criterion for the ATOPS study and exclusion criteria for the UTAH study, it is obvious that cervical length is shorter in the high-risk cohort than in the low-risk cohort (Figure 6-21). In the low-risk patients, cervical length increases in the first and second trimesters and decreases in the third. In high-risk patients, we measured a decrease in cervical length in most patients as the pregnancy progressed. Cervical outer diameter (CD1) experienced an overall positive trend in low-risk (UTAH) patients and a negative trend in high-risk (ATOPS) patients. Overall, cervical volume is lower in the high-risk (ATOPS) patients than in the low-risk (UTAH) patients. In most high-risk patients, cervical volume decreases throughout gestation.

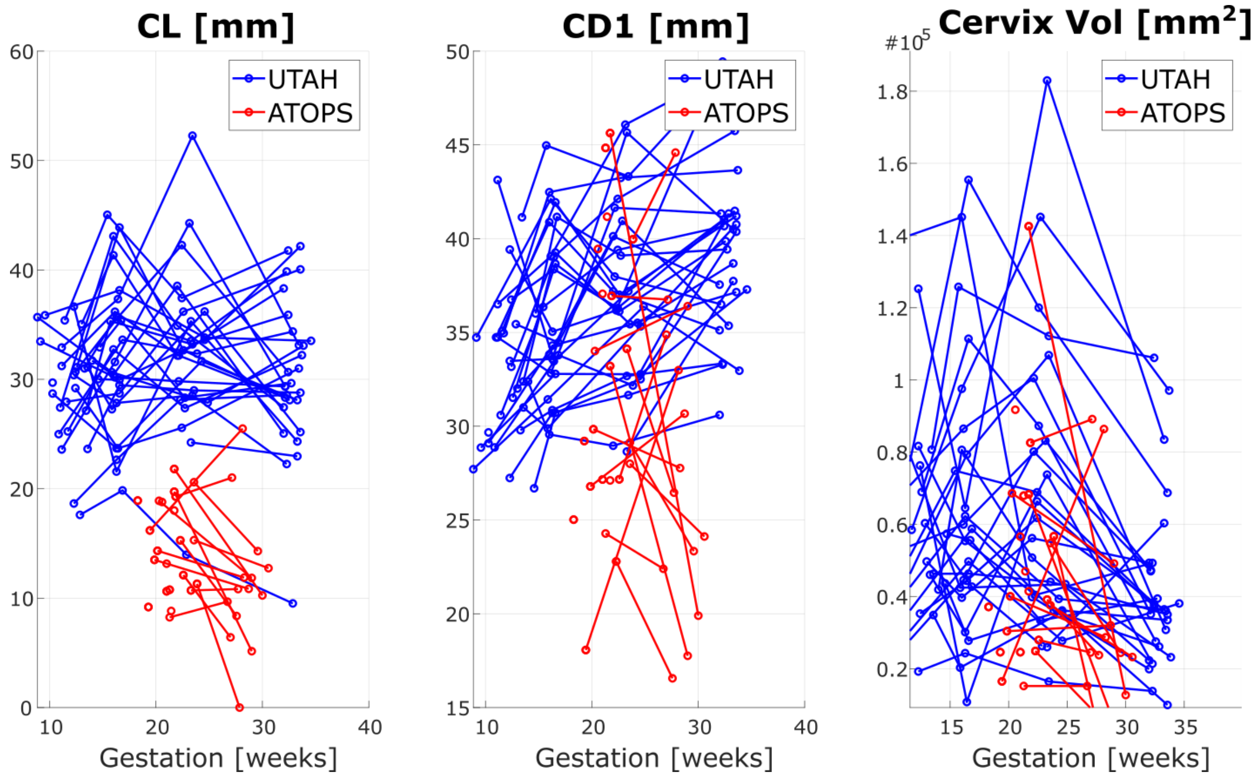

Figure 6-21: Cervical length (CL) and outer cervical diameter (CD1) throughout gestation comparing low-risk (UTAH) and high-risk (ATOPS) cohorts.

Amongst the high-risk (ATOPS) cohort, the data seems to imply that cervical length (CL) increases slightly immediately after pessary placement, but decreases by visit 2 (Figure 6-22). Some patients in the progesterone only group also saw a decrease in cervical length, though this decrease was not as large as in the pessary group. In the progesterone+pessary subgroup, cervical outer diameter (CD1) decreases slightly immediately after pessary placement but then increases by visit 2. In the progesterone only group, cervical diameter did not change as much. In both the pessary and non-pessary groups, it seems that cervical volume decreases throughout gestation.

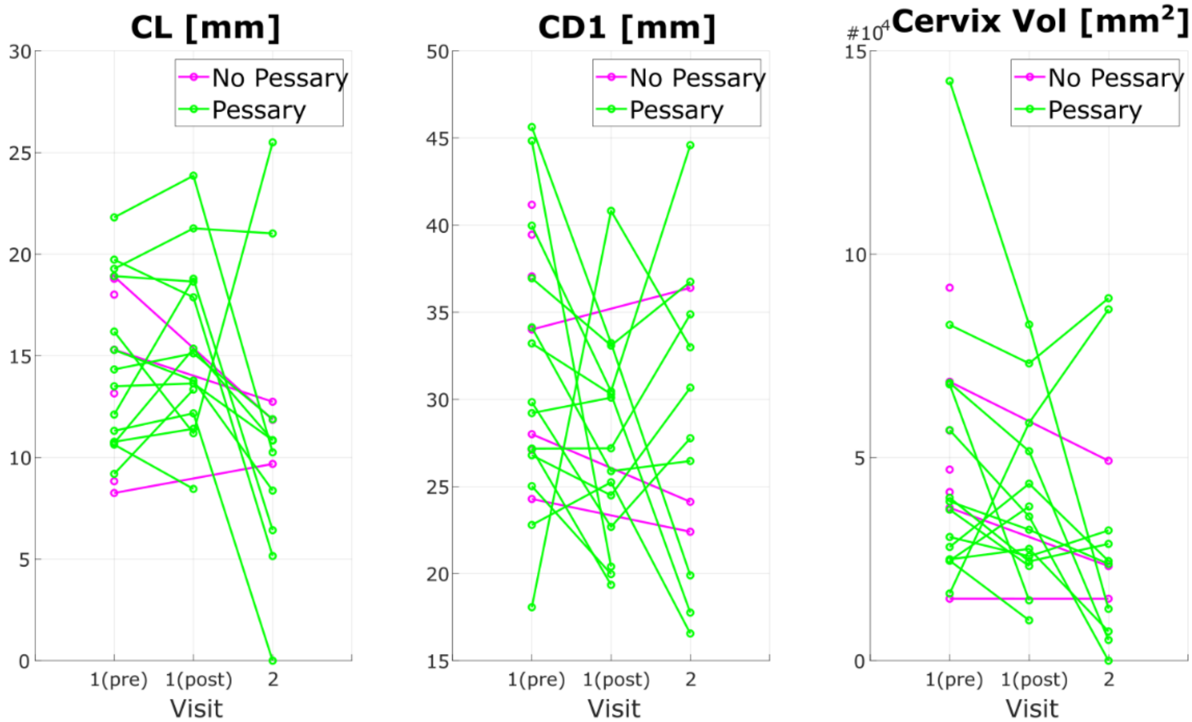

Figure 6-22: Cervical length (CL) and outer cervical diameter (CD1) at recruitment and follow-up visits comparing progesterone only and progesterone+pessary treatment groups in a high-risk (ATOPS) cohort. The pessary subgroup was measured both prior to (Visit 1(pre)) and immediately after (Visit 1(post)) pessary insertion, while the progesterone only group was only measured once during the first visit. Both groups were scanned once at the follow-up visit (Visit 2).

Anterior uterocervical angle (AUCA) and posterior cervical offset (PCO) did not have a noticeable overall trend in either the low- (UTAH) or high-risk (ATOPS) patient cohorts (Figure 6-23). In some low-risk patients, the posterior cervical offset increases in the first trimester, but then decreases after the 16th week of pregnancy. However, this trend is not evident in the overwhelming majority of patients.

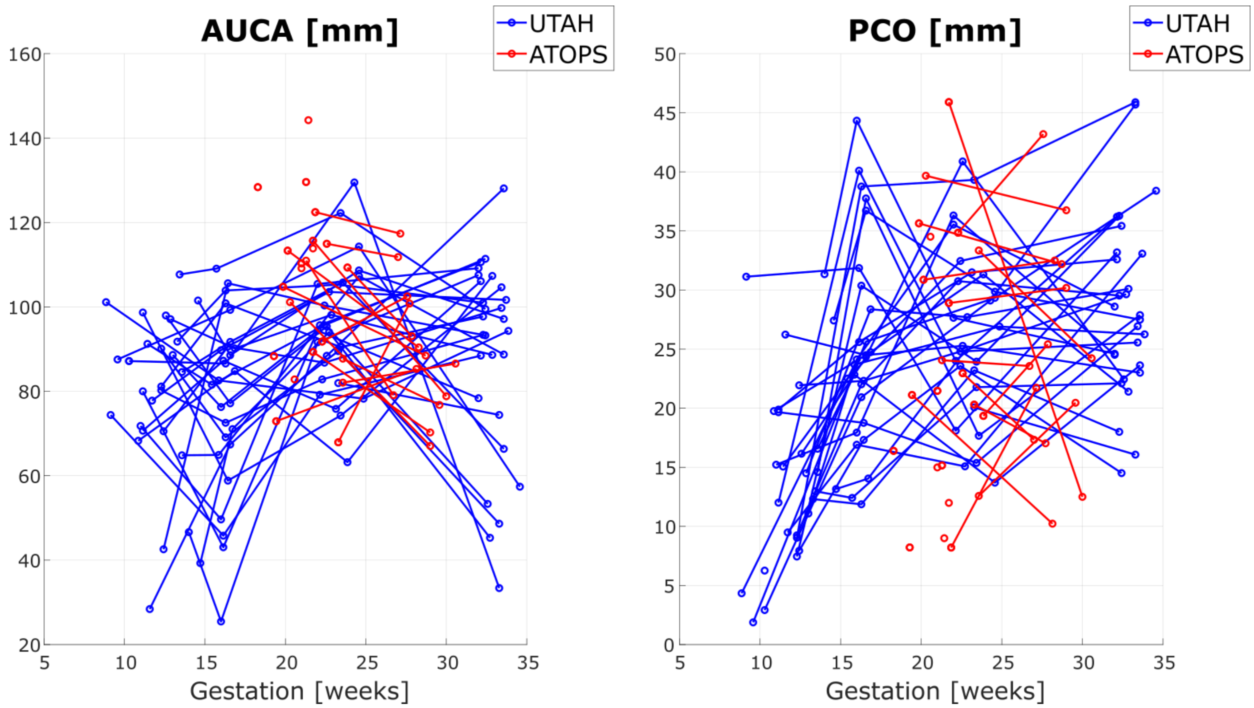

Figure 6-23: Anterior uterocervical angle (AUCA) and posterior cervical offset (PCO) throughout gestation comparing low-risk (UTAH) and high-risk (ATOPS) cohorts.

In the high-risk (ATOPS) cohort, the pessary slightly increased anterior uterocervical angle (AUCA) immediately after pessary placement, but there was a sharp decrease at visit 2 in most patients. In most patients, the pessary moved the cervix more posteriorly immediately after insertion as shown by an increase in posterior cervical offset (PCO). These PCOs also decreased by visit 2.

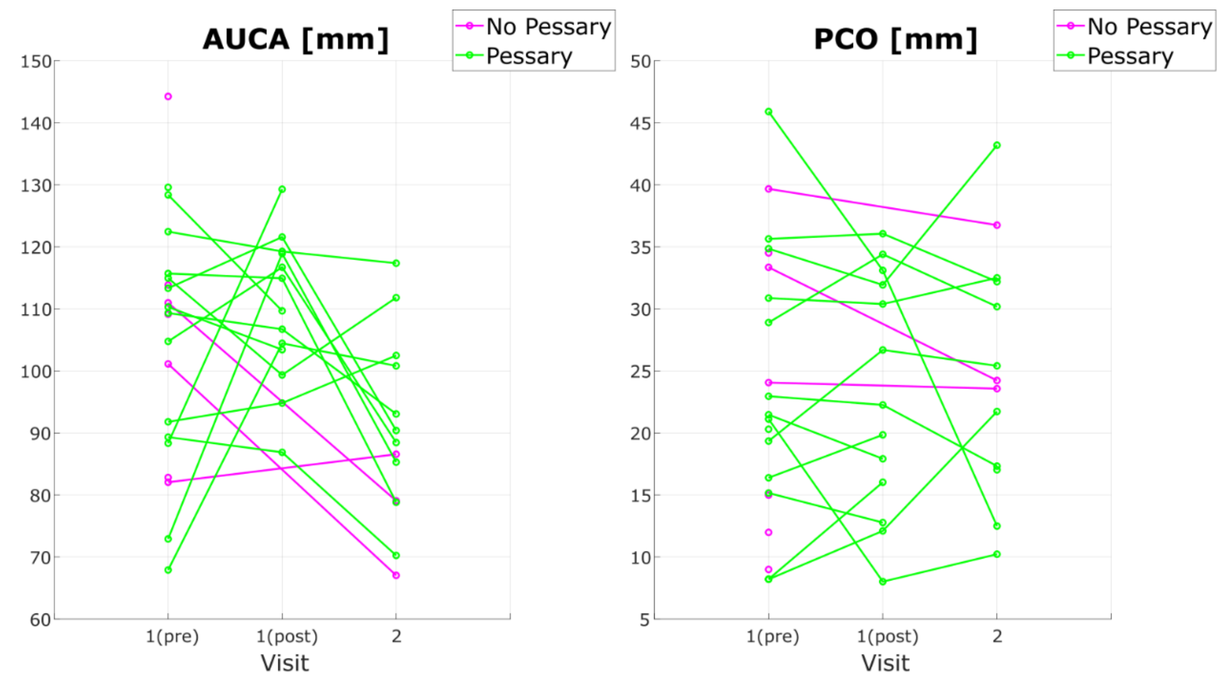

Figure 6-24: Anterior uterocervical angle (AUCA) and posterior cervical offset (PCO) at recruitment and follow-up visits comparing progesterone only and progesterone+pessary treatment groups in a high-risk (ATOPS) cohort. The pessary subgroup was measured both immediately prior to (Visit 1(pre)) and immediately after (Visit 1(post)) pessary insertion, while the progesterone only group was only measured once during the first visit. Both groups were scanned once at the follow-up visit (Visit 2).

We also measured patient-specific cervical stiffness by aspiration measurement in the high-risk (ATOPS) cohort (Figure 6-25). Patients in the progesterone+pessary treatment group were given aspiration measurements prior to pessary placement in visit 2. Results show that in the progesterone only subgroup, all patients experienced a reduction in cervical stiffness between visits 1 and 2. While this occurred in some progesterone+pessary placements, many patients in this subgroup actually saw an increase in cervical aspiration pressure measurements as their pregnancy progressed. Interestingly, when controlling for pessary insertion, cervical stiffness increased with gestation, as seen by the upward sloping blue trendline. This trend was fit to Visit 1 aspiration measurements only in order to rule out the influence of pessary intervention.

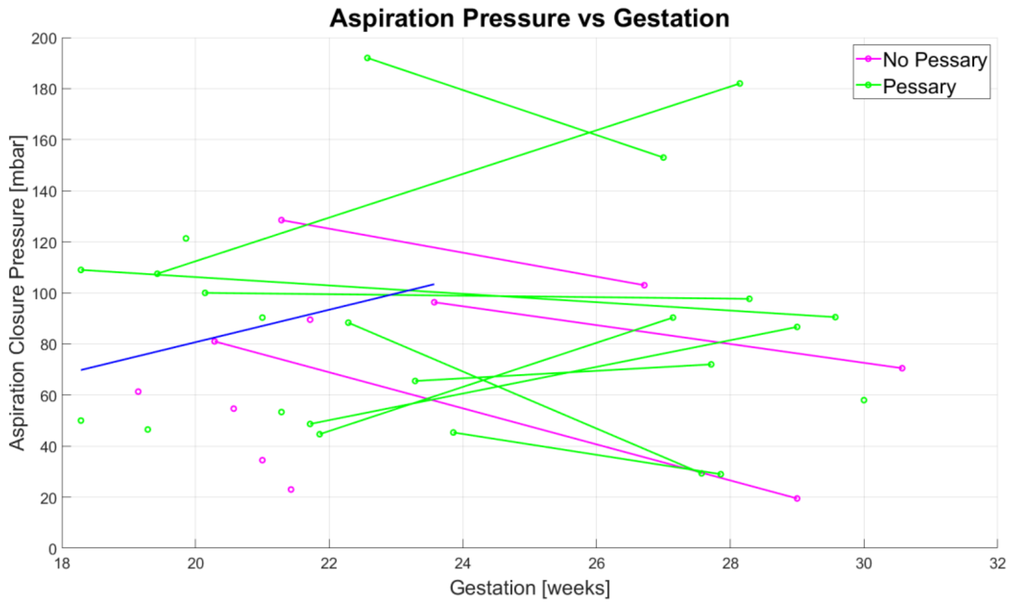

Figure 6-25: Aspiration close pressure p_{cl} at recruitment and follow-up visits comparing progesterone only and progesterone+pessary treatment groups in a high-risk (ATOPS) cohort. Both subgroups were given aspiration once per visit. The pessary group was measured before pessary insertion. The blue line is a trendline fit to the patients' first visit data only in order to rule out the influence of pessary intervention.

Results in Figure 6-26 show aspiration closure pressure as a function of time to delivery. Time to delivery is the number of weeks between the aspiration pressure measurement and when the patient delivered. An overall positive trend is seen between aspiration pressure and time to delivery, as seen by the upward sloping blue trendline. This trend was fit to Visit 1 aspiration measurements only in order to rule out the influence of pessary intervention. This indicates a softer cervix leads to an increased likelihood of a patient going into labor.

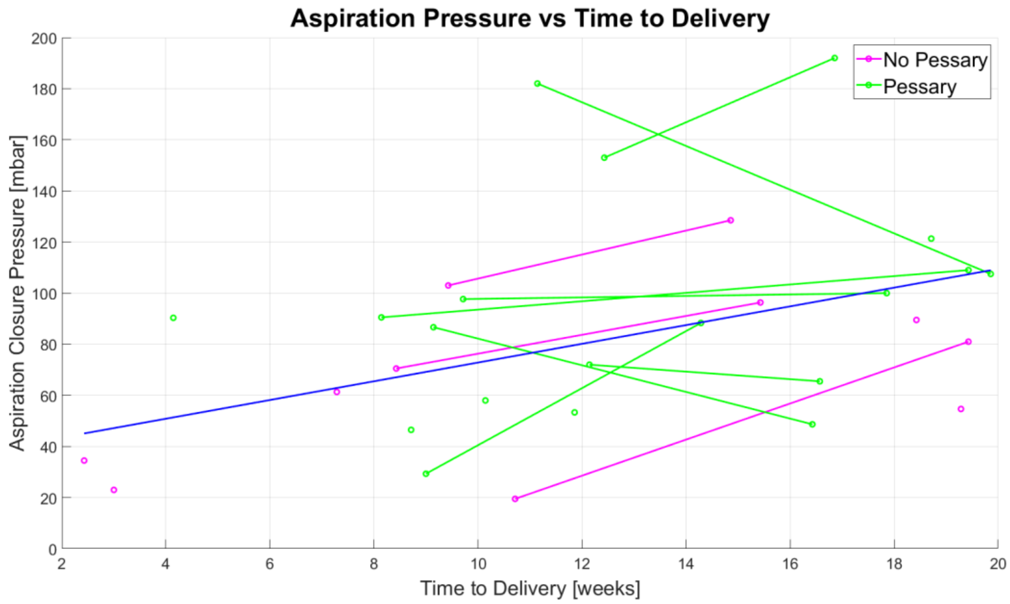

Figure 6-26: Aspiration closure pressure pcl vs. time to delivery comparing progesterone only and progesterone+pessary treatment groups in a high-risk (ATOPS) cohort. Both subgroups were given aspiration once per visit. The pessary group was measured before pessary insertion. The blue line is a trendline fit to the patients' first visit data only in order to rule out the influence of pessary intervention.

6.2.2.2 Finite element analysis

A stiffer cervix, by increase of cervical collagen fiber stiffness ξ, undergoes less deformation than a softer cervix. In P3, for example, the measured cervical aspiration is 34.5mbar, which is softer than the "normal" aspiration pressure of 90mbar[146]. The resultant cervical fiber stiffness for the measured value, ξ= 1.8 kPa, is therefore lower than the normal fiber stiffness of ξ= 15 kPa. The mean, median, and 95th percentile 1st, 2nd, and 3rd principal right stretch in the cervix at its measured stiffness are all higher than those at an assumed normal, higher stiffness (Figure 6-27).

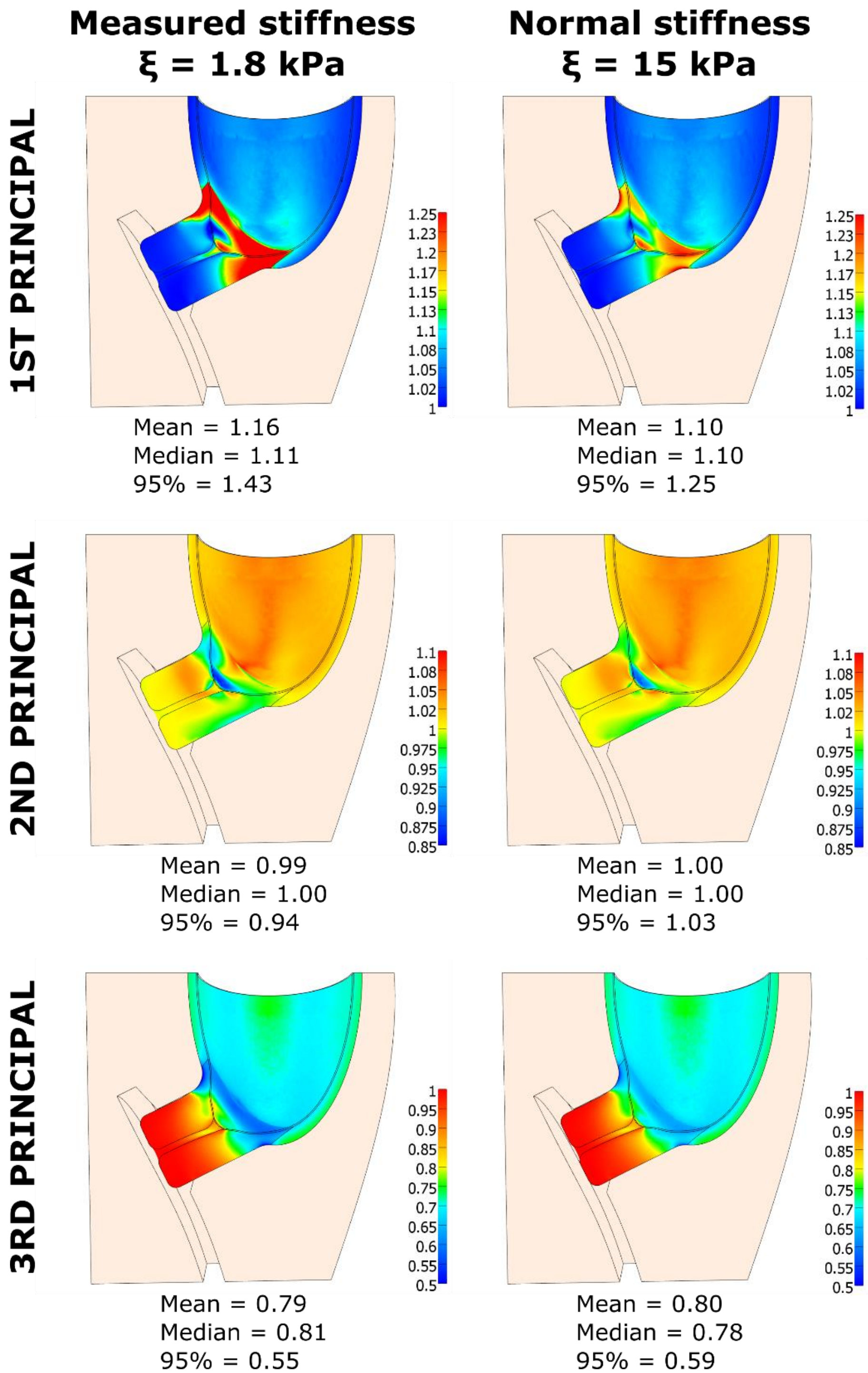

Figure 6-27: 1st, 2nd, and 3rd principal right stretch in P3 model at measured (left) and assumed normal (right) cervical fiber stiffness.

The mean, median, and 95th percentile 1st principal right stretch in the P3 cervix at measured stiffness are 1.16, 1.11, and 1.43, respectively. In the same patient with assumed normal cervical collagen fiber stiffness, the mean, median, and 95th percentile right stretch in the cervix are 1.10, 1.10, and 1.25, respectively. Additionally, stretch in the cervix is not equibiaxial. 1st, 2nd, and 3rd principal right stretch directions for P3 with a measured cervical stiffness are shown in Figure 6-28.

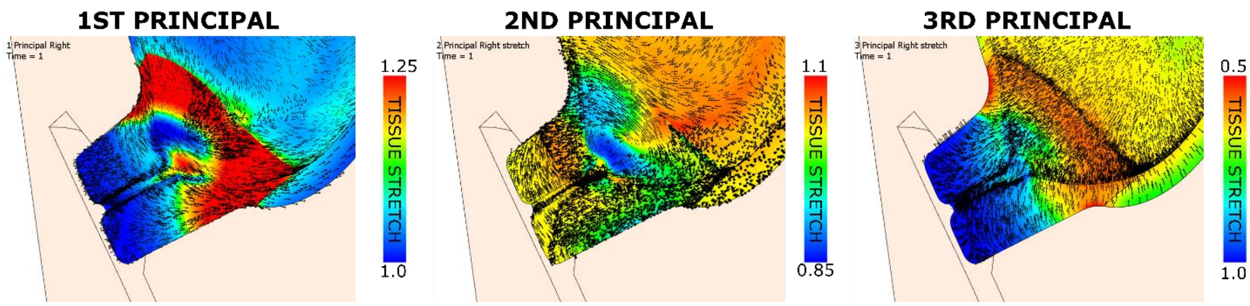

Figure 6-28: Baseline results with vector plots to show stretch directions for 1st, 2nd, and 3rd principal stretch in the uterus and cervix. For 1st principal right stretch, circumferential stretch is exhibited at the internal os while radial stretch is observed at the anterior and posterior sections of the uterocervical interface.

Effective stress shows a similar pattern to the tissue stretch, with concentrations at the internal os and at the top of the cervix (Figure 6-29). The maximum Von Mises stress in the cervix for P3 is 8.7 kPa.

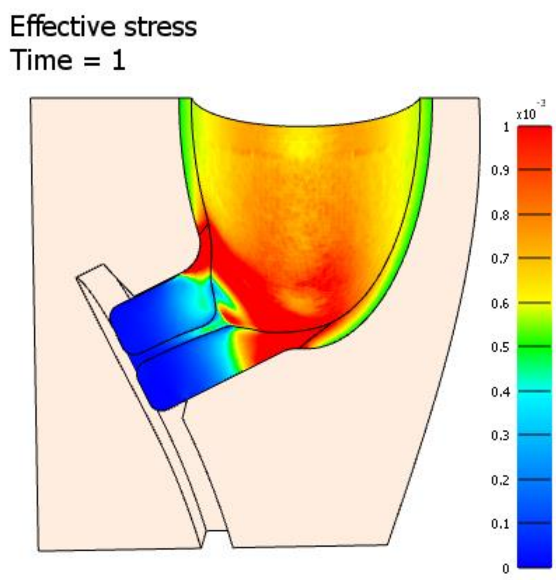

Figure 6-29: Effective stress in the uterus and cervix for P3.

Loading patterns of 1st principal right stretch in each patient modeled with both a soft and stiff cervix are shown in Figure 6-30, as well as comparisons between 1st, 2nd, and 3rd principal stretch magnitudes for each. These results show that although cervical stiffness influences cervical stretch, patient anatomies also have a direct influence. When all patients are compared with a cervix of assumed normal stiffness, stretch is still greatest in the patients that delivered preterm (P3 and P7).

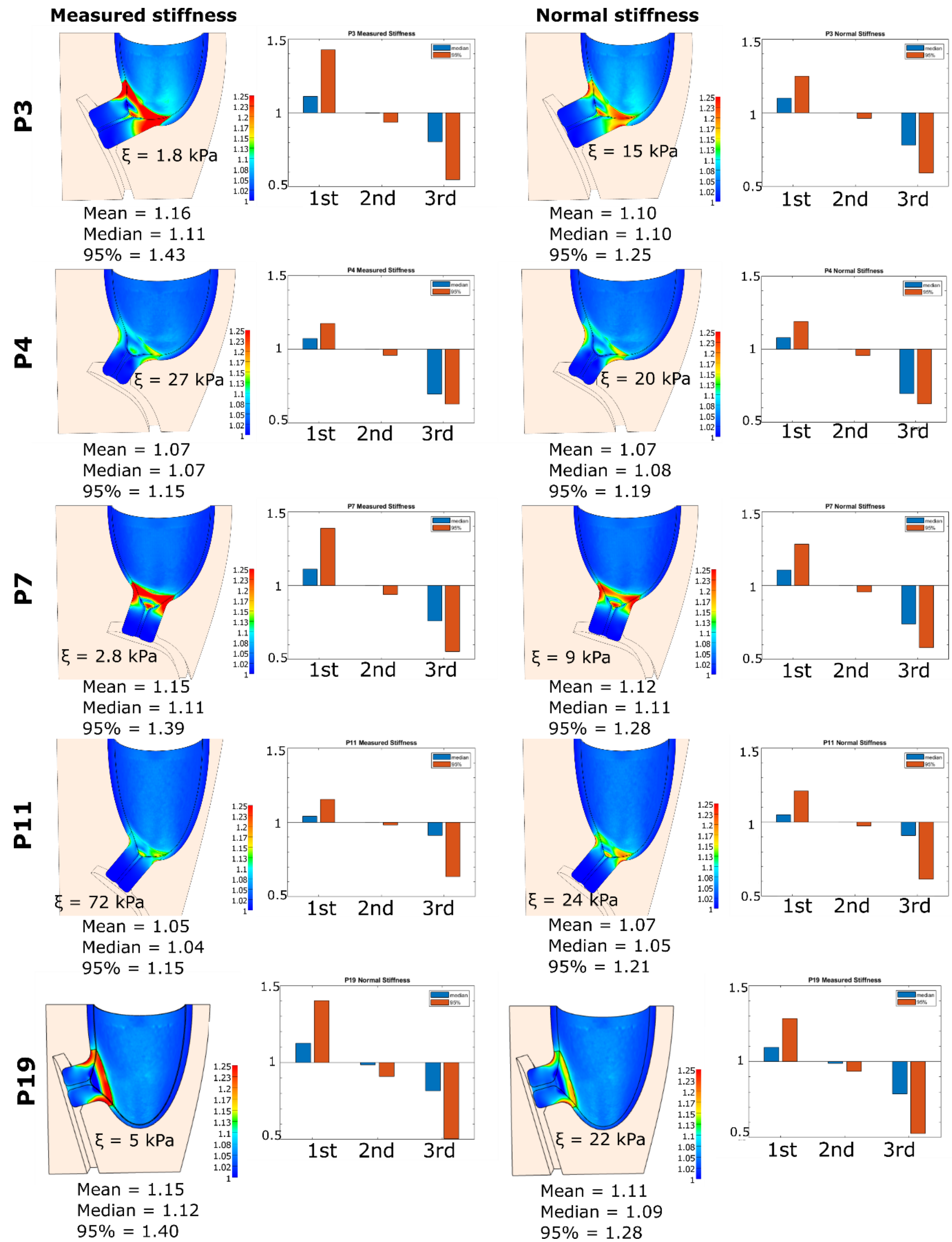

Figure 6-30: 1st principal right stretch visualization of each patient with a measured (left) and assumed normal (right) cervical fiber stiffness. Bar graph of median and 95th percentile of 1st, 2nd, and 3rd principal stretch in each patient.

The stretch in the cervix is larger than the stretch in the uterus in all patients. Each patient has large compression at the top of the cervix at the uterocervical interface, causing extreme thinning of the lower uterine segment which eventually begins to open at the internal os as evident in Figure 6-30. Cervical fiber stiffness ξ and resultant 1st principal cervical stretches for each patient at a measured and assumed normal cervical stiffness are shown in Table 6-9.

Patient	Aspiration closure pressure p_{cl} [mbar]	Input cervical fiber stiffness ξ [kPa]	Mean right cervical stretch	Median right cervical stretch	95th percentile right cervical stretch
P3	Measured – 34.5	1.8	1.16	1.11	1.43
P3	Normal - 90	15	1.10	1.10	1.25
P4	Measured – 107.5	27	1.07	1.07	1.18
P4	Normal - 90	20	1.07	1.08	1.19
P7	Measured – 46.5	2.8	1.15	1.11	1.39
P7	Normal - 90	9	1.12	1.11	1.28
P11	Measured – 160.5	72	1.05	1.04	1.15
P11	Normal - 90	24	1.07	1.05	1.21
P19	Measured – 48.7	5	1.15	1.12	1.40
P19	Normal – 90	22	1.11	1.09	1.28

Table 6-9: 1st principal right cervical stretch results for each patient at their measured value and the assumed normal value for their gestation.

In all patients, the softer cervix has a magnitude of 1st principal right stretch in the softer cervix that is greater than or equal to that in the stiffer cervix. The differences in stretch also correlate to differences in gestational outcome in 4 of the 5 patients. In Table 6-10, we show the patients' measured value for 95th percentile 1st principal stretch and their gestational outcome. While P19 is the only patient that delivers at term with a soft cervix, Figure 6-30 shows this patient does not have large stretch at the internal os.

Patient	**95th percentile 1st principal right cervical stretch**	**Gestational outcome [weeks+days]**
P3	1.43	23+3
P4	1.18	39+2
P7	1.39	28+0
P11	1.15	39+2
P19	1.40	38+1

Table 6-10: 95th percentile magnitude of 1st principal cervical stretch correlates to gestational outcome.

While results demonstrated the initiation of cervical funneling at the internal os, all patients have a similar shape funnel which is not evident in the clinic. Cervical funnels can take on various shapes and sizes. The sonographic funnel of each patient is shown in comparison to simulation results in Figure 6-31. Funnel shape is reasonably matched in simulations of P7, P11, and P19, but P4 and especially P3 are distinctly different shapes than corresponding finite element results.

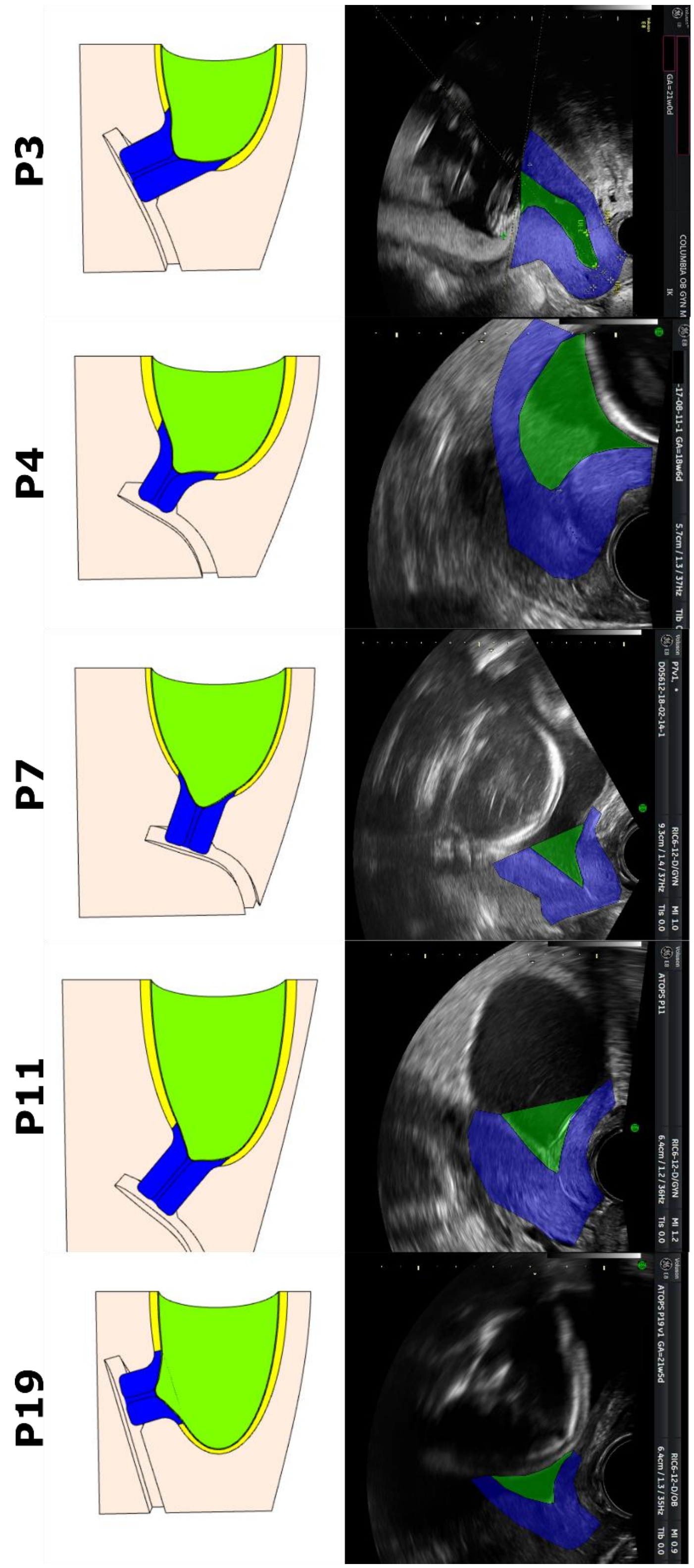

Figure 6-31: Cervical funnel in finite element analysis (left) vs. ultrasound images (right).

Location of pessary insertion impacts cervical stretch differently. When the pessary is inserted lower near a patient's external os, overall stretch in the cervix increased, as there is a magnitude in both mean and median 1st principal stretch. However, when the pessary is inserted higher closer to the internal os, overall stretch in the cervix decreases or remains the same, except for in P19 where it still increases. From the visualizations of stretch in Figure 6-32, it is clear that while there is added stretch in the cervix at the location of pessary placement in both scenarios, there is a reduction of stretch at the internal os when the pessary inserted high along the cervix.

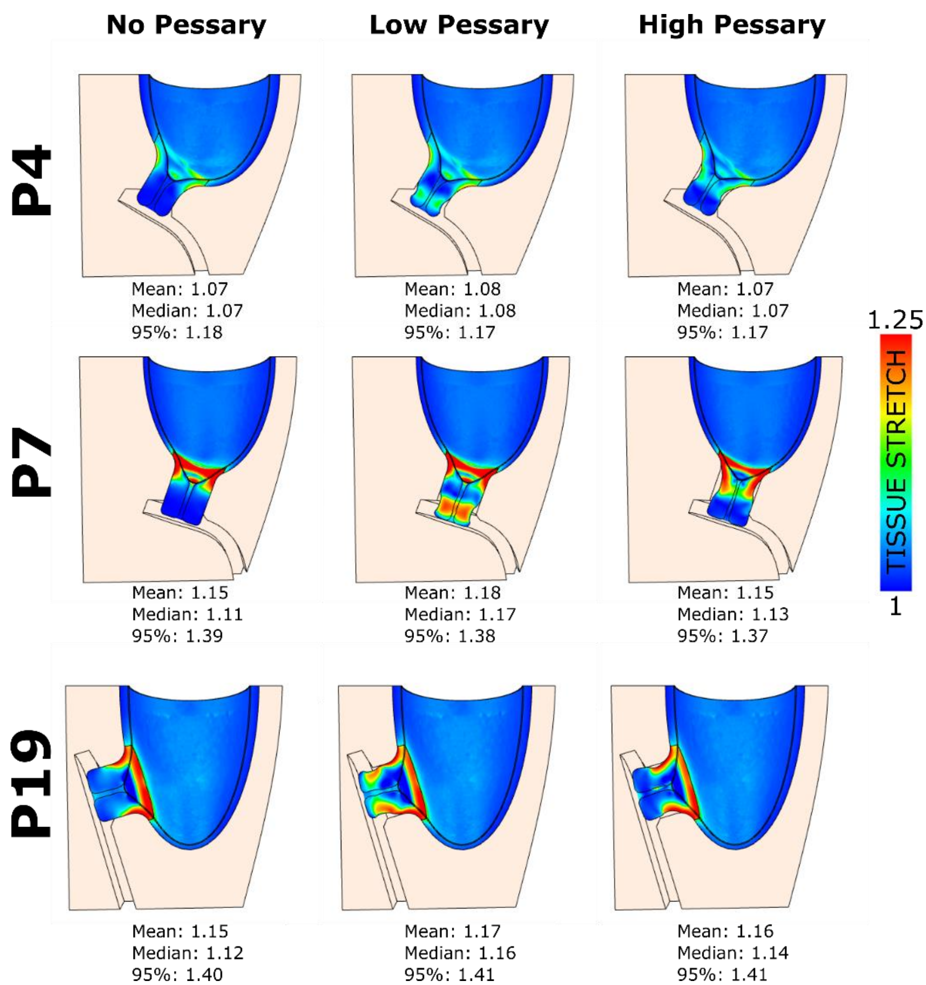

Figure 6-32: Visualization of 1st principal right stretch in two patients with no pessary, a low pessary inserted near the external os, and a high pessary inserted closer to the internal os.

The 95th percentile stretch decreased slightly after lower pessary insertion in patients P4 and P7, and increased slightly in P19. When the pessary is placed higher on the cervix, there is a noticeably larger decrease in 95th percentile cervical stretch in each patient, again with P19 as an anomoly. 1st principal stretch magnitudes in each pessary patient with no pessary, a low pessary near the external os, and a high pessary near the internal os are shown in Table 6-11.

Patient	**Pessary or No**	**Mean right cervical stretch**	**Median right cervical stretch**	**95th percentile right cervical stretch**
P4	No Pessary	1.07	1.07	1.18
P4	Low Pessary	1.08	1.08	1.17
P4	High Pessary	1.07	1.07	1.17
P7	No Pessary	1.15	1.11	1.39
P7	Low Pessary	1.18	1.17	1.38
P7	High Pessary	1.15	1.13	1.37
P19	No Pessary	1.15	1.12	1.40
P19	Low Pessary	1.17	1.16	1.41
P19	High Pessary	1.16	1.14	1.41

Table 6-11: 1st principal right cervical stretch values for patients with and without the insertion of a pessary.

The difference in cervical stretch before and after cervical placement was larger in the patients with a softer cervix.

6.2.3 Discussion

This study highlights important differences between the anatomies and material properties in high- and low-risk pregnancy cohorts. We compared various maternal anatomy dimensions between the patients of each cohort. Results showed that patients in the high-risk cohort had smaller anterior-posterior and left-right diameters than those in the low-risk cohort. These high-risk patients also had thinner lower uterine segments than those at low risk. This supports the belief that uterine overdistention and higher stretch in the uterus can lead to preterm labor[65,179]. However, in singleton pregnancies, the overstretching of the uterus may not be due to increased intrauterine volume. Instead, it seems that the uterus in high-risk patients lacks the ability to grow normally, and therefore the uterine cavity volume remains smaller and the tissue thins out earlier than it would in a normal pregnancy.

Measurements from this study of patients before and after pessary placement also showed that the insertion of a pessary may increase wall thickness and decrease uterine cavity volume initially. These results may be misleading because the introduction of an external force in most cases can cause the uterus to contract and only seem smaller temporarily. In these patients, the uterus grows similarly to the progesterone-only group by visit 2.

Due to each study's inclusion and exclusion criteria, it is to be expected that the patients in the high-risk cohort have shorter cervical lengths than those in the low-risk cohort. We see a trend in the high-risk cohort of decreasing cervical length throughout gestation, which is not prominent in the low-risk patients. Instead, in the low-risk patients, cervical length increases in the first and second trimesters and decreases only slightly in the third. An interesting finding is that cervical outer diameter increased throughout gestation in most low-risk patients, whereas it decreased in the majority of high-risk patients. This may be due to the thinning of the cervical walls and lower uterine segment as seen in our finite element analysis. As the cervix is loaded, the top of the tissue undergoes large amounts of compression and eventually becomes so thin that the cervix begins to funnel. Furthermore, we postulate that patients with a short cervix may experience funneling simply due to having less volume than those with a long cervix. A patient with less cervical volume will have less tissue to distribute the fetal load, and the cervix will both shorten and thin as the amniotic sac continues to grow. To confirm this hypothesis, we also compared cervical volume between low- and high-risk patient cohorts. The high-risk cohort does have smaller cervical volumes than the low-risk, which confirms this theory. However, the difference between patient cohorts is not as apparent; patients with a short cervix may also have a wide cervix, and vice versa.

Amongst the high-risk patient cohort, most patients see a decrease in cervical length between visits 1 and 2. Cervical length increases slightly immediately after pessary placement but then decreases at a much faster rate than the progesterone only group by visit 2. These data show the pessary may actually increase the likelihood of preterm birth by shortening the cervix in some way. However, this result differs from that found by Goya et al. which showed that 4-6 weeks after insertion, cervical length in a pessary group increased by 1.47mm while that in the control group decreased by 2.56 mm[174]. They did, however, find the same result as our study in that cervical length increased slightly immediately after pessary insertion. In the progesterone+pessary subgroup, the cervical outer diameter decreases slightly after pessary placement but then increases by visit 2. Goya et al. found consistent results. This may be due to inflammation in the cervix from increased pressure along the outside. Many clinicians explain they see the cervix swell into the pessary as the pregnancy progresses. In some extreme cases, the pessary has been so tight that it cuts off circulation to the cervix and has led to amputation at pessary removal. For this reason, they recommend placing the largest pessary possible that fits comfortably inside the patient's vagina. This is very subjective, as the pessary is not actually measured for insertion for each patient. In the progesterone only group, the cervix did not see a substantial change in diameter. These results show that while the pessary may initially move the location of tissues and provide temporary relief to reduce cervical stretch, the uterus and cervix will eventually go back to its intended configuration. This may be because these patients lack pelvic geometry boundaries which can keep the pessary in a fixed position, which causes it to float on the cervix wherever it moves. Therefore, the pessary most likely does not provide a long-term solution to prevent preterm birth in these patients.

There was no distinct trend in changes in anterior uterocervical angle or in posterior cervical offset in either patient cohort, consistent with the Goya et al study. In some low-risk patients, the posterior cervical offset increases in the first trimester, but then decreases after the 16^{th} week of pregnancy. This is likely due to the initial growth of the uterus in a spherical shape, and the transition during the second trimester to elongation instead of continuing to grow outward in the anterior-posterior direction. As the uterus grows into a globular shape, the cervix moves posteriorly along the curvature of the widening lower uterine segment. At around 20 weeks, the uterus stops growing posteriorly and therefore the cervix does not continue to move in that direction.

In the high-risk cohort, the pessary slightly increased anterior uterocervical angle immediately after pessary placement. Yet, anterior uterocervical angle sharply decreased in these patients by visit 2. This means that while the pessary may angle the cervix more posteriorly initially, it may actually move the cervix more anteriorly as it settles into place over the next few weeks. This contradicts the claim by the Arabin pessary that the device may move the fetal load onto the anterior lower uterine segment, as the cervix does not remain angled to the posterior direction. In the majority of pessary patients, the device moved the cervix more posteriorly along the uterus immediately after insertion as shown by an increase in posterior cervical offset. However, this dimension also decreased by visit 2.

This study is one of the first to quantitatively measure patient-specific cervical stiffness in a high-risk patient cohort. Our results indicate that the cervical aspiration closure pressure p_{cl} corresponds to both gestational age and birthing outcome. Surprisingly, based on patients' first aspiration measurements only, cervical stiffness increased with gestational age. This is likely an artifact of our recruitment protocol in which patients with a short cervix are recruited anywhere between 18-24 weeks. Take for example a patient with a very soft cervix – their soft cervix will most likely shorten sooner, and they will be recruited earlier near 18 weeks. A second patient with a stiffer cervix will not shorten until a few weeks later, and therefore they will be recruited closer to 24 weeks. This means that softer cervices are measured sooner and the stiffer cervices a bit later. This would give the impression of cervical stiffness increasing throughout gestation, but this is not likely based on previous studies. Then, as gestational age increased in the progesterone-only cohort, cervical stiffness decreased. In contrast, the cervical stiffness of many pessary patients increased with gestational outcome. This increase in stiffness may be due to inflammation of the tissue, but is most likely due to the compression of a nonlinear material. Because the cervix is nonlinear, it becomes more difficult to compress the tissue as it is squeezed. By the pessary applying initial deformation by squeezing on the cervix, it is more difficult to pull the cervical tissue into the aspiration. In the future, we will measure cervical stiffness immediately after pessary placement in an attempt to confirm this idea. It contradicts our hypothesis that increased cervical pressure may lead to tissue remodeling and therefore actually soften the cervix. Yet, it is contradictory that cervical stiffness increases, as we saw that the pessary also decreases cervical length in patients at their follow-up visit, and one would think a stiffer cervix will not shorten as easily. Overall in the high-risk patients, a softer cervix correlated with a sooner time to delivery. This finding emphasizes the importance of measuring in-vivo cervical stiffness in patients that may deliver preterm and potentially finding a solution that can mechanically stiffen the tissue substrate.

The finite element analyses in this study compared five patients at their first visit with gestational intrauterine pressure applied to the inner fetal membranes surface. Three of these patients received a pessary in the ATOPS study and two did not. In the pessary arm, one patient delivered preterm and the other two at term. In the progesterone-only group, one patient delivered preterm and the other at term. Evidence from ex vivo cervical fibroblast studies suggests that cervical tissue stretch controls cervical material modeling processes[122–124]. Hence, it is postulated that excessive cervical tissue stretch triggers premature cervical remodeling, and therefore we use cervical stretch as the study outcome parameter. In addition, Von Mises stress in the cervix may line up with damage or failure of tissues and is important to consider.

Results showed that patients whodelivered preterm experience greater cervical stretch than those who did not, particularly at the internal os. This is largely due to the softer material properties of the cervical tissue in these patients. When comparing patients with their measured cervical stiffness and the assumed normal pregnancy aspiration closure pressure of 90mbar, we see that the softer cervix in each scenario experiences greater cervical stretch. However, when controlling for differences in cervical stiffness and setting each patient model cervical stiffness to the assumed normal value, the patients that delivered preterm still experience high cervical stretches than those who did not, except in the case of one patient (P19). Although P19 did have similar overall stretch to the two other preterm patients (P3 and P11), P19 had noticeably less cervical stretch at the internal os. This is especially significant as we used reference cervical length in this study, and therefore it was not due to the clinical predictor of a short cervix. This information emphasizes the importance of further studies to determine which biomechanical parameters are most important in predicting preterm birth in addition to cervical length and stiffness. This also portrays the potential utilization of patient-specific computational models to be developed as clinical prediction tools.

While insertion of a pessary in our models showed an increase in both mean and median stretch, it did show a small decrease in 95th percentile 1st principal stretch in the cervix. This may be important as we showed in Table 6-10 that the largest cervical stretch magnitudes can correlate to gestational outcome. However, the pessary only reduces this value slightly, which may not make a direct impact on most patients. We saw a large reduction in stretch specifically at the internal os when the pessary was inserted near the internal os, whereas that reduction was much more limited when the pessary was inserted lower near the external os. We therefore believe that if a patient's anatomy allows insertion of a pessary high onto the cervix as close to the reference internal os as possible, this patient may be a better candidate for a cervical pessary and will see a reduction stretch at the internal os to close the cervical funnel. Furthermore, even with a higher pessary, we saw reduced internal os stretch by a greater amount in the patient with a soft cervix, but it did not have a significant impact on the patient with a stiff cervix. Therefore, we conclude that a pessary is not useful in patients with stiff cervices, as they are likely to make it near full term already without additional interventions.

The increase the pessary creates in both the mean and median value of stretch in the cervix could lead to inflammation and mechanosensitive remodeling of collagen in the cervix, thereby softening the cervix and increasing the likelihood of preterm delivery. This contradicts our findings from cervical aspiration measurements, where the majority of pessary patients saw an increase in cervical stiffness between visits 1 and 2, whereas patients in the progesterone only cohort all saw a decrease in cervical stiffness (Figure 6-25). This provides the need for more investigation into the effect of cervical contact pressures on tissue material properties, and how that change in properties may help or hinder birthing outcomes.

6.2.3.1 Limitations

We acknowledge that there are various limitations in this study, most importantly the error in ultrasound dimension measurement. In ultrasound, the combined absolute distance measurement error due to pixel size and operator cursor placement errors was found to be 1.5 pixel widths, which can be as large as 0.5mm in our images[180]. We also realize the uterus and cervix are dynamic environments, and due to contractions and fetal movements, measurements can change very quickly. Final publications will have error quantification of measurements by dimensional calipers being placed by multiple trained sonographers.

Another limitation is the patient sample size. Due to clinical trial randomization, we had more pessary patients in this study than those without a pessary. Additionally, only three of the patients in the already small subset of progesterone-only patients made it to their second visit. For this reason, our conclusions comparing the pessary to no pessary group are limited. Future peer-reviewed publication of this work will calculate statistical p-values to confirm or disprove our hypothesis and observations. Due to geometric incompatibilities between patient anatomies and our parametric model, it was not possible to create a finite element analysis of many of these patients. We will make model improvements that more accurately capture the anatomy of a wide variety of patients in order to combat this issue in the future.

In using the aspiration device to measure cervical stiffness, we are measuring closure pressure on each patient's cervix at the external os. We do not have means to measure material properties at the internal os, and therefore we assume that the parameters are consistent throughout the cervix. Still, external os cervical stiffness seems to have a direct correlation to gestational outcomes.

We were able to achieve the initiation of cervical funneling in finite element analysis of each patient by only applying a gestational intrauterine pressure due to implementation of a fetal membrane material that more accurately models the amnion's ability to bend *in vivo*. However, the resultant funnel shapes for some patients do not match those seen on ultrasound. We attempted to increase intrauterine pressure instead to 2kPa, but it did not change funnel shape. There are various methods we believe can capture funnel shape in our finite element analyses in the future. First, we may need to reassess the material model used for the cervix in our analyses. The orientation of collagen fibers in the patient's cervix may be preventing it from opening, whereas high-risk patients may have weakening of these fibers to produce cervical funneling. Because we do not have preferential fiber alignment in our models, we are not able to capture this phenomenon. Similarly, we see large stretches at the uterocervical interface due to a jump in material properties. It would be ideal to implement a gradient of material properties from the uterus to the cervix in future simulations, and to investigate different fiber architecture. Additionally, we could add the presence of an external force such as a contraction or baby kick directly at the internal os to force the membrane into the cervical canal. Likely the most influential trait of our models determining the shape of cervical funneling is the boundary condition of the cervical canal. Currently, the cervix is required to compress into the stiffer wall of the vagina, though the vaginal wall is actually quite flexible *in vivo*. This causes our current models to deform in the shape of the curvature of the boundary conditions instead of changing shape. Future investigations need to be performed by varying vaginal boundary conditions and determining which is most realistic.

6.2.4 Conclusions

We present here a direct comparison between the anatomical dimensions of pregnant patients in low- and high-risk studies. We also compare patients in the high-risk cohort who receive the clinical intervention of a pessary and those who do not. Using finite element analysis, we calculate the 1st principal right stretch under gestational IUP levels. We then vary cervical stiffness, pessary placement location, and patient geometries to analyze the sensitivity of each parameter on cervical stretch. Our simulation result supports the need for clinical measurement of cervical stiffness, and the added necessity to measure maternal anatomy parameters in addition to cervical length. It also demonstrates that an Arabin pessary may only be useful in patients with a soft cervix. Results from this study stress the need for pessary placement to be as high on the external cervix as possible, as the device does little in the case of low insertion. In future studies, we will measure maternal dimensions and cervical stiffness of an additional low-risk cohort in order to compare results further. Our goal is that our model will serve as a preliminary platform for the development of preterm birth diagnostic tools and procedures.

7 Conclusions and future work

Preterm birth is a devastating clinical dilemma that affects 10% of babies worldwide. It is the leading cause of death in children under the age of 5 and often leads to lifelong disabilities in those that survive. Yet, the pathways and mechanisms causing preterm birth are still poorly understood. The goal of this dissertation work was to use finite element analyses to investigate the effect of various material and structural components of the womb on tissue mechanics and gestational outcomes.

A full three-dimensional finite element model of a pregnant patient consisting of the uterus, cervix, fetal membranes, and surrounding abdomen was created and used as a tool to investigate the parameters that influence tissue stretch and stress in primarily the cervix but also its surrounding tissues. Parametric sensitivity studies were conducted and showed that:

- Cervical length affects the structural response of the cervix only when the cervical tissue is soft.
- Posterior cervical offset of the cervix affects the load on the internal os, and anterior uterocervical angle does not.
- Increased ellipticity of the uterus results in increased stretch at the internal os.
- Preferentially aligned uterine collagen fiber orientation, with a degree of fiber dispersion, does not greatly influence the stretch or stress in the cervix.
- Fetal membrane adhesion affects the stretch distribution and magnitude in the uterus and cervix.
- Boundary conditions, specifically those of the abdominal wall, spine, and vaginal canal, can greatly change the shape of cervical and uterine deformation.

In addition to these sensitivity studies, patient-specific geometries and finite element model results were compared between patients in both low- and high-risk clinical studies. Findings showed that the anatomies and growth of the uterus and cervix between patients are very diverse. Patients that have a short cervix often also have a thinner lower uterine segment and a smaller cervical diameter. These properties likely further increase the amount of stretch experienced by the cervix at the internal os.

We also emphasize the need for ways to quantitatively measure cervical stiffness of high-risk patients *in vivo*. Cervical aspiration pressure measurements showed that patients with a softer cervix have a shorter time to delivery, and our finite element analyses show greater stretch in patients with a soft cervix. Yet when controlled for cervical stiffness, our finite element analyses show that there are still strong influences of cervical and uterine geometries on cervical stretch.

Lastly, we investigated the effect of the Arabin pessary on the geometry, stiffness, and stretch of the cervix. We conclude that the pessary does decrease maximum cervical stretches in most patients, especially those with a soft cervix. However, we stress that inserting the pessary as high onto the cervix as possible is critical, as low pessary placement does little to decrease stretch at the internal os, and actually increases stretch at the external os which may lead to premature tissue remodeling. The pessary may not be as effective in patients with a stiff cervix because its effect is negligible in these patients.

7.1 Recommendations for future work

More sensitivity studies are required to determine what may lead to different cervical funnel shapes in patients with a short cervix. We recommend that further investigations be conducted on the realistic *in vivo* fetal membrane properties, especially the adhesion of the membranes to the uterine decidua, as we saw this had a large impact on the magnitude and pattern of cervical stretch. There are many questions about cervical funneling and membrane adhesion that need to be answered. For example, does the cervix open first, causing increased fetal load on the lower membrane, resulting in a weakened membrane funneling into the cervix, or does membrane detachment occur first increasing cervical load and resulting in cervical funneling. Similarly, does a short cervix allow the introduction of bacteria into the uterus causing the membranes to lose adhesion and preterm birth to occur, or does the placenta become infected and cause the uterus to contract, membranes to detach, and the cervix to shorten. As preterm birth is multifactorial, it is important to distinguish the order of these phenomena in future clinical studies to determine effective treatments.

The finite element model presented here will benefit from further validation of how accurately it captures tissue geometries and mechanics. Future iterations of this model should consider taking additional measurements of the uterine diameters from ultrasound, as the uterus is in fact kidney bean-shaped and cannot always be easily approximated as an ellipsoid. Taking additional measurements of the posterior radius of the uterus should improve model accuracies immensely. Furthermore, future studies should implement the effect of gravity into the finite element analyses, as we have already collected data of patients in both supine and standing orientations. The change in geometries between supine and standing scans could be used as another method of validation.

We also recommend that as more data is collected from both high- and low-risk cohorts of pregnant patients, more thorough statistical analysis should be performed to determine the impact of all geometric parameters on gestational outcomes.

References

[1] Cunningham, F. G., Leveno, K. J., Bloom, S. L., Spong, C. Y., Dashe, J. S., Hoffman, B. L., Casey, B. M., and Sheffield, J. S., 2013, “Maternal Physiology,” *Williams Obstetrics, 24e*, McGraw-Hill Education, New York, NY.

[2] Morreale, R., Visual Explanations LLC, and American Society of Clinical Oncology, 2003, “Medical Illustrations Gallery | Cancer.Net” [Online]. Available: https://www.cancer.net/es/navigating-cancer-care/cancer-basics/medical-illustrations-gallery?mitid=228. [Accessed: 30-Apr-2019].

[3] Langlois, P. L., 1970, “The Size of the Normal Uterus.,” J. Reprod. Med., **4**(6), pp. 220–8.

[4] Abrams, J., 1970, “What Is the Normal Size of the Uterus?,” J. Reprod. Med., **4**(6), pp. 208–9.

[5] Sheikhazadi, A., Sadr, S. S., Ghadyani, M. H., Taheri, S. K., Manouchehri, A. A., Nazparvar, B., Mehrpour, O., and Ghorbani, M., 2010, “Study of the Normal Internal Organ Weights in Tehran’s Population,” J. Forensic Leg. Med., **17**(2), pp. 78–83.

[6] Sosa-Stanley, J. N., and Peterson, D. C., 2019, *Anatomy, Abdomen and Pelvis, Uterus*, StatPearls Publishing.

[7] Lutz Slomianka, 2009, “Blue Histology - Female Reproductive System” [Online]. Available:http://www.lab.anhb.uwa.edu.au/mb140/CorePages/FemaleRepro/FemaleRepro.htm. [Accessed: 30-Apr-2019].

[8] Wynn, R., 1967, *Cellular Biology of the Uterus.*, Appleton-Century-Crofts, [New York].

[9] Goldstuck, N., 2018, “Dimensional Analysis of the Endometrial Cavity: How Many Dimensions Should the Ideal Intrauterine Device or System Have?,” Int. J. Womens. Health, **Volume 10**, pp. 165–168.

[10] Gillespie, E. C., 1950, “Principles of Uterine Growth in Pregnancy.,” Am J Obs. Gynecol, **59**(5), pp. 949–959.

[11] Danforth, D. N., 1947, “The Fibrous Nature of the Human Cervix, and Its Relation to the Isthmic Segment in Gravid and Nongravid Uteri.,” Am J Obs. Gynecol, **53**(4), pp. 541–560.

[12] Buhimschi, C. S., Buhimschi, I. A., Malinow, A. M., Saade, G. R., Garfield, R. E., and Weiner, C. P., 2003, “The Forces of Labour,” Fetal Matern. Med. Rev., **14**(4), pp. 273–307.

[13] Degani, S., Leibovitz, Z., Shapiro, I., Gonen, R., and Ohel, G., 1998, “Myometrial Thickness in Pregnancy: Longitudinal Sonographic Study.,” J Ultrasound Med, **17**(10), pp. 661–665.

[14] Durnwald, C. P., and Mercer, B. M., 2008, “Myometrial Thickness According to Uterine Site, Gestational Age and Prior Cesarean Delivery.,” J Matern Fetal Neonatal Med, **21**(4), pp. 247–250.

[15] Buhimschi, C. S., Buhimschi, I. A., Malinow, A. M., and Weiner, C. P., 2003, “Myometrial Thickness during Human Labor and Immediately Post Partum,” Am J Obs. Gynecol, **188**(2), pp. 553–559.

[16] Steinkeler, J., Coldwell, B.-J., and Warner, M. A., 2012, “Ultrasound of the Postpartum Uterus,” Ultrasound Q., **28**(2), pp. 97–103.

[17] Bae, H. S., Ahn, K. H., Oh, M. J., Kim, H. J., and Hong, S. C., 2012, “Potpartum Uterine

Involution: Sonographic Changes in the Endometrium between 2 and 6 Weeks Postpartum Related to Delivery Mode and Gestational Age at Delivery," Ultrasound Obstet. Gynecol., **39**(6), pp. 727–728.

[18] Vink, J. Y., Qin, S., Brock, C. O., Zork, N. M., Feltovich, H. M., Chen, X., Urie, P., Myers, K. M., Hall, T. J., Wapner, R., Kitajewski, J. K., Shawber, C. J., and Gallos, G., 2016, "A New Paradigm for the Role of Smooth Muscle Cells in the Human Cervix.," Am J Obs. Gynecol.

[19] Leppert, P. C., 1995, "Anatomy and Physiology of Cervical Ripening.," Clin Obs. Gynecol, **38**(2), pp. 267–279.

[20] Kleissl, H. P., van der Rest, M., Naftolin, F., Glorieux, F. H., and de Leon, A., 1978, "Collagen Changes in the Human Uterine Cervix at Parturition.," Am. J. Obstet. Gynecol., **130**(7), pp. 748–53.

[21] Myers, K. M., Paskaleva, a. P., House, M., and Socrate, S., 2008, "Mechanical and Biochemical Properties of Human Cervical Tissue," Acta Biomater., **4**(1), pp. 104–116.

[22] "Guide to Cervix Dilation" [Online]. Available: http://www.yourchildbirthguide.com/cervix-dilation.html. [Accessed: 08-May-2019].

[23] Newman, R. B., Goldenberg, R. L., Iams, J. D., Meis, P. J., Mercer, B. M., Moawad, A. H., Thom, E., Miodovnik, M., Caritis, S. N., Dombrowski, M., and National Institute of Child Health and Human Development (NICHD) Maternal-Fetal Medicine Units Network (MFMU), G., 2008, "Preterm Prediction Study: Comparison of the Cervical Score and Bishop Score for Prediction of Spontaneous Preterm Delivery.," Obstet. Gynecol., **112**(3), pp. 508–15.

[24] Iams, J. D., 2014, "Prevention of Preterm Parturition," N. Engl. J. Med., **370**(19), pp. 1860–1861.

[25] To, M. S., Skentou, C., Liao, A. W., Cacho, A., and Nicolaides, K. H., 2001, "Cervical Length and Funneling at 23 Weeks of Gestation in the Prediction of Spontaneous Early Preterm Delivery," Ultrasound Obstet. Gynecol., **18**(3), pp. 200–203.

[26] Berghella, V., Roman, A., Daskalakis, C., Ness, A., and Baxter, J. K., 2007, "Gestational Age at Cervical Length Measurement and Incidence of Preterm Birth," Obstet. Gynecol., **110**(2, Part 1), pp. 311–317.

[27] Naim, A., Haberman, S., Burgess, T., Navizedeh, N., and Minkoff, H., 2002, "Changes in Cervical Length and the Risk of Preterm Labor.," Am. J. Obstet. Gynecol., **186**(5), pp. 887–9.

[28] Mcintosh, J., Feltovich, H., Berghella, V., and Manuck, T., 2016, *The Role of Routine Cervical Length Screening in Selected High- and Low-Risk Women for Preterm Birth Prevention*.

[29] O'Hara, S., Zelesco, M., and Sun, Z., 2013, "Cervical Length for Predicting Preterm Birth and a Comparison of Ultrasonic Measurement Techniques.," Australas. J. ultrasound Med., **16**(3), pp. 124–134.

[30] Berghella, V., Kuhlman, K., Weiner, S., Texeira, L., and Wapner, R. J., 1997, "Cervical Funneling: Sonographic Criteria Predictive of Preterm Delivery," Ultrasound Obstet. Gynecol., **10**(3), pp. 161–166.

[31] House, M., and Socrate, S., 2006, "The Cervix as a Biomechanical Structure," Ultrasound Obstet. Gynecol., **28**(6), pp. 745–749.

[32] Peralta, L., Rus, G., Bochud, N., and Molina, F. S., 2015, "Mechanical Assessment of

Cervical Remodelling in Pregnancy: Insight from a Synthetic Model," J. Biomech., **48**(9), pp. 1557–1565.
[33] Myers, K. M., Feltovich, H., Mazza, E., Vink, J., Bajka, M., Wapner, R. J., Hall, T. J., and House, M., 2015, "The Mechanical Role of the Cervix in Pregnancy.," J Biomech, **48**(9), pp. 1511–1523.
[34] BOURNE, G., 1962, "The Foetal Membranes. A Review of the Anatomy of Normal Amnion and Chorion and Some Aspects of Their Function.," Postgrad. Med. J., **38**, pp. 193–201.
[35] Helmig, R., Oxlund, H., Petersen, L. K., and Uldbjerg, N., 1993, "Different Biomechanical Properties of Human Fetal Membranes Obtained before and after Delivery.," Eur. J. Obstet. Gynecol. Reprod. Biol., **48**(3), pp. 183–189.
[36] Buerzle, W., Haller, C. M., Jabareen, M., Egger, J., Mallik, A. S., Ochsenbein-Koelble, N., Ehrbar, M., and Mazza, E., 2013, "Multiaxial Mechanical Behavior of Human Fetal Membranes and Its Relationship to Microstructure.," Biomech. Model. Mechanobiol., **12**(4), pp. 747–62.
[37] Matsuura, H., Takio, K., Titani, K., Greene, T., Levery, S. B., Salyan, M. E., and Hakomori, S., 1988, "The Oncofetal Structure of Human Fibronectin Defined by Monoclonal Antibody FDC-6. Unique Structural Requirement for the Antigenic Specificity Provided by a Glycosylhexapeptide.," J. Biol. Chem., **263**(7), pp. 3314–22.
[38] Matsuura, H., and Hakomori, S., 1985, "The Oncofetal Domain of Fibronectin Defined by Monoclonal Antibody FDC-6: Its Presence in Fibronectins from Fetal and Tumor Tissues and Its Absence in Those from Normal Adult Tissues and Plasma.," Proc. Natl. Acad. Sci. U. S. A., **82**(19), pp. 6517–21.
[39] Kiefer, D. G., and Vintzileos, A. M., 2008, *The Utility of Fetal Fibronectin in the Prediction and Prevention of Spontaneous Preterm Birth*.
[40] "Why Fetal Fibronectin Matters" [Online]. Available: http://ffntest.com.au/patient.html#wif. [Accessed: 02-May-2019].
[41] Hills, B. A., and Cotton, D. B., 1984, "Premature Rupture of Membranes and Surface Energy: Possible Role of Surfactant.," Am. J. Obstet. Gynecol., **149**(8), pp. 896–902.
[42] Hills, B. A., and Cotton, D. B., 1986, "Release and Lubricating Properties of Amniotic Surfactants and the Very Hydrophobic Surfaces of the Amnion, Chorion, and Their Interface.," Obstet. Gynecol., **68**(4), pp. 550–4.
[43] Malak, T. M., Ockleford, C. D., Bell, S. C., Dalgleish, R., Bright, N., and Macvicar, J., "Confocal Immunofluorescence Localization of Collagen Types I, III, IV, V and VI and Their Ultrastructural Organization in Term Human Fetal Membranes.," Placenta, **14**(4), pp. 385–406.
[44] Bachmaier, N., and Graf, R., 1999, "The Anchoring Zone in the Human Placental Amnion: Bunches of Oxytalan and Collagen Connect Mesoderm and Epithelium.," Anat. Embryol. (Berl)., **200**(1), pp. 81–90.
[45] Hollenstein, M. W., 2011, "Mechanics of the Human Liver, Experiments and Modeling."
[46] Millar, L. K., Stollberg, J., DeBuque, L., and Bryant-Greenwood, G., 2000, "Fetal Membrane Distention: Determination of the Intrauterine Surface Area and Distention of the Fetal Membranes Preterm and at Term.," Am J Obs. Gynecol, **182**(1 Pt 1), pp. 128–134.
[47] Hampson, V., Liu, D., Billett, E., and Kirk, S., 1997, "Amniotic Membrane Collagen

Content and Type Distribution in Women with Preterm Premature Rupture of the Membranes in Pregnancy.," Br. J. Obstet. Gynaecol., **104**(9), pp. 1087–91.
[48] Jabareen, M., Mallik, A. S., Bilic, G., Zisch, A. H., and Mazza, E., 2009, "Relation between Mechanical Properties and Microstructure of Human Fetal Membranes: An Attempt towards a Quantitative Analysis.," Eur J Obs. Gynecol Reprod Biol, **144 Suppl**, pp. S134--41.
[49] Hieber, A. D., Corcino, D., Motosue, J., Sandberg, L. B., Roos, P. J., Yu, S. Y., Csiszar, K., Kagan, H. M., Boyd, C. D., and Bryant-Greenwood, G. D., 1997, "Detection of Elastin in the Human Fetal Membranes: Proposed Molecular Basis for Elasticity.," Placenta, **18**(4), pp. 301–12.
[50] Wilshaw, S.-P., Kearney, J. N., Fisher, J., and Ingham, E., 2006, "Production of an Acellular Amniotic Membrane Matrix for Use in Tissue Engineering.," Tissue Eng., **12**(8), pp. 2117–29.
[51] Bibbo, C., Little, S. E., Bsat, J., Botka, K. A., Benson, C. B., and Robinson, J. N., 2016, "Chorioamniotic Separation Found on Obstetric Ultrasound and Perinatal Outcome.," AJP Rep., **6**(3), pp. e337-43.
[52] Fisk, N. M., Ronderos-Dumit, D., Tannirandorn, Y., Nicolini, U., Talbert, D., and Rodeck, C. H., 1992, "Normal Amniotic Pressure throughout Gestation.," Br. J. Obstet. Gynaecol., **99**(1), pp. 18–22.
[53] H, A., and R, C., 1950, "Contractility of the Human Uterus Recorded by New Methods.," Surg. Gynecol. Obstet., **91**(1), pp. 1–13.
[54] Newman, R. B., 2005, "Uterine Contraction Assessment," Obstet. Gynecol. Clin. North Am., **32**(3), pp. 341–367.
[55] CALDEYRO-BARCIA, R., and POSEIRO, J. J., 1960, "PHYSIOLOGY OF THE UTERINE CONTRACTION," Clin. Obstet. Gynecol., **3**(2).
[56] Verbruggen, S. W., Kainz, B., Shelmerdine, S. C., Hajnal, J. V., Rutherford, M. A., Arthurs, O. J., Phillips, A. T. M., and Nowlan, N. C., 2018, "Stresses and Strains on the Human Fetal Skeleton during Development," J. R. Soc. Interface, **15**(138).
[57] Mercer, B. M., Sklar, S., Shariatmadar, A., Gillieson, M. S., and D'Alton, M. E., 1987, "Fetal Foot Length as a Predictor of Gestational Age," Am. J. Obstet. Gynecol., **156**(2), pp. 350–355.
[58] 2016, "WHO | Preterm Birth," WHO.
[59] March of Dimes, PMNCH, Save the Children, and WHO, 2012, "Born Too Soon: The Global Action Report on Preterm Birth," World Heal. Organ.
[60] Norman, J. E., and Shennan, A. H., 2013, "Prevention of Preterm Birth—Why Can't We Do Any Better?," Lancet, **381**, pp. 184–185.
[61] Landau, E., 2009, "Study: Average Preemie Costs $49,000 in First Year - CNN.Com," CNN.com [Online]. Available: http://www.cnn.com/2009/HEALTH/03/17/premature.babies/index.html?eref=rss_us. [Accessed: 24-Apr-2017].
[62] Harger, J. H., 2003, "ACOG Practice Bulletin," Clin. Manag. Guidel. Obstet., **102**(5), pp. 1091–1099.
[63] Gardner, M. O., Goldenberg, R. L., Cliver, S. P., Tucker, J. M., Nelson, K. G., and Copper, R. L., 1995, "The Origin and Outcome of Preterm Twin Pregnancies.," Obs. Gynecol, **85**(4), pp. 553–557.

[64] Goldenberg, R. L., Iams, J. D., Miodovnik, M., Van Dorsten, J. P., Thurnau, G., Bottoms, S., Mercer, B. M., Meis, P. J., Moawad, A. H., Das, A., Caritis, S. N., and McNellis, D., 1996, “The Preterm Prediction Study: Risk Factors in Twin Gestations. National Institute of Child Health and Human Development Maternal-Fetal Medicine Units Network.,” Am J Obs. Gynecol, **175**(4 Pt 1), pp. 1047–1053.
[65] Adams Waldorf, K. M., Singh, N., Mohan, A. R., Young, R. C., Ngo, L., Das, A., Tsai, J., Bansal, A., Paolella, L., Herbert, B. R., Sooranna, S. R., Michael Gough, G., Astley, C., Vogel, K., Baldessari, A. E., Bammler, T. K., MacDonald, J., Gravett, M. G., Rajagopal, L., and Johnson, M. R., 2015, “Uterine Overdistention Induces Preterm Labor Mediated by Inflammation: Observations in Pregnant Women and Nonhuman Primates,” Am. J. Obstet. Gynecol., **213**, pp. 830.e1-830.e19.
[66] Woods, J. R., 2001, “Reactive Oxygen Species and Preterm Premature Rupture of Membranes—A Review,” Placenta, **22**, pp. S38–S44.
[67] Naeye, R. L., and Peters, E. C., 1980, “Causes and Consequences of Premature Rupture of Fetal Membranes.,” Lancet (London, England), **1**(8161), pp. 192–194.
[68] Iams, J. D., and Berghella, V., 2010, “Care for Women with Prior Preterm Birth,” Am J Obs. Gynecol, **203**(2), pp. 89–100.
[69] Feltovich, H., Hall, T. J., and Berghella, V., 2012, “Beyond Cervical Length: Emerging Technologies for Assessing the Pregnant Cervix,” Am J Obs. Gynecol, pp. 1–43.
[70] Humphrey, J. D. (Jay D., and O’Rourke, S. L., *An Introduction to Biomechanics : Solids and Fluids, Analysis and Design*.
[71] Fung, Y. C., 1993, *Biomechanics: Mechanical Properties of Living Tissues*, Springer-Verlag.
[72] Leake, J. M., and Borgerson, J. L., *Engineering Design Graphics : Sketching, Modeling, and Visualization*.
[73] House, M., McCabe, R., and Socrate, S., 2013, “Using Imaging-Based, Three-Dimensional Models of the Cervix and Uterus for Studies of Cervical Changes during Pregnancy,” Clin. Anat., **26**(1), pp. 97–104.
[74] Fernandez, M., House, M., Jambawalikar, S., Zork, N., Vink, J., Wapner, R., and Myers, K., 2015, “Investigating the Mechanical Function of the Cervix during Pregnancy Using Finite Element Models Derived from High-Resolution 3D MRI,” Comput. Methods Biomech. Biomed. Engin., (May), pp. 1–14.
[75] Westervelt, A. R., Fernandez, M., House, M., Vink, J., Nhan-Chang, C.-L., Wapner, R., and Myers, K. M., 2017, “A Parameterized Ultrasound-Based Finite Element Analysis of the Mechanical Environment of Pregnancy,” J. Biomech. Eng., **139**(5), p. 051004.
[76] House, M., Feltovich, H., Hall, T. J., Stack, T., Patels, A., Socrate, S., Patel, A., and Socrate, S., 2012, “Three-Dimensional, Extended Field-of-View Ultrasound Method for Estimating Large Strain Mechanical Properties of the Cervix during Pregnancy,” Ultrason Imaging, **34**(1), pp. 1–14.
[77] House, M., Bhadelia, R. a., Myers, K., and Socrate, S., 2009, “Magnetic Resonance Imaging of Three-Dimensional Cervical Anatomy in the Second and Third Trimester,” Eur. J. Obstet. Gynecol. Reprod. Biol., **144**(SUPPL 1), pp. 65–69.
[78] Mahmoud, H., Wagoner Johnson, A., Chien, E. K., Poellmann, M. J., and McFarlin, B., 2013, “System-Level Biomechanical Approach for the Evaluation of Term and Preterm Pregnancy Maintenance,” J. Biomech. Eng., **135**(2), p. 021009.

[79] Henninger, H. B., Reese, S. P., Anderson, A. E., and Weiss, J. a, 2010, "Validation of Computational Models in Biomechanics.," Proc. Inst. Mech. Eng. H., **224**(7), pp. 801–812.
[80] Baah-Dwomoh, A., McGuire, J., Tan, T., and De Vita, R., 2016, "Mechanical Properties of Female Reproductive Organs and Supporting Connective Tissues: A Review of the Current State of Knowledge," Appl. Mech. Rev., **68**(6), p. 060801.
[81] Cowin, S. C., 2004, "Tissue Growth and Remodeling," Annu Rev Biomed Eng, **6**(1), pp. 77–107.
[82] Myers, K., Paskaleva, A., House, M., and Socrate, S., 2008, "Mechanical and Biochemical Properties of Human Cervical Tissue," Acta Biomater., **4**, pp. 104–116.
[83] Zhang, Y., Barocas, V. H., Berceli, S. A., Clancy, C. E., Eckmann, D. M., Garbey, M., Kassab, G. S., Lochner, D. R., McCulloch, A. D., Tran-Son-Tay, R., and Trayanova, N. A., 2016, "Multi-Scale Modeling of the Cardiovascular System: Disease Development, Progression, and Clinical Intervention," Ann. Biomed. Eng., **44**(9), pp. 2642–2660.
[84] Brown, A. S., 2015, "A MODEL HEART: Digital Simulation Takes on Its Toughest Challenge," Mech. Eng.
[85] Mendis, K. K., Stalnaker, R. L., and Advani, S. H., 1995, "A Constitutive Relationship for Large Deformation Finite Element Modeling of Brain Tissue," J. Biomech. Eng., **117**(3), p. 279.
[86] van Rietbergen, B., Weinans, H., Huiskes, R., and Odgaard, A., 1995, "A New Method to Determine Trabecular Bone Elastic Properties and Loading Using Micromechanical Finite-Element Models," J. Biomech., **28**(1), pp. 69–81.
[87] Belleza, A. J., Hart, R. T., and Burgoyne, C. F., 1977, "The Optic Nerve Head as a Biomechanical Structure: Initial Finite Element Modeling," Biomed. Eng. Soc., **1**(10), p. 213.
[88] Sigal, I. A., Flanagan, J. G., Tertinegg, I., and Ethier, C. R., 2004, "Finite Element Modeling of Optic Nerve Head Biomechanics," Investig. Opthalmology Vis. Sci., **45**(12), p. 4378.
[89] Moreno, J. D., Zhu, Z. I., Yang, P.-C., Bankston, J. R., Jeng, M.-T., Kang, C., Wang, L., Bayer, J. D., Christini, D. J., Trayanova, N. A., Ripplinger, C. M., Kass, R. S., and Clancy, C. E., 2011, "A Computational Model to Predict the Effects of Class I Anti-Arrhythmic Drugs on Ventricular Rhythms," Sci. Transl. Med., **3**(98).
[90] Ukwatta, E., Yuan, J., Qiu, W., Wu, K. C., Trayanova, N., and Vadakkumpadan, F., 2014, "Myocardial Infarct Segmentation and Reconstruction from 2D Late-Gadolinium Enhanced Magnetic Resonance Images.," Med. Image Comput. Comput. Assist. Interv., **17**(Pt 2), pp. 554–61.
[91] Vadakkumpadan, F., Arevalo, H., Ceritoglu, C., Miller, M., and Trayanova, N., 2011, "Image-Based Estimation of Ventricular Fiber Orientations for Patient-Specific Simulations," *2011 Annual International Conference of the IEEE Engineering in Medicine and Biology Society*, IEEE, pp. 1672–1675.
[92] Westervelt, A. R., and Myers, K. M., 2017, "Computer Modeling Tools to Understand the Causes of Preterm Birth," Semin. Perinatol.
[93] Joyce, E. M., Diaz, P., Tamarkin, S., Moore, R., Strohl, A., Stetzer, B., Kumar, D., Sacks, M. S., and Moore, J. J., 2016, "In-Vivo Stretch of Term Human Fetal Membranes.," Placenta, **38**, pp. 57–66.

[94] Paskaleva, A., 2008, "Biomechanics of Cervical Function in Pregnancy - Case of Cervical Insufficiency," Massachusetts Institute of Technology.
[95] House, M., Paskaleva, A., Myers, K., Craigo, S., and Socrate, S., 2005, "The Biomechanics of Cerclage Placement: The Effect of Cerclage Position and Stress Relaxation on Cervical Stress," *Am J Obstet Gynecol*, p. S21.
[96] Verbruggen, S. W., Oyen, M. L., Phillips, A. T. M., and Nowlan, N. C., "Function and Failure of the Fetal Membrane: Modelling the Mechanics of the Chorion and Amnion."
[97] Goldenberg, R. L., Culhane, J. F., Iams, J. D., and Romero, R., 2008, "Epidemiology and Causes of Preterm Birth," Lancet, **371**(9606), pp. 75–84.
[98] Tajik, P., Monfrance, M., van 't Hooft, J., Liem, S. M. S., Schuit, E., Bloemenkamp, K. W. M., Duvekot, J. J., Nij Bijvank, B., Franssen, M. T. M., Oudijk, M. A., Scheepers, H. C. J., Sikkema, J. M., Woiski, M., Mol, B. W. J., Bekedam, D. J., Bossuyt, P. M., and Zafarmand, M. H., 2016, "A Multivariable Model to Guide the Decision for Pessary Placement to Prevent Preterm Birth in Women with a Multiple Pregnancy: A Secondary Analysis of the ProTWIN Trial," Ultrasound Obstet. Gynecol., **48**(1), pp. 48–55.
[99] Liem, S., Schuit, E., Hegeman, M., Bais, J., de Boer, K., Bloemenkamp, K., Brons, J., Duvekot, H., Bijvank, B. N., Franssen, M., Gaugler, I., de Graaf, I., Oudijk, M., Papatsonis, D., Pernet, P., Porath, M., Scheepers, L., Sikkema, M., Sporken, J., Visser, H., van Wijngaarden, W., Woiski, M., van Pampus, M., Mol, B. W., and Bekedam, D., 2013, "Cervical Pessaries for Prevention of Preterm Birth in Women with a Multiple Pregnancy (ProTWIN): A Multicentre, Open-Label Randomised Controlled Trial," Lancet, **382**(9901), pp. 1341–1349.
[100] Goya, M., Pratcorona, L., Merced, C., Rodó, C., Valle, L., Romero, A., Juan, M., Rodríguez, A., Muñoz, B., Santacruz, B., Bello-Muñoz, J. C., Llurba, E., Higueras, T., Cabero, L., Carreras, E., and Pesario Cervical para Evitar Prematuridad (PECEP) Trial Group, 2012, "Cervical Pessary in Pregnant Women with a Short Cervix (PECEP): An Open-Label Randomised Controlled Trial," Lancet, **379**(9828), pp. 1800–1806.
[101] Goya, M., de la Calle, M., Pratcorona, L., Merced, C., Rodó, C., Muñoz, B., Juan, M., Serrano, A., Llurba, E., Higueras, T., Carreras, E., Cabero, L., and PECEP-Twins Trial Group, 2016, "Cervical Pessary to Prevent Preterm Birth in Women with Twin Gestation~and Sonographic Short Cervix: A Multicenter Randomized~controlled Trial (PECEP-Twins).," Am J Obs. Gynecol, **214**(2), pp. 145–152.
[102] Arabin, B., and Alfirevic, Z., 2013, "Cervical Pessaries for Prevention of Spontaneous Preterm Births: *Past, Present and Future*," Ultrasound Obstet. Gynecol., **42**(4), p. n/a-n/a.
[103] Goya, M., Pratcorona, L., Merced, C., Rodó, C., Valle, L., Romero, A., Juan, M., Rodríguez, A., Muñoz, B., Santacruz, B., Bello-Muñoz, J. C., Llurba, E., Higueras, T., Cabero, L., Carreras, E., and Pesario Cervical para Evitar Prematuridad (PECEP) Trial Group, 2012, "Cervical Pessary in Pregnant Women with a Short Cervix (PECEP): An Open-Label Randomised Controlled Trial," Lancet, **379**(9828), pp. 1800–1806.
[104] Nicolaides, K. H., Syngelaki, A., Poon, L. C., de Paco Matallana, C., Plasencia, W., Molina, F. S., Picciarelli, G., Tul, N., Celik, E., Lau, T. K., and Conturso, R., 2016, "Cervical Pessary Placement for Prevention of Preterm Birth in Unselected Twin Pregnancies: A Randomized Controlled Trial.," Am J Obs. Gynecol, **214**(1), pp. 3.e1--9.
[105] Nicolaides, K. H., Syngelaki, A., Poon, L. C., Picciarelli, G., Tul, N., Zamprakou, A., Skyfta, E., Parra-Cordero, M., Palma-Dias, R., and Rodriguez Calvo, J., 2016, "A

Randomized Trial of a Cervical Pessary to Prevent Preterm Singleton Birth," N. Engl. J. Med., **374**(11), pp. 1044–1052.
[106] Myers, K. M., Hendon, C. P., Gan, Y., Yao, W., Yoshida, K., Fernandez, M., Vink, J., and Wapner, R. J., 2015, "A Continuous Fiber Distribution Material Model for Human Cervical Tissue," J. Biomech., **48**(9), pp. 1533–1540.
[107] Yoshida, K., Mahendroo, M., Vink, J., Wapner, R., and Myers, K., 2016, "Material Properties of Mouse Cervical Tissue in Normal Gestation.," Acta Biomat, **36**, pp. 195–209.
[108] Myers, K. M. K. M., Paskaleva, A. P., House, M., and Socrate, S., 2008, "Mechanical and Biochemical Properties of Human Cervical Tissue," Acta Biomater., **4**(1), pp. 104–116.
[109] Myers, K. M., Socrate, S., Paskaleva, A., and House, M., 2010, "A Study of the Anisotropy and Tension/Compression Behavior of Human Cervical Tissue," J Biomech Eng, **132**(2), p. 21003.
[110] Conrad, J. T., Johnson, W. L., Kuhn, W. K., and Hunter, C. A., 1966, "Passive Stretch Relationships in Human Uterine Muscle.," Am J Obs. Gynecol, **96**(8), pp. 1055–1059.
[111] Gan, Y., Yao, W., Myers, K. M., Vink, J. Y., Wapner, R. J., and Hendon, C. P., 2015, "Analyzing Three-Dimensional Ultrastructure of Human Cervical Tissue Using Optical Coherence Tomography.," Biomed Opt Express, **6**(4), pp. 1090–1108.
[112] Yao, W., Gan, Y., Myers, K. M., Vink, J. Y., Wapner, R. J., and Hendon, C. P., 2016, "Collagen Fiber Orientation and Dispersion in the Upper Cervix of Non-Pregnant and Pregnant Women.," PLoS One, **11**(11), p. e0166709.
[113] Buerzle, W., and Mazza, E., 2013, "On the Deformation Behavior of Human Amnion.," J Biomech, **46**(11), pp. 1777–1783.
[114] American College of Obstetricians and Gynecologists., and American Academy of Obstetrics and Gynecology., 2004, "Intrauterine Pressure During the Second Stage of Labor in Obese Women," Obstet. Gynecol., **103**(2), pp. 225–230.
[115] Dziadosz, M., Bennett, T. A., Dolin, C., West Honart, A., Pham, A., Lee, S. S., Pivo, S., and Roman, A. S., 2016, "Uterocervical Angle: A Novel Ultrasound Screening Tool to Predict Spontaneous Preterm Birth," Am. J. Obstet. Gynecol., **215**(3), pp. 376.e1-376.e7.
[116] Prado, C. A. de C., Araujo Júnior, E., Duarte, G., Quintana, S. M., Tonni, G., Cavalli, R. de C., and Marcolin, A. C., 2016, "Predicting Success of Labor Induction in Singleton Term Pregnancies by Combining Maternal and Ultrasound Variables.," J. Matern. Fetal. Neonatal Med., pp. 1–35.
[117] Sokolowski, P., Saison, F., Giles, W., McGrath, S., Smith, D., Smith, J., and Smith, R., 2010, "Human Uterine Wall Tension Trajectories and the Onset of Parturition.," PLoS One, **5**(6), p. e11037.
[118] Fisk, N. M., Tannirandorn, Y., Nicolini, U., Talbert, D. G., and Rodeck, C. H., 1990, "Amniotic Pressure in Disorders of Amniotic Fluid Volume.," Obstet. Gynecol., **76**(2), pp. 210–4.
[119] Nicolini, U., Fisk, N. M., Talbert, D. G., Rodeck, C. H., Kochenour, N. K., Greco, P., Hubinont, C., and Santolaya, J., 1989, "Intrauterine Manometry: Technique and Application to Fetal Pathology.," Prenat. Diagn., **9**(4), pp. 243–54.
[120] Martini, F. H., Nath, J. L., and Bartholomew, 2014, "Development and Inheritance," *Fundamentals of Anatomy & Physiology*.
[121] Buhimschi, C. S., Buhimschi, I. A., Norwitz, E. R., Sfakianaki, A. K., Hamar, B., Copel,

J. A., Saade, G. R., and Weiner, C. P., 2005, "Sonographic Myometrial Thickness Predicts the Latency Interval of Women with Preterm Premature Rupture of the Membranes and Oligohydramnios.," Am J Obs. Gynecol, **193**(3 Pt 1), pp. 762–770.
[122] Yoshida, M., Sagawa, N., Itoh, H., Yura, S., Takemura, M., Wada, Y., Sato, T., Ito, A., and Fujii, S., 2002, "Prostaglandin F(2alpha), Cytokines and Cyclic Mechanical Stretch Augment Matrix Metalloproteinase-1 Secretion from Cultured Human Uterine Cervical Fibroblast Cells.," Mol. Hum. Reprod., **8**(7), pp. 681–7.
[123] Takemura, M., Itoh, H., Sagawa, N., Yura, S., Korita, D., Kakui, K., Kawamura, M., Hirota, N., Maeda, H., and Fujii, S., 2005, "Cyclic Mechanical Stretch Augments Hyaluronan Production in Cultured Human Uterine Cervical Fibroblast Cells," MHR Basic Sci. Reprod. Med., **11**(9), pp. 659–665.
[124] Takemura, M., Itoh, H., Sagawa, N., Yura, S., Korita, D., Kakui, K., Hirota, N., and Fujii, S., 2004, "Cyclic Mechanical Stretch Augments Both Interleukin-8 and Monocyte Chemotactic Protein-3 Production in the Cultured Human Uterine Cervical Fibroblast Cells," Mol. Hum. Reprod., **10**(8), pp. 573–580.
[125] C.Y., S., 2007, "Prediction and Prevention of Recurrent Spontaneous Preterm Birth," Obstet. Gynecol., **110**(2 I), pp. 405–415.
[126] Society for Maternal-Fetal Medicine Publications Committee, with assistance of Vincenzo Berghella, 2012, "Progesterone and Preterm Birth Prevention: Translating Clinical Trials Data into Clinical Practice.," Am J Obs. Gynecol, **206**(5), pp. 376–386.
[127] Iams, J. D., Johnson, F. F., Sonek, J., Sachs, L., Gebauer, C., and Samuels, P., 1995, "Cervical Competence as a Continuum: A Study of Ultrasonographic Cervical Length and Obstetric Performance.," Am J Obs. Gynecol, **172**(4 Pt 1), pp. 1097–1103.
[128] Guzman, E. R., Mellon, R., Vintzileos, A. M., Ananth, C. V, Walters, C., and Gipson, K., 1998, "Relationship between Endocervical Canal Length between 15-24 Weeks Gestation and Obstetric History.," J Matern Fetal Med, **7**(6), pp. 269–272.
[129] Guzman, E. R., Walters, C., Ananth, C. V., O'Reilly-Green, C., Benito, C. W., Palermo, A., and Vintzileos, A. M., 2001, "A Comparison of Sonographic Cervical Parameters in Predicting Spontaneous Preterm Birth in High-Risk Singleton Gestations," Ultrasound Obstet. Gynecol., **18**(3), pp. 204–210.
[130] Moroz, L. A., and Simhan, H. N., 2012, "Rate of Sonographic Cervical Shortening and the Risk of Spontaneous Preterm Birth.," Am J Obs. Gynecol, **206**(3), pp. 234.e1--5.
[131] Romero, J., Rebarber, A., Saltzman, D. H., Schwartz, R., Peress, D., and Fox, N. S., 2012, "The Prediction of Recurrent Preterm Birth in Patients on 17-Alpha-Hydroxyprogesterone Caproate Using Serial Fetal Fibronectin and Cervical Length.," Am J Obs. Gynecol, **207**(1), pp. 51.e1--5.
[132] Melamed, N., Hiersch, L., Domniz, N., Maresky, A., Bardin, R., and Yogev, Y., 2013, "Predictive Value of Cervical Length in Women With Threatened Preterm Labor," Obstet. Gynecol., **122**(6), pp. 1279–1287.
[133] Bastek, J. A., Hirshberg, A., Chandrasekaran, S., Owen, C. M., Heiser, L. M., Araujo, B. A., McShea, M. A., Ryan, M. E., and Elovitz, M. A., 2013, "Biomarkers and Cervical Length to Predict Spontaneous Preterm Birth in Asymptomatic High-Risk Women," Obstet. Gynecol., **122**(2, PART 1), pp. 283–289.
[134] Sananes, N., Langer, B., Gaudineau, A., Kutnahorsky, R., Aissi, G., Fritz, G., Boudier, E., Viville, B., Nisand, I., and Favre, R., 2014, "Prediction of Spontaneous Preterm Delivery

in Singleton Pregnancies: Where Are We and Where Are We Going? A Review of Literature.," J Obs. Gynaecol, (0), pp. 1–5.

[135] Uquillas, K. R., Fox, N. S., Rebarber, A., Saltzman, D. H., Klauser, C. K., and Roman, A. S., 2017, "A Comparison of Cervical Length Measurement Techniques for the Prediction of Spontaneous Preterm Birth," J. Matern. Neonatal Med., **30**(1), pp. 50–53.

[136] Hui, S., Chor, C., Lau, T., Lao, T., and Leung, T., 2012, "Cerclage Pessary for Preventing Preterm Birth in Women with a Singleton Pregnancy and a Short Cervix at 20 to 24 Weeks: A Randomized Controlled Trial," Am. J. Perinatol., **30**(04), pp. 283–288.

[137] Kirkinen, P., and Jouppila, P., 1977, "Polyhydramnion. A Clinical Study.," *Ann Chir Gynaecol*, pp. 117–122.

[138] Gravett, M. G., Rubens, C. E., and Nunes, T. M., 2010, "Global Report on Preterm Birth and Stillbirth (2 of 7): Discovery Science," BMC Pregnancy Childbirth, **10**(Suppl 1), p. S2.

[139] Myers, K. M., and Elad, D., 2017, "Biomechanics of the Human Uterus," Wiley Interdiscip. Rev. Syst. Biol. Med., **9**(5), p. e1388.

[140] Young, R. C., and Hession, R. O., 1999, "Three-Dimensional Structure of the Smooth Muscle in the Term-Pregnant Human Uterus.," Obstet. Gynecol., **93**(1), pp. 94–9.

[141] Vink, J., and Feltovich, H., 2016, "Cervical Etiology of Spontaneous Preterm Birth," Semin. Fetal Neonatal Med., **21**(2), pp. 106–112.

[142] Perez-Colon, M., Westervelt, A., Vink, J., Wapner, R., Gallos, G., House, M., and Myers, K., 2017, "Uterine Tissue Orientation and Stiffness Influence Cervical Tissue Stretch," *Reprod Sci 24*, p. 171A.

[143] Westervelt, A., Fernandez, M., Mazza, E., Ehret, A., Vink, J., Wapner, R., House, M., and Myers, K., 2017, "Biomechanical Simulations of Pregnancy: Fetal Membrane Properties Influence Cervical Tissue Stretch at the Internal Os," *Reprod Sci*, pp. 243A-244A.

[144] Conrad, J. T., Kuhn, W. K., and Johnson, W. L., 1966, "Stress Relaxation in Human Uterine Muscle.," Am. J. Obstet. Gynecol., **95**(2), pp. 254–265.

[145] Bürzle, W., Mazza, E., and Moore, J. J., 2014, "About Puncture Testing Applied for Mechanical Characterization of Fetal Membranes.," J Biomech Eng, **136**(11), p. 111009.

[146] Badir, S., Mazza, E., Zimmermann, R., and Bajka, M., 2013, "Cervical Softening Occurs Early in Pregnancy: Characterization of Cervical Stiffness in 100 Healthy Women Using the Aspiration Technique," Prenat. Diagn., **33**(8), pp. 737–741.

[147] Pearsall, G., and Roberts, V., 1978, "Passive Mechanical Properties of Uterine Muscle (Myometrium) Tested in Vitro," J. Biomech., **11**, pp. 167–176.

[148] Genbačev, O., Vićovac, L., and Larocque, N., 2015, "The Role of Chorionic Cytotrophoblasts in the Smooth Chorion Fusion with Parietal Decidua.," Placenta, **36**(7), pp. 716–22.

[149] Westervelt, A. R., Fernandez, M., House, M., Vink, J., Nhan-Chang, C.-L., Wapner, R., and Myers, K. M., 2017, "A Parameterized Ultrasound-Based Finite Element Analysis of the Mechanical Environment of Pregnancy," J. Biomech. Eng., **139**(5).

[150] Fernandez, M., House, M., Jambawalikar, S., Zork, N., Vink, J., Wapner, R., and Myers, K., 2015, "Investigating the Mechanical Function of the Cervix during Pregnancy Using Finite Element Models Derived from High-Resolution 3D MRI," Comput. Methods Biomech. Biomed. Engin., **19**(4), pp. 404–417.

[151] Oyen, M. L., Calvin, S. E., and Landers, D. V., 2006, "Premature Rupture of the Fetal

Membranes: Is the Amnion the Major Determinant?," Am. J. Obstet. Gynecol., **195**(2), pp. 510–515.
[152] Niknejad, H., Peirovi, H., Jorjani, M., Ahmadiani, A., Ghanavi, J., and Seifalian, A., 2008, "Properties of the Amniotic Membrane for Potential Use in Tissue Engineering," Eur. Cells Mater., **7**, pp. 88–99.
[153] Chua, W. K., and Oyen, M. L., 2009, "Do We Know the Strength of the Chorioamnion? A Critical Review and Analysis.," Eur J Obs. Gynecol Reprod Biol, **144 Suppl**, pp. S128--33.
[154] Alger, L. S., and Pupkin, M. J., 1986, "Etiology of Preterm Premature Rupture of the Membranes.," Clin Obs. Gynecol, **29**(4), pp. 758–770.
[155] Romero, R., Gonzalez, R., Sepulveda, W., Brandt, F., Ramirez, M., Sorokin, Y., Mazor, M., Treadwell, M. C., and Cotton, D. B., 1992, "Infection and Labor. VIII. Microbial Invasion of the Amniotic Cavity in Patients with Suspected Cervical Incompetence: Prevalence and Clinical Significance.," Am. J. Obstet. Gynecol., **167**(4 Pt 1), pp. 1086–91.
[156] Cyron, C. J., and Humphrey, J. D., 2017, "Growth and Remodeling of Load-Bearing Biological Soft Tissues.," Meccanica, **52**(3), pp. 645–664.
[157] Buerzle, W., Haller, C. M., Jabareen, M., Egger, J., Mallik, A. S., Ochsenbein-Koelble, N., Ehrbar, M., and Mazza, E., 2013, "Multiaxial Mechanical Behavior of Human Fetal Membranes and Its Relationship to Microstructure," Biomech. Model. Mechanobiol., **12**(4), pp. 747–762.
[158] Zimmerman, B., Westervelt, A. R., Myers, K. M., and Ateshian, G. A., 2019, "A Finite Element Algorithm For Evolving Contact Between Bonded Surfaces With Implicit Damage: Application To Premature Funneling Of Fetal Membranes," *16th International Symposium on Computer Methods in Biomechanics and Biomedical Engineering and the 4th Conference on Imaging and Visualization (CMBBE 2019)*.
[159] "Why Do I Have Pelvic Pain During My Pregnancy?" [Online]. Available: https://myphysiosa.com.au/pelvic-pain-during-pregnancy/. [Accessed: 24-May-2019].
[160] Cowin, S., and Humphrey, J., 2001, *Cardiovascular Soft Tissue Mechanics*.
[161] Guo, Z. Y., Peng, X. Q., and Moran, B., 2007, "Mechanical Response of Neo-Hookean Fiber Reinforced Incompressible Nonlinearly Elastic Solids," Int. J. Solids Struct., **44**(6), pp. 1949–1969.
[162] "Parámetro ELCV=1 Para Convertir Elementos Sólidos CHEXA u/p de 20-Nodos En 27-Nodos" [Online]. Available: http://www.iberisa.com/soporte/femap/nolinealavanzado/brick27nodos.htm. [Accessed: 24-May-2019].
[163] Boelig, R. C., Feltovich, H., Spitz, J. L., Toland, G., Berghella, V., and Iams, J. D., 2017, "Assessment of Transvaginal Ultrasound Cervical Length Image Quality," Obstet. Gynecol., **129**(3), pp. 536–541.
[164] Saul, L. L., Kurtzman, J. T., Hagemann, C., Ghamsary, M., and Wing, D. A., 2008, "Is Transabdominal Sonography of the Cervix after Voiding a Reliable Method of Cervical Length Assessment?," J. Ultrasound Med., **27**(9), pp. 1305–11.
[165] Schindelin, J., Arganda-Carreras, I., Frise, E., Kaynig, V., Longair, M., Pietzsch, T., Preibisch, S., Rueden, C., Saalfeld, S., Schmid, B., Tinevez, J.-Y., White, D. J., Hartenstein, V., Eliceiri, K., Tomancak, P., and Cardona, A., 2012, "Fiji: An Open-Source Platform for Biological-Image Analysis," Nat. Methods, **9**(7), pp. 676–682.

[166] Humphrey, J. D., 2003, “Continuum Biomechanics of Soft Biological Tissues, Editorial,” Proc. R. Soc. Lond.A, **459**(2029), pp. 3–46.
[167] Humphrey, J. D., 2009, “Vascular Mechanics, Mechanobiology, and Remodeling,” J Mech Med Biol, **9**(02), pp. 243–257.
[168] Omens, J. H., 1998, “Stress and Strain as Regulators of Myocardial Growth.,” Prog. Biophys. Mol. Biol., **69**(2–3), pp. 559–72.
[169] “ARABIN® Cerclage Pessary Non-Perforated – Dr. Arabin GmbH & Co. KG” [Online]. Available: https://dr-arabin.de/produkt/arabin-cerclage-pessary-non-perforated/?lang=en. [Accessed: 23-May-2019].
[170] 2017, “Treatment for Premature Birth/Cervical Incompetence” [Online]. Available: https://www.tommys.org/pregnancy-complications/prem-birth/treatment/cervical-incompetence. [Accessed: 23-May-2019].
[171] Arabin, B., Halbesma, J. R., Vork, F., Hübener, M., and Eyck, J. van, 2003, “Is Treatment with Vaginal Pessaries an Option in Patients with a Sonographically Detected Short Cervix?,” J. Perinat. Med., **31**(2), pp. 122–133.
[172] Cannie, M. M., Dobrescu, O., Gucciardo, L., Strizek, B., Ziane, S., Sakkas, E., Schoonjans, F., Divano, L., and Jani, J. C., 2013, “Arabin Cervical Pessary in Pregnant Women at High-Risk of Premature Birth: An MR Imaging Observational Follow-up Study,” Ultrasound Obstet. Gynecol., **42**(4), p. n/a-n/a.
[173] Becher, N., Waldorf, K. A., Hein, M., and Uldbjerg, N., 2009, “The Cervical Mucus Plug: Structured Review of the Literature,” Acta Obstet. Gynecol. Scand., **88**(5), pp. 502–513.
[174] Mendoza, M., Ribera, I., Maiz, N., Goya, M., and Carreras, E., 2019, “Cervical Modifications after Pessary Placement in Singleton Pregnancies with Maternal Short Cervical Length: 2D and 3D Ultrasound Evaluation,” Acta Obstet. Gynecol. Scand., p. aogs.13647.
[175] Badir, S., Bajka, M., and Mazza, E., 2013, “A Novel Procedure for the Mechanical Characterization of the Uterine Cervix during Pregnancy,” J. Mech. Behav. …, **27**(C), pp. 143–53.
[176] Mazza, E., Parra-Saavedra, M., Bajka, M., Gratacos, E., Nicolaides, K., and Deprest, J., 2014, “In Vivo Assessment of the Biomechanical Properties of the Uterine Cervix in Pregnancy,” Prenat. Diagn., **34**(1), pp. 33–41.
[177] Myers, K. M., Paskaleva, a. P., House, M., and Socrate, S., 2008, “Mechanical and Biochemical Properties of Human Cervical Tissue,” Acta Biomater., **4**(1), pp. 104–116.
[178] Shi, L., Yao, W., Gan, Y., Zhao, L., Mckee, W., Vink, J., Wapner, R., Hendon, C., and Myers, K., 2019, *Anisotropic Material Characterization of HumanCervix Tissue Based on Indentation*.
[179] Shynlova, O., Kwong, R., and Lye, S. J., 2010, “Mechanical Stretch Regulates Hypertrophic Phenotype of the Myometrium during Pregnancy.,” Reproduction, **139**(1), pp. 247–53.
[180] Goldstein, A., 2000, “Errors in Ultrasound Digital Image Distance Measurements.,” Ultrasound Med. Biol., **26**(7), pp. 1125–32.